

Science

17 May 2013 | \$10



BD Horizon™ Brilliant Violet™ Polymer Conjugates

Bright dyes help resolve rare and dim cell populations

Helping nature to reveal itself.

Now you can resolve rare or dim cell populations with BD Horizon™ Brilliant Violet™ polymer conjugates from BD Biosciences.

Developed from pioneering polymer dye technology acquired from Singen Ltd., BD Horizon Brilliant Violet dyes are brighter than conventional dyes. Improved brightness enables you to identify cell populations with lower receptor density than was previously possible, resolving cell populations previously obscured.



Helping all people
live healthy lives

The complete portfolio of BD conjugated antibodies can be used to explore cellular features and characterize cells through surface, intracellular, or secreted markers. To ensure you can use BD reagents across your entire multicolor panel, our portfolio contains a broad selection of fluorochrome-conjugated antibodies.

Request a free sample, or find out how you can use BD Horizon Brilliant Violet polymer conjugates with our expanded set of tools and information at bdbiosciences.com/go/brilliant.



cell sciences[®]
cytokine center



Buy one, get one free

Stock up now on select cytokines, growth factors and chemokines.

Order any two vials from this list for just \$235

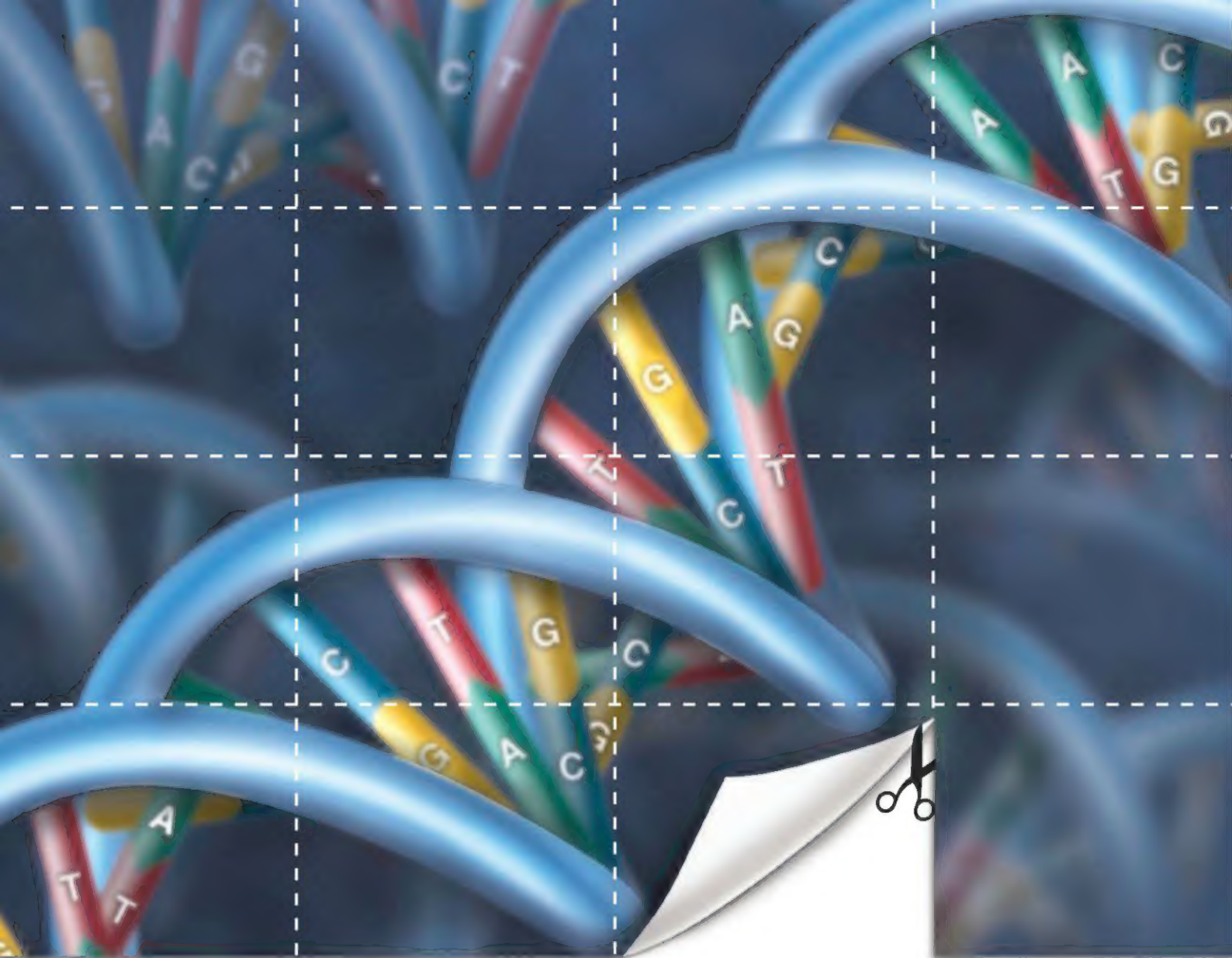
Enter promo code CYT241 when you place your order on-line or mention the promo code to get your discount when calling our toll-free number 888-769-1246.

These recombinant proteins are low endotoxin, carrier-free, highly pure, biologically active and suitable for cell culture and animal studies. Get two of the same item or pick any two different items from the list.* See our web site for complete product specifications.

Browse our web site of recombinant proteins, including hundreds more cytokines, growth factors, chemokines and neurotrophins. Bulk quantities of these proteins are available at competitive pricing. Call or visit our web site for details. Cell Sciences also carries corresponding antibodies and ELISA kits.

Catalog No:	Item:	Size:
CRB100B	Recombinant Human BMP-2	10 µg
CRC400B	Recombinant Human CNTF	20 µg
CRF000B	Recombinant Human FGF-acidic/FGF1	50 µg
CRF001B	Recombinant Human FGF-basic/FGF2	50 µg
CRK300B	Recombinant Human FGF-7/KGF	10 µg
CRG300B	Recombinant Human G-CSF/CSF3	10 µg
CRG100B	Recombinant Human GM-CSF/CSF2	20 µg
CRG101B	Recombinant Mouse GM-CSF/CSF2	20 µg
CRG500B	Recombinant Human GRO-alpha/CXCL1	25 µg
CRG502B	Recombinant Rat GRO-alpha/KC/CXCL1	25 µg
CRI004B	Recombinant Human IFN-alpha 2b	100 µg
CRI000B	Recombinant Human IFN-gamma	100 µg
CRI001B	Recombinant Mouse IFN-gamma	100 µg
CRI002B	Recombinant Rat IFN-gamma	100 µg
CRI500B	Recombinant Human IGF-1	100 µg
CRI100B	Recombinant Human IL-2	50 µg
CRI153B	Recombinant Human IL-10	10 µg
CRI137B	Recombinant Human IL-15	10 µg
CRI162B	Recombinant Human IL-17	25 µg
CRI172B	Recombinant Human IL-21	10 µg
CRI225B	Recombinant Human IL-33	10 µg
CRM151B	Recombinant Human M-CSF/CSF1	10 µg
CRR000B	Recombinant Human RANTES/CCL5	20 µg
CRS000B	Recombinant Human SDF-1 alpha	10 µg
CRS002B	Recombinant Human SDF-1 beta	10 µg
CRT100B	Recombinant Human TNF-alpha	50 µg
CRT192B	Recombinant Mouse TNF-alpha	20 µg
CRV000B	Recombinant Human VEGF 165	10 µg
CRV014B	Recombinant Mouse VEGF 165	10 µg

* Good on orders in US and Canada only. This offer may not be combined with other offers or discounts. All products for research use only.



Cut smarter.

Restriction enzymes from NEB –
now with CutSmart™ Buffer

You make smart choices every day. Why stop there? The choice to use restriction enzymes from New England Biolabs is now even easier.

- Choose from > 200 restriction enzymes supplied with a single buffer
- Simplify your double digest reactions
- Reduce your pipetting steps by no longer having to add BSA

Now, that's Smart!



Explore the smarter choice at
NEBCutSmart.com

 NEW ENGLAND
BioLabs Inc.
enabling technologies in the life sciences

EDITORIAL

- 787 Impact Factor Distortions
Bruce Alberts

NEWS OF THE WEEK

- 792 A roundup of the week's top stories

NEWS & ANALYSIS

- 795 Human Stem Cells From Cloning, Finally
797 Synthetic Vaccine Strain May Speed Up Pandemic Response
 >> Science Translational Medicine Research Article by P. Dormitzer et al.
798 Melting Glaciers, Not Just Ice Sheets, Stoking Sea-Level Rise
 >> Report p. 852
799 More Genomes From Denisova Cave Show Mixing of Early Humans
801 Lawmakers Await NSF's Response to Query About Grants

NEWS FOCUS

- 802 Troubled Waters for Ancient Shipwrecks
 From Quarry to Temple
808 Following the Flavor
 A Floating Lab Explores the Fringes of Science and Gastronomy
 >> Science Podcast

LETTERS

- 810 China's "Love Canal" Moment?
 C. Zheng and J. Liu
 The True Challenge of Giant Marine Reserves
 D. M. Kaplan et al.
 Response
 C. Pala

811 TECHNICAL COMMENT ABSTRACTS

BOOKS ET AL.

- 812 Ginkgo
 P. Crane, reviewed by J. C. McElwain
813 The Great Fossil Enigma
 S. J. Knell, reviewed by P. Donoghue

POLICY FORUM

- 814 Troubling Trends in Scientific Software Use
 L. N. Joppa et al.
 >> Science Podcast

PERSPECTIVES

- 816 Immunity and Invasive Success
 S. E. Reynolds
 >> Report p. 862
817 Insulin Finds Its Niche
 S. W. Cheetham and A. H. Brand
818 Quartz on Silicon
 C. J. Brinker and P. G. Clem
 >> Research Article p. 827
820 Our Viral Inheritance
 R. A. Weiss and J. P. Stoye
821 Ghost Imaging in Three Dimensions
 D. Faccio and J. Leach
 >> Report p. 844
822 Complexity from Simplicity
 E. Vlieg
 >> Research Article p. 832
823 (Poly)Combing the Pediatric Cancer Genome for Answers
 M. A. Morgan and A. Shilatifard
 >> Report p. 857
825 Retrospective: Robert G. Edwards (1925–2013)
 S. J. Fisher and L. C. Giudice

REVIEW

- 826 Impact of Shale Gas Development on Regional Water Quality
 R. D. Vidic et al.
 Review Summary; for full text:
 <http://dx.doi.org/10.1126/science.1235009>
 >> Science Podcast

CONTENTS continued >>



page 802



page 813

ON THE WEB THIS WEEK

>> Science Podcast

Listen to stories on fracking, troubling science software, taste science, and more.

>> Find More Online

Check out Science Express, our podcast, videos, daily news, our research journals, and Science Careers at www.sciencemag.org.



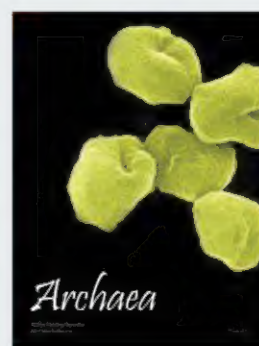
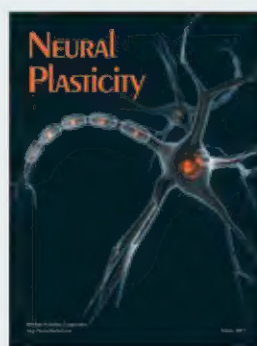
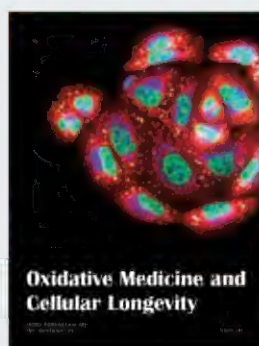
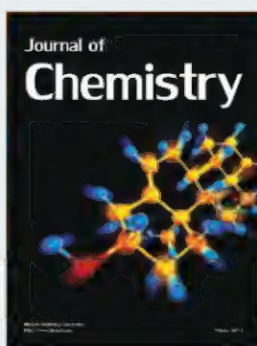
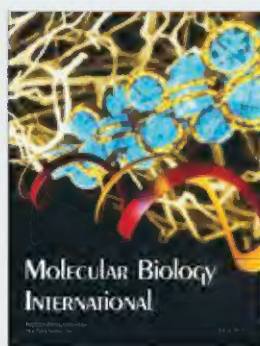
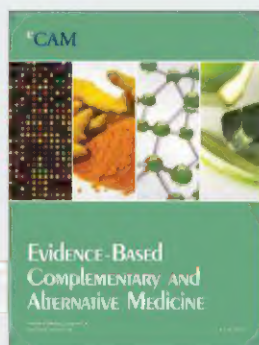
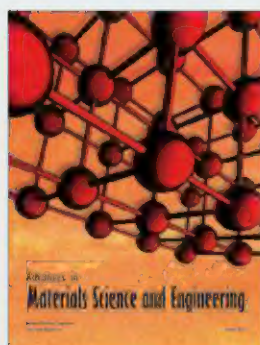
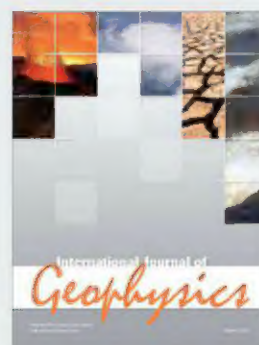
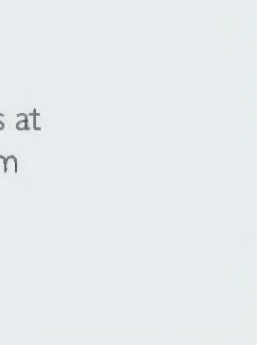
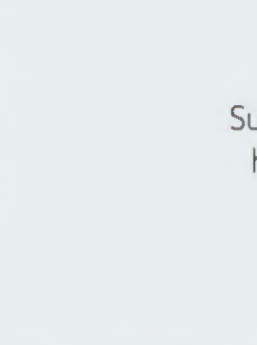
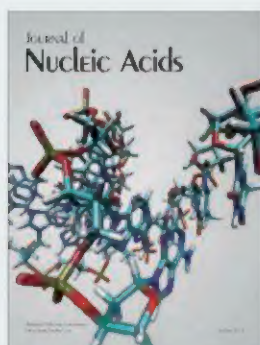
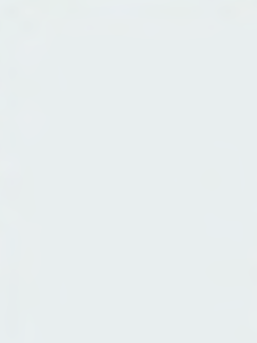
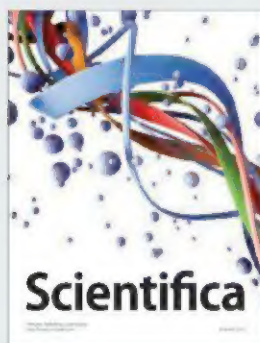
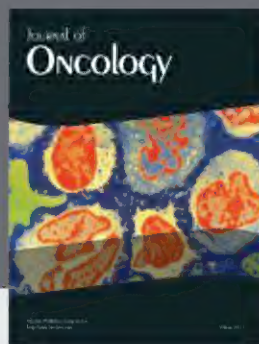
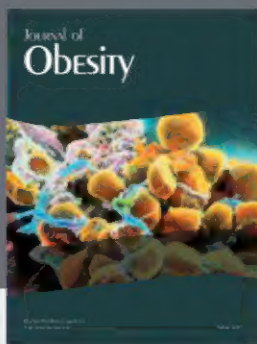
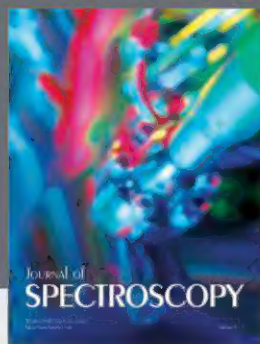
COVER

False-colored scanning electron microscopy image of carbonate-silica "flowers," each ~50 micrometers high. A vast array of similarly complex, well-defined microstructures can be sculpted by manipulating conditions such as pH, temperature, and carbon dioxide concentration. With insight into molecular growth mechanisms, these structures are dynamically steered toward arbitrary, hierarchically assembled architectures. See pages 822 and 832, as well as a slideshow online.

Image: Wim Noorduin and Joanna Aizenberg

DEPARTMENTS

- 785 This Week in Science
788 Editors' Choice
790 Science Staff
883 New Products
884 Science Careers



Hindawi

Submit your manuscripts at
<http://www.hindawi.com>

RESEARCH ARTICLES

- 827 Soft-Chemistry–Based Routes to Epitaxial α -Quartz Thin Films with Tunable Textures**
A. Carretero-Genevri et al.
 Porous and dense piezoelectric films of α -quartz crystals are epitaxially grown on silicon substrates.
 >> *Perspective p. 818*
- 832 Rationally Designed Complex, Hierarchical Microarchitectures**
W. L. Noorduin et al.
 Complex solids are crafted through small changes to the solution conditions in a reaction-diffusion coupled system.
 >> *Perspective p. 822; Slideshow*
- 837 Dual Molecular Signals Mediate the Bacterial Response to Outer-Membrane Stress**
S. Lima et al.
 Gram-negative bacteria monitor lipopolysaccharide and outer-membrane protein status to detect and respond to problems.

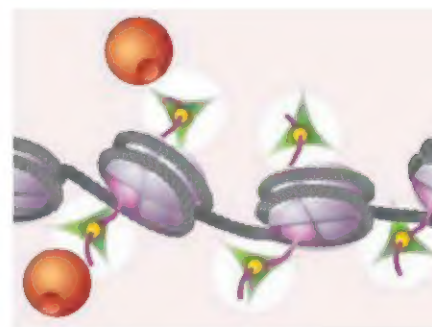
REPORTS

- 841 Phase Diagram of the Topological Superfluid ^3He Confined in a Nanoscale Slab Geometry**
L. V. Levitov et al.
 Geometrical confinement affects the stability of the superfluid phases of helium-3.
- 844 3D Computational Imaging with Single-Pixel Detectors**
B. Sun et al.
 A computational imaging method is used to reconstruct a three-dimensional scene, without the need for lenses.
 >> *Perspective p. 821*
- 847 Computationally Assisted Identification of Functional Inorganic Materials**
M. S. Dyer et al.
 A method using extended building blocks is developed for computationally viable predictions of stable crystal structures.
- 852 A Reconciled Estimate of Glacier Contributions to Sea Level Rise: 2003 to 2009**
A. S. Gardner et al.
 A model is developed to describe the complex dynamics of dry foams across a range of time and length scales.
 >> *News story p. 798*

- 857 Inhibition of PRC2 Activity by a Gain-of-Function H3 Mutation Found in Pediatric Glioblastoma**
P. W. Lewis et al.
 Mutations of histones in some cancers result in inhibition of enzymes that lay down epigenetic marks on chromatin.
 >> *Perspective p. 823*
- 862 Invasive Harlequin Ladybird Carries Biological Weapons Against Native Competitors**
A. Vilcinskas et al.
 Invasive ladybugs harbor microsporidia that kill nonresistant beetles contributing to the original residents' decline.
 >> *Perspective p. 816*
- 864 Nuclear Actin Network Assembly by Formins Regulates the SRF Coactivator MAL**
C. Baarlink et al.
 A dynamic polymeric actin structure inside the nucleus is part of the serum response in mammalian tissue culture cells.
- 867 Wnt Stabilization of β -Catenin Reveals Principles for Morphogen Receptor-Scaffold Assemblies**
S.-E. Kim et al.
 The scaffold protein Axin has an active role in modulating signaling through the Wnt pathway.
- 871 Activation of the Yeast Hippo Pathway by Phosphorylation-Dependent Assembly of Signaling Complexes**
J. M. Rock et al.
 A scaffold protein provides a two-step regulatory mechanism to control the exit from mitosis in yeast.
- 875 ATAXIN-2 Activates PERIOD Translation to Sustain Circadian Rhythms in *Drosophila***
C. Lim and R. Allada
- 879 A Role for *Drosophila* ATX2 in Activation of PER Translation and Circadian Behavior**
Y. Zhang et al.
 Fruit fly circadian clock function requires protein translation regulated by an RNA-binding protein.



pages 821 & 844



pages 823 & 857

SCIENCE (ISSN 0036-8075) is published weekly on Friday, except the last week in December, by the American Association for the Advancement of Science, 1200 New York Avenue, NW, Washington, DC 20005. Periodicals Mail postage (publication No. 484460) paid at Washington, DC, and additional mailing offices. Copyright © 2013 by the American Association for the Advancement of Science. The title SCIENCE is a registered trademark of the AAAS. Domestic individual membership and subscription (S1 issues): \$149 (\$74 allocated to subscription). Domestic institutional subscription (S1 issues): \$990; Foreign postage extra: Mexico, Caribbean (surface mail) \$55; other countries (air assist delivery) \$85. First class, airmail, student, and emeritus rates on request. Canadian rates with GST available upon request, GST #1254 88122. Publications Mail Agreement Number 1069624. Printed in the U.S.A.

Change of address: Allow 4 weeks, giving old and new addresses and 8-digit account number. Postmaster: Send change of address to AAAS, P.O. Box 96178, Washington, DC 20090-6178. Single-copy sales: \$10.00 current issue, \$15.00 back issue prepaid includes surface postage; bulk rates on request. Authorization to photocopy material for internal or personal use under circumstances not falling within the fair use provisions of the Copyright Act is granted by AAAS to libraries and other users registered with the Copyright Clearance Center (CCC) Transactional Reporting Service, provided that \$30.00 per article is paid directly to CCC, 222 Rosewood Drive, Danvers, MA 01923. The identification code for Science is 0036-8075. Science is indexed in the Reader's Guide to Periodical Literature and in several specialized indexes.

Demanding Transfection. Easy Solution.



Focus your efforts on discovery. Efficiently transfect difficult cells, including more than 100 cancer cell lines using **X-tremeGENE DNA Transfection Reagents**.



Free sample and protocols at
www.x-tremegene.roche.com

For life science research only.
Not for use in diagnostic procedures.

X-TREMEGENE is a trademark of Roche.

Roche Diagnostics GmbH
Sandhofer Straße 116
68305 Mannheim, Germany

© 2013 Roche Diagnostics.
All rights reserved.





<< Surprise Attack

Humans conduct the largest ecological experiment ever by continually moving species between continents. For example, the harlequin ladybird beetle, native to Asia, has become highly invasive in many regions after being introduced for biological control, but we do not understand why this species should so readily outcompete native ladybirds. **Vilcinskis *et al.*** (p. 862; see the Perspective by **Reynolds**) show that harlequin beetles have parasitic microsporidia within their hemolymph, which are fatal to other ladybird beetles that prey on harlequin beetle eggs and larvae. Harlequin beetles thus have an innate advantage over species that are otherwise equivalent in their abilities, but this sort of competitive advantage can be hard to spot.

Fracturing Hydrology?

Hydraulic fracturing, widely known as "fracking," is a relatively inexpensive way to tap into what were previously inaccessible natural gas resources. **Vidic *et al.*** (p. 826) review the current status of shale gas development and discuss the possible threats to water resources. In one of the hotbeds of fracking activity, the Marcellus Shale in the eastern United States, there is little evidence that additives have directly entered groundwater supplies, but the risk remains. Ensuring access to monitoring data is an important first step toward addressing any public and environmental health concerns.

Fabricating Quartz

Quartz is used industrially as an abrasive, as an inert glassy material, or for high-quality crystals in microelectronics. It is also valued for its piezoelectronic properties. However, it is hard to grow quartz as a patterned material or to integrate it into nanostructured devices. **Carretero-Genevri *et al.*** (p. 827; see the Perspective by **Brinker and Clem**) have developed a method for preparing oriented epitaxial thin films of polycrystalline α -quartz on single-crystal silicon substrates using ambient pressure and temperatures below 1000°C. Different processing conditions can be used to fabricate quartz films with a variety of pore sizes or as a dense nonporous α -quartz film.

Falling Out

During simple precipitation, molecules fall out of solution from locations of highest concentration and, consequently, the shape of the precipitate will be dictated by its crystal-

lization thermodynamics. **Noorduyn *et al.*** (p. 832; see the Perspective by **Vlieg**) designed micrometer-scale structures by varying the reaction conditions for silica and carbonate precipitation in which precipitation changes the local concentration and acidity to alter the next stage of precipitation, thus controlling whether the solid phase grows toward or away from the bulk solution. The result is the ability to design and generate a variety of complex structures by simple reaction-diffusion processes.

Stress Inside Out

In Gram-negative bacteria, the integrity of the outer membrane is crucial for survival and is an important aspect of resistance to antibiotics. The biogenesis of the major components lipopolysaccharide (LPS) and outer-membrane protein (OMP) of the outer membrane begins in the cytoplasmic compartment, involves export across the inner membrane and transport through the periplasm, and finally requires active insertion into the outer membrane by specialized assembly machines. **Lima *et al.*** (p. 837) supply results for a model in which serious defects in LPS biogenesis also create problems for OMP biogenesis, thereby producing the two signals needed to activate the σ^F stress response pathway.

ATAXIN Clock

Although core components of circadian clocks in flies and mammals are transcriptional circuits, recent evidence indicates posttranscriptional regulation of the clock occurs. Studies from **Lim and Allada** (p. 875) and **Zhang *et al.*** (p. 879) converge to show that the protein ATAXIN-2, associated with neurodegenerative diseases in humans, is a regulator of translation required

for normal clock function in pacemaker neurons and for daily rhythms of behavior. ATAXIN is an RNA-binding protein and cooperates in the accumulation of the Per (Period) protein, a core transcriptional regulatory component of the clock.

Melting Away

We assume the Greenland and Antarctica ice sheets are the main drivers of global sea-level rise, but how large is the contribution from other sources of glacial ice? **Gardner *et al.*** (p. 852) synthesize data from glaciological inventories to find that glaciers in the Arctic, Canada, Alaska, coastal Greenland, the southern Andes, and high-mountain Asia contribute approximately as much melt water as the ice sheets themselves: 260 billion tons per year between 2003 and 2009, accounting for about 30% of the observed sea-level rise during that period.



Nuclear Actin in Action

Actin polymerization is essential for structures in mammalian cells. Although actin filament network structures are observed in the cytoplasm and at the plasma membrane, monomeric actin is also seen in the nucleus. **Baarlank *et al.*** (p. 864, published online 4 April) directly visualized a distinct and dynamic actin network within the nucleus in living cells. The network spanned the entire nucleus and appeared to be enriched along the nuclear cortex. Transient formation of a nuclear actin network may be induced by the transcriptional serum response.

Grete Lundbeck European Brain Research Foundation

Call for Nominations for

THE BRAIN PRIZE

THE PRIZE OF € 1 MILLION WILL BE AWARDED IN COPENHAGEN 1 MAY 2014

Nominations by 15 September 2013

Nominations will be reviewed by the Selection Committee:

YVES AGID, FRANCE

HUDA AKIL, USA

ANDERS BJÖRKLUND, SWEDEN, VICE-CHAIRMAN

COLIN BLAKEMORE, UNITED KINGDOM, CHAIRMAN

FRED H. GAGE, USA

FLORIAN HOLSBOER, GERMANY

RANGA R. KRISHNAN, SINGAPORE

JES OLESEN, DENMARK

FOR THE NOMINATION FORM AND DETAILS OF THE NOMINATION PROCEDURE, PLEASE VISIT:

WWW.THEBRAINPRIZE.ORG

Prize Winners 2013

Ernst Bamberg, MPIBP, Frankfurt am Main, Germany, Ed Boyden, MIT, Cambridge, MA, USA,
Karl Deisseroth, Stanford University, CA, USA, Peter Hegemann, Humboldt University, Berlin, Germany,
Gero Miesenböck, University of Oxford, United Kingdom and Georg Nagel, University of Würzburg, Germany



The Brain Prize recognizes and rewards outstanding contributions to European neuroscience, from basic to clinical



Bruce Alberts is Editor-in-Chief of *Science*.

Impact Factor Distortions

THIS EDITORIAL COINCIDES WITH THE RELEASE OF THE *SAN FRANCISCO DECLARATION ON RESEARCH Assessment* (DORA), the outcome of a gathering of concerned scientists at the December 2012 meeting of the American Society for Cell Biology.* To correct distortions in the evaluation of scientific research, DORA aims to stop the use of the “journal impact factor” in judging an individual scientist’s work. The *Declaration* states that the impact factor must not be used as “a surrogate measure of the quality of individual research articles, to assess an individual scientist’s contributions, or in hiring, promotion, or funding decisions.” DORA also provides a list of specific actions, targeted at improving the way scientific publications are assessed, to be taken by funding agencies, institutions, publishers, researchers, and the organizations that supply metrics. These recommendations have thus far been endorsed by more than 150 leading scientists and 75 scientific organizations, including the American Association for the Advancement of Science (the publisher of *Science*). Here are some reasons why:

The impact factor, a number calculated annually for each scientific journal based on the average number of times its articles have been referenced in other articles, was never intended to be used to evaluate individual scientists, but rather as a measure of journal quality. However, it has been increasingly misused in this way, with scientists now being ranked by weighting each of their publications according to the impact factor of the journal in which it appeared. For this reason, I have seen curricula vitae in which a scientist annotates each of his or her publications with its journal impact factor listed to three significant decimal places (for example, 11.345). And in some nations, publication in a journal with an impact factor below 5.0 is officially of zero value. As frequently pointed out by leading scientists, this impact factor mania makes no sense.†

The misuse of the journal impact factor is highly destructive, inviting a gaming of the metric that can bias journals against publishing important papers in fields (such as social sciences and ecology) that are much less cited than others (such as biomedicine). And it wastes the time of scientists by overloading highly cited journals such as *Science* with inappropriate submissions from researchers who are desperate to gain points from their evaluators.‡

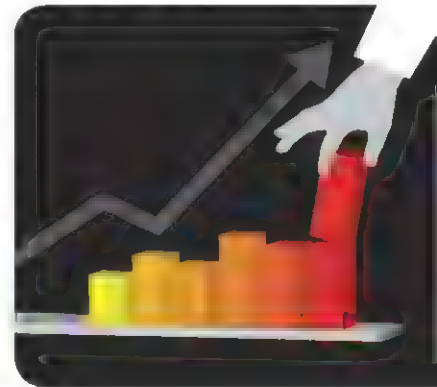
But perhaps the most destructive result of any automated scoring of a researcher’s quality is the “me-too science” that it encourages. Any evaluation system in which the mere number of a researcher’s publications increases his or her score creates a strong disincentive to pursue risky and potentially groundbreaking work, because it takes years to create a new approach in a new experimental context, during which no publications should be expected. Such metrics further block innovation because they encourage scientists to work in areas of science that are already highly populated, as it is only in these fields that large numbers of scientists can be expected to reference one’s work, no matter how outstanding. Thus, for example, in my own field of cell biology, new tools now allow powerful approaches to understanding how a large single-celled organism such as the ciliate *Stentor* can precisely pattern its surface, creating organlike features that are presently associated only with multicellular organisms.§ The answers are likely to bring new insights into how all cells operate, including our own. But only the very bravest of young scientists can be expected to venture into such a poorly populated research area, unless automated numerical evaluations of individuals are eliminated.

The DORA recommendations are critical for keeping science healthy. As a bottom line, the leaders of the scientific enterprise must accept full responsibility for thoughtfully analyzing the scientific contributions of other researchers. To do so in a meaningful way requires the actual reading of a small selected set of each researcher’s publications, a task that must not be passed by default to journal editors.

—Bruce Alberts

10.1126/science.1240319

*www.ascb.org/SFdeclaration.html. † K. Simons, *Science* **322**, 165 (2008). ‡ B. Alberts, B. Hanson, K. L. Kelner, *Science* **321**, 15 (2008). § For example, see M. Kirschner, J. Gerhart, T. Mitchison, *Cell* **100**, 79 (2000).





Hawaii's Deep Plumbing System

Mauna Loa and Kilauea—separated by only ~30 km on the island of Hawaii—are presently two of the most active volcanoes in the world. They are fueled by the magmatic activity associated with the Hawaiian hot spot, which provides a rich source of melted mantle materials. Does the activity at one influence the other? Shirzaei *et al.* show, using gas measurements and geophysical data, that the two volcanoes were linked during surges of uprising mantle material between 2006 and 2008. Satellite data of ground deformation and time-dependent inverse modeling suggest that the two volcanoes simultaneously inflated during a time of increased magma supply. A cluster of seismic events 20 km below Mauna Loa, near the deep magma source, immediately preceded activity at Kilauea—including increased CO₂ emissions and a series of shallow “silent earthquakes.” During times when the deep magma supply is not surging, there may be independent or anticorrelated volcanic activity at either volcano, related to older, shallower trapped magma. — NW

Geophys. Res. Lett. **40**, 10.1002/rgl.50470 (2013).

ECONOMICS

A Look at the Data

A lot of people in the United States do not have health insurance, and one aim of the Patient Protection and Affordable Care Act is to expand the coverage of low-income individuals. In 2008, Oregon enrolled about 6000 new applicants, chosen via lottery, in its Medicaid plan. Baicker *et al.* now describe the 2-year outcomes for these individuals in comparison to a control group of 6000 people who had applied but were not chosen. In terms of finances, the enrollees had fared better: They had lower medical expenses and had incurred less debt. In terms of health care access, the enrollees had made more office visits and taken more advantage of preventive screenings. Neither of these outcomes is particularly surprising given the function of health insurance. What was surprising, and disappointing to some, was the lack of effect of coverage on the health of these individuals. This was assessed via many measures, but the most critical were three pre-specified indicators of high blood pressure (mm Hg), high cholesterol (mg/dl), and high blood sugar (glycated Hb); these parameters reflect underlying conditions that predict mortality due to chronic noncommunicable diseases. Changes in these measures might reasonably have been expected to be detectable within the time frame of 2 years, but none were seen. A final take-home message, much less actively debated in the blogosphere, is the importance of performing impact evaluations. — GJC

N. Engl. J. Med. **368**, 1713 (2013).

PATHOGENS

The End of Antiquity

The Justinian Plague, which resurfaced regularly between the 6th and 8th centuries, is thought to have assisted the decline of the Roman Empire, but it has, until now, only been speculatively diagnosed as bubonic plague caused by the bacterium *Yersinia pestis*. Using stringent ancient DNA anticontamination protocols, Harbeck



et al. have genotyped new material from the early medieval graveyard at Aschheim, Bavaria, dating from the 6th century. This graveyard contained 438 individuals, often in multiple burials—a sign of crisis. The amount of bacterial material available was scant, but *Y. pestis* was identified from one individual using five key

single-nucleotide polymorphisms identified in recent phylogenies. Genotyping confirmed this isolate as basal to isolates from the 14th-century Black Death and the modern (19th-century) third pandemic and that, like the other pandemics, it originated in China or Mongolia. — CA

PLoS Pathogens **9**, 10.1371/journal.ppat.1003349 (2013).

CHEMISTRY

UN Coaxed to Neutrality

The enormous quantity of energy released through fission of the uranium (U) nucleus has lent the element a widespread, intimidating reputation. At the lower energies prevailing in conventional chemistry, where electrons rather than neutrons are exchanged, U remains an intriguing target of study, chiefly on account of the involvement of f orbitals in its bonding motifs. In this context, a long-sought coordination complex in which U formed a triple bond to nitrogen (N) was recently prepared (King *et al.*, Reports, 10 August 2012, p. 717). The complex had a net negative charge (with U in the +5 oxidation state) that was compensated for by a sodium ion and relied for its stability on a protective chelating ligand. King *et al.* have now built on this prior work to oxidize the U(V) anion and thereby isolate, and structurally characterize, a neutral U(VI) nitride complex. Iodine proved the optimal outer sphere oxidant, and it was necessary that the sodium remain sequestered by a crown ether; attempts to oxidize a dimeric precursor with sodium

bridging the terminal Ns led to competing halogenation in the coordination sphere. The U(VI)=N linkage was prone to photoaccelerated C-H insertion chemistry, perhaps accounting for the failure of prior attempts to generate related motifs photolytically. — JSY

Nat. Chem. **5**, 10.1038/nchem.1642 (2013).

CHEMISTRY

Shepherding Stem Cells

Stem cells, because of their ability to differentiate into multiple cell types, are of interest in aiding tissue repair and for treating diseases such as diabetes. However, their lack of specificity also makes it hard to guide them to the target tissue of concern. Leukocytes express transmembrane receptors that will bind with overexpressed proteins on damaged or pathologic tissues. Using this as their model, Jeong *et al.* synthesized a hyperbranched polyglycerol (HPG) that was covalently modified with octadecyl chains and vasculature binding peptides of sequence VHSPNKK, chosen for its binding affinity toward vascular endothelial adhesion molecules overexpressed by inflamed blood vessels. The modified HPG showed an affinity to bind to cell surfaces but without interfering with the metabolic activity of the cells. Two types of adipose-derived mesenchymal stem cells (MSCs) were used in a flow cell across an endothelial cell sheet that had been exposed to tumor necrosis factor- α . The peptide-modified HPG decreased the rolling rate of the MSCs and increased the adhesion of the cells to the endothelium, although only by a factor of 2. — MSL

J. Am. Chem. Soc. **135**, 10.1021/ja400636d (2013).

PHYSICS

Spin Thermometers

Developing sensitive, noninvasive nanoscale thermometry is of great interdisciplinary interest, for example, as a tool for measuring tiny intracellular temperature gradients. Fluorescence-based thermometry provides probes of an appropriate size, but conventional techniques have limited temperature resolution. Toyli *et al.* use the temperature dependence of the energy levels of defect spins in diamond as a basis for sensitive fluorescence thermometry. The defects are of the type called the nitrogen vacancy (NV) center, previously used in magnetic and electric field sensing. To improve the

sensitivity, the researchers extended the spin coherence time using dynamical decoupling; they also showed that the technique worked reliably at temperatures as high as 500 K, whereas a 0.1 K shift was easily resolved. It is expected that the temperature sensitivity can be further improved by extending the coherence times, for example, by using isotopically purified diamond to eliminate the main source of decoherence, ^{13}C . In addition to cellular thermometry, potential thermal sensing applications for NV centers in nanostructured diamond include microfluidic thermometry and scanning thermal microscopy. — JS

Proc. Natl. Acad. Sci. U.S.A. **110**, 10.1073/pnas.1306825110 (2013).

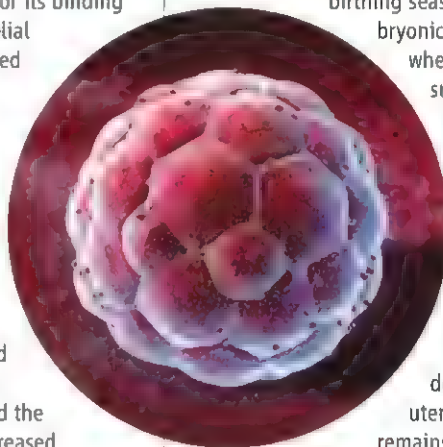
DEVELOPMENTAL BIOLOGY

Putting on the Brakes

Many mammals can delay embryo implantation in order to postpone pregnancy when conditions are unfavorable, or until later birthing seasons. Such embryonic diapause occurs when development is suspended in the blastocyst stage and implantation is prevented. Endocrine factors trigger diapause; however, the mechanism coordinating blastocyst dormancy and uterine quiescence remains unknown. Cha *et al.* show that the gene *Msx1*

is expressed when implantation is delayed, whether it occurs because of maternal lactation, ovariectomy, or the addition of antiestrogen. When implantation initiates, *Msx1* expression is down-regulated. Further, genetic inactivation of *Msx1* or *Msx2* in the uterus results in the development of fewer blastocysts. In order for delayed implantation to occur, blastocyst dormancy must coincide with uterine quiescence. This work demonstrates a critical role of *Msx1* in maternal regulation of embryonic diapause. The study finds that three distantly related mammalian orders—Rodentia (mouse), Carnivora (American mink), and Diprotodontia (Australian tammar wallaby)—display correlations between *Msx* expression and diapause, suggesting the presence of a conserved reproductive strategy across mammalian species. — BAP

Open Biol. **3**, 10.1098/rsob.130035 (2013).



Join the Conversation!

Twitter is a great way to connect with AAAS members and staff about the issues that matter to you most. Be a part of the discussion while staying up-to-date on the latest news and information about your personal member benefits.

Follow us
@AAASmember
and join the
conversation with
#AAAS



MemberCentral.aaas.org



STAY INFORMED! STAY CONNECTED!

Get more from your AAAS membership

Are you currently registered to receive e-mails from AAAS and *Science*?

E-mail is the primary way that AAAS communicates with our members about AAAS programs, new member benefits, invitations to special events, and, of course, the latest news and research being published in *Science*.

Sign up today to receive e-mails from AAAS and ensure that you are getting the most out of your membership and *Science* subscription.*

To get started visit: promo.aaas.org/stayconnected

You'll need your AAAS Member number. Find it above your name on your *Science* mailing label.

Don't miss a thing. Sign up for e-mail communications from AAAS today!



AROUND THE WORLD



Washington, D.C. 1

Supreme Court Upholds Soybean Patents

Don't blame the bean: In a unanimous decision on 13 May, the U.S. Supreme Court backed the agribusiness firm Monsanto on its soybean patents. The justices concluded that an Indiana farmer, Vernon Hugh Bowman, violated the company's intellectual property rights when he refused to pay royalties on unlabeled soybeans that he bought that contained genes patented by the company.

Bowman didn't dispute Monsanto's patents, which apply to genes that make soybeans resistant to the herbicide glyphosate. But he argued that his seed purchases weren't covered by Monsanto's patent license, claiming that the company's right to charge royalties had been "exhausted" because the unlabeled seeds he bought and planted were the progeny of plants grown from previously purchased Monsanto seed.

The court also rejected an argument that Bowman was not liable because the beans themselves—and not the farmer—replicated Monsanto's patented genes. "We think that blame-the-bean defense tough to credit," Justice Elena Kagan wrote in the 13 May opinion. "Bowman was not a passive observer of his soybeans' multiplication." <http://scim.ag/monsantoruling>



No beans. Bowman at the Supreme Court in February.

Moscow 2

Scientists Decry New Funding Rules

Russian researchers are up in arms over a government decree issued last month, which requires any organization that wants to award a grant to Russian researchers to obtain permission from the Ministry of Education and Science. If the project to be funded is not in line with the priorities of basic research and R&D in Russia approved by the government, the ministry may decline the request and the organization will not be allowed to award the grants.

"Effectively, the decree introduces a total ban on foreign grant funding of research," says Andrey Tsaturyan of Moscow State University's Mechanics Research Institute. "If organizations know that each time they award a grant to a Russian candidate they will have to request permission and risk refusal, they will just stop giving us grants," he says. The decree does include a list of 13 agencies that are exempt from the rules, including IAEA [the International Atomic Energy Agency], a few U.N. organizations, the Council of the Baltic Sea States, etc., "that is, bodies of which Russia is a member," Tsaturyan adds. "There is no serious scientific foundation on this list." <http://scim.ag/Russfund>

Paris 3

No Financial Misconduct, Says Institut

The Institut Pasteur has denied accusations by a government watchdog that it misleads research donors. In a scathing report published earlier this month, the Inspection Générale des Affaires Sociales (IGAS) said the biomedical research organization mas-



Unfounded? Institut Pasteur denies misconduct.

sages figures to attract private donations and government funding. The institute "artificially" presents its balance sheet to funders as "structurally in the red" to appear vulnerable, the authors write, although the institute's endowment was worth €658 million in investment funds in 2011—bringing its total wealth to about €1 billion.

The accusations have shaken up the venerable institute, a nonprofit research foundation focused on infectious diseases. Pasteur receives about €60 million from the French government and €50 million in donations every year.

In a statement dated 3 May, Institut Pasteur dismissed IGAS's accusations as unfounded. "The endowment allows the Institut Pasteur to shield itself from uncertainties that could affect the level of its different funding sources in the long term," the statement says.

But Alain Guédon, who served as Pasteur's vice president for business development between 2007 and 2009, says the report reflects his own experience and frustration during his stint at the institute.

<http://scim.ag/Pastmisc>

Berlin 4

Unraveling the History of East German Clinical Trials

Germany's Charité University Hospital has halted the routine destruction of decades-old clinical trial records to help researchers piece together whether drug tests performed in the East Berlin hospital during the Cold War adhered to international ethics standards. Allegations that pharma companies used East Germany as a cheap testing ground have been voiced before. But on 13 May, the news magazine *Der Spiegel* charged that more than 600 such trials had been carried out in East German hospitals by German, Swiss, and U.S. companies, often without informing patients about possible risks and side effects.

Volker Hess, director of the Charité's institute of the history of medicine, responded in a 13 May statement that he is preparing to examine how patients at the time were informed, how consent was handled, and how doctors dealt with side effects.

CREDITS (TOP TO BOTTOM): IP3 PRESS/MAXPPP/NEWS.COM, J. SCOTT APPLEWHITE/AP PHOTO

Lending STEM a Helping Hand

Last week, the National Science Foundation (NSF) announced the winners of a unique initiative addressing President Barack Obama's call for U.S. high-tech companies to help train 1 million more STEM graduates by 2020. Nine university-based teams taking novel approaches to lowering dropout rates among minorities, women, and low-income students in computer science and engineering will share \$10 million—and the money comes not from federal coffers but from Intel and GE, under a unique arrangement spawned by the President's Council on Jobs and Competitiveness.

The jobs council is defunct, but Intel's Tiffany Sargent worked with NSF officials to piggyback on an existing \$25-million-a-year NSF program to expand the undergraduate STEM talent pool. Acting NSF Director Cora Marrett, shown with computer science major Cassandra Martin at an event honoring the winners, calls the Graduate 10K+ initiative "a starting point" for further government collaborations with corporate and nonprofit donors.



"We're hoping to achieve a fairly systematic report on this contract research," he said. A spokesperson for the German Association of Research-Based Pharmaceutical Companies, meanwhile, said that standards for clinical studies in East Germany had been similar to international standards and were adhered to in practice.

Mogadishu 5

Wild Polio Reappears in Somalia

Wild poliovirus is back in Somalia after a 6-year hiatus. On 11 May, the World Health Organization (WHO) confirmed a case of poliovirus type 1 in a 32-month-old girl in Banadir in south central Somalia. Virus was also isolated from three of the child's close contacts. This is the first case of wild polio since March 2007, although the country has had an ongoing outbreak of vaccine-derived poliovirus (VDPV) since 2009, with 18 reported vaccine-derived cases, the most recent in January 2013. Last year, the vaccine strain spread to Kenya, causing three cases in a refugee camp. (VDPVs occur when the virus used to make the attenuated, live vaccine regains its virulence and transmissibility.)

NOTED

>Prepare for a lean year at the National Institutes of Health (NIH), which expects to slash its number of funded new and competing research grants by 703. Total awards, including continuing grants, will fall by around 1357 to 34,902, the lowest in a decade. The figures reflect a 5.5% cut to NIH's \$30.9 billion 2012 budget, mostly due to sequestration. <http://scim.ag/NIHcuts>

The new outbreak poses a serious threat—both to Somalia and across the Horn of Africa—a WHO spokesman says, because large swaths of conflict-torn Somalia have not conducted vaccination campaigns since 2009. On 14 May, the country began vaccinating in the Banadir region, with the goal of reaching 350,000 children.



More rounds are being planned. Meanwhile, a genetic investigation is under way to determine which country the wild virus came from.

San Francisco, California 6

Call to Abandon Journal Impact Factors

More than 150 prominent scientists and 75 scientific groups have taken a stand against using impact factors, a measure of how often a journal is cited, to gauge the quality of an individual's work. They say researchers should be judged by the content of their papers, not where the studies are published.

Journal impact factors, calculated by the company Thomson Reuters, were developed to help libraries decide which journals to order. Some scientists consider the metric flawed: It doesn't distinguish primary research from reviews, and a few highly cited papers can skew a journal's score. Yet

impact factors are also now widely used to assess the performance of individuals and research institutions.

In a declaration drafted last December in San Francisco at the annual American Society for Cell Biology meeting and posted online this week, scientists write: "It is ... imperative that scientific output is measured accurately and evaluated wisely." Their 18 recommendations include urging the research community to "eliminate" the use of journal impact factors in funding, hiring, and promotion decisions. Signatories include *Science's* editor-in-chief (see p. 787); AAAS, *Science's* publisher; dozens of other editors, journals, and societies; and the Wellcome Trust, a major research charity. <http://scim.ag/impact>

NEWSMAKERS

Mass Spectrometry Innovator Nabs Dreyfus Prize

R. Graham Cooks, a chemist at Purdue University in West Lafayette, Indiana, has been awarded the 2013 Dreyfus Prize in the Chemical Sciences.



Cooks was hailed by the award foundation as an "innovative giant" in mass spectrometry, which identifies molecules by tearing them apart, weighing their constituents, and determining their likely original structures.

Cooks is best known for pioneering tandem mass spectrometry, in which molecules in a sample are repeatedly subjected to an electric field that rips the molecules apart and ionizes their components. Doing so successively allows researchers to first separate one class of molecules—say, protein >>

>>NEWSMAKERS

fragments called peptides—and then separate individual peptides further to identify them. The pharmaceutical industry uses this technique to identify both drug targets and potential therapeutics.

Cooks also pioneered efforts to shrink automobile-sized mass spectrometers down to the size of a shoebox—opening the door to myriad uses in homeland security, food safety, and forensics. “Mass spectrometry has had an extraordinary impact on modern science, and Graham Cooks has changed the field in many important ways,” says Richard Zare, a physical chemist at Stanford University in Palo Alto, California. The Dreyfus Prize comes with a medal and a \$250,000 award.

Cell Biology Pioneer Dies

Biochemist **Christian de Duve**, who helped reveal the internal organization and operation of cells, died on 4 May. Suffering from cancer and other ailments, the 95-year-old Nobel laureate opted for euthanasia.

De Duve earned his M.D. and Ph.D. at the Catholic University of Louvain in Belgium. When he began research as a faculty member there in 1947, his ambition was to determine how insulin works. But de Duve's career detoured into cell structure and function when he decided to follow up on a tangential observation about a metabolic enzyme.



de Duve

He likened himself to a voyager, writing, “I have roamed through living cells, but with the help of a centrifuge rather than of a microscope.” Using

centrifugation to sift cellular contents, de Duve discovered the lysosome, a digestive organelle that breaks down food and debris. He also identified another organelle, the peroxisome, which is important for metabolism. De Duve, Albert Claude, and George Palade, all of whom were recognized as

“largely responsible for the creation of modern Cell Biology,” shared the Nobel Prize in physiology or medicine in 1974.

FINDINGS

New Fossils Provide Earliest Glimpse of Ape Origins



When did apes, the group that today includes gorillas, chimpanzees, and humans, splinter off from Old World monkeys, such as baboons and macaques, and go their own

evolutionary way? The answer is critical to understanding primate evolution and the origins of our own species. Molecular evidence from living primates suggests that this split occurred between 25 million and 30 million years ago, but no one has found fossils that old from either group—until now. This week in *Nature*, a team led by scientists at Ohio University in Athens reports finding teeth and partial jaws of an ape ancestor and an Old World monkey ancestor, both dated to 25 million years ago, in the Rukwa Rift in Tanzania. The new species, named *Rukwapithecus fleaglei* (left) and *Nsungwepithecus gunnelli* (right), respectively, arose

at a time when East Africa was undergoing tumultuous climatic, environmental, and tectonic upheavals. <http://scim.ag/apeorig>

U.S. East Coast Not So Passive

A geological tenet holds that so-called “passive” continental margins—coastlines not shaped by earthquakes or volcanoes but instead by the slow accumulation of sediments from rivers and the oceans—tell a relatively straightforward geological history. Those margins, some scientists have suggested, can therefore be used to trace the rise and fall of global sea level over millions of years—and perhaps to assess past melting of the Greenland and Antarctic ice sheets.

But a new study, published online this week in *Science*, notes that these passive margins have a dynamic side (<http://scim.ag/DBRowley>): The slow circulation of hot mantle deep beneath the surface warps the topography over time. In particular, a ridge that runs along much of the U.S. East Coast called the Orangeburg Scarp, previously a centerpiece of past sea-level assessments, has been warped in several places by this mantle flow, the authors note. River incisions and ongoing post-glacial rebound following the retreat of heavy ice sheets further complicate the story. Global models of mantle convection will be needed to make real headway in interpreting past sea-level changes and ice sheet melting, researchers say.

Random Sample

Eating Bugs Could Save the World

With global population rising almost as fast as atmospheric greenhouse gas levels, food security experts are scrambling to find sustainable, environmentally friendly sources of protein to feed those extra mouths. According to a new report by the Food and Agriculture Organization of the United Nations (FAO), the answer may be one that makes many Westerners squirm: edible insects.

The FAO estimates that about 2 billion people regularly dine on more than 1900 species of insects, mostly as part of traditional diets in Asia, Africa, and Latin America. Small, flightless grasshoppers called *chapulines* and maguey worms are often on the menu in Mexico, while fried Thai zebra tarantulas are so popular in Cambodia that they may soon be driven to extinction. To prevent such overharvesting of wild insects, FAO recommends that sustainable insect farming strategies be developed in concert with local farmers, for whom edible insects can provide an important source of income.

But for those who aren't excited to chow down on a plate full of termites, no matter how protein-rich (and delicious) they may be, don't worry: FAO argues that insects have even more potential as affordable, nutritious, and environmentally friendly feed for the animals we'd rather eat, such as chickens and cows.



Science LIVE

Join us on Thursday, 23 May, at 3 p.m. EDT for a live chat on the **new Diagnostic and Statistical Manual of Mental Disorders standards**. Are they still a good guide to psychiatric illness? <http://scim.ag/science-live>

CHM Microscopy Lab
2013/05/30 10:06:54 AM
20x Olympus

BIOMEDICINE

Human Stem Cells From Cloning, Finally

This time it looks like it's for real: Researchers have made personalized human embryonic stem (ES) cells with a method similar to how Dolly the sheep was cloned—though with an added jolt of caffeine.

The success, which produced stem cells carrying DNA belonging to a baby with an inherited disorder, comes 9 years after South Korean researchers claimed in a famously faked paper that they had achieved a similar feat. After their story unraveled, a handful of researchers continued trying, but human eggs, or oocytes, responded poorly to the techniques that have worked in sheep, mice, cows, pigs, and other animals.

Now, thanks to years of work in monkey cells, a group led by Shoukhrat Mitalipov of the Oregon National Primate Research Center in Beaverton reports a recipe that works for human cells. In a paper published online by *Cell* on 16 May, the scientists describe removing the DNA-containing nucleus from human oocytes and then fusing them with either fetal skin cells or skin cells from an 8-month-old baby, producing embryos that carried DNA from the skin cells. They were then able to use those embryos to derive ES cells, which in theory can form any of the body's cell types. "It's a fantastic paper," says Dieter Egli, who studies somatic cell nuclear transfer (SCNT)—the technical term for the cloning technique—at the New York Stem Cell Foundation. "We are looking forward to replicating their results." The result is "a hard-won triumph after many years of diligent research," adds George Daley, a stem cell researcher at Children's Hospital Boston.

While welcomed by many researchers, who envision creating personalized stem cells for therapies or research, the achievement is also likely to stir up old ethical debates about human SCNT, including whether it should be regulated to prevent attempts at reproductive human cloning. In the short term, that shouldn't be a worry, Mitalipov says. Despite more than 100 tries, he and his colleagues have not managed to get any SCNT-derived monkey embryos to implant in a surrogate mother and trigger pregnancy. The cells that give rise to the placenta are underdeveloped in the cloned monkey embryos, he says, and the human SCNT embryos have similar abnormalities.

Those issues don't seem to interfere with deriving stem cells from the embryos. In some experiments, half of the human SCNT embryos that developed to the blastocyst stage (when the embryo forms a hollow ball of cells) gave rise to stable ES cell lines, Mitalipov and his colleagues report.

Given the years of unsuccessful tries, the team had surprisingly good success generating embryos. Fragile human oocytes are easily damaged by the manipulations necessary for nuclear transfer, so the researchers made several tweaks to the process based upon their monkey work. Instead of using an electric pulse to fuse the enucleated oocyte and the nuclear donor cell, they exposed the cells to surface proteins from an inactivated virus, an old technique that had fallen out of favor after Dolly was born. They also added caffeine to the medium that bathed oocytes during the nucleus removal and cell fusion. The caffeine stabilizes key molecules in the oocyte cytoplasm that help reprogram the fused cells into

Caffeinated. Adding a dose of caffeine helps produce cloned human embryos (left) that can provide tailor-made stem cell lines.

an embryonic state, Mitalipov says. Without caffeine, only 11% of the SCNT embryos developed to the blastocyst stage, and none of them produced ES cells. With caffeine, 23% of the SCNT embryos formed blastocysts, and half of them produced ES cells.

This high efficiency could mean that SCNT is not as impractical for creating personalized human stem cells as many observers had expected. But it faces stiff competition from the current method of making genetically matched pluripotent cells, called induced pluripotent stem (iPS) cells. By adding extra copies of several genes to skin or other cells, scientists can reprogram them to behave like ES cells. That technique is much easier than SCNT, and it doesn't require a supply of human oocytes. (The oocytes used in Mitalipov's experiments were donated by healthy volunteers for research purposes; donors were paid \$5000 for their time and trouble, the local rate paid to egg donors for fertility treatments.)

Some researchers have found evidence, however, that there may be subtle but potentially significant differences between the genes expressed in iPS cells and ES cells derived from embryos. The chance to compare SCNT-derived human ES cells with iPS counterparts is one of the most important aspects of the new advance, Daley says. "There may be advantages to SCNT-ES cells, but this must be rigorously proven," he says. In practice, he says, making iPS cells "remains considerably easier."

Rudolf Jaenisch, who studies cellular reprogramming at the Whitehead Institute for Biomedical Research in Cambridge, Massachusetts, says he doubts that human SCNT will be widely used. "For practical reasons, I don't think it will play a major role," Egli and Mitalipov see things differently. "We don't know whether one or another technology has an advantage," Egli says. "I see them as both very useful."

The use of the baby's DNA offers a therapeutic proof of principle, but the researchers have not yet shown that the technique works with adult cells as nucleus donor cells. In previous experiments, it has been easier to clone fetal cells or those from young animals than those from adults. "It needs to be shown that it works with more cells of various ages," Egli says. "But I expect it does."

—GRETCHEN VOGEL

New accessory:
Eppendorf
ThermoTop®



Multiple Talents

The new generation of Eppendorf Temperature Control and Mixing Instruments offer you more than what meets the eye.

Not only do they provide the versatility and accurate temperature control you come to expect, they now also offer you superior mixing performance, outstanding ergonomic operation and a unique ThermoTop.

- > 2D Mix-Control: perfect mixing results in all vessel formats
- > Eppendorf QuickRelease™: ergonomic block exchange in just 2 seconds
- > Intuitive operation: pre-optimized program and temperature keys
- > Eppendorf ThermoTop prevents condensate formation for more accurate results.



www.eppendorf.com/thermomixer-c

Eppendorf®, the Eppendorf logo and Eppendorf ThermoTop® are registered Trademarks of Eppendorf AG, Germany
Eppendorf ThermoMixer™, Eppendorf SmartBlocks™, Eppendorf ThermoStat™ and Eppendorf QuickRelease™ are Trademarks of Eppendorf AG
All rights reserved, including images and graphics. Copyright © 2013 by Eppendorf AG.

INFLUENZA

Synthetic Vaccine Strain May Speed Up Pandemic Response

A new influenza strain called H7N9 that has killed 35 people in China and sickened close to a hundred more has raised an important question once again: Can we produce enough vaccine fast enough if this flu virus, or any other one, turns pandemic tomorrow? Experience with the H1N1 strain in 2009 wasn't reassuring; although vaccines were produced faster than ever before, most doses became available only after that pandemic had run out of steam.

But a group of scientists says we can do better today. In early April, right after H7N9 emerged in China, they used a new gene synthesis method to develop a so-called seed strain, the starter virus from which large amounts of flu vaccine are produced. Details of their method appear in a paper in this week's issue of *Science Translational Medicine* that also describes a dry run with the same technique in 2011; by coincidence, H7N9 was used for that as well (<http://scim.ag/PDormitzer>).

The paper shows that rather than wait for the arrival of a pandemic virus in their labs, companies can produce a vaccine from its gene sequence as soon as that becomes available online—a big step forward, says J. Craig Venter, whose company Synthetic Genomics devised the method with vaccine manufacturer Novartis. The technique could shave up to 4 weeks off vaccine production time, which during a pandemic could save tens of thousands of lives, says team member and virologist Stephan Becker of the University of Marburg in Germany. But other scientists say that the advance alone may leave the world no better prepared for a pandemic.

Seed strains for influenza are made of a lab strain known as PR8, in which the genes for flu's surface proteins, hemagglutinin (HA) and neuraminidase (NA), are replaced by the corresponding genes from the flu strain that the vaccine needs to target. After isolating the target virus from a patient, researchers grow it and ship it to specialized labs, where eggs are co-infected with the target virus and PR8 so that their genomes can mix, or reassort. Scientists then select viruses that carry the HA and NA genes of the target virus and the other six from PR8. The resulting virus is grown in massive amounts and the two proteins are harvested for use in the new vaccine. Now, creating the seed strain alone takes weeks.

Researchers have tried to synthesize the HA and NA genes directly and splice them into PR8's genome, but to correct the errors

that invariably appear—mostly deletions—the genes had to be built up stepwise from small pieces. At each step, the fragments had to be sequenced and the correct ones selected for further assembly; it was “synthesize fast, or synthesize accurately,” says Novartis's Philip Dormitzer in Cambridge, Massachusetts, who led the work on H7N9.



Too little, too late. In 2009, most of the vaccine doses against a new flu strain arrived after the pandemic peaked.

The new method erases this dilemma by producing two complementary strands of the viral genome, from hundreds of synthesized fragments, in a single step. When the two strands latch onto each other, as DNA strands do, they serve as each other's proofreader: Wherever a deletion occurs, a kink appears in the double strand that can be easily detected and corrected by error-correcting enzymes. Some other tweaks also help bring down production time for a seed virus.

The work was initiated by the Biomedical Advanced Research and Development Authority (BARDA), a U.S. agency set up to counter public health emergencies. In an exercise in August 2011, BARDA asked the U.S. Centers for Disease Control and Prevention (CDC) to send Venter's group and Novartis an unknown flu virus—“a curveball,” Dormitzer says—to produce a vaccine against. As it happened, the agency picked an H7N9 strain.

A real-life test came little more than a

month ago, on 31 March, when the Chinese CDC revealed human H7N9 infections and deposited viral sequences in an online database. The next day, scientists at the J. Craig Venter Institute in San Diego synthesized the HA and NA genes; they were immediately sent to the Novartis lab in Cambridge and integrated into PR8. “By April 6, we had our first [seed] virus,” Dormitzer says.

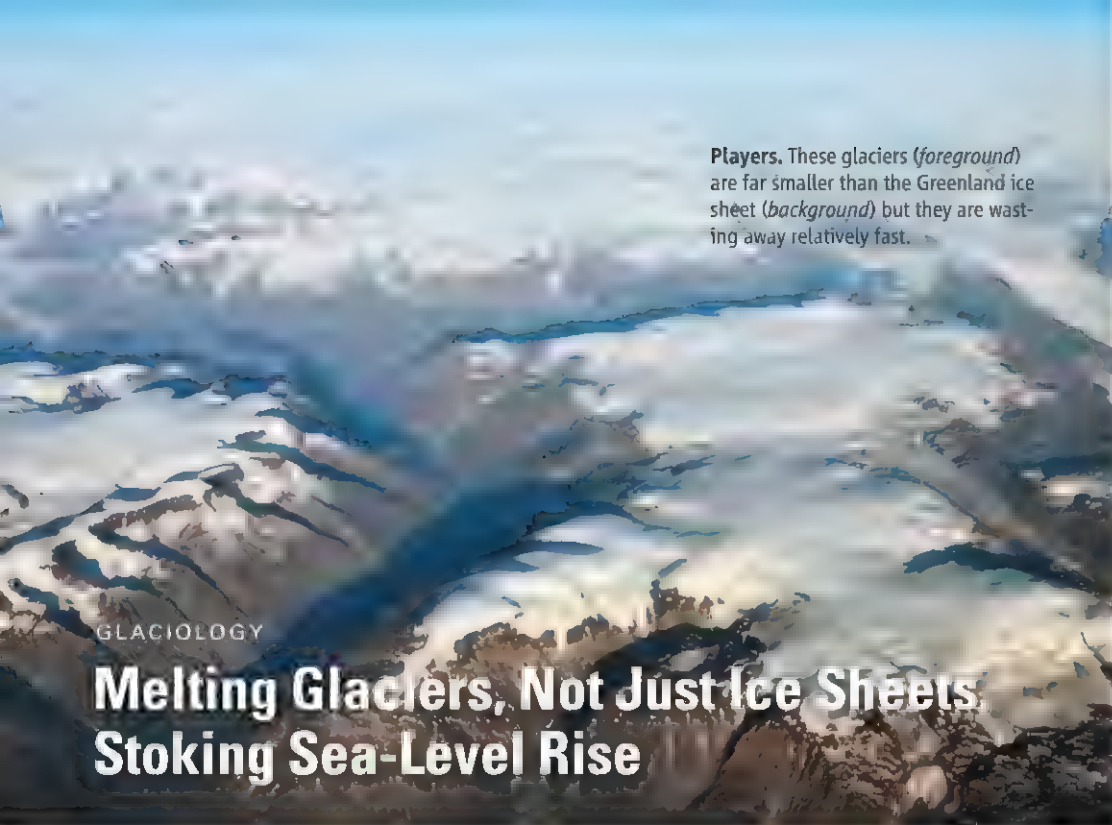
More improvements in the production process are possible. One is a shift from the current, decades-old production system, a cumbersome process that uses massive numbers of chicken eggs, to production in mammalian cells, Venter says. Ultimately, the idea is to have gene synthesis, seed virus production, and vaccine manufacture all under one roof: “All that the government has to do is to send an e-mail there with the sequence and the whole production starts,” he says.

Michael Osterholm of the Center for Infectious Disease Research and Policy at the University of Minnesota, Twin Cities, calls the work “very good science” but says that it may not help much because seed strain production isn't always the limiting factor. Companies don't switch production from seasonal to pandemic flu vaccine until the World Health Organization declares a pandemic, which in 2009 was 7 weeks after the new virus surfaced; a rapidly produced seed strain could just sit around until that decision is made, Osterholm says.

What's more, the most important thing may not be how fast a seed strain is produced, but how easy it is to grow up in massive quantities—and here conventionally produced seed vaccines might have the edge. In the old-fashioned reassortment process, different virus genomes compete with each other, favoring the fastest-growing strain, says John McCauley, an influenza expert at the National Institute for Medical Research in London.

Osterholm argues that it's better to go back to the drawing board. Last year, a study group that he chaired identified a range of other unsolved problems; for instance, manufacturers can produce vaccines for only about 15% of the world's population—with little incentive to make more—and vaccines based on HA and NA offer only a moderate degree of protection. A major investment in radically new vaccines is needed, Osterholm says. Modernizing production methods, he says, is “like putting a 1940 transmission in a 2013 car.”

—KAI KUPFERSCHMIDT



Players. These glaciers (*foreground*) are far smaller than the Greenland ice sheet (*background*) but they are wasting away relatively fast.

GLACIOLOGY

Melting Glaciers, Not Just Ice Sheets Stoking Sea-Level Rise

Glaciologists trekking onto remote, inhospitable streams of flowing ice year after year, decade after decade, brought back some especially bad news early in the last decade. The world's glaciers have been shrinking frighteningly fast, so fast that their melting was pushing up sea level far faster than the shrinking ice sheets of Greenland and Antarctica. But then 21st century monitoring from space began to show a much smaller role for glacial ice loss in sea-level rise. Which to believe?

A new study brings together both boots-on-the-ice and high-tech glaciologists. The study has found that, although the field measurements were painting an accurate picture of the few glaciers being monitored, they were not representative of the world's glaciers. All 19 glacierized regions of the world are losing ice, the study finds, but the iconic glaciers long-studied by field glaciologists are disappearing faster than most. Still, the world's glaciers are losing ice just as fast as the great ice sheets.

"I think there really was a consensus" among the diverse study authors, says J. Graham Cogley of Trent University in Peterborough, Canada, one of the 16 authors on the study. Even after he had spent 20 years compiling field observations that proved to be unrepresentative, Cogley thinks that the group managed to reconcile the conflicting estimates.

The trick to reconciling disparate gauges of ice loss proved to be comparing apples with apples. Before, it was mostly apples and oranges. Field glaciologists had driven poles

vertically into some 300 glaciers out of the world's 160,000 and returned year after year for decades to measure how much more of a pole had been exposed as warming removed ice. Then, they extrapolated the results to the globe as a whole by assuming that the unmeasured glaciers were behaving the same way.

In contrast, a satellite study, which started only in 2003, took a less detailed but global approach. Together, the two satellites of the Gravity Recovery and Climate Experiment (GRACE) measured the minuscule changes of gravity as ice melted away beneath them. GRACE couldn't "see" most individual glaciers, much less the detailed changes revealed by the widely scattered rod surveys, but it surveyed all 734,400 square kilometers of the 19 glacierized regions. And it found far less glacial ice being lost than the field glaciologists had.

To reconcile the difference between gravity-determined and field-determined ice losses, glaciologist Alex Gardner of Clark University in Worcester, Massachusetts, and colleagues put all the data on an equal footing. They compared the most refined versions of GRACE and field data for the same regions over the same period, 2003 to 2009. They then compared them with glacier changes gauged by the orbiting Ice, Cloud, and land Elevation Satellite, another global surveyor that uses a laser to measure changing ice height and therefore volume.

Within the uncertainties, the three gauging techniques agreed wherever they could be compared. Some glaciers might not be

losing ice or might even be gaining a bit, but all 19 glacierized regions lost ice between 2003 and 2009 at a global rate of 259 billion plus or minus 28 billion tonnes per year. That's enough water to raise sea level around the world about 0.7 millimeters per year, an amount roughly equal to the contribution from the shrinking Greenland and Antarctic ice sheets.

"We think this is a very strong result confirmed by three independent methods," Gardner says. The study also showed that field geologists had gotten the shrinkage right for the glaciers they had monitored but that the other glaciers in the same regions were not losing ice as fast.

Space-based geophysicist Erik Ivins of NASA's Jet Propulsion Laboratory in Pasadena, California, says it's "remarkable" that the multidisciplinary team

reached a result so different from conclusions based on traditional field methods. Ground-based glaciologists may not agree at first, he adds, but "over time, I think there will be greater unanimity."

No one quite knows why fieldwork gave larger losses. "I'm inclined to attribute it to bad luck," Cogley says. The glaciers that were accessible and small enough to manage with the available resources turned out to be more vulnerable to warming, he says. Ivins speculates that the hardest glaciers for glaciologists to reach—the most remote, the highest, the coldest, the windiest, those in the roughest terrain—may be more stable in the face of warming.

Space-based ice monitoring may have scaled back the looming disaster among the world's glaciers, but it isn't making it go away. The closely watched glaciers visibly shrinking from year to year will not slow their retreat as the world warms further. Water supply problems—farmers losing meltwater in streams and rivers in the hot, dry summer months—will only get worse. And glaciers will be helping drive up sea level through the end of the century and a bit beyond. But with all glacierized regions losing ice in the present climate and more warming expected, Gardner says, all but the most resilient glaciers are likely to disappear within the millennium. Some glaciers in the Arctic and Antarctic might last that long, but particularly vulnerable regions like the Alps will likely see most of their glaciers disappear by the end of the century.

—RICHARD A. KERR

CREDIT: FRANK PAUL

HUMAN EVOLUTION

More Genomes From Denisova Cave Show Mixing of Early Human Groups

COLD SPRING HARBOR, NEW YORK In 2010, a girl's pinkie bone from Denisova Cave in Siberia added a new branch to the human family tree. The bone was so well preserved that researchers could fully sequence its genome and glimpse the DNA of archaic people now called Denisovans (*Science*, 28 January 2011, p. 392; 26 August 2011, p. 1084). Now, researchers have analyzed three more samples from that same cave using a powerful new method that reveals ancient genomes in brilliant detail. One sample, a Neanderthal toe bone, has yielded a nearly complete, high-coverage genome of our closest cousins, paleogeneticist Svante Pääbo from the Max Planck Institute for Evolutionary Anthropology in Leipzig, Germany, reported at a meeting here last week.*

The analyses paint a complex picture of mingling among ancient human groups, Pääbo reported. The data suggest inbreeding in Neandertals, a large Denisovan population, and mixing between Denisovans and an even earlier mystery species. "It's wonderful; amazing," says Eric Lander, director of the Broad Institute in Cambridge, Massachusetts. "It opens up a vista on the past world."

Neandertals, the closest known relatives to modern humans, ranged across Europe to western Asia from perhaps 300,000 years ago until about 30,000 years ago. Their overlap in time and space with our ancestors had fueled debate about whether the two species had interbred. Then, in 2010, Pääbo's group published a low-coverage sequence (1.3 copies on average) of DNA from three Neanderthal bones from Croatia, which showed interbreeding: About 2% of the DNA in living people from outside Africa originally comes from Neandertals (*Science*, 7 May 2010, pp. 680 and 710).

That first Neanderthal sequence was a huge accomplishment, as Neanderthal DNA made up just a few percent of the DNA in the fossils, the rest being bacterial and other contaminants. Since then, the Leipzig group has found ways to zero in on human genetic material and to get more from degraded ancient DNA by using a sequencing method that

starts with single, rather than double, strands of DNA. The approach provided a startlingly detailed view of the Denisovan pinkie bone (*Science*, 31 August 2012, p. 1028).

But this powerful technique had yet to be applied to Neandertals. So Pääbo was thrilled when the DNA in the sample taken from the toe bone proved to be 60% Neanderthal. The researchers were able to sequence each base 50 times over, on average—enough coverage to ensure the sequence is correct. This approach also provided low coverage of the genome from another fossil, a Neanderthal baby's rib, more than 50,000 years old, from a cave in Russia's Caucasus region between the Caspian and Black seas.

In a 10 p.m. talk to a full house, Pääbo



A cave for all people. Denisova Cave in Siberia yielded a Neanderthal toe bone (inset) as well as fossils of a new group of humans called the Denisovans.

offered some surprising results from the toe bone. For long stretches, the DNA from each parental chromosome is closely matched, strongly suggesting that this Neanderthal was the offspring of two first cousins, he said. Comparing the data with those from the fossils from Croatia and the Caucasus showed that these populations were fairly separated from one another. The group also compared the chunks of Neanderthal DNA found in living people with each of these three Neanderthal samples. The closest match was with the Caucasus population, suggesting that interbreeding with our ancestors most likely occurred closer to that region.

From the detailed genomes of both Neandertals and Denisovans, Pääbo and Montgomery Slatkin of the University of California, Berkeley, estimated that 17% of the Deniso-

van DNA was from the local Neandertals. And the comparison revealed another surprise: Four percent of the Denisovan genome comes from yet another, more ancient, human—"something unknown," Pääbo reported. "Getting better coverage and more genomes, you can start to see the networks of interactions in a world long ago," says David Kingsley, an evolutionary biologist at Stanford University in Palo Alto, California.

With all the interbreeding, "it's more a network than a tree," points out Carles Lalueza-Fox, a paleogeneticist from the Institute of Evolutionary Biology in Barcelona, Spain. Pääbo hesitates to call Denisovans a distinct species, and the picture is getting more complicated with each new genome.

Pääbo's team also deciphered additional Denisovan DNA, both nuclear and mitochondrial, from two teeth found in different layers in Denisova Cave. The nuclear DNA confirmed that both teeth are Denisovan. But, surprisingly, one tooth showed more than 80 mitochondrial DNA differences from both the other tooth and the pinkie bone. These Denisovans, who lived in the same cave at different times, were as genetically diverse as two living humans from different continents and more diverse than Neandertals from throughout their range, says Susanna Sawyer from Pääbo's lab. Such diversity implies that the Denisovans were a relatively large population "that at some point may have outnumbered Neandertals," Pääbo said.

In addition, the genomes are clarifying genetic changes that underlie our own evolution. "We will be able to know all the changes that are ancestral," Lalueza-Fox says.

Pääbo and his colleagues have lined up the chimp, modern human, Neanderthal, and Denisovan genomes to see what's unique to our species. The catalog includes 31,000 single-base changes, which led to 96 protein changes, and more than 3000 changes in regulatory regions, as well as 125 small insertions and deletions, Pääbo reported.

Peter Sudmant from the University of Washington, Seattle has already begun scanning the Neanderthal genome for uniquely human duplications and deletions. "It's something we thought we would never be able to do," he says. Adds Kingsley: "It will take a long time to figure out the real causative events and figure out what traits they control, but it's a finite list."

ELIZABETH PENNISI

*The Biology of Genomes, 7 to 11 May.

eppendorf
& Science
PRIZE FOR
NEURO
BIOLOGY



2012 Winner
Dr. Marlene R. Cohen
Assistant Professor
University of Pittsburgh

Call for Entries

Application Deadline
June 15, 2011

Eppendorf & Science Prize for Neurobiology

The annual Eppendorf & Science Prize for Neurobiology, an international award, honors young scientists for their outstanding contributions to neurobiological research. The winner and finalists are selected by a committee of independent scientists, chaired by Science's Senior Editor, Dr. Peter Stern. To be eligible, you must be 35 years of age or younger.

You could be next to win this prize and to receive

- > Prize money of US\$25,000
- > Publication of your work in Science
- > Full support to attend the Prize Ceremony held in conjunction with the Annual Meeting of the Society for Neuroscience in the USA
- > An invitation to visit Eppendorf in Hamburg, Germany

It's easy to apply!

Learn more at: www.eppendorf.com/prize

eppendorf



© 2011 Eppendorf AG, Hamburg, Germany. All rights reserved. The American Society for Neuroscience (SfN) is a 501(c)(3) non-profit organization. The SfN is not affiliated with Eppendorf AG. The SfN is not responsible for the content of this advertisement. The SfN is not responsible for the content of this advertisement. The SfN is not responsible for the content of this advertisement.

U.S. SCIENCE POLICY

Lawmakers Await NSF's Response to Query About Grants

Fifty-seven words have created a firestorm within the U.S. scientific community and provoked a clash with an influential member of Congress. This week that confrontation could come to a head.

On 25 April, Representative Lamar Smith (R-TX), the chairman of the House of Representatives science committee, asked the National Science Foundation (NSF) to justify the agency's funding of five recent research grants in the social sciences. On 9 May, acting NSF Director Cora Marrett informed Smith that the agency couldn't meet the 2-week deadline Smith had set; the next day, she told members of the National Science Board, NSF's oversight body, that the agency would respond by 17 May. The tone and substance of its reply could determine whether tensions escalate or begin to subside.

The nub of Smith's request is contained in these two sentences from his letter: "To better understand how NSF makes decisions to approve and fund grants, it would be helpful to obtain detailed information on specific research projects awarded NSF grants. ... Members of the committee would benefit from access to the scientific/technical reviews and the Program Officers Review Analysis for the following [five] research projects that have been awarded NSF funding."

Smith says he is simply trying to ensure that NSF's vaunted peer-review system is working properly and that the agency isn't wasting tax dollars. But many researchers regard his letter, along with a bill he has drafted that would alter NSF's grant-making process, as an attempt to inject politics into a process with an outstanding track record (*Science*, 10 May, p. 670). They cite the fact that NSF has supported the work of more than 200 Nobelists over its 63-year history as evidence that the system is working fine.

Last week, the community ratcheted up its criticism. Three former NSF directors and three past leaders of the agency's oversight board wrote to Smith, asking him to rescind his letter and drop the draft legislation. In a second letter, 18 former top NSF officials

described the request as setting "a very dangerous precedent [that] puts Congress in the position of second-guessing the scientific judgment of experts." University presidents and leaders of several scientific organizations also gave an earful to a science committee aide during a testy meeting in Washington.

Smith's response has been to play down his differences with the community. In a statement issued soon after the former directors released their letter, Smith said, "We

Scientists also worry that researchers might decline to be reviewers if they know their comments could become public. The risk of exposure could also make reviewers think twice about what they write: Some scientists might soften a critical review for fear of being seen as too harsh, while others might water down a positive review to avoid leaving the impression they are trying to curry favor with an applicant who may be a major figure in the field.

NSF's legal standing to share or withhold what Smith has requested is murky. Reviewers' comments are part of what the federal government calls a system of records, and NSF has rules governing access to those records. In 1996, for example, a federal court rejected a request by an unsuccessful grant applicant for the names of the reviewers and upheld NSF's interpretation of federal privacy laws. At the same time, congressional committees generally have broad authority to examine the records of agencies that they oversee. NSF officials declined to discuss whether there is precedent for Smith's request and, if so, how it might affect what information the agency will share.

NSF asks reviewers to use two criteria in weighing a grant application: intellectual merit and broader impacts. The second criterion has long been a sore point among some researchers, who feel that it is too vague or not essential. Last year, the science board decided to retain the second criterion after conducting a lengthy dialogue with the community about its meaning (*Science*, 14 October 2011, p. 169). Smith's draft legislation would in essence replace it with a three-part formula assessing the project's relevance to national security, health, or economic development.

Dan Arvizu, National Science Board chair, declined to comment on any advice the board may have provided Marrett, and an NSF spokesperson said Marrett had nothing to add to her comments to the board. Scientists are waiting anxiously to see how NSF defends a process that they hold dear.

—JEFFREY MERVIS



Reply requested. Acting NSF Director Cora Marrett with Representative Chaka Fattah (D-PA) at an exhibition last week of NSF-funded research.

agree that the peer review process should remain intact, and that basic research should be supported." Smith also signaled a willingness to listen. The draft bill "was circulated as a starting point to determine how the NSF grant process can be improved," he wrote. "And I welcome the input of individuals involved in that process."

What exactly is at stake? In deciding how to respond to Smith's request, NSF officials must weigh several factors.

The first is NSF's promise to preserve the confidentiality of reviewers. Smith doesn't want their names, according to a committee staffer. Even so, some scientists are worried that a reviewer might be identifiable by his or her distinctive writing style or point of view. That's especially true, they say, in a subfield with a handful of recognized experts.

Troubled Waters for Ancient Shipwrecks

As archaeologists find new ways to pull precious data from wrecks, they are squaring off against those salvaging ships for profit



IN 1993, ARCHAEOLOGISTS SURVEYING THE seafloor near Lisbon spied several pieces of old timber jutting out from a mash of mud and peppercorns 10 meters below the water's surface. The site was modest in appearance and partially looted, but it contained a key find: fragments of an ancient wooden ship known as a Portuguese Indiaman, built during the Renaissance to sail what was then the longest and most dangerous commercial route in the world—from Portugal to India, the land of pepper and spice. Designed for an age of discovery, the Indiaman “was the space shuttle of its time,” says nautical archaeologist Filipe Vieira de Castro of Texas A & M University in College Station.

Historical accounts described the ship as a miniature floating city that carried 450 people—but many researchers thought the accounts were exaggerated. Castro and colleagues began excavating in 1996 and in 17 years of detailed study have produced research on everything from the ship's design to its sailing abilities; their latest findings appear in the February issue of the *Journal of Archaeological Science*. The team has extracted “more data

[from the wreck] than you would think possible,” says nautical archaeologist Wendy Van Duivenvoorde of Flinders University in Adelaide, Australia. The overall conclusion: the Indiaman lived up to its press and was indeed a sophisticated—if congested—craft.

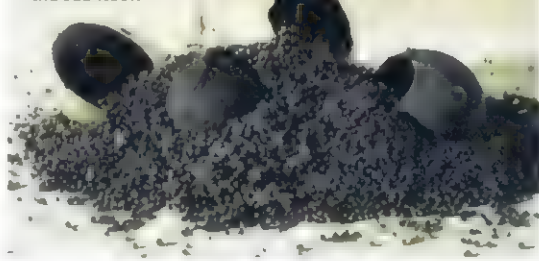
This detailed portrait of a Renaissance ship is just part of the scientific bounty now accruing from advanced new techniques for excavating and analyzing underwater wrecks. But as scientists dig into this wealth of data, they are also waging bitter, high-profile battles to protect these sites. Finding shipwrecks has never been easier, and a spectrum of archaeologists, explorers, salvage operators, and treasure hunters all are setting out to do so. Local

divers scavenge wrecks for coins and ingots, while companies equipped with remote-sensing technology recover artifacts for sale to collectors and museums. Specialized antiquity dealers do a brisk trade in shipwreck artifacts such as coins and Chinese porcelain.

For years, the law of the sea was essentially finders keepers, and salvors who located shipwrecks and brought up their cargo were entitled to a reward at the least. But in recent years, archaeologists have argued that this maritime right of salvage should not be applied to ancient, archaeologically valuable ships. “We stand to lose access to enormous segments of the human story, information about our ancestors and ourselves,” says archaeologist Douglas Comer of Cultural Site Research and Management, an independent consulting firm in Baltimore, Maryland. Underwater archaeologist James Delgado, director of maritime heritage at the National Oceanic and Atmospheric Administration in Washington, D.C., asks: “Where does it all stop, if we accept that evidence of our past can be converted into something that people can buy and take home?”

Firms that sell artifacts say there is nothing inherently wrong with the practice, particularly when it applies to only coins and

Renaissance fortune. When the Pepper Wreck sank, it spilled tonnes of peppercorns and the odd coconut across the sea floor.



CREDITS (TOP TO BOTTOM): T.A. SANTOS ET AL. JOURNAL OF ARCHAEOLOGICAL SCIENCE 39 (SEPTEMBER 2012); MIGUEL ALLUVA IGESPAR PORTUGAL; AUDREY WELLS/TEXAS A&M UNIVERSITY

Timber treasure. Careful analysis of every remaining hull timber allowed archaeologists to reconstruct the Pepper Wreck.

duplicate cargo items. Such sales can benefit museums struggling to maintain large collections, points out Greg Stemm, chief executive officer of Odyssey Marine Exploration Inc., a deep-ocean exploration company based in Tampa, Florida, in an e-mail interview.

Most archaeologists, however, sharply disagree with the idea of selling artifacts. The history of archaeology has repeatedly shown that “where exploration and fieldwork were steered by the market value of objects, the approach and documentation are so compromised that even the most basic observations become unreliable,” says maritime archaeologist Thijs Maarleveld of the University of Southern Denmark in Esbjerg.

As more and more ancient wrecks are revealed, shipwreck preservation stands “on a knife edge internationally,” says archaeologist Colin Renfrew of the University of Cambridge in the United Kingdom. He also holds a seat in the House of Lords, and from there he recently blasted plans to allow Odyssey and a charitable trust known as the Maritime Heritage Foundation to excavate a historic British warship, HMS *Victory*, which foundered in the English Channel in the mid-18th century. It is very clear, he told *Science*, that governments should not allow “salvage of this kind.”

The battle lines are hardening. “We speak two different languages,” says Castro. “We are after knowledge and they are after money.”

Aboard a Renaissance craft

Sunken ships are packed with archaeological information, says maritime archaeologist Paul Johnston of the National Museum of American History in Washington, D.C. Often the vessels went down with all the tools, supplies, and cargo needed to succeed on their voyage, and “the organic artifacts tend to be much better preserved than they are on land,” he says, due to anaerobic conditions in many marine sites. Unlike terrestrial sites that were often occupied

repeatedly over centuries, shipwrecks date to one moment in time, offering tight chronological control.

However, wresting knowledge from an underwater site is often a slow, laborious task. In the case of the Pepper Wreck found near Lisbon, Castro’s team used \$500,000 from the Portuguese government to dig the site and raise the hull timbers over four field seasons under the supervision of Portugal’s national agency for nautical archaeology. (The equipment the team bought became part of a new national center for underwater archaeology in Lisbon.) Team members spent 2 years conserving artifacts to avoid rapid deterioration on land.

To help identify the wreck, the researchers searched historical records. In 1606, they learned, a Portuguese Indiaman christened *Our Lady of the Martyrs* sank in the area of the wreck site with a large cargo of peppercorns. Many artifacts from the Pepper Wreck fit that ship’s description, including Chinese

porcelain dated to 1600 and a navigational instrument called an astrolabe inscribed with the date 1605. Because the ship “was built in the royal shipyard in Lisbon, and wasn’t just an anonymous ship, the level of analysis that could be carried out was immensely greater,” says nautical archaeologist Brad Loewen of the University of Montreal in Canada, who was not part of the team.

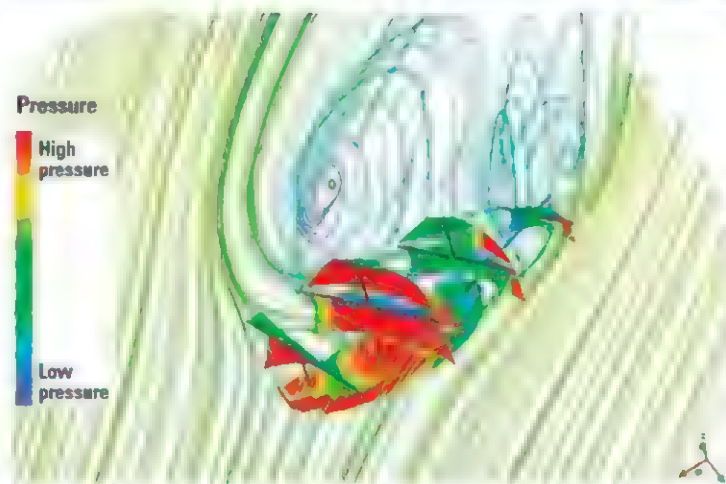
To reconstruct the ship’s design, Castro painstakingly recorded the size and shape of every piece of wood, as well as the location of shipwright marks, caulking, and spikes used to join pieces together. Then he studied shipwright marks and design formulae in ancient shipbuilding treatises. By combining the formulae with their measurements, Castro and colleagues extrapolated the design, revealing a sturdy, massive ship with a 28-meter-long keel and a 31-meter-tall main mast (see image).

Could such a ship really carry 450 people and some 250 metric tonnes of cargo safely around Africa’s Cape of Good Hope and through Indian Ocean monsoons? Castro and a small team combed historical records to compile a list of items needed to outfit an Indiaman for this voyage and calculated their volume and weight, from 175 tonnes of ballast to 292 tonnes of water, wine, and food. Using 3D software, the team positioned the items inside the digitally reconstructed ship to determine how much space was left for passengers and crew. Their study, published in *Historical Archaeology* in 2010, revealed that the ship indeed could have departed from Lisbon with 450 people, although conditions aboard would have been very crowded early in the voyage (when the ship was fully loaded with food and water), with just 1.3 square meters of living space per person. Such cramped quarters were “common at the time,” Castro says.

What about safety? One well-known 18th century book, *The Tragic History of the Sea*, painted a bleak picture of the Indiaman’s record. So the team used modern mathematical tools to see how well the reconstructed ship rode out storms. In a *Journal of Archaeological Science* paper in 2012, they

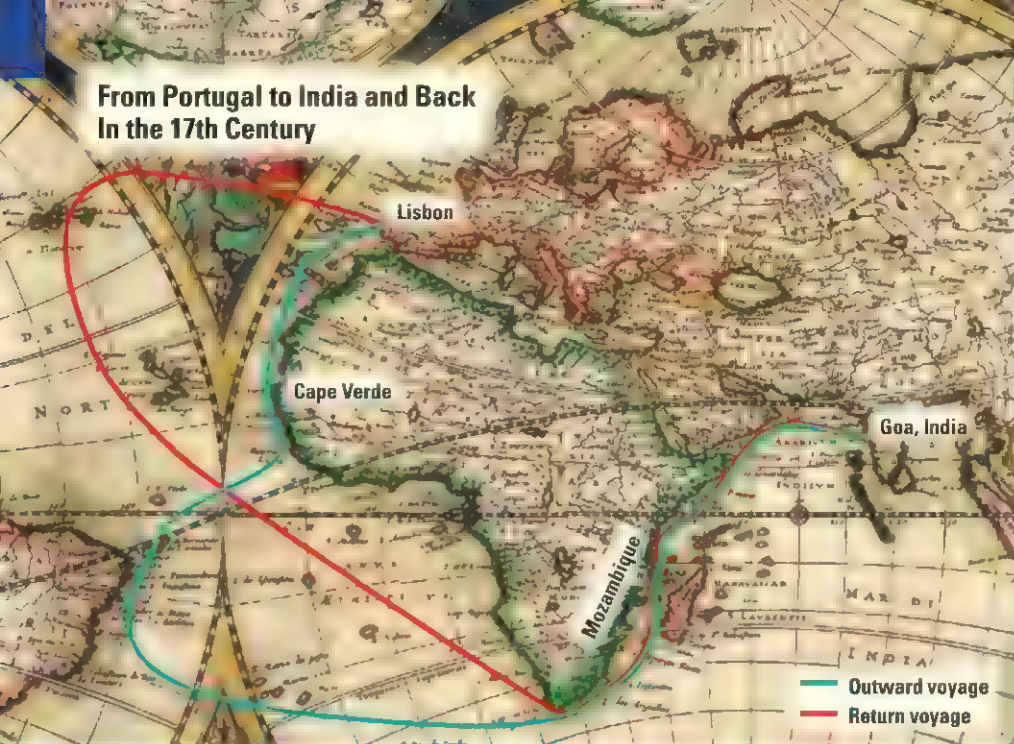


Floating city. A digital reconstruction of the Pepper Wreck showed it could carry 450 people.



Seaworthy. Computer models of a Portuguese Indiaman and the air pressure around it show that the ship met modern stability criteria; sails colored red took most of the wind.

From Portugal to India and Back In the 17th Century



Passage to India. Archaeologist Filipe Castro (above) recovered artifacts and wood from the Pepper Wreck (below), which would have made the long journey around Africa to India and then back to Portugal in routes shown on this antique map.

found that the reconstructed Indiaman met modern stability criteria set by the U.S. Coast Guard for large wooden sailing ships. Even when the wind gusts strongly, the reconstructed ship goes “back to the vertical condition so quickly that seasoned sailors could get seasick,” Castro says.

Van Duivenvoorde, who was not involved in the research, calls the work “valid and very important,” adding that “we now know that these ships were well designed and well built, given the constraints of the period.”

Laws of the sea

Castro and his colleagues’ three books and 17 primary publications serve as an outstanding example of the archaeological knowledge that a single shipwreck can generate. Other wrecks are also yielding rare and detailed findings about the past. Seeds from Israel’s Hahotrim wreck, for example, have revealed the ancient spread of an exotic plant along the Mediterranean coast, probably carried by ships, while marble aboard the Kizilburun ship has yielded new information on the workings of marble quarries in Roman-era Turkey (see sidebar, p. 805). Sailors’ personal effects found in the 17th century Swedish warship, *Vasa*, are shedding light on the privations of naval life, including the lack of medical equipment. Such studies fill in many blanks in the archaeological record, says archaeologist Deborah Carlson of Texas A&M University, offering “tremendous insight into what people were doing and eating, where they were going, what music they were listening to, and what games they were playing.”

The superb preservation that attracts archaeologists to shipwreck sites, however,

also draws local divers hunting for treasure. As a result, wrecks around the world are being outright looted or salvaged quickly, with little if any attention paid to documenting the sites. “It’s a very, very serious problem,” says Wu Chunming, a maritime archaeologist at Xiamen University in China.

It’s not a new problem for archaeologists—terrestrial sites have long been plagued by looters and still are. But on land, researchers have several legal weapons: A U.N. Educational, Scientific and Cultural Organization (UNESCO) convention bars international trade in looted artifacts, and some archaeologically-rich countries have declared all undiscovered artifacts state property. The situation in the sea is different. Under the ancient maritime law of salvage and the common law of finds, salvors who find sunken ships and their cargo are often entitled to a reward, either a flat fee or a percentage of the value of the discovery. Sometimes they can even claim legal ownership of a wreck and its contents. As a result, salvors are often entitled to sell part if not all of what they discover on a wreck, a nearly universal right that long extended to ships carrying key archaeological data.

Recently, advances in remote-sensing technology have allowed salvors to locate ancient ships where they never looked before—in deep water—putting more of the world’s archaeological record in danger. So in the mid-1990s, nautical archaeologists began pressing for a new international law to protect



ancient sunken ships. The 2001 UNESCO Convention on the Protection of the Underwater Cultural Heritage is the result. It recommends the preservation of shipwrecks in situ as the first option, and prohibits buying, selling, and dispersing their artifacts, because this practice encourages excavation for the marketplace rather than for knowledge and boosts trade in objects of scientific value.

The convention entered into force in 2009, after 20 countries ratified it, and the number of states signing on is steadily climbing. It’s now 42. Public opinion appears to back shipwreck preservation: 60% of American adults agreed that artifacts from the

RMS *Titanic* should not be auctioned off, according to a poll released last week by the Marist College and Sea Research Foundation. But nations as diverse as Mozambique, the United States, and Cape Verde have yet to sign on to the convention, leaving wrecks in many waters open to salvage.

Tracking salvage in the world's oceans is difficult, so nautical archaeologists monitor eBay and online auction catalogs, and watch high-profile lawsuits to find out what's happening. One such case heard by the U.S. District Court in Florida in 1997 reveals how some treasure-hunting operations have worked.

In this case, the U.S. government alleged that a Florida company, Salvors Inc., illegally destroyed seagrass and removed artifacts from a shipwreck site in the Florida Keys National Marine Sanctuary, a protected area. In its findings of fact, the court determined that Salvors used three ships equipped with propeller-wash deflectors, large bent pipes that channel the powerful thrust of a ship's engines towards the ocean floor, blasting sediments away in order to swiftly find coins and ingots. Archaeologists don't use this technique because it also blows away important but lightweight organic materials such as leather and wood. In 3 months, Salvors blasted more than 600 holes of 6 to 9 meters in diameter in the seafloor, seriously damaging at least 1.63 acres of sensitive seagrass habitat, according to the findings of fact. The court ordered the company to pay restoration costs and compensation totaling \$589,311 and to return the recovered artifacts to the government.

This kind of operation would be legal in many waters today, a situation that worries most nautical archaeologists. Equipped with sophisticated gear for locating wrecks, these operators "drain a non-renewable resource," Johnston says.

Rights to wrecks

Many companies that today excavate and sell artifacts from shipwrecks vigorously disavow such destructive practices. The Lisbon-based company, Arqueonautas Worldwide Arqueologia Subaquática, S.A., for example, has a scientific board, employs two archaeologists, and self-publishes archaeological reports on its website, which proudly proclaims: "Saving World Maritime Heritage since 1995." Arqueonautas has negotiated exclusive licences with the governments of Cape Verde and Mozambique to conduct maritime archaeological operations, according to documents posted on its website.

Arqueonautas has located 150 historic shipwrecks worldwide and excavated 20 in Africa over the past 18 years, notes com-

pany spokesperson Miguel Gomes da Costa. He argues that sunken ships are seriously threatened globally by both local looters and fishing trawlers' nets, and that this demands rapid recovery operations.

But the firm does sell artifacts. In developing nations such as Mozambique, Gomes says, you can't expect "these countries to finance with the taxpayers' money marine archaeol-

ogy." He says that Arqueonautas provides an important service in Mozambique, excavating endangered ships and recovering important cultural objects which are then displayed in the country's museums—work it funds in part by selling "repetitive cargo artifacts," primarily coins and old Chinese porcelain. According to its website, the company has also sold a rare, 17th century mariner's astrolabe from

From Quarry to Temple

Sometime between 100 B.C.E. and 25 B.C.E., a wooden ship carrying almost 60 tonnes of stone foundered in Aegean waters just off the coast of Turkey. It went down bearing its entire cargo, including eight massive drum-shaped blocks of white marble. Those blocks fit together to form part of a tapering column that likely stood more than 11 meters tall, plus a square uppermost piece: a Doric column.

Two thousand years after the ship went down, archaeologists excavating what is now called the Kizilburun shipwreck have figured out exactly where the marble blocks came from and where they were heading, illuminating the marble trade in the Roman province of Asia Minor. The work shows how underwater archaeology can add a new dimension and precise information to a period researchers thought they knew well (see main story, p. 802). "In the 1st century B.C.E., the Mediterranean was the highway by which everyone in the region was linked," says nautical archaeologist Deborah Carlson at Texas A&M University in College Station, who led the analysis. "This means shipwrecks connect sites on land in ways that archaeologists didn't see before."

Carlson and classical archaeologist William Aylward of the University of Wisconsin, Madison, first set out to learn where the marble came from. As reported in a 2010 study in the *American Journal of Archaeology*, the team sent out samples of the marble for stable isotope analysis and other tests. The marble's values of the isotopes $\delta^{13}\text{C}$ and $\delta^{18}\text{O}$ and its spectroscopic details led them to Marmara Island, known as Proconnesos in Roman times, in the Sea of Marmara, the inland sea connecting the Aegean and Black seas. This island was the site of an important marble quarry when Asia Minor became a Roman province around 130 B.C.E.

But where was the marble heading? The blocks' size and style suggest that the column was intended for a major public building, most likely a temple. Carlson and Aylward drew up a list of all the Doric-style monumental buildings under construction in the 1st century B.C.E. on coastlines south of the wreck site, the probable direction of travel away from the quarry. Then they searched for sites with a finished lower-column diameter of about 1.73 meters. They concluded that the marble was headed for the Temple of Apollo at Claros, where people in Roman times flocked to seek advice from oracles, just 50 kilometers from the wreck. That finding is "utterly convincing," says architectural historian Lothar Haselberger of the University of Pennsylvania.

The data show that the quarry workers on Proconnesos were in close contact with the temple builders some 500 kilometers or more away, shaping the marble to the builders' exact specifications. The findings also show that the builders received columns in pieces in small shipments, hinting at a lengthy construction process. This information, says Carlson, "is the missing link that tells us a lot about this process."

—H.P.



Missing link. A shipwreck's marble cargo reveals the construction of a Roman-era temple.

a wreck off the coast of Cape Verde, which was purchased by an American museum for some \$200,000 at a Sotheby's auction in 2000. "Of course this [selling of artifacts] is not accepted by a lot of the fundamentalists, principally, that like very much the UNESCO convention," Gomes says.

The Sotheby's lots also included what Gomes described as Arqueonautas's "share" of recovered artifacts from the American warship USS *Yorktown*, which sank near a Cape Verde coast in 1850; the artifacts included items such as a powder flask and an inscribed teaspoon. But the U.S. Navy claims jurisdiction to its wrecks all over the world, and does not allow salvage, in order to prevent trade in artifacts and to protect sailors' graves. A member of the scientific board of Arqueonautas noted in a letter to the U.S. Department



Going, going, gone. To learn what salvors have found on wreck sites, archaeologists monitor the catalogs of shipwreck artifacts sold at auctions around the world.



of Justice that the company's staff members couldn't identify the ship until after excavation. Sotheby's cooperated with the U.S. Navy to return some *Yorktown* artifacts, and the Navy is still seeking any items retrieved from the ship (<http://www.history.navy.mil/branches/org12-9b.htm>).

Some archaeologists think that the Arqueonautas license in Mozambique, which covers 700 kilometers of coastline, has hindered the development of underwater archaeology by local researchers. Local studies were just gaining momentum before the Arqueonautas deal was signed, says Ricardo Teixeira Duarte of Eduardo Mondlane University in Inhassoro, Mozambique. "Why does a group of scientists need exclusivity?" he asks.

In a paper published in the peer-reviewed *Journal of Maritime Archaeology* in 2012, Duarte uses data from the Arqueonautas website to suggest that the firm's choice of excavation sites looks like cherry-picking of wrecks that are likely to contain valuable goods such as gold and silver. The selection suggests that "the real objective of the interventions is profit," Duarte wrote. The paper adds that the company's online scientific reports for its operations in one region, Mozambique Island, are "incomplete," chiefly presenting "brief documentation in view of determining the financial value [of] the finds." Exclusive licenses to salvage firms, Duarte says, are "a wrong approach."

Other researchers critical of such recovery

Narragansett Bay. Brennan and colleagues found that this policy works, in a study published in *Continental Shelf Research* last year. They analyzed remote-sensing images and calculated the numbers of broken and unbroken amphorae on 14 shipwrecks off Turkey's coast, finding breakage rates from 0.6% to 62.5%. Some damage was clearly due to trawler nets. But the closer ships lay to shore, the fewer the shattered amphorae. Brennan argues that governments are better off creating no-trawl zones around shipwreck concentrations than opening these areas to companies that sell artifacts. "Trawling may threaten an important site to the point that excavation is warranted," he says, but "it does not in any way justify or make commercial salvage acceptable."

Victory, or defeat?

In the developed world, governments are also grappling with the issues of what to do with wrecks and how best to pay for the cost of underwater excavation. In the United Kingdom, an intense battle is brewing over a plan that many archaeologists say would commercially exploit *Victory*, once "the most powerful ship afloat," says Robert Yorke, chair of the Joint Nautical Archaeology Policy Committee, an umbrella organization representing 26 organizations as well as individual members in the United Kingdom. *Victory* sank in a violent storm in the English Channel in October 1744, claiming the lives of more than 1100 British sailors. Six weeks later, a Dutch newspaper reported that "people will have it that on board the *Victory* was a sum of £400,000 that it had brought from Lisbon for our merchants."

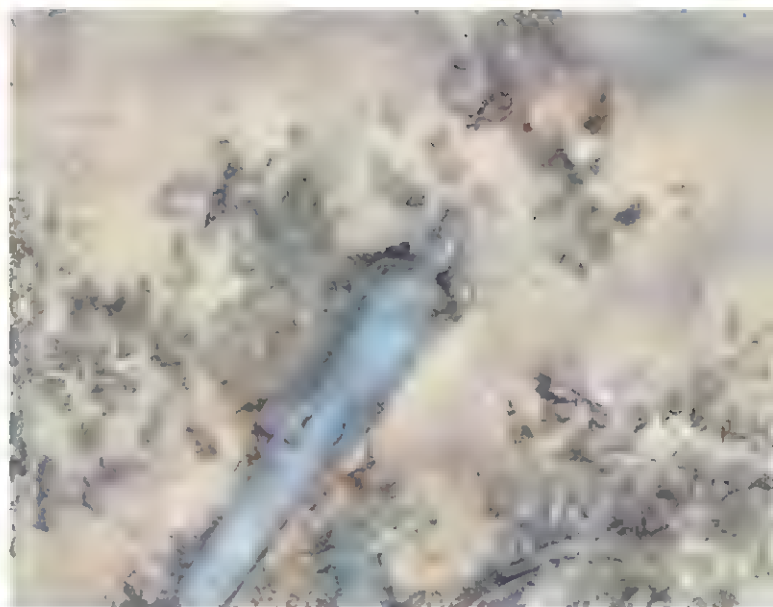
In 2008, Odyssey located the ship's wreckage beyond the United Kingdom's territorial waters, at a depth of about 75 meters. Since then, the company has described itself as "salvor-in-possession," and published online archaeological papers arguing that fishing and looters are damaging the wreck. These are "signs that the idea of preserving the site in situ is clearly not practical," noted CEO Stemmi in a 2012 company press release.



Law of the sea.

Salvors have used destructive equipment such as propeller wash deflectors (above) to quickly find and recover valuables like these old coins from Spain and the New World.





Bitter battle. Despite its cannons, viewed today on the seafloor (right), *Victory* sank in 1744, as depicted in this painting, and researchers now debate the fate of what was once considered the most powerful ship afloat.

Under a provision of international maritime law, the U.K. government claims jurisdiction over its naval wrecks, and it has adopted the UNESCO convention's annex, which rules out buying and selling artifacts, as "archaeological best practice."

Nevertheless, in January 2012, the government gifted *Victory* to The Maritime Heritage Foundation, a charitable trust established in October 2010 by Robert Balchin—a prominent Conservative peer who holds the title Lord Lingfield—and two other trustees. One week after the deed of gift was announced, Odyssey posted an online press release stating that it had signed an agreement with the foundation to excavate the wreck. The government later explained the gift by noting that it did not want to spend its money on managing the wreck.

Many archaeologists are up in arms over this proposed excavation, given some of Odyssey's practices: The company currently sells shipwreck artifacts on its website, and its business model includes "commercial monetization of recovered cargo" from wrecks, according to the 2012 annual report that Odyssey filed with the U.S. Securities Exchange Commission. In 2004, the company obtained in court legal ownership of a treasure-bearing 19th century steamer and its contents, the *SS Republic*, that the firm discovered in international waters off the east coast of the United States. Odyssey retrieved more than 51,000 gold and silver coins from the wreck, plus 14,000 artifacts, some of which it currently sells on its website.

In an online press release concerning the

Victory deal, Odyssey noted that The Maritime Heritage Foundation has agreed to reimburse the firm for its project costs, as well as paying a percentage ranging from 50% to 80% of the "fair value" of the coins and other artifacts recovered. The announcement also noted that the preferred plan was to pay the company in cash, but that the foundation "may choose to compensate Odyssey with artifacts in lieu of cash." These announced terms infuriate Yorke. "This is a salvage contract," he says. "It is not an archaeological contract."

Stemm says critics have based their attacks on "false and misleading information." Odyssey, he says, employs four archaeologists, has conducted substantial excavations on "about half a dozen" wrecks, self-publishes its own scientific reports, and creates museum exhibits that have been seen by more than 2 million people. "I believe that the quality of our fieldwork equals and in terms of deep-sea capabilities surpasses that of most academic archaeologists because of the quality of equipment and technology we can afford," he says. But this comes at a cost. With today's technology and remotely operated vehicles, the work costs \$20,000 to well over \$30,000 per day, according to Stemm.

Critics wonder where the money for the *Victory*'s excavation will come from. "The UNESCO Convention on the Protection of Underwater Cultural Heritage makes clear that the excavation of historic wrecks should not be financed by selling off the finds recovered," stated Renfrew in the House of Lords (he holds the title Lord Renfrew of

Kaimsthorn). "But that may be just what is now being planned for HMS *Victory*."

Stemm denies this, however. The foundation will own the ship's artifacts, and Stemm notes that the charity doesn't have to sell them in order to compensate Odyssey—the payment could come from many sources. But the foundation's plans for coming up with this compensation are unclear. Asked about this last November in the House of Lords, Balchin said that "such things will be revealed" when the foundation reported on its finances at the end of its financial year. However, the charity's year-end statement filed a few weeks later revealed a fund balance of just £13,275 (about \$21,000)—sufficient at best to cover just one day of Odyssey's fieldwork.

Renfrew and other opponents are now waiting to see whether the Ministry of Defence will consent to Odyssey's proposed excavation. Renfrew believes that the decision will influence governments around the world. "There are major ethical issues involved here," he said during the House of Lords debate, "and it is difficult to avoid the impression that the government are giving a poor and ill-informed lead internationally in their dealings with Britain's underwater heritage."

Nautical archaeologists and excavators around the world are watching the bitter struggle over *Victory* closely. It's a symbolic battle in a widening front, as more and more wrecks are located in their deep-water resting places.

—HEATHER PRINGLE

Heather Pringle is a science writer based in Victoria, Canada.

FOOD SCIENCE

Following the Flavor

Scientists are beginning to unravel why we love some types of food and hate others. It's a vastly more complex topic than they once thought

COPENHAGEN—When Per Møller, a Danish food scientist, was in the United States a few years back, he tried a well-known U.S. chocolate bar. “It tasted awful to me, like vomit,” he says. His American colleagues disagreed. “They told me this is what chocolate is supposed to taste like,” he says. To Møller, who works at the University of Copenhagen in a yellow building known as “the cheese,” the episode illustrates how little we understand why some things taste great and others awful—or why people can disagree so strongly on the issue.

Møller is one of a growing group of researchers trying to answer these questions. Using a variety of approaches—including genetics, physiology and psychology—they are beginning to piece together a picture of how genes, receptors, nerve cells, and experiences interact to create a flavor experience in the brain.

They find questions everywhere. It's well known that humans are born liking the tastes of sweet and fat, and disliking bitterness—but it's a mystery why steak and Béarnaise sauce go well together, or gin and tonic, and why some people learn to like Campari, olives, and cilantro, and others don't. Even more important, says Katrin Ohla, who

heads a research group at the German Institute of Human Nutrition in Potsdam, little is known about the path a stimulus takes from the moment food touches the tongue to the diner's decision that it's disgusting, delicious, or somewhere in between.

Compared to the other senses, science has long neglected taste, Ohla says. The receptors for umami, which lets humans taste glutamate and other amino acids, were discovered only in the 2000s, for instance, and scientists are still looking for fat receptors. Only in February did they discover why too much salt in your soup tastes bad: In high concentrations, it activates sour and bitter receptors on the tongue, presumably to prevent intake of dangerous amounts of salt.

How sweet it is

In recent years, scientists have found a number of genetic variants that seem to affect how people perceive certain foods. A mutation that influences whether cilantro tastes soapy, for instance, or one that determines whether someone can taste a bitter chemical called phenylthiocarbamide.

But DNA tells only a very small part of the story, says geneticist Danielle Reed of the Monell Chemical Senses Center in Philadelphia. She compares taste to vision. There are individual differences in color perception, and an impressionist painting may be less appealing to the colorblind. “But overall, your vision does not affect what kind of art you like,” Reed says. “It is the same for food.” In fact, the researchers who discovered the genetic variant affecting cilantro taste calculated that it accounted for only half a percent of the variance in its perceived soapiness.

What makes flavor so difficult to study is that it consists of much more than molecules sensed by taste receptors. For one, when you swallow a piece of food, some air is forced up at the back of the mouth, so that receptors in your nasal cavity can detect its odor, a process called retronasal olfaction. “We used to think that was the same as smelling, but in fact, the brain records which way the odor came in and sends it to a different place,” says Linda Bartoshuk, a psychologist at the University of Florida's Center for Smell and

Taste in Gainesville. “Flavor is created in the brain through integrating taste and retronasal olfaction,” she says.

Just how important volatile compounds are became clear from an experiment in which Bartoshuk studied the flavor of tomatoes. She found that subjects perceived a tomato variety called matina as twice as sweet as one called yellow jelly bean, even though it contained less sugar. The effect appears to be due to the fact that matina has higher levels of six volatile compounds that enhance the perception of sweetness.

Even things as difficult to measure as expectations seem to influence flavor. In a study published last year, Ohla showed participants photos of high-calorie or low-calorie food; afterward, a short electric current was passed through their tongue to create a standardized, slightly metallic sensation. Participants who had seen pictures of high-calorie food described that taste as more pleasant than those who had not. Food color and temperature also have a strong effect, Ohla says: “It's as if we're not really trusting our sense of taste alone.”

Past exposure appears to play an important role as well. In one experiment, Møller gave pureed artichokes to 2- and 3-year-old kids. Over ten consecutive sessions, they then received either the normal puree, a sweetened version, or one fortified with sunflower oil. The idea was that the children would learn to like the puree through association with sweetness or the energy-density of oil, both known to affect food choices. But at the end of the experiment, those exposed to the unmodified puree the whole time liked



Change on the menu. Per Møller believes his research on taste will help chefs create better dishes.



A Floating Lab Explores the Fringes Of Science and Gastronomy

COPENHAGEN—Ben Reade wants to know if you can serve toxic mushrooms for dinner. From a paper he recently read, Reade learned that the toxins in *Amanita muscaria*, a mushroom commonly known as fly agaric, are soluble in water. Now he is waiting for the fall to collect some specimens; by slicing and parboiling them, he hopes to get rid of the toxins and create a new dish.

It's just one of many experiments at the Nordic Food Lab, which Reade, a chef with a degree in gastronomic sciences, leads. Housed on a small boat in the harbor here and connected to Noma, a nearby, world-famous restaurant, the lab employs cooks and scientists to develop new cooking techniques and mouth-watering new dishes. They're investigating how well bee larvae go with granola (very well) or what happens when garlic cloves sealed and stored for weeks at 60°C turn black. (Among other things, the enzyme alliinase, which produces garlic's pungent compounds, stops working).

Whether people like Reade are actually doing science is a point of debate. Occasionally, results are published—as in a recent paper about seaweeds and umami flavor—but the work is “not driven by wanting to discover something,” says University of Copenhagen food scientist Per Møller. “It is more that if a problem arises they consult with whatever scientific field is necessary.” Still, labs like this can help him and other scientists, for instance by creating the unusual dishes needed in experiments to test how expectations modify the perception of taste, Møller says: “If somebody comes up with a creation that really freaks out your nervous system, you get a stronger signal.” Chefs like Reade “are also asking questions and doing experiments that are opening up new questions for basic science,” says Harold McGee, an American author who has explored the interplay between science and cooking.

The Nordic Food Lab is part of a movement known as molecular gastronomy that started in the 1990s as a project to understand how ingredients are transformed during cooking. Pioneers like French physical chemist Hervé This were advocating a new, evidence-based way of cooking. “They thought it strange that we know more about what goes on in the nucleus of a star thousands of light-years away than about what goes on in a soufflé,” Møller says. But they also wanted to introduce new tools and methods—and invent new recipes.

it the most. “We come to like what we eat,” Møller says—which may be why Americans liked the chocolate bar he found repulsive. This type of learning starts in the womb: In

Online

sciencemag.org

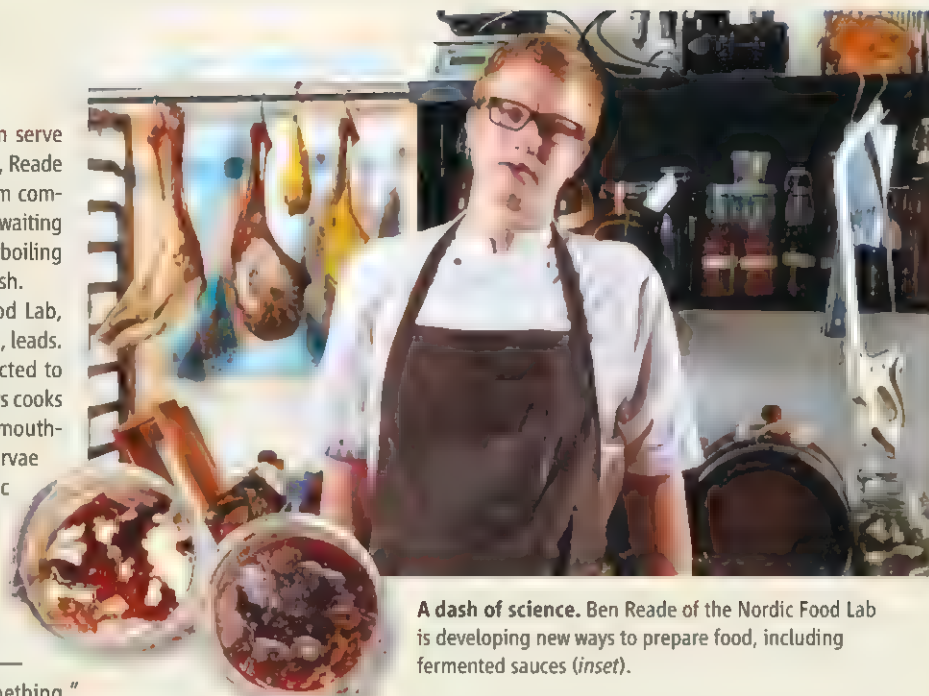
Podcast interview with author Kai Kupferschmidt (http://scim.ag/pod_6134).

several studies, babies from mothers who ate anise or garlic during pregnancy showed an increased preference for those foods. That taste is conservative isn't surprising from an evolutionary viewpoint. “You need a system that will protect you from eating foods that will poison you and kill you,” Møller says. That's the reason a preference for sweet and an aversion to bitter are hardwired in our brain, says Bartoshuk. But it appears that retronasal

olfaction allows learning and refining food choices during life. “What makes lasagna loved is that the odors have been paired to a source of calories,” she says.

Smoked salmon ice cream

As the field of flavor perception develops, it's seeking collaborations with the world of gastronomy. Møller started a new journal last year, *Flavour*, that seeks papers not just from scientists, “but also from the growing number of chefs and other food professionals who are introducing science into their kitchens.” Flavor scientists are also joining hands with culinary labs associated with top restaurants, such as the Nordic Food Lab, not far from Møller's office (see sidebar, above). Psychologists at the University of Sussex worked together with famed chef



A dash of science. Ben Reade of the Nordic Food Lab is developing new ways to prepare food, including fermented sauces (inset).

Indeed, renowned chefs started using professional laboratory equipment such as water baths, liquid nitrogen, and rotary evaporators to produce radically new dishes. Ferran Adrià's restaurant El Bulli in Spain, voted the world's best restaurant five times between 2002 and 2009 by *Restaurant* magazine, became the beacon of this new, science-inspired cuisine. Reade says research at the Nordic Food Lab, which opened in 2008, is ultimately driven by the “pursuit of deliciousness.” As one researcher at the lab put it in a recent paper, “if it's not delicious yet, experiment and play with it until something interesting happens.”

The approach has proven successful from a gastronomic and business point of view. Noma dethroned El Bulli as the world's best restaurant in 2010, a position it held on to until last month. Its popular \$260 menu currently features items like live shrimp and fermented pears. The restaurant also serves ground grasshoppers, and the Nordic Food Lab is experimenting with other ways of preparing insects—which scientists say could provide an abundant and green protein source (see p. 794). “Very few of them,” Reade observes, “are concentrating on making recipes that are delicious.”

—K.K.

Heston Blumenthal of The Fat Duck, a top-notch eatery in Bray, U.K., to examine how people reacted to ice cream with a smoked salmon flavor. (Not surprisingly, they liked it better if they were told what to expect).

In the long run, understanding why things taste well will allow chefs to come up with better food, Møller believes. “Romans built bridges but they didn't know anything about Newtonian mechanics. We do, and, therefore, we can build enormous bridges that do not collapse,” he says. Similarly, humanity has developed paella and pizza, without knowing why they are so good. If chefs understood the principles, they too, could build bolder and bigger, Møller argues. And maybe create a chocolate bar that everyone likes.

—KAI KUPFERSCHMIDT

LETTERS

edited by Jennifer Sills

China's "Love Canal" Moment?

IN FEBRUARY 2013, A POSTING IN CHINA'S BURGEONING BLOGOSPHERE ACCUSED BUSINESS owners in Shandong Province of disposing waste water through injection wells and contaminating shallow groundwater (1). This seemingly innocuous message, describing a practice that is not uncommon, ignited a firestorm on the Internet (2). The outburst of condemnation and concern caught many observers by surprise and reached the uppermost echelon of the Chinese government (3). Du Ying, Vice Chair of the powerful National Development and Reform Commission, declared that "China needs a law specifically designed for groundwater protection" (4).

Groundwater provides about 20% of total water supplies for China, and 50 to 80% of water in water-scarce north and northwest regions of the country (5). However, the outlook for groundwater quality is bleak. According to the latest round of water well sampling in 2011 in more than 200 cities and administrative regions by China's Ministry of Land and Resources, fully 55% of more than 4700 samples indicated groundwater of category IV or V [on a scale of I to V from the best to poorest quality (6)]. Still, no one knows the true extent and severity of groundwater pollution in China.

It is imperative that the Chinese government move aggressively and assertively to combat groundwater pollution. The challenges and action of the United States and other developed countries should serve as an example. The United States alone has spent hundreds of billions of dollars on detecting, monitoring, assessing, and remediating contaminated groundwater since the 1970s (7), when groundwater contamination of the Love Canal neighborhood in New York brought groundwater protection to the American public's consciousness and the forefront of national priorities. China should formulate and enforce strong groundwater pollution prevention and protection plans, backed by adequate financial resources, sufficient incentives not to pollute, and strong implementation of the existing regulations. This is urgent, as potable water is scarce in the most populated areas and China cannot afford the destruction of its groundwater resources. Perhaps the Internet storm of 2013 would be remembered kindly by history if it were to become China's "Love Canal" moment.

CHUNMIAO ZHENG* AND JIE LIU

Call to action. A child protests in the Love Canal neighborhood in 1978.

Center for Water Research, Peking University, Beijing 100871, China, and Department of Geological Sciences, University of Alabama, Tuscaloosa, AL 35487, USA.

*Corresponding author. E-mail: czheng@pku.edu.cn

References

1. Sohu Business News Portal, "Multiple enterprises said to be disposing deadly waste water through injection wells" (17 February 2013).
2. Xinhua News Network, "A lost cause: China's groundwater" (24 February 2013).
3. China Daily, "Advisory body sets sights on pollution" (12 March 2013).
4. China Radio Network, "Du Ying: Overall groundwater protect does not rule out trend of increased pollution" (7 March 2013).
5. J. Qiu, *Nature* **466**, 308 (2010).
6. China Ministry of Environmental Protection, "National Quality Standard for Ground Water (GB/T 14848-93)" (1994).
7. National Research Council, "Alternatives for managing the nation's complex contaminated groundwater sites" (National Academies Press, Washington, DC, 2012).

6. China Ministry of Environmental Protection, "National Quality Standard for Ground Water (GB/T 14848-93)" (1994).
7. National Research Council, "Alternatives for managing the nation's complex contaminated groundwater sites" (National Academies Press, Washington, DC, 2012).

The True Challenge of Giant Marine Reserves

THE NEWS FOCUS STORY "GIANT MARINE reserves pose vast challenges" (C. Pala, 8 February, p. 640) discusses the potential role of large marine reserves in conserving pelagic species. We highlight three points that are misrepresented in the article.

First, the story describes tropical tuna stocks in the Indian Ocean as "depleted," implying that they are severely overexploited (1). Fishery overcapacity is certainly worrisome, but these stocks are not currently overexploited (2). This clarification by no means precludes appropriate use of area-based management, but stock status is central to weighing different management options.

Second, the article claims that "mainstream marine biologists are more optimistic" about the efficacy of the Chagos Islands reserve because "tuna there don't necessarily swim vast distances." We disagree. Juvenile tuna are rarely caught in the Chagos, indicating that Chagos tuna originate elsewhere (3). Moreover, an Indian Ocean mark-recapture project (4) found average juvenile tuna displacements of over 1150 km, exceeding distances observed in other oceans (4). Mainstream scientists have conducted independent modeling studies integrating habitat variability and observed movement rates that demonstrate that Chagos-sized reserves have little impact on tuna populations (5, 6).

Third, monitoring is a major challenge, but the example provided—Chagos-only camera surveys—is highly unlikely to identify reserve effects. Control sites and reliable fish movement data are necessary but will require much larger surveys. Without

CREDIT: AP PHOTO/US



these, it will be impossible to unequivocally identify as reserve effects observed trends that may well be due to other changes in fishing activity, such as Somali piracy impacts (7, 8) and the Indian Ocean time-area closure (9).

Decisions to create large oceanic marine protected areas for managing pelagic species should use evidence-based evaluations of potential benefits before implementation, followed by careful estimation of their efficacy rather than relying on tallies of square kilometers. That is the true challenge of giant marine reserves.

DAVID M. KAPLAN,^{1*} PASCAL BACH,¹ SYLVAIN BONHOMMEAU,² EMMANUEL CHASSOT,¹ PIERRE CHAVANCE,³ LAURENT DAGORN,¹ TIM DAVIES,³ SIBYLLE DUERI,¹ RICK FLETCHER,⁴ ALAIN FONTENEAU,¹ JEAN-MARC FROMENTIN,² DANIEL GAERTNER,¹ JOHN HAMPTON,⁵ RAY HILBORN,⁶ ALISTAIR HOBDAI,⁷ ROBERT KEARNEY,⁸ PIERRE KLEIBER,⁹ PATRICK LEHODEY,¹⁰ FRANCIS MARSAC,^{1,11} OLIVIER MAURY,^{1,11} CHRIS MEES,¹² FRÉDÉRIC MÉNARD,¹ JOHN PEARCE,¹² JOHN SIBERT¹³

¹Institut de Recherche pour le Développement (IRD), Unité Mixte de Recherche (UMR) 212 Exploited Marine Ecosystems (EME), 34203 Sète cedex, France. ²(Ifremer), UMR 212 EME, 34203 Sète cedex, France. ³Imperial College London, Silwood Park Campus, Ascot SL5 7PY, UK. ⁴Department of Fisheries Research, North Beach, WA 6020, Australia. ⁵Oceanic Fisheries Programme, Secretariat of the Pacific Community, 98848 Noumea Cedex, New Caledonia. ⁶School of Aquatic and Fishery Sciences, University of Washington, Seattle, WA 98195, USA. ⁷Commonwealth Scientific and Industrial Research Organisation (CSIRO) Marine and Atmospheric Research, Hobart, Tasmania, 7000, Australia. ⁸Institute for Applied Ecology, University of Canberra, ACT 2601, Australia. ⁹U.S. National Marine Fisheries Service (retired), Honolulu, HI 96814, USA. ¹⁰Marine Ecosystems Department, Space Oceanography Division, Collecte Localisation Satellites, 31520 Ramonville Saint-Agne, France. ¹¹International Centre for Education, Marine and Atmospheric Sciences over Africa, Department of Oceanography, University of Cape Town, Rondebosch 7701, South Africa. ¹²MRAG Ltd, London, W11 5PN, UK. ¹³Joint Institute for Marine and Atmospheric Research, University of Hawaii, Honolulu, HI 96822, USA.

*Corresponding author. E-mail: david.kaplan@ird.fr

References and Notes

1. UN Food & Agriculture Organization (FAO), Glossary, Depleted Stock (www.fao.org/fi/glossary/spec-term.n.asp?id_glo=832&id_lang=TERMS).
2. M. J. Juan-Jordá, I. Mosqueira, A. B. Cooper, J. Freire, N. K. Dulvy, *Proc. Natl. Acad. Sci. U.S.A.* **108**, 20650 (2011).
3. Historical Chagos purse-seine juvenile catch of major tropical tunas represents just 0.6% of the Indian Ocean total, and juveniles represent only 0.5% of the Chagos

purse seine catch biomass. By comparison, historical catch in the Somalia EEZ is 4% juvenile (by mass), and ~22 times more juvenile biomass is caught in the Somali EEZ than in the Chagos (~17 times the catch per unit-area). Calculations are based on publicly available IOTC catch data (www.iotc.org/English/index.php) from the period 1993–2004, the last year fishing agreements were in place for the Somalia EEZ. In terms of total catch, Chagos represents approximately 1.5 and 0.5% of total Indian Ocean purse-seine and longline catch, respectively.

4. J.-P. Hallier, J. Million, The Indian Ocean Tuna Tagging Programme (2012) (www.iotc.org/files/proceedings/2012/sym/D2_PSym.pdf).
5. J. Sibert, I. Semna, P. Lehodey, J. Hampton, *Proc. Natl. Acad. Sci. U.S.A.* **109**, 18221 (2012).
6. S. Dueri, O. Maury, *Aquat. Living Res.* **10.1051/alr/2012032** (19 December 2012).
7. E. Chassot *et al.*, "Analysis of the effects of Somali piracy on the European tuna purse seine fisheries of the Indian Ocean" (Indian Ocean Tuna Commission, Victoria, Seychelles, 2010), p. 26.
8. F. Marsac, "Impacts of piracy threats in the West Indian Ocean on the activity and yield of the longline and purse seine fisheries" (Indian Ocean Tuna Commission, Victoria, Seychelles, 2009), p. 10.
9. IOTC, *For the Conservation and Management of Tropical Tuna Stocks in the IOTC Area of Competence* (Indian Ocean Tuna Commission, 2010), p. 5.

Response

KAPLAN *ET AL.* CLAIM THAT TROPICAL TUNA stocks in the Indian Ocean are not currently overexploited. However, the study they cite (1) points out that only bigeye and yellowfin stocks have been the subject of scientific assessments, meaning that we lack information about the skipjack, a major target species. In fact, the limited evidence (2) points the other way: Of the two stocks assessed, yellowfin (down by 66% over 40 years) is being fished above its maximum sustainable yield, and the catch rate of the bigeye (down by 77% over 60 years) is still declining, even though it is supposedly exploited at its estimated maximum sustainable yield level. If "stock status is central to weighing different management options," as Kaplan *et al.* suggest, the limited stock status information should dictate a precautionary approach.

Kaplan *et al.* then question the claim that tuna in the Chagos don't migrate great distances. Yet, their own study (3) concludes that the lifetime median distance traveled by yellowfin and skipjack in the Western Pacific is between 420 and 470 nautical miles—less than the diameter of the Chagos exclusive economic zone. This may not apply exactly to the Indian Ocean populations, but it does

suggest that nonnegligible parts of the Chagos stocks of these two species spend their entire lives in the no-take area and are now able to reproduce freely.

Kaplan *et al.*'s last point concerns effective monitoring. I did not write that the method I cited was camera-only; on the contrary, I specified that it combined acoustic surveys, which have been used for stock assessments, in the same location at the same time. Tagging programs and oceanographic analyses are also being planned.

CHRISTOPHER PALA

Science News Contributor

References

1. M. J. Juan-Jordá, I. Mosqueira, A. B. Cooper, J. Freire, N. K. Dulvy, *Proc. Natl. Acad. Sci. U.S.A.* **108**, 20650 (2011).
2. IOTC, *For the Conservation and Management of Tropical Tuna Stocks in the IOTC Area of Competence* (Indian Ocean Tuna Commission, 2010).
3. J. Sibert, J. Hampton, *Mar. Pol.* **27**, 87 (2003).

TECHNICAL COMMENT ABSTRACTS

Comment on "Stress in Puberty Unmasks Latent Neuropathological Consequences of Prenatal Immune Activation in Mice"

Stanley E. Lazic

Giovanoli *et al.* (Reports, 1 March 2013, p. 1095) applied an immune challenge to pregnant females, and therefore to all offspring, and subsequently applied stress to offspring on a per cage basis. The data, however, were analyzed as a completely randomized design, which is inappropriate given these restrictions on randomization. This will increase both false positives and false negatives. Full text at <http://dx.doi.org/10.1126/science.1237793>

Response to Comment on "Stress in Puberty Unmasks Latent Neuropathological Consequences of Prenatal Immune Activation in Mice"

Sandra Giovanoli and Urs Meyer

Lazic criticizes the statistical analyses used to support the conclusions in our mouse model. His theory-biased criticism is disproportionate in view of the robustness of our findings (even if different statistical methods are applied) and falls short in explaining the postpubertal onset of effects.

Full text at <http://dx.doi.org/10.1126/science.1238060>

Letters to the Editor

Letters (~300 words) discuss material published in *Science* in the past 3 months or matters of general interest. Letters are not acknowledged upon receipt. Whether published in full or in part, letters are subject to editing for clarity and space. Letters submitted, published, or posted elsewhere, in print or online, will be disqualified. To submit a letter, go to www.submit2science.org.

PLANT BIOLOGY

The Life and Times of a Living Fossil

J. C. McElwain

Of the hundred thousand or so species of trees on our planet, Peter Crane chose *Ginkgo biloba*, an evolutionary singleton, as the vehicle through which he explores the deep evolutionary history of our natural world and the comparatively “shallow roots” of plant hunting expeditions, discovery, cultivation, and propagation. His choice is not surprising: *Ginkgo* is among Earth’s oldest-living organisms, reaching

cultural importance, how it came to be growing in this place at this time, and its reproductive biology, economic uses, and phylogenetic position.

In the chapters “Sex” and “Gender,” Crane uses the ginkgo’s reproductive biology to explore broader evolutionary themes such as the advantages and disadvantages of hermaphroditism (as opposed to being single sexed). Despite being a seed plant closely related to conifers, ginkgo (unlike all living conifers) has motile sperm. Crane suggests this is an evolutionary holdover from its aquatic algal ancestors. He conveys the excitement and determination behind Sakugoro Hirase’s 1896 discovery of ginkgo’s swimming sperm (similar to those found in much more ancient plants, such as bryophytes).

Crane continues the theme of plant reproduction with accounts of early experiments on sex determination in ginkgo by Joseph Franz von Jacquin (1766–1839) at the University of Vienna. By grafting female ginkgo branches onto male trees, von Jacquin demonstrated that sex is determined in tissues rather than at the whole-organism level and that plants must therefore be modularly constructed (in contrast with most animals). Later, Crane recounts his own observations of a male tree at Kew spontaneously producing a branch bearing female ovules. He suggests that confused gender identity (“leaky maleness”) may, along with vegetative reproductive traits such as sprouting and the production of lignotubers, be among ginkgo’s adaptations that have ensured its persistence and resilience through hundreds of millions of years of global change.

In the section “Origin and prehistory,” Crane simply asks where ginkgo comes from. Through 13 chapters, he tracks the fossil record of ginkgos from the likely earliest known ancestral lineages to the living species today. He takes the reader along on a fossil-collecting journey from the Late Triassic of east Greenland, to the middle Jurassic of North Yorkshire, England, and into the Cretaceous, where excellent specimens crop up in the Tico flora of Argentina and in the famous Jehol Biota of China. Throughout this his-

tory, ginkgo’s characteristic bilobed leaf form changes only subtly, which is why *Ginkgo* has become a poster child for morphological stasis; however, there is a pattern of reduction and simplification in female reproductive morphology over the same time interval. Crane includes accounts of localities with exceptionally preserved fossils and how they inform us about the tempo and nature of plant macroevolution. He introduces both Hennig’s theoretical framework for inferring evolutionary relationships and modern molecular phylogenetics. He holds that Darwinian micro-

evolutionary processes and contingency can account for most of the patterns observed in the plant fossil record, and he downplays (but does not entirely discount) the roles of evolutionary innovations and environmentally driven macroevolutionary processes.

Crane also draws a nice parallel between the trajectories of horse and ginkgo evolution—both belonged to once highly diverse families and both were “winnowed” to a single extant species.

Ginkgos underwent major range contraction over the past 65 million years, likely due to global climatic cooling and coincident contraction of the temperate climatic envelope to which *Ginkgo biloba* and its Tertiary ancestors were adapted. In the Eocene, around 55 million years ago, *Ginkgo*’s range extended beyond the Arctic circle, as evidenced by abundant fossils from Ellesmere Island. Iceland at the time was covered in rich forests of ginkgos, oak, swamp cypress, and coast redwoods. In the Miocene of Europe, ginkgos thrived alongside Chinese swamp cypress and dawn redwood. These forests are no longer present in Europe but can be found in warm-temperate regions of East Asia. *Ginkgo biloba* just scraped through the Ice Ages, surviving in two refugial mountain populations in China (Zhejiang Province and Chongqing Municipality). In North America, as in Europe, the ginkgo fossil record is abruptly truncated in the Miocene, with the last known occurrence 15.5 million years ago. Crane uses this biogeographic history to discuss determinants of extinction risk (such as loss of dispersal agents and climate change) and how these in turn influence the ecological associations of living forest communities.

After charting ginkgo’s evolutionary history, Crane segues into its cultural and economic heritage. We learn that the first reliable written account of *Ginkgo* in cultivation comes from a monk in the year 980. Evidence indicates that by the 11th century, seeds



Refuge. *Ginkgo biloba* in the Tianmu Mountain National Nature Reserve (Zhejiang Province, China), which harbors one of the two possible remaining natural populations of the species.

ages of around 1500 years. It is a “living fossil,” belonging to a family line extending back over 200 million years. It is a symbol of morphological stasis yet incredible persistence, having survived two of the five great mass extinction events in Earth history. And, according to Crane (a botanist at Yale University), it is a rare “good news story,” a species we have saved from extinction. Throughout his account, Crane interweaves aspects of ginkgo’s biology and paleobotany with the history of the explorers, botanists, nurserymen, and conservationists who led the species to becoming the most abundant cityscape tree in the world. After reading this captivating book, you will never simply just look at a tree of any species again, and most certainly not a ginkgo, without pondering its

The reviewer is at the School of Biology and Environmental Science, University College Dublin, Belfield, Dublin, Ireland. E-mail: jennifer.mcelwain@gmail.com

Ginkgo
The Tree That Time Forgot
by Peter Crane
Yale University Press
New Haven, CT, 2013. 404 pp.
\$40. ISBN 9780300187519

(known as silver apricots) had been spread across China; by the 13th, *Ginkgo* was in widespread cultivation. The author's account of the economic exploitation of ginkgos across Asia involves shipwrecks and ancient trade routes from China as well as the western discovery (1690) of ginkgo by physician-botanist Englebert Kaempfer in Japan.

Crane concludes *Ginkgo* where he started, with a passionate advocacy for the importance of trees in the wild and in our cities. He highlights that 8000 tree species, representing around 10% of the global diversity, are currently threatened with extinction, and he stresses the importance of ex situ conservation measures involving collections of living specimens in botanic gardens around the world. The actions of *Homo sapiens* have led to species loss at an unprecedented rate, but in the case of *Ginkgo biloba*, we have served as a highly effective dispersal agent. As a result, a once-dwindling population in China is now represented and loved in botanic gardens and cities around the world.

10.1126/science.1237432

PALEONTOLOGY

"Fascinating Little Whatzits"

Philip Donoghue

Conodonts have captured the imagination of paleontologists like no other group, perhaps because they are among the most common and, paradoxically, the rarest of all fossils. Conodonts usually manifest themselves as microscopic, toothlike "elements," the biology of which remained a mystery for much of the time following their discovery in the 1850s. Not until the 1980s was some flesh added to these meager bones by a handful of specimens that preserved the soft-tissue anatomy of these eel-like organisms.

The mystery of the nature of the animal might not have inspired any attention were it not for the fact that conodonts became phenomenally useful geological tools, employed by hundreds of researchers in academia and industry. On the



basis of "species" identified through subtle differences in the tooth elements, it became possible to determine the relative age of rock sequences with unrivaled accuracy and precision, correlating time-equivalent strata across hydrocarbon-bearing basins and among continents of the Paleozoic and Triassic. And through analysis of the effects of carbonization on the organics entombed with the calcium phosphate skeleton, conodonts revealed the thermal history of rock sequences, making them invaluable in hydrocarbon and precious metal exploration. Very little of this utilitarian research evoked interest in conodont biology except when it occasionally boggled the minds of those who spent their working lives staring down microscopes at the fascinating little whatzits.

The history of research into conodont biology, particularly of attempts to deduce the animal's position on the tree of life, can be viewed as one long parlor game, the rules of which required participants to find in candidate relatives structures similar in size, shape, and composition to conodont elements. Because many organisms have aspects of their anatomy that are small and pointy (e.g., the teeth of molluscs, priapulids, and chaetognaths), conodonts have been identified as fossils of just about every major group of animals, as well as fungi, plants, and algae.

Simon Knell's *The Great Fossil Enigma* recounts this history of conodontology by drawing on the primary research literature and also on interviews with and personal correspondence among the participants and witnesses. He does not shirk interest in the development of conodonts as geological tools, but his focus is on the development of conodont biology. In so doing, Knell (a historian of science at the University of Leicester) takes the unexpected and thought-provoking approach of building a narrative on the shifting concept of a conodont organism that occu-

pled the minds of conodontologists and how this affected other spheres of research from taxonomy to biostratigraphy to paleoecology. He documents also the discovery of the flesh behind the conodont's enigmatic smile and how those additional anatomical details removed debate over conodont biology from the parlor to the laboratory bench. No longer was it necessary to imagine the conodont—there was hard evi-

dence of the organism's soft-tissue anatomy written in stone.

There can be no doubt that Knell has written a singular history of conodont research, and likely anyone else would have written it differently. In particular, conodont specialists will lament Knell's focus on biology rather than the rich practical utility of these fossils. Equally, those whose interest is piqued by conodont biology will complain that Knell fails to exact critical judgment over the differing interpretations of the evidence marshaled in debates over their biological affinities. Such approaches, however, would have made for very obvious and very boring alternative narratives, as may be predicted from Knell's foray into the development of conodont biostratigraphy—which makes hard work of an esoteric debate over the dating of some parochial rock sequences.

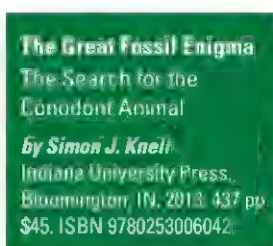
Instead, Knell uses the history of conodont research to show how the ideas and actions of scientists are influenced not merely by the clinical interpretation of the evidence but also by their imagination. And surely the history of the field shows that until comparatively recently there was precious little evidence to constrain imagination. It also shows how the scope for such speculation is inevitably diminished by the discovery of new evidence—of the architecture of the conodont dentition, of the function of conodont elements, and, ultimately, of the anatomy and biological affinity of conodonts.

If you want an authoritative interpretation of the biology of conodonts, then you can do no better than to review the meager evidence and exact your own critical judgment. However, if you want a far more entertaining and interesting account of the discovery of knowledge through the analytical, political, and idiosyncratic activities of researchers, *The Great Fossil Enigma* will serve you well.

References and Notes

1. Title of this review after (2).
2. W. C. Sweet, *J. Paleontol.* **59**, 485 (1985).

10.1126/science.1235837



personal correspondence among the participants and witnesses. He does not shirk interest in the development of conodonts as geological tools, but his focus is on the development of conodont biology. In so doing, Knell (a historian of science at the University of Leicester) takes the unexpected and thought-provoking approach of building a narrative on the shifting concept of a conodont organism that occu-

The reviewer is at the School of Earth Sciences, University of Bristol, Wills Memorial Building, Queens Road, Bristol BS8 1RJ, UK. E-mail: phil.donoghue@bristol.ac.uk

Troubling Trends in Scientific Software Use

Lucas N. Joppa,^{1*} Greg McInerny,¹² Richard Harper,¹ Lara Salido,³ Kenji Takeda,¹ Kenton O'Hara,¹ David Gavaghan,² Stephen Emmott¹

Software pervades every domain of science (1–3), perhaps nowhere more decisively than in modeling. In key scientific areas of great societal importance, models and the software that implement them define both how science is done and what science is done (4, 5). Across all science, this dependence has led to concerns around the need for open access to software (6, 7), centered on the reproducibility of research (1, 8–10). From fields such as high-performance computing, we learn key insights and best practices for how to develop, standardize, and implement software (11). Open and systematic approaches to the development of software are essential for all sciences. But for many scientists this is not sufficient. We describe problems with the adoption and use of scientific software.

One might assume that two principal scientific considerations drive the adoption of modeling software: the ability to enable the user to ask and answer new scientific questions (12) and the ability of others to reproduce the science (13). Alas, diffusion innovation theory defies such objectivity, indicating the importance of communication channels, time, and a social system, as well as the innovation itself (14). An individual's adoption of an innovation relies on awareness, opinion leaders, early adopters, and subjective perceptions. Scientific considerations of the consequences of adoption generally occur late in the process, if at all.

This may be appropriate when deciding which smartphone application one uses. But we must hold scientific inquiry and adoption of scientific software to higher standards. Does use of modeling software conform to basic tenets of scientific methods? We describe survey findings suggesting that many scientists adopt and use software critical to their research for nonscientific reasons. These reasons are scientifically limiting. This result has potentially wider implications

across all disciplines that are dependent upon a computational approach.

Surveying Species Distribution Modelers

We surveyed scientists across a single domain, species distribution modeling (SDM) (15) [see supplementary materials for details]. This strategic targeting separates our analysis from previous efforts in important ways, allowing an analysis spanning computational skill sets, while addressing the interplay between models and computation. Our ~400 respondents ranged from those who “find it difficult to use software” to those “very experienced and very technical.” Asking people to first identify with a scientific domain and addressing models and software through that lens extended the diversity of respondents and minimized self-selection bias that potentially plagued previous efforts (16).

We studied modelers of complex interactions between species and their environment because previous studies have typically chosen atypical groups predefined by computational, and not scientific, expertise [e.g., high-performance computing (11)], where the domain leads to self-selection by those comfortable with computational methods. We flip that approach and investigate the diversity of computational expertise within a domain defined by scientific, rather than computational, problems. Although there are limits to the extent that one can generalize from a domain-targeted study [but also the value of case studies (17)], SDM modelers likely represent a wider ecological, biological, and/or environmental science community: (i) a range of software packages for modeling is available, (ii) scientists are principally educated as biologists and ecologists, and (iii) scientific challenges are broadly the same. Nonetheless, extending the line of inquiry, we present here more widely through further studies, is clearly desirable [such as in (18)].

Our results are intuitive but provide troubling insight at the intersection of scientific pursuits and the adoption of computational methods. Nearly 30% reported that they used particular software because it had been “validated against other methods in peer-review publications.” This rose to 57% for those who

“Blind trust” is dangerous when choosing software to support research.

used “click-and-run” software with easy-to-manipulate user interfaces and dropped to 11% for those who used “syntax-driven” platforms. Further, 7, 9, and 18% of scientists cited “the developer is well-respected,” “personal recommendation,” and “recommendation from a close colleague,” respectively, as reasons for using software. Only 8% claimed they had validated software against other methods as a primary reason for choice; 79% expressed a desire to learn additional software and programming skills.

Many of these scientists rely on the fact that the software has appeared in a peer-reviewed article, recommendations, and personal opinion, as their reason for adopting software. This is scientifically misplaced, as the software code used to conduct the science is not formally peer-reviewed (6). This is especially important when a disconnect occurs between equations and algorithms published in peer-reviewed literature and how those are actually implemented in software reportedly used in those papers (6, 19, 20).

Reliance on personal recommendations and trust is a strategy with risks to science and scientist. “End-user developers” commonly create scientific software (17, 21, 22), but they are often unaware of or ignore traditional software engineering standards, leaving trust in their coding expertise potentially misplaced (1, 2, 9). A “well-respected” end-user developer will almost certainly have earned that respect through scientific breakthroughs, perhaps not for their software engineering skills (although agreement on what constitutes “appropriate” scientific software engineering standards is still under debate).

Most people, in some form, “trust” software without knowing everything about how it works. More complex modeling software is a special case, particularly when the answer cannot be checked without the software, and there is thus no ability to validate its output. We have reason for approaching scientific software with healthy circumspection, rather than blind trust.

Given that scientists in general want to learn “enough” to do their science, our finding that an overwhelming majority of scientists wanted increased computational skills suggests something more. Perceived insuff-

¹Microsoft Research, Cambridge CB1 2FB, UK. ²Department of Computer Science, University of Oxford, Oxford OX1 3QD, UK. ³Centre for Ecology and Hydrology, Penicuik, EH26 0QB, UK.

*Corresponding author. E-mail: ljoppa@microsoft.com

SELECTED QUOTES FROM SURVEY RESPONDENTS

"The research question and the data should be king, with an approach being selected on the basis that it is appropriate to both the research question and the data rather than the research question and the data being selected to fit the approach which a person knows how to use."

"I regularly see peer-reviewed articles that apply SDM incorrectly from either a statistical or inferential perspective. This is largely a user problem rather than a software problem as some people treat [SDM Software] as black boxes rather than inferential tools, and thus do not put in the intellectual effort required to do good work."

"We don't need fancier software, we need people who understand ecology and the importance of multiple types of data ... The key is the ability to think in ecological terms."

ficient understanding of what the software is doing suggests that users fret over whether it is indeed doing what is expected.

The most popular click-and-run software in our study was specifically designed for SDM, released in 2006 (23), and has been cited >1800 times. Confusion around the implementation of the software's algorithms is common (24), even though the algorithms have been published in peer-reviewed literature (23). An explanation was published aiming to describe the methods from a "viewpoint likely to be more accessible (to ecologists) ... than previous ones" (25). Clearly, there were many in the SDM domain unable to interpret the original algorithms, much less understand how they were implemented in the distributed code.

Recommendations, Moving Forward

Education: Universities should produce scientists capable of instantiating science in code such that other scientists are able to peer-review code as they would other aspects of science. Formal training in statistics, computational methods, mathematics, and software engineering should be a core part of the science curriculum at undergraduate and research student levels.

The UK Research Council-funded Doctoral Training Centres (DTCs) were designed to provide such a contextualized curriculum. The Life Sciences Interface DTC at the University of Oxford takes students from both physical science (e.g., mathematics, computer science, and engineering) and life science (e.g., biologists, biochemists, and zoologists) backgrounds to produce multidisciplinary natural scientists. Graduates are fluent in biological, mathematical, computer science, and statistical methods and are capable of conversing and collaborating across these disciplines.

Scientific publication: Scientific software code needs to be not only published and made available (6, 7) but also peer-reviewed. That

this is not part of the current peer-review model means that papers of which science is primarily software-based (i.e., most modeling papers) are not currently fully or properly peer-reviewed. It also means peer-reviewers need to be able to peer-review the code (i.e., be highly computationally literate). Scientific software code should meet a baseline standard of intelligibility in how it is written (and commented on) (1, 2, 9). This requirement is analogous to the widely used standard of English in peer-reviewed publications in order to ensure general accessibility of

articles. A standard of transparency and intelligibility of code that affords precise, formal replication of an experiment, model simulation, or data analysis, as well as peer-review of scientific software, needs to be a condition of acceptance of any paper using such software.

There are journals providing examples of how this might be done. The journal *IPOL: Image Processing on Line* requires authors to submit source code for peer-review. *Insight Journal* has an emphasis on automated code compilation and testing. The *Journal of Open Research Software* peer-reviews code and publishes concise descriptions of the software. Dealing with citable, peer-reviewed software in this way would relieve some of the burden on the peer-review process at more general journals.

Journals can also educate. The *British Medical Journal*, with many submissions deficient in statistical implementation, initiated a series of tutorial articles (26). These cover a wide range of statistical concepts clearly and concisely, giving detailed worked examples and explaining how to describe the results of such studies in a manner that makes it easy for the reader to validate for him- or herself the statistical calculations. Journals publishing research relying on computational science software might publish tutorial papers covering the mathematical and computational underpinnings of key software in their domains, authored by leading authorities.

Changing the status quo will not be easy. Despite the promise of these early efforts, it remains to be seen if they are effective, scalable, and, most important, will be adopted by the broader scientific community. Most scientists, despite an increasing number of programming skills and practices initiatives aimed at scientists (e.g., Software Carpentry, Software Sustainability Institute), continue to emerge from natural science research training without formal training in computational methods and software development and/or

engineering. A 2010 survey showed that only 3 of the 20 most highly cited journals required even the most basic step of making source code available upon publication (7). Current models for how scientists and journals are rewarded must change, as the would-be editors of the *Open Research Computation* journal (now a series of the journal *Source Code for Biology and Medicine*) discovered during efforts to establish a journal for publishing peer-reviewed software (27).

Societally important science relies on models and the software implementing them. The scientific community must ensure that the findings and recommendations put forth based on those models conform to the highest scientific expectation. Learning from efforts such as those noted here, and acting upon their findings, may help transform scientific peer-review and training.

References and Notes

1. S. M. Baxter et al., *PLOS Comput. Biol.* **2**, e87 (2006).
2. G. Wilson, *Am. Sci.* **97**, 360 (2009).
3. Advisory Committee for CyberInfrastructure, National Science Foundation, *Task Force on Software for Science and Engineering Final Report* (NSF, Arlington, VA, 2011).
4. S. Emmott et al., *Towards 2020 Science* (Microsoft Research, Cambridge, 2006).
5. T. Hey et al., *The Fourth Paradigm: Data-Intensive Scientific Discovery* (Microsoft Press, Redmond, WA, 2009).
6. D. C. Ince et al., *Nature* **482**, 485 (2012).
7. A. Morin et al., *Science* **336**, 159 (2012).
8. L. Hatton, A. Roberts, *IEEE Trans. Softw. Eng.* **20**, 785 (1994).
9. D. A. Aruliah et al., arXiv.org, arXiv:1210.0530v1 (2012).
10. C. Drummond, in *ICML '09: Proceedings of the Evaluation Methods for Machine Learning Workshop* (Association for Computing Machinery, New York, 2009), article no. 7.
11. B. R. Basu et al., *IEEE Softw.* **25**, 29 (2008).
12. G. Wilson, *Am. Sci.* **94**, 5 (2006).
13. G. Wilson, *Comput. Sci. Eng.* **10**, 5 (2008).
14. E. M. Rogers, *Diffusion of Innovation* (Free Press, New York, ed. 5, 2003).
15. J. Elith, J. R. Leathwick, *Annu. Rev. Ecol. Evol. Syst.* **40**, 677 (2009).
16. J. E. Hannay et al., in *SECSE '09: Proceedings of the Second International Workshop on Software Engineering for Computational Science and Engineering* (IEEE Computer Society, Washington, DC, 2009), pp. 1–8.
17. J. Segal, C. Morris, *J. Organ. End User Comput.* **23**, 51 (2011).
18. R. Sanders, thesis, Queen's University (2008); <http://hdl.handle.net/1974/1188>.
19. G. Miller, *Science* **314**, 1856 (2006).
20. Z. Merali, *Nature* **467**, 775 (2010).
21. J. Segal, VL-HCC '07 *IEEE Symposium on Visual Languages and Human-Centric Computing* (IEEE Computer Society, Washington, DC, 2007), pp. 111–118.
22. D. F. Kelly, *IEEE Softw.* **24**, 120 (2007).
23. S. J. Phillips et al., *Ecol. Modell.* **190**, 231 (2006).
24. I. W. Renner, D. I. Warton, *Biometrics* **69**, 274 (2013).
25. J. Elith et al., *Divers. Distrib.* **17**, 43 (2011).
26. S. Mallett et al., *BMJ* **345**, (j4021), e3999 (2012).
27. C. Neylon et al., *Source Code Biol. Med.* **7**, 2 (2012).

Acknowledgments: The authors thank scientists who participated in the survey on SDM and S. Pimm for comments.

Supplementary Materials

www.sciencemag.org/cgi/content/full/340/6134/814/DC1

10.1126/science.1231535

ECOLOGY

Immunity and Invasive Success

Stuart E. Reynolds

Biological invasions can be serious threats to local and even global biodiversity, but despite much study, little is known about the factors that enable particular introduced species to be successful invaders (1). On page 862 of this issue, Vilcinskas *et al.* (2) report an important advance in understanding these factors. They show that the almost worldwide invasive triumph of the harlequin ladybird *Harmonia axyridis* (3) depends on the presence of a coexisting pathogen within the invading insect and also the insect's immunity to the pathogen.

This discovery recalls some famous invasions in human history. In *Guns, Germs, and Steel* (4), Diamond explored why small numbers of invaders from a technically more "advanced" continent were often able to overthrow much larger numbers of long-established residents of a less "advanced" one. He noted that, among other factors, the diseases of advanced human societies have been instrumental in enabling them to conquer less advanced ones. In the 16th century conquest of the Americas, smallpox, measles, and other diseases imported by the Europeans decimated the aboriginal peoples, spreading even in advance of the arrival of the invaders. Long coexistence had led the genomes of the European pathogens to be lavishly provided with virulence genes and those of the European hosts to be replete with defenses against them. The immune systems of native Americans were adapted to defending against a different set of associated pathogens and were unequal to the task of defending against European germs. This was thus a case, at least in part, of conquest by an invading host-pathogen alliance.

Biological invasions may also be promoted by the presence within the invading population of endemic pathogens to which invaders but not hosts are resistant or tolerant (5, 6). For example, populations of the native European crayfish *Austropotamobius pallipes* have been locally extinguished by the crayfish plague *Aphanomyces astaci* carried by the introduced North American crayfish *Pascifastacus leniusculus* (7).

Department of Biology and Biochemistry, University of Bath, Claverton Down, Bath BA2 7AY, UK. E-mail: s.e.reynolds@bath.ac.uk

The Asian harlequin ladybird has successfully invaded ecosystems around the world with the help of a pathogen that it carries.



Concealed weapon. Vilcinskas *et al.* show that the invasive Asian harlequin ladybird, *H. axyridis*, carries a pathogen that is lethal to other ladybird species.

The example reported by Vilcinskas *et al.* allows the mechanism of toleration by the invader to be explored. The authors have found that invasive harlequin ladybirds are chronically infected with a blood parasite, a microsporidian from the genus *Nosema* that is tolerated by *H. axyridis* but lethal to closely related ladybirds such as *Coccinella septempunctata* and *Adalia bipunctata*.

Microsporidia are intracellular, spore-forming fungal parasites. Chronic asymptomatic microsporidian infections are relatively common among some insects, whereas in other insect hosts the parasites are lethal. It is not known how *Nosema* is transmitted among ladybirds, but two features of the host's ecology may facilitate the spread of the parasite. First, extensive intraguild predation occurs, in which ladybird larvae attack and consume each other. Feeding by *C. septempunctata* on eggs and larvae of *H. axyridis* is known to be lethal (8). Second, in winter harlequin ladybirds form large aggregations, and this close proximity may facilitate conspecific transfer of infection (see the figure).

The presence of microsporidia in the invading ladybirds is only half of the story, however. Why is *H. axyridis* able to tolerate *Nosema*, whereas other ladybirds are not? We might similarly ask why during the invasion of the Americas, Europeans were able to resist their own diseases when native inhabitants were not. Long exposure to a parasite

leads a host to acquire defenses that, if they do not enable it to rid itself of infection, at least allow it to tolerate the parasite.

A similar reasoning appears to explain why *H. axyridis* is not killed by *Nosema*. The harlequin ladybird's innate immune system is constitutively activated by the presence of the microsporidian and secretes huge amounts of an antimicrobial alkaloid, harmonine, into the insect's hemolymph. Other ladybirds lack this chemical. Further, the harlequin ladybird genome contains an exceptionally large number of antimicrobial peptide genes. These defenses do not kill the parasites, but the low abundance of *Nosema* transcripts in *H. axyridis* RNA suggests that the parasite is kept in a quiescent state. Perhaps when released from such controls in other species of ladybirds, the microsporidians are much more damaging to their hosts.

It has been proposed (9) that invasive species should invest more in their immune systems than noninvasive species, because in newly colonized habitats the invaders must resist parasites to which they are not pre-adapted. At first glance, the findings for *H. axyridis* appear to bear this out: Immune defenses are expensive, and harmonine is accumulated to very high levels in harlequin ladybirds. But here the necessity for greater expenditure on immune defenses appears driven by the need not only to resist novel parasites in the new environment but also to

CREDIT: ANDREAS VILCINSKAS

tolerate old parasites brought from the old one. The expensive immune defenses of *H. axyridis* have, thus, allowed *Nosema* to be used as a biological weapon against sympatric competitors, a trait only revealed as a pre-adaptation to invasiveness when the insect was introduced by human agency into new ecosystems far from home.

References

1. J. G. Ehrenfeld, *Annu. Rev. Ecol. Evol. Syst.* **41**, 59 (2010).
2. A. Vilcinskas, K. Stoecker, H. Schmidtberg, C. R. Röhrich, H. Vogel, *Science* **340**, 862 (2013).
3. J. J. Sloggett, *Entomol. Sci.* **15**, 261 (2012).
4. J. Diamond, *Guns, Germs, and Steel* (Norton, New York, 1997).
5. J. Prenter, C. Macneil, J. T. A. Dick, A. M. Dunn, *Trends Ecol. Evol.* **19**, 385 (2004).
6. A. Strauss, A. White, M. Boots, *Funct. Ecol.* **26**, 1249 (2012).
7. J. C. Dunn, H. E. McClymont, M. Christmas, A. M. Dunn, *Biol. Invasions* **11**, 315 (2009).
8. A. Katsanis, D. Babendreier, W. Nentwig, M. Kenis, *Bio-Control* **58**, 73 (2013).
9. K. A. Lee, K. C. Klasing, *Trends Ecol. Evol.* **19**, 523 (2004).

10.1126/science.1238998

CELL BIOLOGY

Insulin Finds Its Niche

Seth W. Cheetham and Andrea H. Brand

Coordination of organ growth and metabolism in response to changing environmental conditions is essential for physiological homeostasis. A central metabolic control mechanism in multicellular organisms is insulin signaling. Under conditions of elevated blood sugar, insulin promotes the storage of glucose in tissues such as muscle, fat, and liver. Classically, the role of insulin signaling is systemic. In mammals, insulin is produced by pancreatic beta cells and released into the bloodstream in response to increased concentrations of blood glucose, inducing global changes in growth and metabolism. Intriguingly, recent studies have demonstrated that insulin signaling can also occur locally, over a short range. Why have local insulin signaling? Local signals allow organ-specific, rather than organismal responses to changing environmental conditions (see the figure). This allows the modulation of the growth and development of individual tissues to be separately controlled, and raises the question of whether this phenomenon could be exploited for therapeutic strategies. Many of these recent findings have arisen from research in invertebrates; however, there are striking parallels in mammals.

The dynamic control of stem cell populations in response to a variety of stimuli is critical to organismal adaptation to environmental conditions. Local insulin signaling has emerged as playing a critical role in regulating stem cell behavior. In the fruit fly *Drosophila melanogaster*, reactivation of neural stem cells from a period of quiescence is critically dependent on the availability of dietary protein (1). Amino acids are sensed by the fat body, the *Drosophila* equivalent of the mammalian liver and adipose tissue. In the pres-

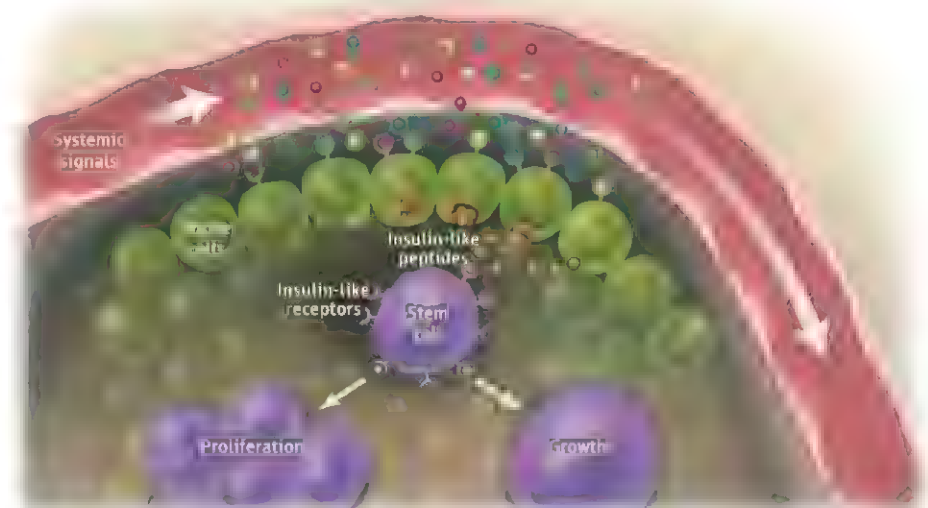
ence of nutrients, the fat body signals to neuroendocrine cells in the brain to secrete insulin-like peptides (dILPs). Circulating dILPs reach target cells in various organs and tissues where they bind to the insulin receptor and activate the conserved phosphatidylinositol 3-kinase (PI3-kinase)–Akt signaling cascade, triggering cell growth and proliferation (2). It was initially speculated that this systemic insulin signaling was responsible for neural stem cell reactivation (3). Surprisingly, however, neural stem cells respond only to locally produced insulin provided by neighboring glial cells that comprise a stem cell niche. The glia secrete the insulin-like peptide dILP6, which stimulates neural stem cells to exit from quiescence. Blocking this insulin release impairs stem cell reactivation. Conversely, forced expression of dILP6 in glial cells rescues neural stem cell reactivation under starvation conditions (4, 5). Thus, the stem cell niche acts as a buffer that insu-

Localized insulin signaling allows organ-specific rather than organism-level responses to the environmental conditions.

lates stem cells from systemic signals and restricts their response to local signals.

Interestingly, local insulin signaling is not a unique feature of the nervous system but is also found in the intestine. Upon feeding, *Drosophila* intestinal stem cells proliferate extensively within their niches. This increase in the stem cell population is induced by dILP3, which is secreted in a nutrient-dependent manner by the visceral muscle that underlies intestinal stem cells. Depletion of dILP3 in this muscle greatly reduces feeding-dependent proliferation (6). The distinct roles for dILP3 and dILP6 and their differential expression patterns suggest that other dILPs may also have defined roles in specific tissues (3).

The modulation of stem cell function by insulin signaling appears to be an evolutionarily conserved mechanism. Mammalian pluripotent stem cells rely on local signals from support cells to maintain self-renewal



Local effects. Diverse systemic signals stimulate niche cells to secrete insulin-like peptides. These peptides bind to cognate receptors expressed by stem cells and change their behavior, triggering growth and proliferation.

and identity. Evidence from in vitro studies demonstrated that human embryonic stem cells depend on basic fibroblast growth factor (bFGF) signaling. bFGF stimulates fibroblast-like support cells to produce insulin-like growth factor-2 (IGF-2), a factor sufficient to maintain human embryonic stem cell cultures (7). Similarly, neonatal spermatogonial stem cell pluripotency is maintained by the secretion of IGF-1 by Leydig support cells in vitro (8). In the mouse small intestine, IGF-1 is expressed in the subepithelial muscle cells (9), suggesting that mammalian intestinal growth may be regulated by a mechanism similar to that observed in *Drosophila*.

Vertebrate niche cells can relay a variety of stimuli through the insulin signaling cascade. Cone photoreceptor cells in the teleost retina produce IGF-1 in a time-of-day-dependent cycle. Application of IGF-1 increases the proliferation of rod progenitor cells in vivo, with the greatest sensitivity at night, coinciding with peak endogenous IGF-1 expression. Conversely, blocking the IGF-1 receptor, which is expressed on the rod progenitor cells, decreases their proliferation (10). Thus, localized insulin signaling can be controlled by nonmetabolic stimuli and may contribute to progenitor cell response to diverse external stimuli.

Local insulin also plays a role in mediating the proliferation of progenitor cells in response to tissue damage. In rats, induction of focal ischemia causes neuronal cell death. After ischemia, brain astrocytes (a type of glial cell) near the damaged area produce IGF-1, promoting proliferation of neighboring neural progenitors in the dentate gyrus of the adult rat hippocampus (11). Forced expression of IGF-1 in astrocytes promotes localized overgrowth of the brain in rodents (11), whereas direct infusion of IGF-1 into specific brain regions can induce neurogenesis in healthy adult mammalian brains (12). This parallels the role of glial-derived insulin in increasing neural stem cell proliferation in *Drosophila* (4, 5). Other stimuli, including exercise, also promote neurogenesis in the proliferative subventricular zone and dentate gyrus regions of the adult mouse brain, although this appears to be through systemic IGF-1 signaling (13, 14).

The discovery that stem cells are sensitive to locally produced insulin could open new avenues in the use of IGFs to activate particular stem cell populations after tissue damage or disease. The cerebrospinal fluid provides access for cerebral cortical progenitor cells in the mouse brain to insulin-like peptides (15). Infusion of insulin-like peptides into this fluid or into particular brain regions may

allow moderation of the effects of injury or neurodegeneration.

Differences in local versus systemic signaling under caloric restriction may favor the maintenance rather than proliferation of stem cell pools. This may help to explain the apparent contradiction that, although reduced insulin signaling increases life span in mammals and invertebrates, insulin signaling has a neuroprotective effect in the central nervous system (16).

Several key questions are yet to be answered about local insulin signaling, including how systemic signals are functionally coupled to niche insulin signals, how different niche signals integrate to control stem cell behavior, and how local insulin signaling changes in aging and disease. Understanding these interactions will enable a greater understanding of stem cell dynamics in response to external signals and metabolic state.

References

1. J. S. Britton, B. A. Edgar, *Development* **2158**, 2149 (1998).
2. D. S. Andersen, I. Colombani, P. Léopold, *Trends Cell Biol.* **10.1016/j.tcb.2013.03.005** (2013).
3. C. Géminard, E. J. Rulifson, P. Léopold, *Cell Metab.* **10**, 199 (2009).
4. J. M. Chell, A. H. Brand, *Cell* **143**, 1161 (2010).
5. R. Sousa-Nunes, L. L. Yee, A. P. Gould, *Nature* **471**, 508 (2011).
6. L. E. O'Brien, S. S. Soliman, X. Li, D. Bilder, *Cell* **147**, 603 (2011).
7. S. C. Bendall *et al.*, *Nature* **448**, 1015 (2007).
8. Y.-H. Huang *et al.*, *FASEB J.* **23**, 2076 (2009).
9. J. B. Pucilowska *et al.*, *Am. J. Physiol. Gastrointest. Liver Physiol.* **279**, G1307 (2000).
10. C. A. Zygar, S. Colbert, D. Yang, R. D. Fernald, *Brain Res. Dev. Brain Res.* **154**, 91 (2005).
11. P. Ye *et al.*, *J. Neurosci. Res.* **78**, 472 (2004).
12. M. A. Aberg *et al.*, *J. Neurosci.* **20**, 2896 (2000).
13. H. van Praag *et al.*, *Nature* **415**, 1030 (2002).
14. J. L. Trejo *et al.*, *J. Neurosci.* **21**, 1628 (2001).
15. M. K. Lehtinen *et al.*, *Neuron* **69**, 893 (2011).
16. N. A. Bishop, T. Lu, B. A. Yankner, *Nature* **464**, 529 (2010).

10.1126/science.1238525

MATERIALS SCIENCE

Quartz on Silicon

C. Jeffrey Brinker^{1,2} and Paul G. Clem²

The integration of quartz with silicon may provide a route to fabricate advanced piezoelectric devices.

The on-chip integration of piezoelectric quartz would be highly beneficial for chemical sensing and accurate timing circuits. However, to date, it has not been possible to achieve single-orientation, single-variant silicon dioxide films with high piezoelectric activity. On page 827 of this issue, Carretero-Genevri *et al.* (1) demonstrate the formation of oriented piezoelectrically active α -quartz thin films directly on silicon. Although the growth mechanism and piezoelectric properties require fuller development, their approach may be an attractive route for developing integrated piezoelectric devices.

Quartz, one of 11 crystalline polymorphs of silicon dioxide, SiO_2 , is the second most abundant mineral on Earth (2). Most forms of SiO_2 are composed of SiO_4 tetrahedra linked together by bridging oxygens to form a rigid three-dimensional network. The relative flexibility of the bond angles accommodates different crystalline symmetries and enhances

the ability of SiO_2 to form amorphous silica glass. The low-temperature form of quartz, α -quartz, possesses trigonal symmetry, a bond angle of 144° , and density of 2.65 g/cm^3 . Due to its high hardness, natural quartz is used as an abrasive (2). Quartz's most important technological use derives from its piezoelectric behavior (3), which is indispensable in electronics for timing control in clocks and microprocessors (4).

The piezoelectric effect, the conversion of strain into electricity (5), requires inversion asymmetry of the crystalline lattice, which is satisfied by the trigonal symmetry of α -quartz; β -quartz, which is stable above 573°C , and β -cristobalite, which is the typical devitrification (crystallization) product of amorphous silica, have hexagonal and tetrahedral symmetry, respectively, and are not piezoelectric. Although abundant, natural quartz seldom has the purity and quality needed for device applications, and almost all quartz oscillators are prepared by "slicing" bulk synthetic quartz crystals prepared hydrothermally (see the figure, panel A).

Carretero-Genevri *et al.* form α -quartz thin films directly on silicon by devitrification of amorphous Sr- or Ba-doped mesoporous

¹Department of Chemical and Nuclear Engineering, the University of New Mexico, Albuquerque, NM 87131, USA.

²Self-Assembled Materials and Electronic, Optical, and Nano Materials Departments, Sandia National Laboratories, Albuquerque, NM 87185, USA. E-mail: cjbrink@sandia.gov; pgclem@sandia.gov



Make it so. (A) Almost all quartz oscillators are prepared by slicing bulk synthetic α -quartz crystals. Common "cuts" like AT are denoted in green. (B and C) Now, highly oriented α -quartz polycrystalline films can be formed directly on Si by devitrification of amorphous mesoporous silica films (1).

silica films prepared by evaporation-induced self-assembly (6). Their process is operationally simple but mechanistically complex: Films are prepared by dip-coating from alcohol/water solutions of soluble silicic acid precursors plus surfactant or block copolymer structure-directing agents. Solvent evaporation drives the self-assembly of amorphous silica films composed of ordered arrays of macropores or large or small mesopores. Doping with $\text{Sr}(\text{NO}_3)_2$ or $\text{Ba}(\text{OH})_2$ is accomplished either in situ or in a secondary step. Heat treatment in air to 900° to 1000°C results in highly oriented α -quartz on silicon (see the figure, panel B).

Although polycrystalline, the α -quartz film bears an epitaxial relationship with the underlying (100) face of the Si substrate (see the figure, panel C), and the columnar crystallites are oriented such that there is a net piezoelectric effect. In comparison, randomly oriented or multivariant crystallites would show no net piezoelectricity, requiring thermal gradients achieved by rapid thermal processing (7) or deposition of seed layers (8) to direct oriented crystal growth.

The use of chemical, stress, and electric field gradients have also been developed as a polar variant-selective or self-polarization mechanism for LiNbO_3 and several other piezoelectric films and crystals (9). The dimensional scale of the oriented cylindrical porosity formed in the amorphous silica precursor films is more or less preserved for macroporous and large mesoporous specimens after crystallization, resulting in optically transparent, piezoelectric quartz thin films composed of oriented arrays of nanopores. In contrast, films composed of small

mesopores (around 3 nm diameter) devitrify to form dense epitaxial α -quartz films.

The detailed mechanism of the devitrification/crystallization process is presently under study, but it is sensitive to Sr or Ba, which, along with the OH content inherent to high-surface-area solution-derived amorphous silica (10), promote devitrification (11). For macroporous and large mesoporous films, devitrification is confined within the pore walls. The columnar nanoscale crystallites suggest that quartz is nucleated at the SiO_2/Si interface, where, through a heteroepitaxial relationship with Si (100), α -quartz is selected for. As crystallization proceeds from the surface by competitive growth of properly oriented crystallites, Sr or Ba as well as OH are excluded at the growth front, or conceivably at the pore walls, and transported to the film surface leaving no trace of Sr or Ba within the film or at the Si interface.

The film porosity and nanoscale dimensions of the silica pores and walls appear key to the growth mechanism. First, below a wall thickness of several nanometers, crystallization consumes the parent film to form an oriented dense α -quartz film, suggesting that the silica pore wall needs to be thicker than a critical nucleus size (or that the pore curvature be less than a critical value) to support confined/templated devitrification. Second, the transformation from amorphous silica to α -quartz is accompanied by a substantial density increase from $\sim 2.0 \text{ g/cm}^3$ to $\sim 2.65 \text{ g/cm}^3$; the thinness and weak lateral constraint of the pore wall may allow this devitrification strain to be accommodated by shrinkage of the walls as opposed to film thickness (shrinkage parallel to the substrate is precluded by coher-

ency of the quartz/Si interface). The influence of differential strain is further evident from crystallographically oriented euhedral/faceted domains that are mechanically detached along their peripheries allowing localized two-dimensional shrinkage and stress release.

The work by Carretero-Genevri *et al.* represents one of the first examples of confined, heteroepitaxial devitrification to form an oriented polycrystalline film. Confined devitrification of monosized amorphous silica nanospheres to form monosized α -quartz by hydrothermal treatment in saline solutions at 200°C has been recently demonstrated (12). Whether hydrothermal processing in NaCl- or Sr^{2+} - or Ba^{2+} -containing solutions could transform macro- or mesoporous silica films to porous α -quartz remains to be seen, but such a treatment would reduce both the processing temperature and the concurrent oxidation of the Si substrate. Additionally, lithographic patterning and ink-jet printing of mesoporous silica films on Si have been reported (5, 13), and it would be of interest to demonstrate the patterned formation of porous piezoelectric quartz. Finally, detailed measurements of the piezoelectric properties of these films are needed (14). Due to their polycrystalline nature and crystallographic alignment directed by the substrate, we might expect quality factors to be inferior to those of single-crystal quartz slabs cut along preferred crystallographic angles (15). However, the coherent Si/quartz interface and film thinness combined with controlled porosity may provide advanced functionality and operational frequency range of potential interest in acoustic wave-based sensing and microelectromechanical systems.

References and Notes

1. A. Carretero-Genevri *et al.*, *Science* **340**, 827 (2013).
2. J. Götz, *Mineral. Mag.* **73**, 645 (2009).
3. E. Benes *et al.*, *Sens. Actuators A Phys.* **48**, 1 (1995).
4. W. P. Mason, *J. Acoust. Soc. Am.* **70**, 1561 (1981).
5. J. Cune, P. Cune, *Bull. Soc. Minéralog. Fr.* **3**, 90 (1880).
6. Y. F. Lu *et al.*, *Nature* **389**, 364 (1997).
7. B. A. Tuttle *et al.*, *J. Am. Ceram. Soc.* **76**, 1537 (1993).
8. R. W. Schwartz *et al.*, *J. Am. Ceram. Soc.* **82**, 2359 (1999).
9. M. Houe, P. D. Townsend, *J. Phys. D Appl. Phys.* **28**, 1747 (1995).
10. C. J. Brinker, G. W. Scherer, *Sol-Gel Science: The Physics and Chemistry of Sol-Gel Processing* (Academic Press, San Diego, CA, USA, 1990).
11. W. S. Fyfe, D. S. McKay, *Am. Mineral.* **47**, 83 (1962).
12. X. Jiang *et al.*, *Chem. Commun. (Camb.)* **47**, 7524 (2011).
13. D. A. Doshi *et al.*, *Science* **290**, 107 (2000).
14. J. E. A. Southin, S. A. Wilson, D. Schmitt, R. W. Whatmore, *J. Phys. D Appl. Phys.* **34**, 1456 (2001).
15. J. Wang *et al.*, *Ultrasonics* **44** (suppl. 1), e869 (2006).

Acknowledgments: Supported by the U.S. Department of Energy Basic Energy Sciences (BES) Materials Science and Engineering Program and BES Catalysis grant DEFG02-02ER15368.

VIOLOGY

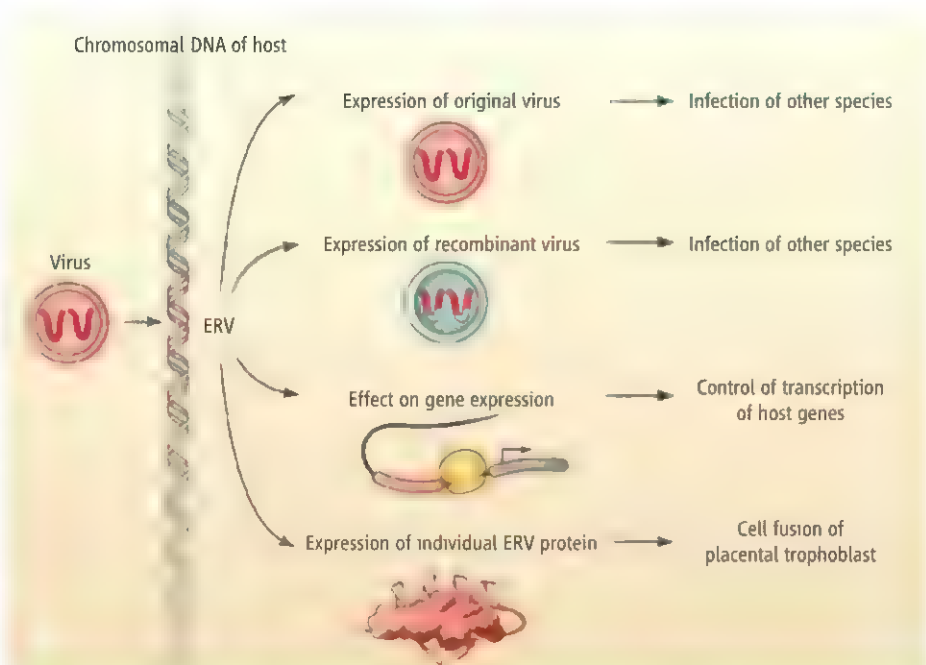
Our Viral Inheritance

Robin A. Weiss¹ and Jonathan P. Stoye²

The enormous scale of the invasion of vertebrate genomes by viral sequences has become apparent through analyses of complete genomes. Sequences derived from many kinds of RNA (1) and DNA (2) viruses have found a convenient resting place in host genomes during evolution, and the process is ongoing. Retroviral genomes, the major and best understood viral insertions (3), alone account for 6 to 14% of the genomes analyzed to date, including ~8% of human DNA. These endogenous retroviruses (ERVs) comprise more genomic DNA than that encoding the host proteome. The functionality or otherwise of this “junk” DNA has become the focus of an intense debate (4, 5). Here we consider a number of consequences of ERV acquisition (see the figure).

How do ERVs affect the host species in which they reside? In theory, the consequences of ERV acquisition may be neutral, detrimental, or beneficial depending on the particular ERV and its integration site. Endogenous retroviruses can serve as a long-lasting viral reservoir and provide evidence for coexistence between retroviruses, in essentially modern form, and their hosts going back many millions of years (6). ERV expression is tightly regulated (7). Even though most ERVs are defective, some maintain their replicative capacity and can reemerge as infectious agents many generations later. Defective ERVs can also recombine to generate an infectious virus (8).

In the coevolutionary interplay between virus and host, the host has developed various strategies to dampen down the efficient replication of activated ERV. These include intracellular restriction factors (3) and mutation of host cell surface receptors (9) so that any reactivated virus can only infect other species, a phenomenon called xenotropism. Examples are retroviruses of gibbons and koalas that are derived from a rodent ERV and which cause leukemia in their new hosts. Moreover, the koala virus is currently colonizing the germ line as a new ERV (10). Thus, a virus embedded in the chromosomes



Functions of ERVs. When the proviral DNA of a retrovirus integrates into germ-line DNA of the host, it becomes inherited alongside all host DNA sequences. The provirus may remain dormant or may be expressed in the ways indicated.

of one host species without causing apparent harm can trigger a potentially devastating epidemic in another.

Retroviral insertion adds DNA to the host genome and may affect the control of host RNA transcription, splicing, or stability through viral signals. Insertion into essential genes may be deleterious but is unlikely to be important on an evolutionary time scale, with affected individuals rapidly lost by selection.

The inserted promoter and enhancer sequences in the long terminal repeat regions of ERV genomes may affect the expression of adjacent host genes. This is a well-known mechanism of activation of cellular genes in retroviral oncogenesis. It may also be important for generating novel patterns of gene expression through introduction of viral promoters or other regulatory sequences (1). For example, the tissue-specific expression of human salivary amylase is controlled by an ERV insertion (11) that may have helped our forebears to switch from a mainly fruit-based diet to one containing starch. Further, tight coexpression of the human endogenous retrovirus H (HERV-H) family with

Viruses incorporated into vertebrate genomes may reemerge after long periods of dormancy to play a range of biological roles in their host.

transcription factors for pluripotent human embryonic stem cells indicates that HERV-H may contribute to pluripotency (12).

Perhaps the most intriguing example of a useful ERV comes with the expression of ERV envelope glycoproteins in the placenta (13, 14), where cell fusion occurs in the trophoblast layer. The function of glycoproteins of enveloped viruses is to bind to target cells and effect fusion of the viral envelope with the host cell membrane. The fusion mechanism of ERV glycoproteins has been purloined on independent occasions by various orders of placental mammals to form the syncytiotrophoblast, and these viral glycoproteins are therefore called syncytins. Studies of knockout mice reveal that these genes are essential for placenta formation. As well as inducing cell-to-cell fusion, syncytins may locally suppress immune recognition at the maternal-fetal interface, implying a possible mechanism by which a mother is tolerant to the fetus(es) she carries (14).

The studies of syncytin show that big science and small science have complementary benefits. Mining the ever-expanding sequence and expression databases to iden-

¹Division of Infection and Immunity, University College London, Gower Street, London WC1E 6BT, UK. ²Division of Virology, MRC National Institute of Medical Research, The Ridgeway, London NW7 1AA, UK. E-mail: rweiss@ucl.ac.uk; jstoye@nimr.mrc.ac.uk

tify ERVs that play interesting biological roles will continue to be of great importance as different ERVs can be deleterious or useful to the host. However, targeted studies of specific ERVs, like the ones encoding syncytins (15), will be required for testing the hypotheses generated by systems biology. There may well be other functions to be discovered, as well as further examples of gene regulation controlled by ERVs.

References

1. C. Feschotte, C. Gilbert, *Nat. Rev. Genet.* **13**, 283 (2012).
2. A. Katzoourakis, R. J. Gifford, *PLoS Genet.* **6**, e1001191 (2010).
3. J. P. Stoye, *Nat. Rev. Microbiol.* **10**, 395 (2012).
4. ENCODE Project Consortium, *Nature* **489**, 57 (2012).
5. D. Graur et al., *Genome Biol. Evol.* **5**, 578 (2013).
6. A. Katzoourakis, M. Tristem, O. G. Pybus, R. J. Gifford, *Proc. Natl. Acad. Sci. U.S.A.* **104**, 6261 (2007).
7. H. M. Rowe, D. Trono, *Virology* **411**, 273 (2011).
8. G. R. Young, G. Kassiotis, J. P. Stoye, *Nature* **491**, 774 (2012).
9. C. A. Kozak, *Retrovirology* **7**, 101 (2010).
10. R. E. Tarlinton, J. Meers, P. R. Young, *Nature* **442**, 79 (2006).
11. C.-N. Ting, M. P. Rosenberg, C. M. Snow, L. C. Samelson, M. H. Meisler, *Genes Dev.* **6**, 1457 (1992).
12. F. A. Santoni, J. Guerra, J. Luban, *Retrovirology* **9**, 111 (2012).
13. D. Haig, *Curr. Biol.* **22**, R609 (2012).
14. A. Dupressoir, C. Lavielle, T. Heidmann, *Placenta* **33**, 663 (2012).
15. A. Dupressoir et al., *Proc. Natl. Acad. Sci. U.S.A.* **108**, E1164 (2011).

10.1126/science.1235148

APPLIED PHYSICS

Ghost Imaging in Three Dimensions

Daniele Faccio and Jonathan Leach

Images are usually captured with a two-dimensional (2D) “device”—the retina, a piece of film, or a detector array—and extra processing is needed to create an image that we perceive as 3D. On page 844 of this issue, Sun *et al.* (1) demonstrate how to create 3D images of an object by capturing light with little more than a few single-pixel detectors. The detectors have only one pixel and cannot possibly reconstruct even a 2D image on their own. Yet, by properly illuminating the scene and using so-called “computational ghost imaging” techniques, the authors can render beautiful 3D images.

We perceive a 3D world through stereoscopic vision. The human brain uses the slightly displaced images formed by our two eyes to accurately judge distances, determine shapes, and calculate how these change in time with respect to our position. In contrast to our ability to see in 3D, most artificial imaging systems rely on only a single observation point—for example, the imaging plane in a digital camera. Thus, all of the additional 3D information, which we often take for granted, is lost. Recently, revamped 3D cinema technology has taken over a substantial share of the entertainment market, precisely because of the enhanced visual experience when compared to traditional 2D cinema. However, there are applications where this approach is either technologically out of reach (e.g., in the far-infrared region) or too costly. So a natural question arises: How simple can we make an imaging system with 3D rendering capability?

Sun *et al.* show that all that is needed to create a 3D image is illuminating an object with

a light source that creates known intensity patterns and a few single-pixel detectors placed in different positions that “view” the scene from different angles. From the data obtained in this way, 3D image reconstruction can proceed through computational ghost imaging. Each detector has no spatial resolution; they are just “light buckets” that collect all of the light that hits them, but they cannot directly record an image. It is only when the single-pixel detector signals are combined with the knowledge of the illumination structure that the full 3D object can be reconstructed.



Illuminating approach to 3D imaging. In the approach described by Sun *et al.*, the object to be rendered in 3D is illuminated by a known pattern of randomly placed black and white areas. The single-pixel detectors measure the total reflected energy from the object. The measurement is then repeated for many different illumination patterns until the full 3D image is reconstructed.

Single-pixel detectors can be used to reconstruct three-dimensional images after patterned illumination of an object.

Ghost imaging is a relatively new technique that has been used to recover 2D images of objects from data obtained with a single-pixel bucket photodetector. Demonstrated in 1995 (2), it was originally thought to be a direct consequence of quantum entanglement and action at a distance, but it was later realized that the only prerequisite is two spatially separated light beams that are correlated (3, 4). A surprising feature of ghost imaging is that a spatially resolved image is obtained by pointing a camera at the light source rather than at the object; an image is obtained by recording light that never actually interacts with the object, hence the term “ghost.”

To understand the principles of ghost imaging, consider a simple example where we create two copies of a light beam that propagate at some given angle. One light beam illuminates the object to be imaged, and a single-pixel bucket detector collects any reflected light. The second light beam does not interact with the object, but its position is recorded with a camera. These two signals are now combined; the image recorded by the camera is multiplied by the intensity of the detector signal to give a “weighted camera image.” This process is repeated for a number of different angles. Finally, adding together all the weighted camera images provides an accurate image of the actual object.

Computational ghost imaging is a variation of the original scheme that came about when researchers realized that it was not necessary to measure the second light beam—all that was required was knowledge of the illumination (5–7). This knowledge can be obtained by illuminating the object with a known pattern rather than a random one. In the same manner as the original scheme, repeated known illuminations are combined

with the corresponding detector signal to create a number of weighted images, from which a full image of the object can again be reconstructed.

Sun *et al.* have combined these ideas and have shown that a full 3D image can be recorded with only a few single-pixel bucket photodetectors and intelligent illumination. In their scheme, the known illumination source is a rapidly changing checkerboard of black and white squares generated by a digital projector, such as that used for project presentations (see the figure). However, this elegant experiment is far from the end of the story. The procedure requires several minutes to reconstruct a full 3D image of a human head. During this time, the head or object must remain perfectly still, much

like early photography with low-speed glass plates. This limitation, mainly caused by the refresh rate of the digital projector, results in relatively slow data acquisition rates. Reduction of recording times will necessarily require the development of a new generation of superfast projectors, or possibly the use of high-repetition laser sources.

We can easily envisage that the technological requirements for reducing the recording times in Sun *et al.*'s technique will soon be resolved, enabling the real-time recording of 3D images using only single pixels. One of the most promising applications is the capability of 3D imaging in wavelength regions limited by current detector array technologies. This blend of simple ideas and complex physics by Sun *et al.* combines to

give us a beautiful new way of seeing the world. It would seem that the answer to the question "How simple can we make a 3D imaging system?" appears to be "Disconcertingly so."

References

1. B. Sun *et al.*, *Science* **340**, 844 (2013).
2. D. V. Strekalov, A. V. Sergienko, D. N. Klyshko, Y. H. Shih, *Phys. Rev. Lett.* **74**, 3600 (1995).
3. R. S. Bennink, S. J. Bentley, R. W. Boyd, *Phys. Rev. Lett.* **89**, 113601 (2002).
4. A. Gatti, E. Brambilla, M. Bache, L. A. Lugiato, *Phys. Rev. Lett.* **93**, 093602 (2004).
5. J. H. Shapiro, *Phys. Rev. A* **78**, 061802 (2008).
6. O. Katz, Y. Bromberg, Y. Silberberg, *Appl. Phys. Lett.* **95**, 131110 (2009).
7. Y. Bromberg, O. Katz, Y. Silberberg, *Phys. Rev. A* **79**, 053840 (2009).

10.1126/science.1238415

MATERIALS SCIENCE

Complexity from Simplicity

Elias Vlieg

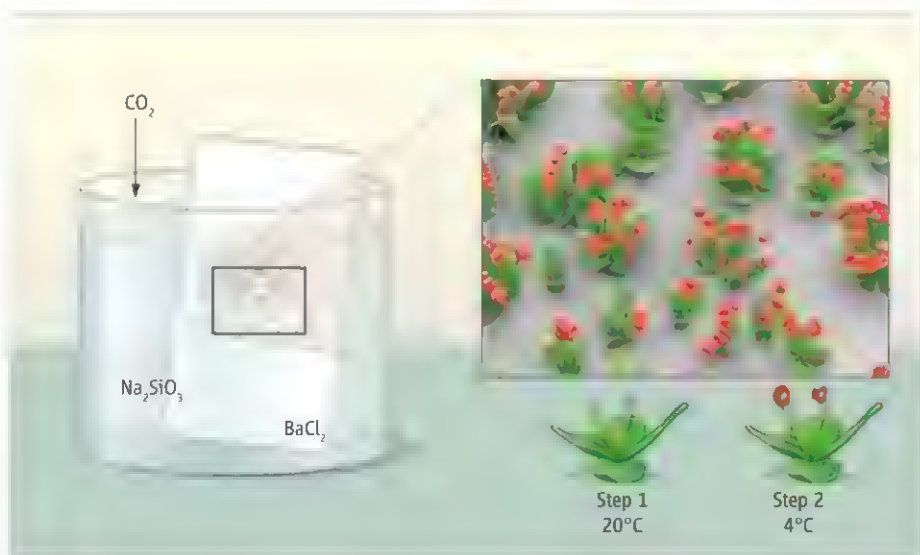
By studying natural shapes and processes, researchers have learned that the key ingredient to arriving at complexity is the coupling between different processes. This coupling leads to self-organization and is an essential feature of life (1). In biominerals, such as diatom skeletons or abalone shells, the interplay between calcium carbonate or similar minerals with organic molecules can lead to highly functional materials with hierarchical architectures and stunning beauty (2). On page 832 of this issue, Noorduin *et al.* (3) bring the man-made design of complex shapes from simple ingredients to a level of control that promises applications in fields such as optics and catalysis.

The authors report a remarkably simple process for growing beautiful flower arrangements at a micrometer scale (see the figure). In an aqueous solution containing barium chloride and sodium metasilicate, a glass plate is positioned more or less vertically. After a few hours, very complex microstructures form, owing to the delicate interplay between the growth of barium carbonate and silicate. The formation of these two minerals not only changes the local pH in opposite ways, but their growth rate also depends on this pH. Silicon also blocks barium carbonate

growth, resulting in two growth regimes in which microstructures either avoid or attract each other. Diffusing CO_2 from the air modifies the pH as a function of depth in the solution, leading to a depth-dependent morphology and density of the microstructures.

Manipulation of crystal growth conditions results in the controlled formation of complex micrometer-scale shapes.

Many feedback and control parameters thus act together to generate the structures. Although the correct growth conditions can be selected experimentally, a mathematical model that includes the different growth rates and their coupling with the local environment



Micro-ikebana. In a solution containing both sodium silicate and barium chloride, the growth of barium carbonate and silicate will depend on, as well as influence, the pH of the solution. The formation of these crystals is thus strongly coupled, resulting in the growth of complex shapes—tuliplike in the example shown. Diffusing CO_2 dictates the pH value as a function of depth and thereby the density of the structures. Through careful control of the growth conditions, Noorduin *et al.* have designed a wide variety of structures with flowerlike features such as stems, branches, and leaves. In the example, the green stems and leaves are grown first, followed by growth at a lower temperature, yielding the thick-walled flowers on top. The colors in the image are artificial, but it is possible to grow such structures by using materials that have different colors and other properties.

Radboud University Nijmegen, Institute for Molecules and Materials, Heyendaalseweg 135, 6525 AJ Nijmegen, Netherlands. E-mail: e.vlieg@science.ru.nl

seems essential to obtain a further understanding and control.

Flower shapes have previously been grown from inorganic materials such as metal oxides, semiconductors, and silicon oxide (4). The choice of materials is not new either: García-Ruiz *et al.* have shown that this system can generate shapes resembling biological forms and that the shapes of the oldest known fossils can also be produced in this inorganic way (5). García-Ruiz *et al.* have more recently proposed a model to explain the shape of such “biomorphs” (6).

Noorduyn *et al.* now provide an improved understanding of the formation process that allows them to design the resulting shapes at will and to combine different growth conditions to generate even more complex shapes. Rather than selecting one set of conditions and letting the system evolve passively, the authors change the process conditions actively, allowing the construction of elements such as stems, vases, branches, and leaves.

The growth conditions are changed by moving the glass plate from one beaker to the next. By using different tilt angles of

the glass plate in the two beakers, an entire matrix of conditions is probed at once, allowing the researchers to pick the flowers they like best. More sophisticated setups, such as microfluidic devices with precise pH, concentration, and flow control, should enable the reproducible production of very complex shapes with desirable properties. This form of bottom-up patterning may become useful, for example, in the design of catalytic surfaces, where the large surface area and the confinement of the reactants may enhance the catalytic activity (7), or in the growth of three-dimensional metamaterials with a negative index of refraction that can be used as optical elements (8).

Other routes to generate (sub)micrometer-scale architectures in a bottom-up fashion include the combination of nanoparticles with organic molecules, which can give rise to self-assembled structures with a complexity that depends on the number of interaction components (9). Properly designed molecules can be self-assembled in supramolecular structures with a functionality that again depends on the interaction between the different components (10). Nanowires can also be

designed so that nanoscale patterning occurs spontaneously (11).

None of these examples, however, combines the simplicity, beauty, and control of the barium carbonate and silicate system. For now, Noorduyn *et al.* have focused on growing flowerlike structures. More control will undoubtedly lead to structures that may be less artistically pleasing, but more technologically useful.

References and Notes

1. J.-M. Lehn, *Angew. Chem. Int. Ed.* **52**, 2836 (2013).
2. S. Weiner, I. Addadi, *J. Mater. Chem.* **7**, 689 (1997).
3. W. L. Noorduyn, A. Grinthal, L. Mahadevan, J. Aizenberg, *Science* **340**, 832 (2013).
4. For a series of beautiful examples, see www.mrs.org/science-as-art/
5. J. M. García-Ruiz *et al.*, *Science* **302**, 1194 (2003).
6. J. M. García-Ruiz, E. Melero-García, S. T. Hyde, *Science* **323**, 362 (2009).
7. J. Ge, J. Lei, R. N. Zare, *Nat. Nanotechnol.* **7**, 428 (2012).
8. C. M. Soukoulis, M. Wegener, *Nat. Photonics* **5**, 523 (2011).
9. H. Göllen, S. Mann, *Angew. Chem. Int. Ed.* **42**, 2350 (2003).
10. J. A. A. W. Elemans, R. van Hameren, R. J. M. Nolte, A. E. Rowan, *Adv. Mater. (Deerfield Beach Fla.)* **18**, 1251 (2006).
11. R. E. Algra *et al.*, *Nature* **456**, 369 (2008).

10.1126/science.1238619

MEDICINE

(Poly)Combing the Pediatric Cancer Genome for Answers

Marc Alard Morgan and Ali Shilatifard

The rapid expansion of high-throughput DNA sequencing now enables the genetic analysis of human diseases at an unprecedented rate and resolution. In particular, whole-genome sequencing of rare childhood diseases promises fundamental insight into basic developmental processes and biochemical pathways (1). Indeed, this approach has identified the first mutations in histones—proteins that package DNA—in human disease (2, 3). About 80% of cases of diffuse intrinsic pontine glioma (DIPG), an aggressive, incurable childhood tumor of the brain stem, harbor these histone mutations. On page 857 of this issue, Lewis *et al.* (4) extend this story by showing that altered activity of polycomb repressive complex 2 (PRC2), a key developmental regulator of gene expression, is involved in the patho-

genesis of gliomas carrying these mutant histones.

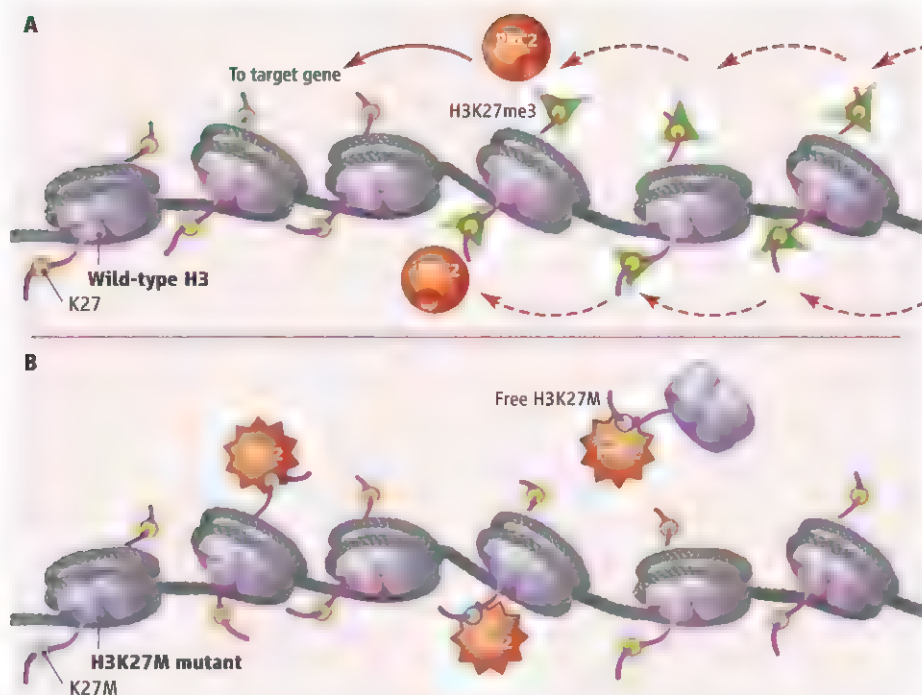
The culprit mutations involve a substitution of lysine 27 to methionine (H3K27M) in one of two histone H3-encoding genes, *H3F3A* (histone H3.3) or *HIST1H3B* (histone H3.1). Histone proteins form the core of eukaryotic chromatin, and their post-translational modifications are associated with various DNA-based processes including transcription (5). Lysine 27 of histone H3 is subject to methylation by PRC2, a multi-protein assemblage essential for repressing transcription during development (6). The precise function of histone lysine methylation is a topic of some contention (7). Studies in the fruit fly *Drosophila melanogaster* suggest that H3K27 modifications are essential for developmental gene regulation, as a lysine-to-arginine substitution activates genes that are normally repressed by PRC2 (8). The remarkably specific nature of the H3 mutation in high-grade (aggressive) pediatric

Misregulation of the pattern and localization of histone modifications may result in cancer development.

gliomas points to a connection with lysine 27 modifications.

Although the H3K27M mutation is heterozygous (occurs in only one of the two gene copies), there is profoundly reduced trimethylation (H3K27me3) of wild-type H3 in gliomas (9), which suggests that the mutation dominantly inhibits PRC2 methyltransferase activity. Indeed, biochemical studies by Lewis *et al.* and others (4, 10) show that the mutant histone binds to the catalytic site of PRC2 to block enzymatic activity (see the figure). This effect was examined in patient tumor cells using chromatin immunoprecipitation followed by DNA sequencing (10). Global trimethylation of wild-type H3K27 is reduced in these tumor cells. However, local increases in this modification, accompanied by PRC2 occupancy of chromatin, were observed at sites involved in repressing tumor suppressors, such as *p16Ink4A* (10). These unexpected findings suggest that the function of mutant H3K27M is more

Stowers Institute for Medical Research, 1000 East 50th Street, Kansas City, MO 64110, USA. E-mail: ash@stowers.org



Histone mutations and gene expression. (A) In wild-type cells, PRC2 is recruited to target genes and mediates the trimethylation (green) of lysine (yellow) on histone 3 (H3K27me3) at repressed loci. (B) In tumor cells harboring the H3K27M mutant, PRC2 may bind more avidly to K27M (blue) on chromatin, leading to reduced chromatin dynamics and a defect in H3K27me3. Binding could induce a PRC2 conformational change. Alternatively, non-chromatin-incorporated "free" H3K27M could inhibit PRC2 prior to its association with chromatin.

complex than thought and may involve gene-specific redistribution of H3K27me3 rather than the simple loss of lysine methylation.

One major unanswered question is whether the histone H3K27M mutation functions as a driver, passenger, or navigator in DIPG pathogenesis. Its prevalence in DIPG points to a functional role in this cancer (2, 3). However, transgenic H3K27M expression in cells lacking the tumor suppressor protein p53 did not produce gliomas in mice (4). Thus, it is unclear whether H3K27M is necessary or sufficient for DIPG pathogenesis. The H3K27M mutation is found in combination with mutations of p53 and an H3.3 chaperone protein [α -thalassemia X-linked mental retardation protein (ATRX)] (2), so it may function as a cooperating rather than an initiating mutation. Perhaps H3K27M is selected for during oncogenesis as a means to evade cell death or suppress the deleterious effects of other acquired mutations. Indeed, mutations in a histone H3K27 demethylase [ubiquitously transcribed tetratricopeptide repeat, X chromosome (UTX)] are associated with altered cellular proliferation (11).

Although H3K27M blocks PRC2 activity, PRC2-independent pathways may also be affected. Histone H3K27 is demethylated

by UTX, a component of the MLL3/4 COMPASS-like complexes that occupy enhancers (DNA elements that regulate tissue-specific gene expression during development) (12). Histone H3K27 acetylation in combination with H3K4 monomethylation marks active enhancers (13), which suggests that UTX may demethylate H3K27 prior to acetylation (12). Intriguingly, Lewis *et al.* found that H3K27M-expressing cells display increased H3K27 acetylation. Moreover, UTX and MLL3/4 are mutated in pediatric medulloblastoma (14), and the histone H3K4M peptide can inhibit H3K4 demethylases [lysine-specific demethylases 1 and 2 (LSD1/2)] (15). Thus, potential H3K27M interactions with the UTX demethylase, H3K27 acetylation, and altered enhancer function in DIPG should be explored.

Future studies regarding the molecular characterization of developmental processes driving DIPG will require the use of in vivo disease models. Lewis *et al.* did not observe gliomas in mice exogenously expressing H3K27M. These experiments were performed postnatally, indicating that H3K27M expression during embryonic development may be required for pathogenesis of DIPG. A mouse allele of the *H3F3A* gene that induc-

ibly converts K27 to K27M (via Cre recombinase) would be a valuable tool. *Drosophila* genetic mosaics will also provide a powerful system to investigate clonal effects of the mutation (8, 12).

Why is histone H3K27M so specific to high-grade pediatric brain stem gliomas, and so rarely detected in other pediatric or adult cancers? Perhaps H3 modification by PRC2 has an early brain-specific function, or possibly other tissues cannot tolerate the H3K27M mutation. Why are only two distinct H3 genes (out of more than a dozen) mutated with K27M? Mutations of *H3F3B* (H3.3B), which encodes a protein identical to that encoded by *H3F3A*, have not been reported; a simple possible explanation is that the DNA codon AAG encodes *H3F3A* Lys²⁷, whereas the codon is AAA in *H3F3B*. Thus, *H3F3A* requires only a single mutation to create a codon for methionine (ATG), whereas *H3F3B* requires two base substitutions. Nonetheless, codon usage is not the only explanation (6 of 10 H3.1 genes have AAG at Lys²⁷), so it is important to investigate potential tissue-specific expression patterns for H3.1 isoforms. The K27M mutation is primarily found in H3.3 and less frequently in the replication-dependent H3.1, implicating possible cell cycle-dependent chromatin assembly. Perhaps the H3K27M mutation alters histone incorporation into chromatin. Determining the genome-wide distribution of this mutant form in chromatin will be informative. Because inactivating mutations of PRC2 have not been reported in DIPG, it is possible that its activity is actually required for DIPG development. It may be that PRC2 dysfunction, rather than total loss of activity, underlies H3K27M function in pediatric brain stem tumors. This would make PRC2 a potential target for therapeutic intervention.

References

1. J. R. Downing *et al.*, *Nat. Genet.* **44**, 619 (2012).
2. J. Schwartzentruber *et al.*, *Nature* **482**, 226 (2012).
3. G. Wu *et al.*, *Nat. Genet.* **44**, 251 (2012).
4. P. W. Lewis *et al.*, *Science* **340**, 857 (2013); 10.1126/science.1232245.
5. E. Smith, A. Shilatifard, *Mol. Cell* **40**, 689 (2010).
6. R. Margueron, D. Reinberg, *Nature* **469**, 343 (2011).
7. S. Henikoff, A. Shilatifard, *Trends Genet.* **27**, 389 (2011).
8. A. R. Pengelly, O. Copur, H. Jäckle, A. Herzig, J. Müller, *Science* **339**, 698 (2013).
9. S. Venetii *et al.*, *Brain Pathol.* 10.1111/bpa.12042 (2013).
10. K. M. Chan *et al.*, *Genes Dev.* **27**, 11101/gad.21778.113 (2013).
11. H. M. Herz *et al.*, *Mol. Cell. Biol.* **30**, 2485 (2010).
12. H. M. Herz *et al.*, *Genes Dev.* **26**, 2604 (2012).
13. M. P. Creighton *et al.*, *Proc. Natl. Acad. Sci. U.S.A.* **107**, 21931 (2010).
14. T. J. Pugh *et al.*, *Nature* **488**, 106 (2012).
15. F. Forneris, C. Binda, A. Adamo, E. Battaglioli, A. Mattevi, *J. Biol. Chem.* **282**, 20070 (2007).

RETROSPECTIVE

Robert G. Edwards (1925–2013)

Susan J. Fisher^{1,2} and Linda C. Giudice^{1,2,3}

Robert G. Edwards, who with his colleagues Patrick Steptoe and Jean Purdy enabled the birth of the first “test tube” baby, died on 10 April at his home near Cambridge University in England. He was 87. In 2010, he was awarded the Nobel Prize in Physiology or Medicine for the team’s work, ushering in the era of in vitro fertilization (IVF), which allows infertile couples to have their own biological children. The societal impact of this revolution in human reproduction has been enormous. An estimated 5 million babies have been born as the result of assisted reproductive technologies, a number that will doubtless increase as a result of delayed childbearing. Sadly, due to failing health and dementia, Edwards was unable to attend the Nobel award ceremony, and it is unlikely that he even knew of this great recognition. His wife, Ruth Fowler Edwards (they met as graduate students), and former trainee, Martin H. Johnson, addressed the audience on his behalf, a cruel irony given the unbridled passion with which he spoke and wrote about his work on human reproduction.

Robert Geoffrey Edwards was born in 1925 in Yorkshire, England. He attended the University of Wales and then earned a Ph.D. in physiology from the University of Edinburgh in 1955. He joined the University of Cambridge faculty in 1963 where he remained for the rest of his career. The notion that human IVF was possible first occurred to Edwards during his graduate work. He realized he could do nothing to help infertile couples until human oocytes (egg cells) were fertilized in vitro. In 1965, after two disappointing years, he coaxed ovarian tissue that had been removed from patients to produce several oocytes. As he described in a *Nature Medicine* article in 2001, after receiving the prestigious Albert Lasker Clinical Medical Research Award, “I waited for 25 hours—and joy unbounding! A beautiful diakinesis, superb chromatids...Now a definite future existed for human IVF.”

Retrieving tissue from a woman’s ovaries required minimal surgery. To this end, Edwards partnered with Patrick Steptoe,



an obstetrician and gynecologist who was an expert in the technique of laparoscopy. They collaborated for ~20 years, until Steptoe’s death in 1988. Against seemingly insurmountable odds—little human material available for research, a modest laboratory, no government funding, as well as strong disapproval from colleagues and the public—Edwards worked passionately and methodically over decades to achieve the dream he had as a graduate student. His publications during the 1960s and 70s lay out the blueprint of his plan for bringing human IVF to fruition. (He also described prenatal genetic diagnosis, stem cells, and cloning.) The initial attempts were frustrating, as egg cells that were matured and fertilized in vitro failed to initiate pregnancy when transferred back into the uterus. Edwards concluded that for IVF to work, eggs that matured during the natural menstrual cycle had to be collected from patients. This key insight, among others, led to the birth of Louise Brown, the first test-tube baby, on 26 July 1978.

Although Edwards and a lawyer, David Sharpe, outlined in a 1971 *Nature* article the difficult social and ethical issues that human embryo research entailed, major arguments in the press and criticism from colleagues formed a constant backdrop to his work with Steptoe. As Edwards wrote in the 2001 article, “Ethicists decried us, forecasting abnormal babies, misleading the infertile and misrepresenting our work as really acquiring human embryos for research.” On one partic-

The work of a pioneer of in vitro fertilization led to the first “test-tube baby” and changed the field of human reproductive biology.

ular day, Edwards issued eight libel actions in the High Court of London. “I won them all, but the work and worry restricted research for several years.”

After Edwards and Steptoe achieved their goal in 1978, they were told that government funding for their work would not be forthcoming. Again, the team entered uncharted waters, but emerged years later once they garnered private support, and founded the Bourn Hall Clinic in Cambridge for training gynecologists and biologists from around the world. Where did his colossal motivation come from? One source was Edwards’s passion for developmental biology. He was also deeply moved by the plight of infertile couples who ultimately made IVF possible by bravely participating in the work before there was any evidence it would succeed. As he and others learned to recapitulate fertilization and the initial steps of embryo development in vitro using animal models, he became increasingly convinced that these technologies could be translated to humans.

Despite the importance of studying human reproductive biology, proven by the work of Edwards and others, many aspects of this research remain challenging. In the United States, the Dickey-Wicker Amendment, passed every year since 1996, prohibits the use of federal funds for research that creates or destroys human embryos. Accordingly, the derivation of human stem cells from embryos, which was first reported by James Thomson in 1998, was accomplished with nonfederal funds as must be the case for all such stem cell lines derived in the United States.

Through Edwards’s energy, determination, and rigorous study, IVF is now considered common medical practice. Unfortunately, societal and governmental views toward studying human development have not evolved apace. What would Edwards, one of the most provocative medical researchers and humanists in modern history, think of this situation? As he wrote in the 1971 article, “When scientists clearly foresee potential conflicts with existing rules of society arising from their work, paradoxically both human progress and scientific freedom may hang on their activism in arenas generally regarded as social or political.”

10.1126/science.1239644

¹Obstetrics, Gynecology and Reproductive Sciences, ²Human Embryonic Stem Cell Program, University of California San Francisco, CA 94143, USA. ³American Society for Reproductive Medicine, Birmingham, AL 35216. E-mail: sfisher@cgl.ucsf.edu; giudice@obgyn.ucsf.edu

Impact of Shale Gas Development on Regional Water Quality

R. D. Vidic,^{1*} S. L. Brantley,² J. M. Vandenbossche,¹ D. Yoxtheimer,² J. D. Abad¹

Background: Natural gas has recently emerged as a relatively clean energy source that offers the opportunity for a number of regions around the world to reduce their reliance on energy imports. It can also serve as a transition fuel that will allow for the shift from coal to renewable energy resources while helping to reduce the emissions of CO₂, criteria pollutants, and mercury by the power sector. Horizontal drilling and hydraulic fracturing make the extraction of tightly bound natural gas from shale formations economically feasible. These technologies are not free from environmental risks, however, especially those related to regional water quality, such as gas migration, contaminant transport through induced and natural fractures, wastewater discharge, and accidental spills. The focus of this Review is on the current understanding of these environmental issues.

Advances: The most common problem with well construction is a faulty seal that is emplaced to prevent gas migration into shallow groundwater. The incidence rate of seal problems in unconventional gas wells is relatively low (1 to 3%), but there is a substantial controversy whether the methane detected in private groundwater wells in the area where drilling for unconventional gas is ongoing was caused by well drilling or natural processes. It is difficult to resolve this issue because many areas have long had sources of methane unrelated to hydraulic fracturing, and pre-drilling baseline data are often unavailable.

Water management for unconventional shale gas extraction is one of the key issues that will dominate environmental debate surrounding the gas industry. Reuse of produced water for hydraulic fracturing is currently addressing the concerns regarding the vast quantities of contaminants that are brought to the surface. As these well fields mature and the opportunities for wastewater reuse diminish, the need to find alternative management strategies for this wastewater will likely intensify.

Outlook: Improved understanding of the fate and transport of contaminants of concern and increased long-term monitoring and data dissemination will help effectively manage water-quality risks associated with unconventional gas industry today and in the future. Confidentiality requirements dictated by legal investigations combined with the expedited rate of development and the limited funding for research are major impediments to peer-reviewed research into environmental impacts. Now is the time to work on these environmental issues to avoid an adverse environmental legacy similar to that from abandoned coal mine discharges in Pennsylvania.



Drilling multiple horizontal wells from a single well pad allows access to as much as 1 square mile of shale that is located more than a mile below. [Image courtesy of Range Resources Appalachia]

READ THE FULL ARTICLE ONLINE
<http://dx.doi.org/10.1126/science.1235009>

Cite this article as R. Vidic *et al.*, *Science* **340**, 1235009 (2013). DOI: 10.1126/science.1235009

ARTICLE OUTLINE

Cause of the Shale Gas Development Surge
 Methane Migration

How Protective Is the "Well Armor"?

The Source and Fate of Fracturing Fluid

Appropriate Wastewater Management Options

Conclusions

BACKGROUND READING

General overview that includes geology of major shale plays, description of the extraction process, relevant regulations, and environmental considerations: www.netl.doe.gov/technologies/oil-gas/publications/EPreports/Shale_Gas_Primer_2009.pdf

Detailed information about individual shale gas wells, including chemical additives used in each hydraulic fracturing treatment: <http://fracfocus.org>

Findings of the U.S. Environmental Protection Agency study on the potential impact of hydraulic fracturing on drinking water resources: www.epa.gov/hfstudy

Comprehensive information from the British Geological Survey about shale gas (including articles and videos): www.bgs.ac.uk/shalegas

Site developed in collaboration with the Geological Society of America promoting the rational debate about energy future: www.switchenergyproject.com

Latest news and findings about shale gas.
www.shale-gas-information-platform.org

¹Department of Civil and Environmental Engineering, University of Pittsburgh, Pittsburgh, PA 15261, USA. ²Earth and Environmental Systems Institute and Department of Geosciences, Pennsylvania State University, University Park, PA 16802, USA.

*Corresponding author. E-mail: vidic@pitt.edu

Impact of Shale Gas Development on Regional Water Quality

R. D. Vidic,^{1*} S. L. Brantley,² J. M. Vandenbossche,¹ D. Yoxtheimer,² J. D. Abad¹

Unconventional natural gas resources offer an opportunity to access a relatively clean fossil fuel that could potentially lead to energy independence for some countries. Horizontal drilling and hydraulic fracturing make the extraction of tightly bound natural gas from shale formations economically feasible. These technologies are not free from environmental risks, however, especially those related to regional water quality, such as gas migration, contaminant transport through induced and natural fractures, wastewater discharge, and accidental spills. We review the current understanding of environmental issues associated with unconventional gas extraction. Improved understanding of the fate and transport of contaminants of concern and increased long-term monitoring and data dissemination will help manage these water-quality risks today and in the future.

Natural gas has recently emerged as an energy source that offers the opportunity for a number of regions around the world to reduce their reliance on energy imports or strive toward energy independence (1, 2). It may also be a potential transition fuel that will allow for the shift from coal to renewable energy resources while helping to reduce the emissions of CO₂, criteria pollutants, and mercury by the power sector (3). The driving force behind this shift is that it has become economically feasible to extract unconventional sources of gas that were previously considered inaccessible. Conventional gas is typically extracted from porous sandstone and carbonate formations, where it has generally been trapped under impermeable caprocks after migration from its original source rock. In contrast, unconventional gas is usually recovered from low-permeability reservoirs or the source rocks themselves, including coal seams, tight sand formations, and fine-grained, organic-rich shales. Unconventional gas formations are characterized by low permeabilities that limit the recovery of the gas and require additional techniques to achieve economical flow rates (2).

The archetypical example of rapidly increasing shale gas development is the Marcellus Shale in the eastern United States (Fig. 1). Intensive gas extraction began there in 2005, and it is one of the top five unconventional gas reservoirs in the United States. With a regional extent of 95,000 square miles, the Marcellus is one of the world's largest known shale-gas deposits. It extends from upstate New York, as far south as Virginia, and as far west as Ohio, underlying 70% of the state of Pennsylvania and much of West Virginia. The formation consists of black and dark gray shales, siltstones, and limestones (4). On the basis of a geological study of natural fractures in the for-

mation, Engelder (5) estimated a 50% probability that the Marcellus will ultimately yield 489 trillion cubic feet of natural gas.

Concerns that have been voiced (6) in connection with hydraulic fracturing and the development of unconventional gas resources in the United States include land and habitat fragmentation as well as impacts to air quality, water quantity and quality, and socioeconomic issues (3, 5, 7). Although shale gas development is increasing across several regions of the United States and the world (such as the United Kingdom, Poland, Ukraine, Australia, and Brazil), this review focuses on the potential issues surrounding water quality in the Appalachian region and specifically the Marcellus Shale, where the majority of published studies have been conducted. Our Review focuses on chemical aspects of water quality rather than issues surrounding enhanced sediment inputs into waterways, which have been discussed elsewhere (4, 7, 8).

Cause of the Shale Gas Development Surge

Recent technological developments in horizontal drilling and hydraulic fracturing have enabled enhanced recovery of unconventional gas in the United States, increasing the contribution of shale gas to total gas production from negligible levels in 1990 to 30% in 2011 (1). Although the first true horizontal oil well was drilled in 1929, this technique only became a standard industry practice in the 1980s (9). Whereas a vertical well allows access to tens or hundreds of meters across a flat-lying formation, a horizontal well can be drilled to conform to the formation and can therefore extract gas from thousands of meters of shale. Horizontal wells reduce surface disturbance by limiting the number of drilling pads and by enabling gas extraction from areas where vertical wells are not feasible. However, horizontal drilling alone would not have enabled exploitation of the unconventional gas resources because the reservoir permeability is not sufficient to achieve economical gas production by natural flow. Hydraulic fracturing—"hydrofracking," or "fracking"—

was developed in the 1940s to fracture and increase permeability of target formations and has since been improved to match the characteristics of specific types of reservoirs, including shales.

Hydraulic fracturing fluids consist of water that is mixed with proppants and chemicals before injection into the well under high pressure (480 to 850 bar) in order to open the existing fractures or initiate new fractures. The proppant (commonly sand) represents generally ~9% of the total weight of the fracturing fluid (10) and is required to keep the fractures open once the pumping has stopped. The number, type, and concentration of chemicals added are governed by the geological characteristics of each site and the chemical characteristics of the water used. The fracturing fluid typically used in the Marcellus Shale is called slickwater, which means that it does not contain viscosity modifiers that are often added to hydrofracture other shales so as to facilitate better proppant transport and placement.

Chemical additives in the fluids used for hydraulic fracturing in the Marcellus Shale include friction reducers, scale inhibitors, and biocides (Table 1 and Box 1). Eight U.S. states currently require that all chemicals that are not considered proprietary must be published online (11), whereas many companies are voluntarily disclosing this information in other states. However, many of the chemicals added for fracturing are not currently regulated by the U.S. Safe Drinking Water Act, raising public concerns about water supply contamination. From 2005 to 2009, about 750 chemicals and other components were used in hydraulic fracturing, ranging from harmless components, including coffee grounds or walnut hulls, to 29 components that may be hazardous if introduced into the water supply (6). An inorganic acid such as hydrochloric acid is often used to clean the wellbore area after perforation and to dissolve soluble minerals in the surrounding formation. Organic polymers or petroleum distillates are added to reduce friction between the fluid and the wellbore, lowering the pumping costs. Antiscalants are added to the fracturing fluid so as to limit the precipitation of salts and metals in the formation and inside the well. Besides scaling, bacterial growth is a major concern for the productivity of a gas well (quantity and quality of produced gas). Glutaraldehyde is the most common antibacterial agent added, but other disinfectants [such as 2,2-dibromo-3-nitropropionamide (DBNPA) or chlorine dioxide] are often considered. Surfactants (alcohols such as methanol or isopropanol) may also be added to reduce the fluid surface tension to aid fluid recovery.

Methane Migration

As inventoried in 2000, more than 40 million U.S. citizens drink water from private wells (12). In some areas, methane—the main component of natural gas—seeps into these private wells from either natural or anthropogenic sources. Given its low solubility (26 mg/L at 1 atm, 20°C), methane

¹Department of Civil and Environmental Engineering, University of Pittsburgh, Pittsburgh, PA 15261, USA. ²Earth and Environmental Systems Institute and Department of Geosciences, Pennsylvania State University, University Park, PA 16802, USA.

*Corresponding author. E-mail: vidic@pitt.edu

that enters wells as a solute is not considered a health hazard with respect to ingestion and is therefore not regulated in the United States. When present, however, methane can be oxidized by bacteria, resulting in oxygen depletion. Low oxygen concentrations can result in the increased solubility of elements such as arsenic or iron. In addition, anaerobic bacteria that proliferate under such conditions may reduce sulfate to sulfide, creating water- and air-quality issues. When methane degasses, it can also create turbidity and, in extreme cases, explode (13, 14). Therefore, the U.S. Department of the Interior recommends a warning if water contains 10 mg/L of CH₄ and immediate action if concentrations reach 28 mg/L (15). Methane concentrations above 10 mg/L indicate that accumulation of gas could result in an explosion (16).

The most common problem with well construction is a faulty seal in the annular space around casings that is emplaced to prevent gas leakage from a well into aquifers (13). The incidence rate of casing and cement problems in unconventional gas wells in Pennsylvania has been reported previously as ~1 to 2% (17). Our count in Pennsylvania from 2008 to March 2013 for well construction problems [such as casing or cementing incidents (18)] cited by the Pennsylvania Department of Environmental Protection (DEP) revealed 219 notices of violation out of 6466 wells (3.4%) (19). Of these, 16 wells in northern Pennsylvania were given notices with respect to the regulation that the "operator shall prevent gas and other fluids from lower formations from entering fresh groundwater" (violation code 78.73A). Most of the time, gas leakage is minor and can be remedied. However, in one case attributed to Marcellus drilling and leaky well casings, stray gas that accumulated in a private water well exploded near the northeastern Pennsylvania town of Dimock. A study of 60 groundwater wells in that area, including across the border in upstate New York (20), showed that both the average and maximum methane concentrations were higher when sampled from wells within 1 km of active Marcellus gas wells as compared with those farther away. Much discussion has since ensued as to whether the methane detected in these wells was caused by drilling or natural processes (21–24) because the area has long had sources of both thermogenic and biogenic methane unrelated to hydraulic fracturing, and no predrilling baseline data are available. The averages reported in that study for sites both near and far from drilling are not dissimilar from values for groundwater from areas of Pennsylvania and West Virginia sampled by the U.S. Geological Survey (USGS) before the recent Marcellus Shale development began, or samples in New York state where high-volume hydrofracturing is currently banned (Fig. 2).

The reason gas is found so often in water wells in some areas is because methane not only forms at depth naturally, owing to high-temperature maturation of organic matter, but also at shallow depths through bacterial processes (25, 26). Both these thermogenic and biogenic gas types can

migrate through faults upward from deep formations or laterally from environments such as swamps (swamp gas) or glacial till (drift gas) (14, 27). In addition, gas can derive from anthropogenic sources such as gas storage fields, coal mines, landfills, gas pipelines, and abandoned gas wells (28). In fact, ~350,000 oil and gas wells have been drilled in Pennsylvania, and the locations of ~100,000 of these are unknown (29). Thus, it is not surprising that gas problems have occurred in Pennsylvania long before the Marcellus development (30). Pennsylvania is not the only state facing this problem because about ~60,000 documented orphaned wells and potentially more than 90,000 undocumented orphaned wells in the United States have not been adequately plugged and could act as vertical conduits for gas (31).

As natural gas moves in the subsurface, it can be partially oxidized, mixed with other gases, or diluted along flow paths. To determine its provenance, a "multiple lines of evidence approach" must be pursued (24). For example, researchers measure the presence of other hydrocarbons as

well as the isotopic signatures of H, O, and C in the water or gas (16, 27, 31). Thermogenic gas in general has more ethane and a higher ¹³C/¹²C ratio than that of biogenic gas. Stable isotopes in thermogenic gas may sometimes even yield clues about which shale was the source of the gas (24, 32). In northeastern Pennsylvania, researchers argue whether the isotopic signatures of the methane in drinking-water wells indicate the gas derived from the Marcellus or from shallower formations (20, 24).

Although determining the origin of gas in water wells may lead to solutions for this problem, the source does not affect liability because gas companies are responsible if it can be shown that any gas—not just methane—has moved into a water well because of shale-gas development activity. For example, drilling can open surficial fractures that allow preexisting native gas to leak into water wells (13). This means that pre- and post-drilling gas concentration data are needed to determine culpability. Only one published study compares pre- and post-drilling water chemistry in the Marcellus Shale drilling area. In that study, a

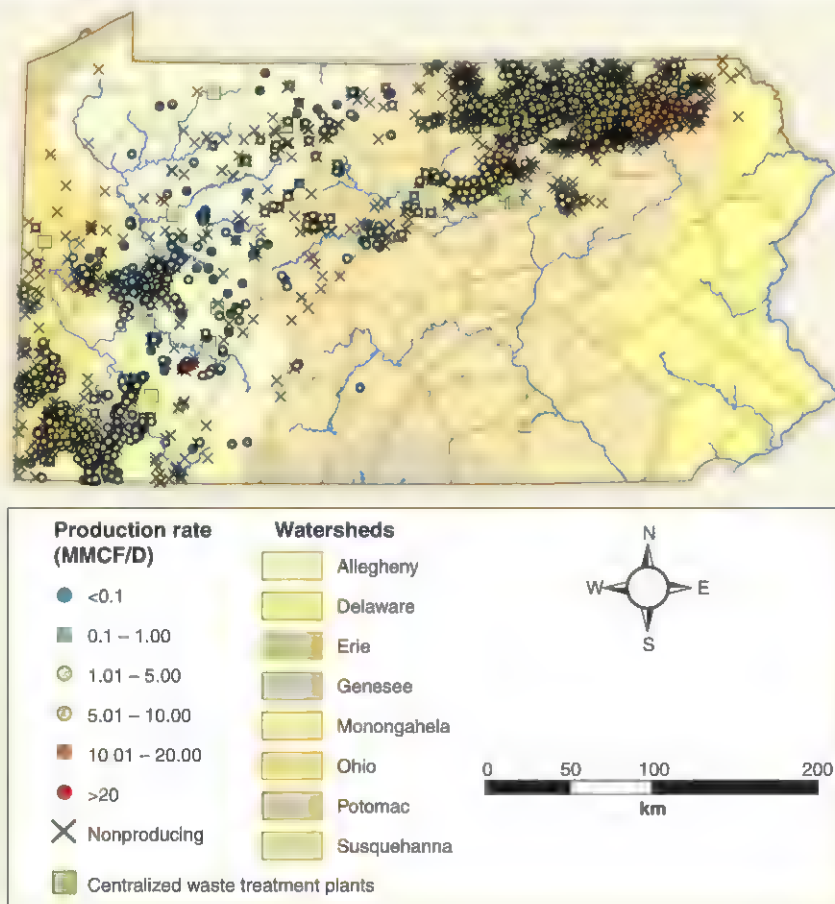


Fig. 1. Marcellus Shale wells in Pennsylvania. Rapid development of Marcellus Shale since 2005 resulted in more than 12,000 well permits, with more than 6000 wells drilled and ~3500 producing gas through December 2012 (average daily production ranged from <0.1 to >20 million cubic feet/day (MMCF/D)). Current locations of centralized wastewater treatment facilities (CWTs) are distributed to facilitate treatment and reuse of flowback and produced water for hydraulic fracturing.

sample of 48 water wells in Pennsylvania investigated between 2010 and 2011 within 2500 feet of Marcellus wells showed no statistical differences in dissolved CH₄ concentrations before or shortly after drilling (33). In addition, no statistical differences related to distance from drilling were observed. However, that study reported that the concentration of dissolved methane increased in one well after drilling was completed nearby,

which is possibly consistent with an average rate of casing problems of ~3%.

The rate of detection of methane in water wells in northeast Pennsylvania [80 to 85% (20, 24)] is higher than in the wider region that includes southwestern Pennsylvania [24% (33)], where pre- and post-drilling concentrations were statistically identical. This could be a result of the small sample sizes of the two studies or because the

hydrogeological regime in the northeast is more prone to gas migration (34). Such geological differences also may explain why regions of the Marcellus Shale have been characterized by controversy in regard to methane migration as noted above, whereas other shale gas areas such as the Fayetteville in Arkansas have not reported major issues with respect to methane (35). Reliable models that incorporate geological characteristics are needed to allow prediction of dissolved methane in groundwater. It is also critical to distinguish natural and anthropogenic causes of migration, geological factors that exacerbate such migration, and the likelihood of ancillary problems of water quality related to the depletion of oxygen. Answering some of these questions will require tracking temporal variations in gas and isotopic concentrations in groundwater wells near and far from drilling by using multiple lines of evidence (16, 24). Research should also focus on determining flow paths in areas where high sampling density can be attained.

Table 1. Common chemical additives for hydraulic fracturing.

Additive type	Example compounds	Purpose
Acid	Hydrochloric acid	Clean out the wellbore, dissolve minerals, and initiate cracks in rock
Friction reducer	Polyacrylamide, petroleum distillate	Minimize friction between the fluid and the pipe
Corrosion inhibitor	Isopropanol, acetaldehyde	Prevent corrosion of pipe by diluted acid
Iron control	Citric acid, thioglycolic acid	Prevent precipitation of metal oxides
Biocide	Glutaraldehyde, 2,2-dibromo-3-nitropropionamide (DBNPA)	Bacterial control
Gelling agent	Guar/xanthan gum or hydroxyethyl cellulose	Thicken water to suspend the sand
Crosslinker	Borate salts	Maximize fluid viscosity at high temperatures
Breaker	Ammonium persulfate, magnesium peroxide	Promote breakdown of gel polymers
Oxygen scavenger	Ammonium bisulfite	Remove oxygen from fluid to reduce pipe corrosion
pH adjustment	Potassium or sodium hydroxide or carbonate	Maintain effectiveness of other compounds (such as crosslinker)
Proppant	Silica quartz sand	Keep fractures open
Scale inhibitor	Ethylene glycol	Reduce deposition on pipes
Surfactant	Ethanol, isopropyl alcohol, 2-butoxyethanol	Decrease surface tension to allow water recovery

Box 1. Glossary of Terms

Casing: steel pipe that is inserted into a recently drilled section of a borehole to stabilize the hole, prevent contamination of groundwater, and isolate different subsurface zones.

Cementing: placing a cement mixture between the casing and a borehole to stabilize the casing and seal off the formation.

Class II disposal wells: underground injection wells for disposal of fluids associated with oil and gas production.

Flowback water: water that returns to the surface after the hydraulic fracturing process is completed and the pressure is released and before the well is placed in production; flowback water return occurs for several weeks.

Produced water: water that returns to the surface with the gas after the well is placed in production; production water return occurs during the life of a well.

Proppant: granular material, such as silica sand, ceramic media, or bauxite, that keeps the fractures open so that gas can flow to the wellbore.

Slickwater fracturing: fracturing with fluid that contains mostly water along with friction reducers, proppants, and other additives; used for predominantly gas-bearing formations at shallower depths.

Source rock: organic-rich sedimentary rocks, such as shale, containing natural gas or oil.

Stray gas: gas contained in the geologic formation outside the wellbore that is accidentally mobilized by drilling and/or hydraulic fracturing.

How Protective Is the "Well Armor"?

The protective armor shielding the freshwater zones and the surrounding environment from the contaminants inside the well consist of several layers of casing (hollow steel pipe) and cement (Fig. 3). When the integrity of the wellbore is compromised, gas migration or stray gas can become an issue (14). Gas migration out of a well refers to movement of annular gas either through or around the cement sheath. Stray gas, on the other hand, commonly refers to gas outside of the wellbore. One of the primary causes of gas migration or stray gas is related to the upper portion of the wellbore when it is drilled into a rock formation that contains preexisting high-pressure gas. This high-pressure gas can have deleterious effects on the integrity of the outer cement annulus, such as the creation of microchannels (36). Temperature surveys can be performed shortly after the cementing job is completed in order to ensure that cement is present behind the casing. Acoustic logging tools are also available to evaluate the integrity of the cement annulus in conjunction with pressure testing.

It is well known that to effectively stabilize wellbores with cement in areas with zones of overpressurized gas, proper cement design and proper mud removal are essential (37, 38). If the hydrostatic pressure of the cement column is not higher than the gas-bearing formation pressure, gas can invade the cement before it sets. Conversely, if this pressure is too high, then the formation can fracture, and a loss of cement slurry can occur. Even when the density is correct, the gas from the formation can invade the cement as it transitions from a slurry to a hardened state (39). The slurry must be designed to minimize this transition time and the loss of fluid from the slurry to the formation. Also, if drilling mud is not properly cleaned from the hole before cementing, mud channels may allow gas migration through the central portion of the annulus or along the cement-formation interface. Even if the well is properly cleaned and the cement is placed properly, shrinkage

of the cement during hydration or as a result of drying throughout the life of the well can result in crack development within the annulus (40, 41).

Although the primary mechanisms contributing to gas migration and stray gas are understood, it is difficult to predict the risk at individual sites because of varying geological conditions and drilling practices. To successfully protect fresh water and the surrounding environment from the contaminants inside the well, the site-specific risk factors contributing to gas migration and stray gas must be better understood, and improvements in the diagnostics of cement and casing integrity are needed for both new and existing wells. Finding solutions to these problems will provide environmental agencies the knowledge needed to develop sound regulations related to the distances around gas wells that can be affected. It will also provide operators the ability to prevent gas migration and stray gas in a more efficient and economical manner.

The Source and Fate of Fracturing Fluid

The drilling and hydraulic fracturing of a single horizontal well in the Marcellus Shale may require 2 million to 7 million gallons of water (42). In contrast, only about 1 million gallons are needed for vertical wells because of the smaller formation contact volume. Although the projected water consumption for gas extraction in the Marcellus Shale region is 18.7 million gallons per day in 2013 (39), this constitutes just 0.2% of total annual water withdrawals in Pennsylvania. Water withdrawals in other areas are similarly low, but temporary problems can be experienced at the local level during drought periods (3). Furthermore, water quantity issues are prevalent in the drier shale-gas plays of the southwest and western United States (43). It is likely that water needs will change from these initial projections as the industry continues to improve and implement water reuse. Nevertheless, the understanding of flow variability—especially during drought conditions or in regions with already stressed water supplies—is necessary to develop best management practices for water withdrawal (44). It is also necessary to develop specific policies regarding when and where water withdrawals will be permitted in each region (45).

After hydraulic fracturing, the pressure barriers such as frac plugs are removed, the wellhead valve is opened, and “flowback water” is collected at the wellhead. Once the well begins to produce gas, this water is referred to as “produced water” and is recovered throughout the life of the well. Flowback and produced waters are a mixture of injected fluids and water that was originally present in the target or surrounding formations (formation water) (42, 46–50). The fraction of the volume of injected water that is recovered as flowback water from horizontal wells in Pennsylvania ranges from 9 to 53% (9, 41), with an average of 10%. It has been observed that the recovery can be even lower than 10% if the well is shut-in for a period of time (51). The well is shut-in—or maintained closed between fracturing and gas production—so as to allow the gas to

move from the shale matrix into the new fractures. Two of the key unanswered questions is what happens to the fracturing fluid that is not recovered during the flowback period, and whether this fluid could eventually contaminate drinking water aquifers (23, 33, 34, 52–54). The analyses of Marcellus Shale well logs indicate that the low-permeability shale contains very little free water (55, 56), and much of the hydraulic fracturing fluid may imbibe (absorb) into the shale.

Fracturing fluid could migrate along abandoned and improperly plugged oil and gas wells, through an inadequately sealed annulus between the wellbore and casing or through natural or induced fractures outside the target formation. Indeed, out-of-formation fractures have been documented to extend as much as ~460 m above the

top of some hydraulically fractured shales (57), but still ~1.6 km or more below freshwater aquifers. Nonetheless, on the basis of the study of 233 drinking-water wells across the shale-gas region of rural Pennsylvania, Boyer *et al.* (33) reported no major influences from gas well drilling or hydrofracturing on nearby water wells. Compared with the pre-drilling data reported in that study, only one well showed changes in water quality (salt concentration). These changes were noticed within days after a well was hydrofractured less than ~460 m away, but none of the analytes exceeded the standards of the U.S. Safe Drinking Water Act, and nearly all the parameters approached pre-drilling concentrations within 10 months.

In the case of methane contamination in groundwater near Dimock, Pennsylvania, contamination

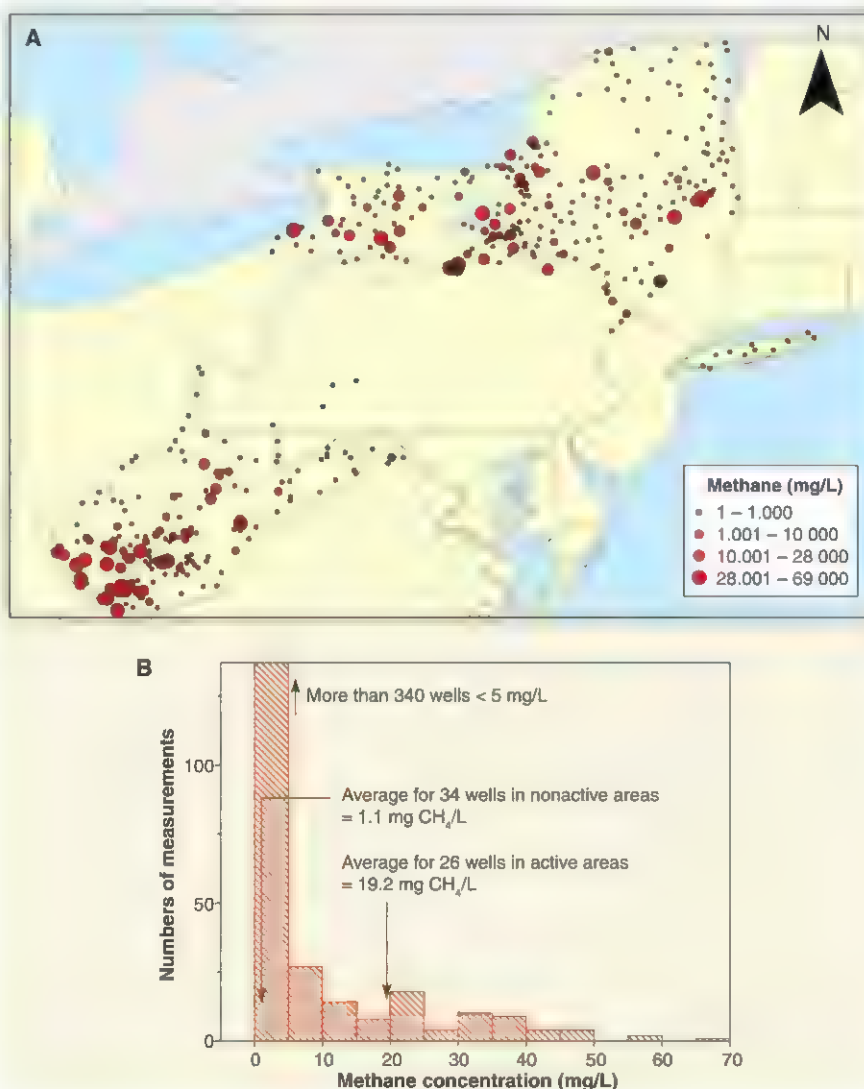


Fig. 2. Methane concentrations in groundwater and springs. (A) Published values for groundwater or spring samples include 239 sites in New York from 1999 to 2011 (84), 40 sites in Pennsylvania in 2005 (27), and 170 sites in West Virginia from 1997 to 2005 (85). Maxima varied from 68.5 mg/L in West Virginia, to 44.8 mg/L in Tioga County, Pennsylvania, where an underground gas storage field was leaking, to a value approaching 45 mg/L in New York. (B) Values shown with down arrows are averages for a set of wells in southeastern New York and northeastern Pennsylvania located <1 km (26 wells) and >1 km (34 wells) from active gas drilling (20).

by saline flowback brines or fracturing fluids was not observed (20). One early U.S. Environmental Protection Agency (EPA) report (54) suggested that a vertically fractured well in Jackson County, West Virginia, may have contaminated a local water well with gel from fracturing fluid. This vertical well was fractured at a depth of just ~1220 m, and four old natural gas wells nearby may have served as conduits for upward contaminant transport. A recent EPA study (53) implicated gas production wells in the contamination of deep groundwater resources near Pavillion, Wyoming. However, resampling of the monitoring wells by the USGS showed that the flowrate was too small to lend confidence to water-quality interpretations of one well, leaving data from only one other well to interpret with respect to contamination, and regulators are still studying the data (58). The Pavillion gas field consists of 169 production wells into a sandstone (not shale) formation and is unusual in that fracturing was completed as shallow as 372 m below ground. In addition, surface casings of gas wells are as shallow

as 110 m below ground, whereas the domestic and stock wells in the area are screened as deep as 244 m below ground. The risk for direct contaminant transport from gas wells to drinking-water wells increases dramatically with a decrease in vertical distance between the gas well and the aquifer.

A recent study applied a groundwater transport model to estimate the risk of groundwater contamination with hydraulic fracturing fluid by using pressure changes reported for gas wells (52). The study concluded that changes induced by hydraulic fracturing could allow advective transport of fracturing fluid to groundwater aquifers in <10 years. The model includes numerous simplifications that compromise its conclusions (59). For example, the model is based on the assumption of hydraulic conductivity that reflects water-filled voids in the geological formations, and yet many of the shale and overburden formations are not water-saturated (60). Hence, the actual hydraulic conductivity in the field could be orders of magnitude lower than that assumed

in the study (59). Furthermore, although deep joint sets or fractures exist (14), the assumption of preexisting 1500-m long vertical fractures is hypothetical and not based on geologic exploration. Hence, there is a need to establish realistic flow models that take into account heterogeneity in formations above the Marcellus Shale and realistic hydraulic conductivities and fracturing conditions.

Last, it has long been known (14, 34, 47, 48, 61, 62) that groundwater is salinized where deeper ancient salt formations are present within sedimentary basins, including basins with shale gas. Where these brines are present at relatively shallow depths, such as in much of the northeastern and southwestern United States and Michigan, brines sometimes seep to the surface naturally and are unrelated to hydraulic fracturing. An important research thrust should focus on understanding these natural brine transport pathways to determine whether they could represent potential risk for contamination of aquifers because of hydraulic fracturing.

Appropriate Wastewater Management Options

The flowback and produced water from the Marcellus Shale is the second saltiest (63) and most radiogenic (50) of all sedimentary basins in the United States where large volume hydraulic fracturing is used. The average amount of natural gas-related wastewater in Pennsylvania during 2008 to 2011 was 26 million barrels per year (a fourfold increase compared with pre-Marcellus period) (64). Compared with conventional shallow wells, Marcellus Shale wells generate one third of the wastewater per unit volume of gas produced (65). However, the wastewater associated with Marcellus development in 2010 and 2011 accounted for 68 and 79%, respectively, of the total oil and gas wastewater requiring management in Pennsylvania. Flowback/produced water is typically impounded at the surface for subsequent disposal, treatment, or reuse. Because of the large water volume, high concentration of dissolved solids, and complex physical-chemical composition of this wastewater, which includes organic and radioactive components, the public is becoming increasingly concerned about management of this water and the potential for human health and environmental impacts associated with the release of untreated or inadequately treated wastewater to the environment (66). In addition, spills from surface impoundments (14) and trucks or infiltration to groundwater through failed liners are potential pathways for surface and groundwater contamination by this wastewater.

Treatment technologies and management strategies for this wastewater are constrained by regulations, economics of implementation, technology performance, geologic setting, and final disposal alternatives (67). The majority of wastewater from oil and gas production in the United States is disposed of effectively by deep underground injection (68). However, the state of Pennsylvania has only five operating Class II disposal wells. Although underground injection disposal wells will likely increase in number in Pennsylvania, shale gas development is currently occurring

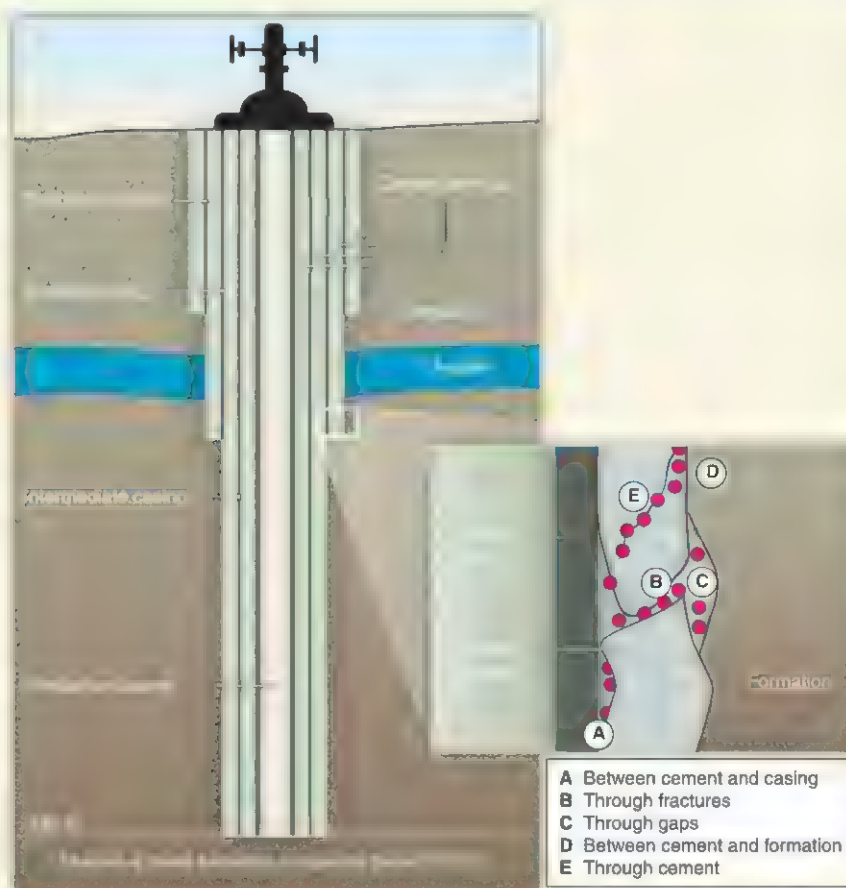


Fig. 3. Typical Marcellus well construction. (i) The conductor casing string forms the outermost barrier closest to the surface to keep the upper portion of the well from collapsing and it typically extends less than 12 m (40 ft) from the surface; (ii) the surface casing and the cement sheath surrounding it that extend to a minimum of 15 m below the lowest freshwater zone is the first layer of defense in protecting aquifers; (iii) the annulus between the intermediate casing and the surface casing is filled with cement or a brine solution; and (iv) the production string extends down to the production zone (900 to 2800 m), and cement is also placed in the annulus between the intermediate and production casing. Potential flaws in the cement annulus (Inset, "A" to "E") represent key pathways for gas migration from upper gas-bearing formations or from the target formation.

in many areas where Class II disposal wells will not be readily available. Moreover, permissions for and construction of new disposal wells is complex, time-consuming, and costly. Disposal of Pennsylvania brines in Ohio and West Virginia is ongoing but limited by high transportation costs.

The lack of disposal well capacity in Pennsylvania is compounded by rare induced low-magnitude seismic events at disposal wells in other locations (69–71). It is likely that the disposal of wastewater by deep-well injection will not be a sustainable solution across much of Pennsylvania. Nonetheless, between 1982 and 1984, Texas reported at most ~100 cases of confirmed contamination of groundwater from oilfield injection wells, saltwater pits, and abandoned wells, even though at that time the state hosted more than 50,000 injection wells associated with oil and gas (72). Most problems were associated with small, independent operators. The ubiquity of wells and relative lack of problems with respect to brine disposal in Texas is one likely explanation why public pushback against hydraulic fracturing is more limited in Texas as compared with the northeastern United States.

Another reason for public pushback in the northeast may be that in the early stages of Marcellus Shale development, particularly in 2008 to 2009, flowback/produced water was discharged and diluted into publicly owned treatment works (POTWs, or municipal wastewater treatment plants) under permit. This practice was the major pathway for water contamination because these POTWs are not designed to treat total dissolved solids (TDS), and the majority of TDS passed directly into the receiving waterways (6, 73), resulting in increased salt loading in Pennsylvania rivers, especially during low flow (74). In response, the Pennsylvania DEP introduced discharge limits to eliminate disposal of Marcellus Shale wastewater to POTWs (75). In early 2010, there were 17 centralized waste treatment plants (CWTs) in Pennsylvania that were exempted from the TDS discharge limits. However, according to Pennsylvania DEP records none of these CWTs reported to be currently receiving Marcellus wastewater, although they may receive produced water from conventional gas wells. Nevertheless, the TDS load to surface waters from flowback/produced water increased from ~230,000 kg/day in 2006 to 350,000 kg/day in 2011 (64).

It is difficult to determine whether shale gas extraction in the Appalachian region since 2006 has affected water quality regionally, because baseline conditions are often unknown or have already been affected by other activities, such as coal mining. Although high concentrations of Na, Ca, and Cl will be the most likely ions detected if flowback or produced waters leaked into waterways, these salts can also originate from many other sources (76). In contrast, Sr, Ba, and Br are highly specific signatures of flowback and produced waters (34, 47). Ba is of particular interest in Pennsylvania waters in that it can be high in sulfate-poor flowback/produced waters but low in sulfate-containing coal-mine drainage. Likewise,

the ratio of $^{87}\text{Sr}/^{86}\text{Sr}$ may be an isotopic fingerprint of Marcellus Shale waters (34, 77).

Targeting some of these “fingerprint” contaminants, the Pennsylvania DEP began a new monitoring program in 2011. Samples are collected from pristine watersheds as well as from streams near CWT discharges and shale-gas drilling. The Shale Network is collating these measurements with high-quality data from citizen scientists, the USGS, the EPA, and other entities in order to assess potential water quality impacts in the northeast (78, 79). Before 2003, mean concentrations in Pennsylvania surface waters in counties with unconventional shale-gas development were 27 ± 32 , 550 ± 620 , and 72 ± 81 $\mu\text{g/L}$ for Ba, Sr, and Br ($\pm 1\sigma$), respectively (Fig. 4). Most values more than 3σ above the mean concentrations since 2003 represent samples from areas of known brine effluents from CWTs. A concern has been raised over bromide levels in the Allegheny River watershed that may derive from active CWTs because of health effects associated with disinfection by-products formed as a result of bromide in drinking water sources (64, 80). Given the current regulatory climate and the fact that the majority of dissolved solids passes through these CWTs, it is expected that these treatment facilities will likely not play a major role in Marcellus Shale wastewater management.

The dominant wastewater management practice in the Marcellus Shale region nowadays is wastewater reuse for hydraulic fracturing [a review of Pennsylvania DEP data for the first 6 months of 2012 indicates 90% reuse rate (81)]. Wastewater is impounded at the surface and used directly, or after dilution or pretreatment. Reuse of wastewater minimizes the volume that must be treated and disposed, thus reducing environmental control costs and risks and enhancing the economic feasibility of shale-gas extraction (67). Currently, operators in the Marcellus region do not fully agree about the quality of wastewater that must be attained for reuse. Major concerns include possible precipitation of BaSO_4 and, to a lesser extent, SrSO_4 and CaCO_3 in the shale formation and the wellbore and the compatibility of wastewater with chemicals that are added to the fracturing fluid (such as friction reducers and viscosity modifiers). Hence, a better understanding of chemical compatibility issues would greatly improve the ability to reuse wastewater and minimize disposal volumes. In addition, radioactive radium that is commonly present in flowback/produced water will likely be incorporated in the solids that form in the wastewater treatment process and could yield a low-concentration radioactive waste that must be handled appropriately and has potential on-site human health implications.

The wastewater reuse program represents a somewhat temporary solution to wastewater management problems in any shale play. This program works only as long as there is net water consumption in a given well field. As the well field matures and the rate of hydraulic fracturing diminishes, the field becomes a net water producer because

the volume of produced water will exceed the amount of water needed for hydraulic fracturing operations (82, 83). It is not yet clear how long it will take to reach that point in the Marcellus region, but it is clear that there is a need to develop additional technical solutions (such as effective and economical approaches for separation and use of dissolved salts from produced water and treatment for naturally occurring radioactive material) that would allow continued development of this important natural resource in an environmentally responsible manner. Considering very high salinity of many produced waters from shale gas development, this is truly a formidable challenge. Research focused on better understanding of where the salt comes from and how hydrofracturing might be designed to minimize salt return to the land surface would be highly beneficial.

Conclusions

Since the advent of hydraulic fracturing, more than 1 million hydraulic fracturing treatments have been conducted, with perhaps only one documented case of direct groundwater pollution resulting from injection of hydraulic fracturing chemicals used for shale gas extraction (54). Impacts from casing leakage, well blowouts, and spills of contaminated fluids are more prevalent but have generally been quickly mitigated (17). However, confidentiality requirements dictated by legal investigations, combined with the expedited rate of development and the limited funding for research, are substantial impediments to peer-reviewed research into environmental impacts. Furthermore, gas wells are often spaced closely within small areas and could result in cumulative impacts (5) that develop so slowly that they are hard to measure.

The public and government officials are continuing to raise questions and focus their attention on the issue of the exact composition of the hydrofracturing fluid used in shale formations. In 2010, the U.S. House of Representatives directed the EPA to conduct a study of hydraulic fracturing and its impact on drinking-water resources. This study will add important information to account for the fate of hydraulic fracturing fluid injected into the gas-bearing formation. It is well known that a large portion (as much as 90%) of injected fluid is not recovered during the flowback period, and it is important to document potential transport pathways and ultimate disposition of the injected fluid. The development of predictive methods to accurately account for the entire fluid volume based on detailed geophysical and geochemical characteristics of the formation would allow for the better design of gas wells and hydraulic fracturing technology, which would undoubtedly help alleviate public concerns. Research is also needed to optimize water management strategies for effective gas extraction. In addition, the impact of abandoned oil and gas wells on both fluid and gas migration is a concern that has not yet been adequately addressed.

Gas migration received considerable attention in recent years, especially in certain parts of the Appalachian basin (such as northeast Pennsylvania).

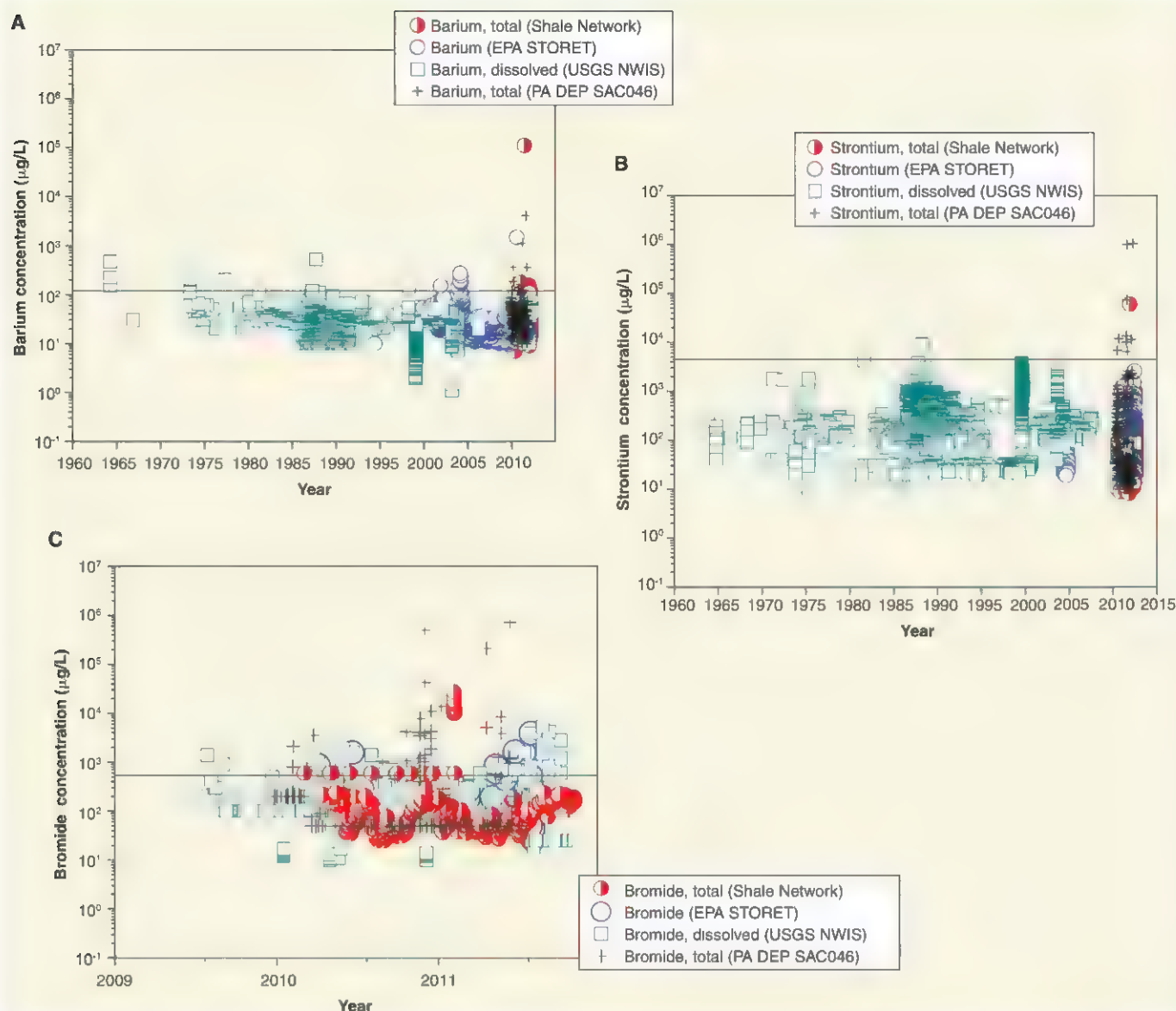


Fig. 4. Concentrations of three ions in surface waters of Pennsylvania in counties with unconventional shale-gas wells: (A) barium, (B) strontium, and (C) bromide. Data reported by EPA (STORET data), USGS (NWIS data), Susquehanna River Basin Commission, Appalachian Geological Consulting and ALLARM [from Shale Network database (78, 79)], and from the Pennsylvania DEP (SAC046) include all rivers, streams, ponds, groundwater drains, lysimeter waters, and mine-associated pit, seep, and discharge waters accessed by using HydroDesktop (www.cuahsi.org) in the relevant counties (data before 2009 for bromide are not shown). Lines indicate 3σ above the mean of data from 1960 to 2003 for the longest duration dataset (USGS). Most values above the lines

since 2003 represent targeted sampling in areas of known brine effluents from conventional oil and gas wells (such as Blacklick Creek receiving brine effluent from a CWT). The highest plotted Ba concentration was measured in Salt Springs in northern Pennsylvania. Three of the four samples with highest Sr and Br are from Blacklick Creek; next highest is from Salt Springs. Original values reported beneath the detection limit are plotted at that limit (10 to 100 μg Sr/L; 10 μg Ba/L; and 10 to 200 μg Br). The EPA maximum contaminant level (MCL) for Ba is 2000 $\mu\text{g/L}$. EPA reports no MCL for Sr or Br. Lifetime and 1-day health advisory levels for Sr are 4000 and 25000 $\mu\text{g/L}$, respectively, and a level under consideration for Br is 6000 $\mu\text{g/L}$.

It has been known for a long time that methane migrates from the subsurface (such as coal seams, glacial till, and black shales), and the ability to ignite methane in groundwater from private wells was reported long before the recent development of the Marcellus Shale (14). However, in the absence of reliable baseline information, it is easy to blame any such incidents on gas extraction activities. It is therefore critical to establish baseline conditions before drilling and to use multiple

lines of evidence to better understand gas migration. It is also important to improve drilling and cementing practices, especially through gas-bearing formations, in order to eliminate this potential pathway for methane migration.

Water management for unconventional shale gas extraction is one of the key issues that will dominate environmental debate surrounding the gas industry. Reuse of flowback and produced water for hydraulic fracturing is currently address-

ing the concerns regarding the vast salt quantities that are brought to the surface (each Marcellus well generates as much as 200 tons of salt during the flowback period). However, there is a need for comprehensive risk assessment and regulatory oversight for spills and other accidental discharges of wastewater to the environment. As these well fields mature and the opportunities for wastewater reuse diminish, the need to find alternative management strategies for this wastewater

will likely intensify. Now is the time to work on these issues in order to avoid an adverse environmental legacy similar to that from abandoned coal mine discharges in Pennsylvania.

References and Notes

- U.S. Energy Information Administration, "Annual Energy Outlook 2013, Early Release" (U.S. Department of Energy, 2013); available at www.eia.gov/forecasts/aeo/erindex.cfm.
- S. H. Ditch, K. Perry, J. Lee, "Unconventional Gas Reservoirs—Tight Gas, Coal Seams, and Shales, Working Document of the National Petroleum Council on Global Oil and Gas Study" (National Petroleum Council, 2007).
- MIT, "The future of natural gas," <http://mitei.mit.edu/publications/reports-studies/future-natural-gas> (Massachusetts Institute of Technology, 2011).
- S. M. Olmstead, L. A. Muehlenbachs, J.-S. Shih, Z. Chu, A. J. Krupnick, *Proc. Natl. Acad. Sci. U.S.A.*, published online 11 March 2013. doi: 10.1073/pnas.1213871110
- T. Engelder, *Fort Worth Basin Oil Gas Mag.* **20**, 18 (2009).
- U.S. House of Representatives Committee of Energy and Commerce Minority Staff, "Chemicals used in Hydraulic Fracturing" (prepared for H. A. Waxman, E. J. Markey, D. DeGette, 2011).
- S. Entekhabi, M. Evans-White, B. Johnson, E. Hagenbuch, Rapid expansion of natural gas development poses a threat to surface waters. *Front. Ecol. Environ.* **9**, 503 (2011). doi: 10.1890/110053
- P. J. Drohan, M. Brittingham, *Soil Sci. Soc. Am. J.* **76**, 1696 (2012).
- Energy Information Administration, *Drilling Sideways—A Review of Horizontal Well Technology and Its Domestic Application*, DOE/EIA-TR-0565 (U.S. Department of Energy, Washington, DC, 1993).
- NYS DEC, "Draft Supplemental Generic Environmental Impact Statement on the Oil, Gas and Solution Mining Regulatory Program, Well Permit Issuance for Horizontal Drilling and High-Volume Hydraulic Fracturing to Develop the Marcellus Shale and Other Low-Permeability Gas Reservoirs" (New York State Department of Environmental Conservation, 2009).
- www.FracFocus.org.
- S. Hutson et al., *Geol. Surv. Circ.* **1268**, 1 (2004).
- A. W. Gorodt, Factors affecting the variability of stray gas concentration and composition in groundwater. *Environ. Geosci.* **19**, 17 (2012). doi: 10.1306/eg.120811101013
- S. S. Harrison, Evaluating system for ground-water contamination hazards due to gas-well drilling on the glaciated Appalachian plateau. *Ground Water* **21**, 689 (1983). doi: 10.1111/j.1745-6584.1983.tb01940.x
- K. K. Eltschlager, J. W. Hawkins, W. C. Ehler, F. J. Baldassare, "Technical measures for the investigation and mitigation of fugitive methane hazards in areas of coal mining" (U.S. Dept. of the Interior, Office of Surface Mining Reclamation and Enforcement, Pittsburgh, PA, 2001).
- K. M. Révész, K. J. Breen, F. J. Baldassare, R. C. Burruss, Carbon and hydrogen isotopic evidence for the origin of combustible gases in water-supply wells in north-central Pennsylvania. *Appl. Geochem.* **25**, 1845 (2010) doi: 10.1016/j.apgeochem.2010.09.011
- T. Cosidine, R. Watson, N. Cosidine, J. Martin, "Environmental Impacts during Marcellus Shale Gas Drilling: Causes, Impacts, and Remedies, Report 2012-1" (Shale Resources and Society Institute, State University of New York, Buffalo, 2012).
- Total count included violations 78.73A, 78.81D1 and D2, 78.83A and B, 78.83GRNDWTR, 78.83COALCSG, 78.84, 78.85, 78.86, and 207B. Wells with multiple violations were counted only once.
- PA DEP Office of Oil and Gas, "Oil and Gas Compliance Report, www.portal.state.pa.us/portal/server.pt?community/oil_and_gas_compliance_report/20299" (Pennsylvania Department of Oil and Gas, 2013).
- S. G. Osborn, A. Vengosh, N. R. Warner, R. B. Jackson, Methane contamination of drinking water accompanying gas-well drilling and hydraulic fracturing. *Proc. Natl. Acad. Sci. U.S.A.* **108**, 8172 (2011). doi: 10.1073/pnas.1100682108; pmid: 21555547
- R. B. Jackson, S. G. Osborn, N. R. Warner, A. Vengosh, "Responses to frequently asked questions and comments about the shale-gas paper by Osborn et al., June 15, 2011" (www.nicholas.duke.edu/cgc/FracFAQ6_15_11.pdf, 2012).
- S. C. Schon, Hydraulic fracturing not responsible for methane migration. *Proc. Natl. Acad. Sci. U.S.A.* **108**, E664 (2011).
- R. J. Davies, Methane contamination of drinking water caused by hydraulic fracturing remains unproven. *Proc. Natl. Acad. Sci. U.S.A.* **108**, E871 (2011).
- L. J. Moofsky, J. A. Connor, S. K. Farhat, A. S. Wylie Jr., T. Wagner, *Oil Gas Dev.* **109**, 54 (2011).
- C. D. Laughrey, F. J. Baldassare, *Am. Assoc. Pet. Geol. Bull.* **82**, 317 (1998).
- M. J. Whiticar, Carbon and hydrogen isotope systematics of bacterial formation and oxidation of methane. *Chem. Geol.* **161**, 291 (1999). doi: 10.1016/S0009-2541(99)00092-3
- G. Etiope, M. A. Drobniak, A. Schimmelmann, *Marine and Petroleum Geology*, <http://dx.doi.org/10.1016/j.marpetgeo.2013.02.009> (2013).
- K. J. Breen, K. Revesz, F. J. Baldassare, S. D. McAuley, "Natural gases in ground water near Tioga Junction, Tioga County, North-central Pennsylvania—Occurrence and use of isotopes to determine origins, 2005" (U.S. Geological Survey, Scientific Investigations Report Series 2007-5085, 2007).
- PA DEP, "Oil and Gas Well Drilling and Production in Pennsylvania" (Pennsylvania Department of Environmental Protection, PA DEP Fact Sheet, 2011).
- W. R. Gough, B. A. Waite, in *Water Resources in Pennsylvania: Availability, Quality, and Management*, S. K. Majumdar, E. W. Miller, R. R. Panizek, Eds. (Pennsylvania Academy of Science, 1990), pp. 384–398.
- IOGC, "Protecting our Country's Resources: The States' Case, Orphaned Well Plugging Initiative" (Interstate Oil and Gas Compact Commission, National Energy Technology Laboratory, 2008).
- S. G. Osborn, J. C. McIntosh, Chemical and isotopic tracers of the contribution of microbial gas in Devonian organic-rich shales and reservoir sandstones, northern Appalachian Basin. *Appl. Geochem.* **25**, 456 (2010). doi: 10.1016/j.apgeochem.2010.01.001
- E. W. Boyer, B. R. Swistock, J. Clark, M. Madden, D. E. Rizzo, "The impact of Marcellus gas drilling on rural drinking water supplies" (The Center for Rural Pennsylvania, Pennsylvania General Assembly, www.rural.palegislatore.us/documents/reports/Marcellus_and_drinking_water_2011_rev.pdf, 2012).
- N. R. Warner et al., Geochemical evidence for possible natural migration of Marcellus Formation brine to shallow aquifers in Pennsylvania. *Proc. Natl. Acad. Sci. U.S.A.* **109**, 11961 (2012). doi: 10.1073/pnas.1121181109; pmid: 22778445
- T. M. Kresse et al., *U.S.G.S. Scientific Investigations Report 2012-5273* (2012).
- G. Bol, H. Grant, S. Keller, F. Marcassa, J. de Rozieres, *Oilfield Rev.* **3**, 35 (1991).
- A. Bonnett, D. Pafitis, *Oilfield Rev.* **8**, 36 (1996).
- V. Gonzalo, B. Aiskely, C. Alicia, in *SPE Latin American and Caribbean Petroleum Engineering Conference, Society of Petroleum Engineers International* (Rio de Janeiro, Brazil, 2005).
- M. J. Rogers, R. L. Dillenbeck, R. N. Eid, *Society of Petroleum Engineers*, 90829 (2004).
- M. B. Dusseault, M. N. Gray, *Society of Petroleum Engineers*, 64733 (2000).
- J. M. Tinsley, E. C. Miller, D. L. Sutton, *Society of Petroleum Engineers*, 8257 (1979).
- T. D. Hayes, "Marcellus Shale water chemistry" (Appalachian Shale Water Conservation and Management Committee, 2009).
- J.-P. Nicot, B. R. Scanlon, Water use for Shale-gas production in Texas, U.S. *Environ. Sci. Technol.* **46**, 3580 (2012). doi: 10.1021/es204602t; pmid: 22385152
- D. Soeder, W. M. Kappell, "Water resources and natural gas production from the Marcellus Shale" (U.S. Geological Survey Fact Sheet 2009-3032, Reston, VA, 2009).
- B. G. Rahm, S. J. Riha, Toward strategic management of shale gas development: Regional, collective impacts on water resources. *Environ. Sci. Policy* **17**, 12 (2012). doi: 10.1016/j.envsci.2011.12.004
- E. Barbot, N. S. Vidic, K. B. Gregory, R. D. Vidic, Spatial and Temporal Correlation of Water Quality Parameters of Produced Waters from Devonian-Age Shale following Hydraulic Fracturing. *Environ. Sci. Technol.* **47**, 2562 (2013). doi: 10.1021/es304638h; pmid: 23425120
- L. O. Haluszczak, A. W. Rose, L. R. Kump, Geochemical evaluation of flowback brine from Marcellus gas wells in Pennsylvania, USA. *Appl. Geochem.* **28**, 55 (2013). doi: 10.1016/j.apgeochem.2012.10.002
- P. E. Dresel, A. W. Rose, Pennsylvania Geological Survey, 4th series Open File Report OFOG 10-01.0, www.dcnr.state.pa.us/topogeo/pub/openfile/ofog10_01.aspx (2010), p. 48.
- M. E. Blau, R. R. Myers, T. R. Moore, B. A. Lipinski, N. A. Houston, paper presented at the SPE Eastern Regional Meeting, Society of Petroleum Engineers SPE 125740, Charleston, WV, 2009.
- E. L. Rowan, M. A. Engle, C. S. Kirby, T. F. Kraemer, "Radium content of oil- and gas-field produced waters in the Northern Appalachian Basin (USA): Summary and discussion of data" (U.S. Geological Survey, Scientific Investigation Report 2011-5135, 2011).
- M. E. Mantell, in *EPA Hydraulic Fracturing Study Technical Workshop 4. Water Resources Management, Chesapeake Energy* (Oklahoma City, OK, 2011).
- T. Myers, Potential contaminant pathways from hydraulically fractured shale to aquifers. *Ground Water* **50**, 872 (2012). doi: 10.1111/j.1745-6584.2012.00933.x; pmid: 22509908
- D. C. DiGiulio, R. T. Wilkin, C. Miller, G. Oberly, "DRAFT: Investigation of Ground Water Contamination near Pavilion, Wyoming" (U.S. Environmental Protection Agency Office of Research and Development, 2011).
- U.S. Environmental Protection Agency, "Report to Congress: Management of wastes from the exploration, development, and production of crude oil, natural gas, and geothermal energy" (U.S. Environmental Protection Agency, Washington, DC, 1987).
- T. Engelder, in *GSA Annual Meeting and Exposition* (Charlotte, NC, 2012); available at <https://gsa.confex.com/gsa/2012AM/webprogram/Paper207549.html>.
- T. Engelder, Capillary tension and imbibition sequester fluid in Marcellus gas shale. *Proc. Natl. Acad. Sci. U.S.A.* **109**, E3625 (2012). doi: 10.1073/pnas.1216133110
- K. Fisher, N. Warpinski, *SPE Prod. Oper.* **27**, 8 (2012).
- P. R. Wright, P. B. McMahon, D. K. Mueller, M. L. Clark, "Groundwater-Quality and Quality-Control Data for Two Monitoring Wells near Pavilion, Wyoming, April and May 2012" (U.S.G.S. Data Series 718, http://pubs.usgs.gov/ds/718/DS718_508.pdf, 2012).
- J. E. Saiers, E. Barth, Potential contaminant pathways from hydraulically fractured shale aquifers. *Ground Water* **50**, 826, discussion 828 (2012). doi: 10.1111/j.1745-6584.2012.00990.x; pmid: 23003107
- K. R. Bruner, R. A. Smosna, "Comparative study of the Mississippian Barnett Shale, Fort Worth Basin, and Devonian Marcellus Shale, Appalachian Basin, DOE/NETL-2011/1478" (Department of Energy, National Energy Technology Laboratory, 2011).
- C. W. Poth, *Pennsylvania Geol. Surv. Bull.* **447**, 1 (1962).
- J. A. Williams, *U.S. Geological Survey Scientific Investigations Report 2010-5224* (2010).
- US DOE, "Cost-Effective Recovery of Low-TDS Frac Flowback Water for Re-use" (U.S. Department of Energy, www.netl.doe.gov, 2011).
- J. M. Wilson, J. M. VanBriesen, *Environ. Pract.* **14**, 288 (2012). doi: 10.1017/S1466046612000427
- B. D. Lutz, A. N. Lewis, M. W. Doyle, Generation, transport, and disposal of wastewater associated with Marcellus Shale gas development. *Water Resour. Res.* **49**, 647 (2013). doi: 10.1002/wrcr.20096
- D. M. Kargbo, R. G. Wilhelm, D. J. Campbell, Natural gas plays in the Marcellus Shale: challenges and potential opportunities. *Environ. Sci. Technol.* **44**, 5679 (2010). doi: 10.1021/es903811p; pmid: 20518558
- K. B. Gregory, R. D. Vidic, D. A. Dzombak, Water Management Challenges Associated with the Production of Shale Gas by Hydraulic Fracturing. *Elements* **7**, 181 (2011). doi: 10.2113/gselements.7.3.181

68. C. E. Clark, J. A. Veil, "Produced Water Volumes and Management Practices in the United States, ANL/EVS/R-09/1" (Environmental Science Division, Argonne National Laboratory, 2009).
69. C. J. de Pater, S. Baisch, "Geomechanical study of Bowland Shale seismicity, Synthesis Report" (Cuadrilla Resources, Ltd., 2011).
70. Reuters, "Ohio earthquake was not a natural event, expert says," *Reuters*, 2012.
71. National Academy of Sciences, *Induced Seismicity Potential in Energy Technologies* (National Academies Press, Washington, DC, 2012).
72. Texas Department of Agriculture, "Agricultural Land and Water Contamination from Injection Wells, Disposal Pits, and Abandoned Wells Used in Oil and Gas Production" (TX Department of Agriculture, Department of Natural Resources, 1985).
73. K. J. Ferrar *et al.*, *Environmental Science & Technology*, dx.doi.org/10.1021/es301411q (2013).
74. D. J. Rozell, S. J. Reaven, Water pollution risk associated with natural gas extraction from the Marcellus Shale *Risk Anal.* **32**, 1382 (2012). doi: 10.1111/j.1539-6924.2011.01757.x; pmid: 22211399
75. PA DEP, "Wastewater Treatment Requirements, 25 PA Code 95" (Pennsylvania Department of Environmental Protection, 2010).
76. J. R. Mullaney, D. L. Lorenz, A. D. Arntson, "Chloride in Groundwater and Surface Water in Areas Underlain by the Glacial Aquifer System, Northern United States" (U.S. Department of the Interior, U.S. Geological Survey, Scientific Investigations Report 2009-5086, 2009).
77. E. C. Chapman *et al.*, Geochemical and strontium isotope characterization of produced waters from Marcellus Shale natural gas extraction. *Environ. Sci. Technol.* **46**, 3545 (2012). doi: 10.1021/es204005g; pmid: 22360406
78. S. L. Brantley, C. Wuderman, J. Abad, Workshop discusses database for Marcellus water issues *Eos Trans. AGU* **93**, 328 (2012). doi: 10.1029/2012EO340006
79. Shale Network database is accessible through HydroDesktop (www.cuahsi.org).
80. S. States *et al.*, paper presented at the AWWA WQTC, Phoenix, AZ, November 13 to 17, 2011.
81. K. O. Maloney, D. A. Yoxheimer, Production and Disposal of Waste Materials from Gas and Oil Extraction from the Marcellus Shale Play in Pennsylvania. *Environ. Pract.* **14**, 278 (2012). doi: 10.1017/S146604661200035X
82. C. Kuijvenhoven *et al.*, paper presented at the Shale Gas Water Management Conference, Dallas, TX, November 30 to December 1, 2011.
83. R. D. Vidic, T. D. Hayes, S. Hughes, in *Shale Gas Water Management Marcellus Initiative* (Pittsburgh, PA, 2011).
84. W. M. Kappell, E. A. Nystrom, Dissolved methane in New York groundwater, 1999–2011. U.S. Geological Survey Open File Report 2012-1162 (2012); available at <http://pubs.usgs.gov/of/2012/1162>.
85. J. S. White, M. V. Mathes, "Dissolved-gas concentrations in ground water in West Virginia" (U.S. Geological Survey Data Series 156, 2006).

Acknowledgments: R.D.V., S.L.B., D.Y., and J.D.A. acknowledge funding for the Shale Network from NSF grant OCE-11-40159.

10.1126/science.1235009

Stem Cell Lawsuit Finally Over. Russian Team Retrieves First Sample from Lake Vostok. Surprise Choices Mark New Leadership on U.S. House Science Panel. India Unveils Ambitious Science Policy.



Now, more than ever, developments in the lab are directly connected to decisions made in the halls of government.

*Science*Insider, the policy blog from the journal *Science*, is your source for news from the intersection of science and policy. From budget debates in the United States Congress, to climate change agreements at the United Nations, *Science*Insider covers the issues that have an impact on your work, your field, and your world.

Keep up to date and keep informed. Go inside the issues at www.ScienceInsider.org



ScienceInsider

Breaking news and analysis from the world of science policy



Soft-Chemistry–Based Routes to Epitaxial α -Quartz Thin Films with Tunable Textures

A. Carretero-Genevri¹, M. Gich², L. Picas³, J. Gazquez², G. L. Drisko¹, C. Boissiere¹, D. Grosso¹, J. Rodriguez-Carvajal⁴, C. Sanchez^{1*}

Piezoelectric nanostructured quartz films of high resonance frequencies are needed for microelectronic devices; however, synthesis methods have been frustrated by the inhomogeneous crystal growth, crystal twinning, and loss of nanofeatures upon crystallization. We report the epitaxial growth of nanostructured polycrystalline quartz films on silicon [Si(100)] substrates via the solution deposition and gelation of amorphous silica thin films, followed by thermal treatment. Key to the process is the combined use of either a strontium (Sr^{2+}) or barium (Ba^{2+}) catalyst with an amphiphilic molecular template. The silica nanostructure constructed by cooperative self-assembly permits homogeneous distribution of the cations, which are responsible for the crystallization of quartz. The low mismatch between the silicon and α -quartz cell parameters selects this particular polymorph, inducing epitaxial growth.

Quartz, the second most abundant mineral in Earth's crust after feldspar, is massively mined for industrial use in the form of sands and gravels for glassmaking,

abrasion, foundry, and hydraulic fracturing. Highly processed monocrystalline quartz plates are desired for a range of high-value applications such as microelectronics and telecommunications.

Owing to its piezoelectricity with a high quality factor, quartz is the material of choice for oscillators in electronic devices and transducers for mass sensors widely used in chemistry and biology (1–7). Quartz has other appealing properties, including optical activity, birefringence, high hardness, a remarkable chemical durability, and light transparency from the vacuum ultraviolet to near-infrared and in the THz regions of the electromagnetic spectrum (8, 9). Electronic-grade quartz is currently synthesized by a multistep top-down approach through the accurate cutting and polishing of large crystals grown in autoclaves via a long hydrothermal process developed by Spezia more than 100 years ago (10). To obtain thinner oscillators with higher resonance frequencies, an additional cumbersome process of shaping and

¹Laboratoire Chimie de la Matière Condensée, UMR UPMC–Collège de France–CNRS 7574, Collège de France, 11 Place Marcelin Berthelot, 75231 Paris, France. ²Institut de Ciència de Materials de Barcelona ICMAB, Consejo Superior de Investigaciones Científicas CSIC, Campus UAB 08193 Bellaterra, Catalonia, Spain. ³U1006 INSERM, Parc Scientifique de Luminy, F-13009, Marseille, France. ⁴Institut Laue-Langevin, 6 rue Jules Horowitz, BP 156, 38042 Grenoble Cedex 9, France.

*Corresponding author. E-mail: clement.sanchez@college-de-france.fr

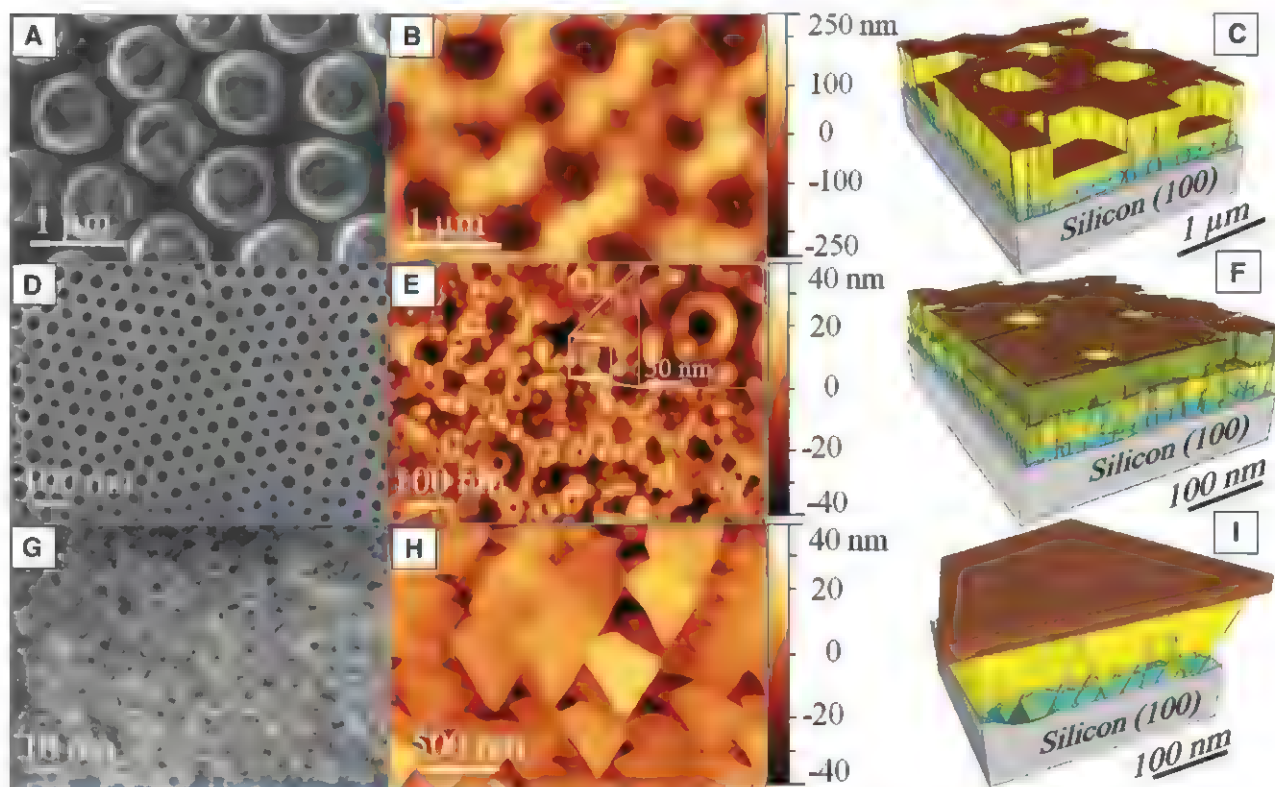


Fig. 1. Representative images showing the heteroepitaxial growth of α -quartz thin films on Si(100) via sol-gel chemistry. FEG-SEM images highlighting the different pore size obtained on amorphous silica films: macroporous (A) ~600 nm and mesoporous with an average pore of (D) ~40 nm and (G) ~3 nm. AFM images (center) display the crystallized nanostructured quartz thin films with different pore sizes: (B) macroporous (one-pot synthetic route), (E) mesoporous, and (H) dense film (two-step synthetic route). The right

panel presents schematic diagrams showing a 3D model of the different nanostructured quartz films obtained: the (C) macroporous, (F) mesoporous, and (I) dense films. Brown indicates the upper face of the porous quartz film, yellow the side face, blue the nucleation points for the quartz, and gray the silicon substrate. In the case of large mesoporous quartz film, a dense quartz layer is beneath the initial mesoporous (40-nm pore size) sol-gel layer (see fig. S3 for more details). Sr^{2+} and Ba^{2+} deposits were removed by chemical etching.

integration is performed. This is needed to get faster device operation, higher frequency filtering, and transducers with lower detection levels and improved sensitivity (11).

To overcome the complex and expensive procedures described above, sol-gel chemistry with an adapted processing technique (microfabrication, chemical solution deposition, spraying, etc.) appears as a straightforward approach to design advanced functional materials with perfect control over their structures and textures (12–16). Despite numerous efforts, monodispersed quartz nanoparticles have only very recently been synthesized in high yield from the crystallization of amorphous silica colloids prepared by the Stöber method under hydrothermal conditions (17, 18). Earlier publications reported the importance of precise control over synthesis conditions (choice of precursors, catalysts, thermal treatment, humidity, and processing technique) for the preparation of single-silica polymorph from amorphous silica (19–23). In another approach, epitaxial dense quartz films were achieved, but on nonsilicon substrates, by chemical vapor deposition (24), and by thermal evaporation in ultrahigh vacuum (25–27). A direct and simple fabrication of quartz nanomaterials on silicon substrates has not yet been developed, and efforts have mostly focused on exploring bottom-up routes (28, 29).

Here, by taking advantage of all the benefits of soft chemistry, we report a procedure to prepare macroporous, mesoporous, and dense epitaxial α -quartz thin films on silicon wafers. Thermally activated crystallization of structured amorphous silica films was assisted by Sr^{2+} - or Ba^{2+} -mediated heterogeneous catalysis under atmospheric conditions. Sr^{2+} and Ba^{2+} depress the silica melting point, promoting devitrification at lower temperatures, and thus facilitate oxygen diffusion, as previously observed for bulk alkaline earth-doped glassy materials (21–23). The crystallographic orientation of the silicon substrate selects only the α -quartz polymorph and controls individual crystallites size, morphology, and orientation. Evaporation-induced phase separation and template agents self-assembly were used to generate controlled porosities in the initial amorphous films that were retained upon crystallization. The combination of soft chemistry and epitaxial growth opens opportunities for the controlled design of textured crystalline solids attractive for further integration of functional oxides on the Si (100) substrate (30).

Experimental Approach

Two protocols were used for generating α -quartz thin films with controlled textures. A prerequisite is the homogeneous distribution of the catalyst-melting agent within the amorphous silica films before thermal treatment. A one-pot approach used a hydro-alcoholic solution containing cetyltrimethylammonium bromide (CTAB) surfactant, tetraethoxysilane silica precursor, and Sr^{2+} salt (31). Dip-coating deposition on a (100) silicon wafer produces a film presenting a periodical two-dimensional (2D) array of homogeneously

sized macrodomains, promoted by an evaporation-induced phase separation, tuned by the surface active agent, and accompanied by the precipitation of the strontium salt (32, 33). Because of the fast evaporation kinetics, a proportion of the catalyst is trapped within the silica-CTAB mesophase. The macrostructure characteristics were faithfully retained in the final α -quartz. Scanning electron microscopy (SEM) images display circular macropores of around 700-nm diameter in a close-packaged distribution (Fig. 1 and fig. S2), which exist both before and after heating between 900° and 1000°C. In a second two-step approach, Sr^{2+} was incorporated by simple infiltration into previously prepared mesoporous silica layers. Matrix templating was engineered through the evaporation induced self-assembled method (34) using poly(butadiene-ethylene oxide) (PB-PEO) diblock copolymer and Brij-56 surfactants for obtaining mesopores of 40 and 3.5 nm, respectively, as evidenced by field emission gun-SEM (FEG-SEM) images in Fig. 1 and fig. S2. Whereas large mesopores are retained upon crystallization, the small ones collapse, leading to dense α -quartz films. Although in the case of 40-nm porous films, the size and shape are maintained, the global morphology is slightly modified. The partial structural collapse is due to quartz nucleation and growth followed by diffusive sintering of the crystalline domains. Both results confirm that a minimum curvature of close to 40 nm can be accommodated by the α -quartz crystals, which are themselves on the order of a few tens of nanometers in lateral dimensions. The presence of mesopores has been

verified by ellipsometry: A refractive index of 1.38 ± 0.02 ($\lambda = 700$ nm) was measured for the PB-PEO-based film (porosity of 23 volume %). On the other hand, the high density of the Brij-templated α -quartz film was confirmed by its refractive index of 1.52 ± 0.02 ($\lambda = 700$ nm) (close to the refractive index of α -quartz single crystal, 1.54). At this point, one must bear in mind that porous α -quartz films lie on a dense bed of α -quartz [evidenced by ellipsometry and FEG-SEM (Fig. 1, C and F; Fig. 3; and figs. S3 and S6)], whose origin will be explained below.

Crystal Growth Mechanism

Irrespective of the synthetic approach, all systems exhibit mono-oriented α -quartz crystals. The homogeneous dispersion of the Sr^{2+} catalyst within the amorphous silica matrix and the low mismatch between the (100)_Q quartz plane and the crystalline (100)_S Si substrate induce the nucleation of α -quartz crystals at the silicon-silica interface (Fig. 2). Other polymorphs of silica do not show a comparable mismatch, so the formation of α -quartz is epitaxially selected by the substrate. The active influence of the silicon substrate mediates the preferential orientation of crystal nuclei, yielding typical competitive growth and producing a columnar microstructure with preferential crystallographic orientation (35) (Fig. 2). In a competitive growth process, crystal aggregates normally grow from randomly oriented seeds that compete for the available space. Only those with the fastest growth perpendicular to the substrate are selected and contribute to the outer surface (36).

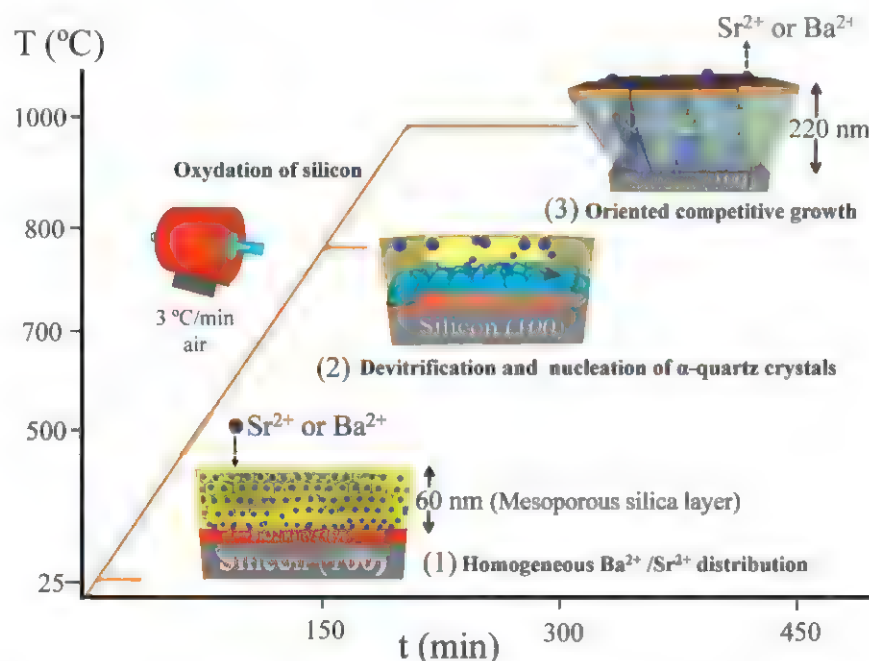


Fig. 2. Scheme of the stages of the crystallization process. 1. Cross section of the original mesoporous film showing homogeneous $\text{Ba}^{2+}/\text{Sr}^{2+}$ distribution within the amorphous silica matrix. 2. Nucleation above 800°C of α -quartz crystals at the silicon-silica interface during the devitrification of the original amorphous mesoporous film. 3. Oriented columnar quartz crystallite growth within the original (100) silicon substrate, where crystallization is limited by the oxygen diffusion. Catalyst agents (Sr^{2+} or Ba^{2+} , blue spheres), used for the devitrification of silica films, migrate to the surface and remain trapped at the crystal boundaries (see fig. S10 for more details).

In our case, we have epitaxially induced nucleation. Quartz crystals with the orientation imposed by the $(100)_S$ silicon substrate, which is parallel to the $[100]_Q^*$ reciprocal direction, or equivalently the $[210]_Q$ direction of α -quartz crystals in real space, will succeed over those that do not have such orientation. Minimum thickness of amorphous silica is needed for nucleation and growth. In the case of dense layers, single crystals with atomically flat terraces and trapezoidal habits are observed in the atomic force microscopy (AFM) image of Fig. 1H.

For dense films, silicon oxidation and, consequently, quartz film growth is limited by oxygen diffusion, as nicely illustrated by the parabolic dependence observed in the thickness increment of quartz films as a function of the duration of thermal treatments (fig. S5). Quartz film thickness can thus be precisely controlled by engineering the original thickness of the SiO_2 sol-gel layer. This oxidation process is responsible for the growth of a dense sublayer under the mesoporous and macroporous α -quartz, as shown in figs. S3 and S6 and illustrated

in Fig. 1, C and E, and Fig. 3. This suggests that the growth of α -quartz takes place at the silicon/quartz interface. Moreover, the analysis of quartz films by backscattered electrons SEM, z-contrast transmission electron microscopy (TEM), and energy electron-loss spectroscopy (fig. S10) revealed that the crystallization process brings about a $\text{Sr}^{2+}/\text{Ba}^{2+}$ depletion that is expelled to the surface of the film, where it forms hemispherical droplets lodged at the crystal boundaries. The rounded shape of these surface deposits suggests a solid dewetting (Fig. 2). The catalyst can be removed using chemical etching with concentrated nitric acid (Fig. 1, E and H).

All final films contain thinner euhedral macro domains of several tens of microns with defined edges, as observed by FEG-SEM and AFM images in Fig. 3, A to C, and figs. S3 and S4. Their long axis is parallel to either the $[100]_S$ or to the $[010]_S$ direction of the silicon substrate. The formation mechanism of the macro domains schematized in the lower panel of Fig. 3 and fig. S3 is related to a break in the continuity of polycrystal-

line quartz films. This break results from the difference of thermal expansion coefficients and the relatively higher mismatch along the $[010]_Q$ crystallographic direction between the quartz film and the silicon substrate. Upon film growth, stresses eventually reach a critical value that cannot be counterbalanced by the adhesion. The formation of cracks relaxes internal stresses in the film, as observed in step 2 (Fig. 3 and fig. S4). Thickness variations observed in AFM profile analysis (Fig. 3, C and E) and cross-sectional FEG-SEM images (fig. S6) of euhedral macro domains reveal that the center of the domains is at the same level as the surrounding continuous layer, which then progressively decreases toward the edge of the domain. The differences in height suggest a lower growth rate at the fracture boundaries than at the center of the euhedral domains. This observation could be explained by stress-dependent oxygen diffusion rates associated with local stress relaxation at Si/quartz interfaces, where the reaction takes place (Fig. 3 and fig. S6). Local stresses are

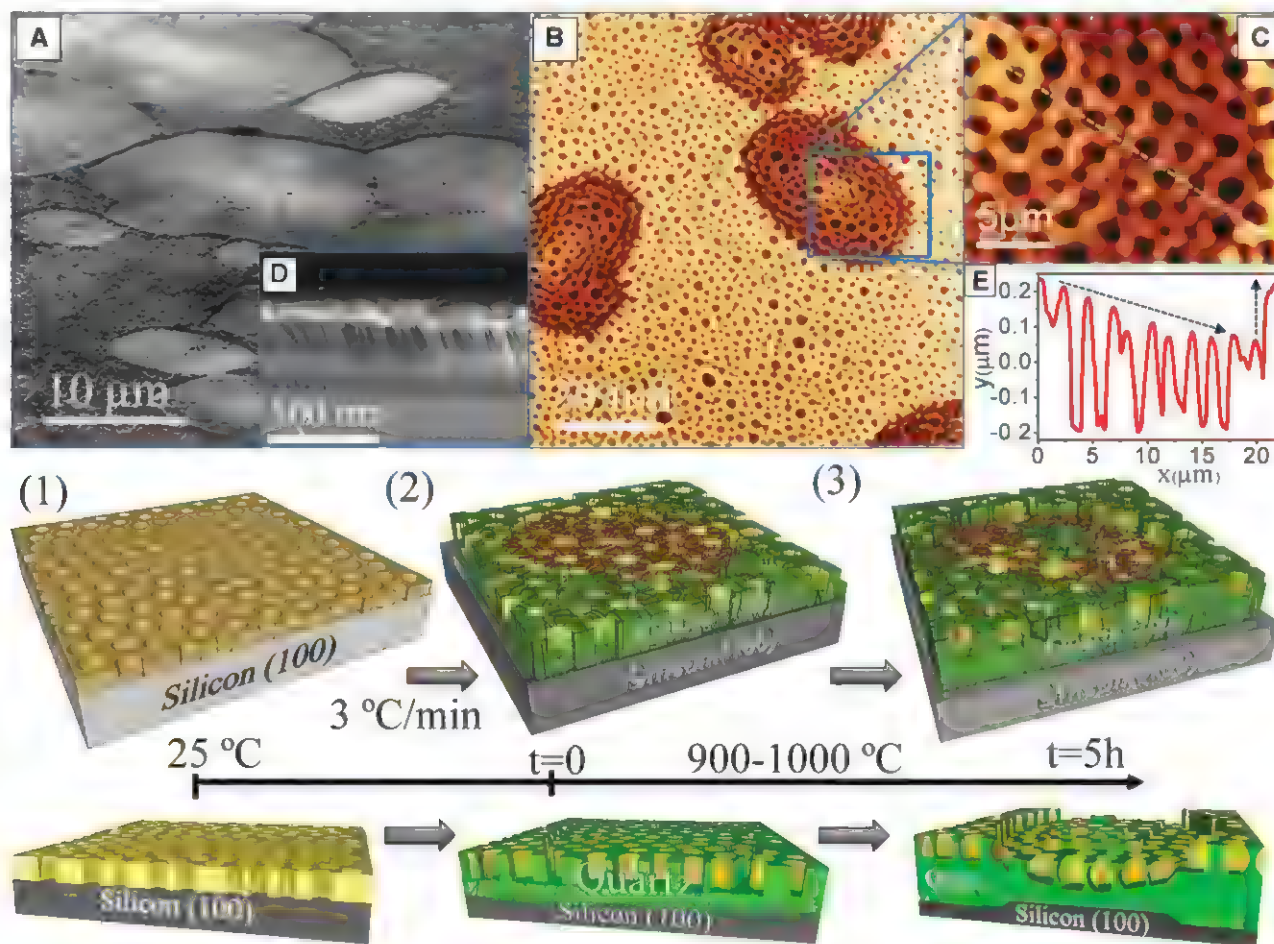


Fig. 3. Crystallization process of quartz films of macroporous silica matrix. (A) FEG-SEM 45°-tilted image showing the macrostructure of a large area in macroporous quartz thin film with euhedral polycrystalline quartz overgrowth with defined edges. (D) FEG-SEM image inset displaying a cross-sectional view of the microstructure in the macroporous quartz thin film. (B) AFM images showing a large scan area of macroporous quartz films. (C and E) Higher magnification and profile analysis of macrodomain facets revealing the thickness variation and a break in the

continuity of polycrystalline quartz films after 5 hours at $>900^\circ\text{C}$. The lower panel presents a schematic of the formation mechanism of quartz macro domains: the macroporous silica matrix on a silicon substrate at room temperature (1), crystallization of quartz films at $900\text{--}1000^\circ\text{C}$ ($t = 0$) and formation of cracks that relax internal stresses within the film (2). Green and brown colors have been used to indicate differences in quartz depth profile. Formation of thinner euhedral macro domains of several tens of microns with defined edges at high temperature (3).

known to induce strong differences in oxygen diffusion rates in metal oxides films (37).

Microstructural and Piezoelectric Characterization

The crystallographic orientation, epitaxial relationship, and microstructure of α -quartz thin films were analyzed through x-ray diffraction (XRD) scans and TEM cross-section analysis. XRD Θ -2 Θ scans (Fig. 4A) of the film displayed in Fig. 1B present only representative (100) and (200) reflections of α -quartz. Peaks corresponding to other quartz orientations or silica polymorphs are completely absent. The (100) film texture was further characterized through a ω scan showing a rocking curve (Fig. 4B) with a full width at half-maximum (FWHM) of 3°, indicating low out-of-plane misorientation of nanostructured α -quartz films. Additionally, pole figures of the Si{111} and α -quartz {010} and {101} reflections (Fig. 4C) confirm that the growth of α -quartz on Si(100) was epitaxial. The Si(111) pole is found 45° apart in azimuth from the (101)_Q and (010)_Q poles of α -quartz, indicating that the in-plane epitaxial relationship is quartz(010)/Si(010) and quartz(001)/Si(001). The presence of additional poles at the same tilt as the α -quartz poles for {010} and {101}, but at 90° rotation in azimuth, supports the existence of two α -quartz domains perpendicular to each other with identical epitaxial relationships with the substrate, which is permitted by the symmetry of the Si(100) surface. According to the (100) out-of-plane texture and the in-plane epitaxial relationships, represented in a 3D schematic model in Fig. 4D, it can be concluded that $[210]_Q/[100]_S$ is the quartz growth direction. An identical epitaxial relationship was confirmed for mesoporous and dense quartz films.

Natural quartz crystals have been found to occur in a large number of habits and growth forms that share a certain number of common characteristics. AFM analyses of the synthetically grown dense quartz films were performed to determine the specific forms and habits of the crystals (Fig. 5D). AFM evaluation of film surfaces, such as that displayed in Fig. 1H and fig. S2L, reveal a planar trapezohedron (100)_Q crystal face of quartz. The angles between the edges of the planar trapezoidal (100)_Q facets of a large quartz crystal are in good agreement with the angles calculated from our experimental data (Fig. 5D). The formation of twinned crystals during thermal treatment of samples, which is detrimental to the piezoelectricity, was not observed after evaluation of the pole figures. We conclude that only the $[100]_Q$ crystalline direction is present without detectable parasitic orientation.

Cross sections of several specimens of quartz films were observed by high-resolution TEM (HRTEM) along different zone axes. The observation of quartz-substrate interfaces confirms the (100)_Q orientation and the high-quality epitaxial growth of quartz thin films on Si(100) substrates. HRTEM images along [001], [011], and [010] zone axes are displayed in Fig. 5, A and B, and fig. S7, B and D. The corresponding fast Fourier

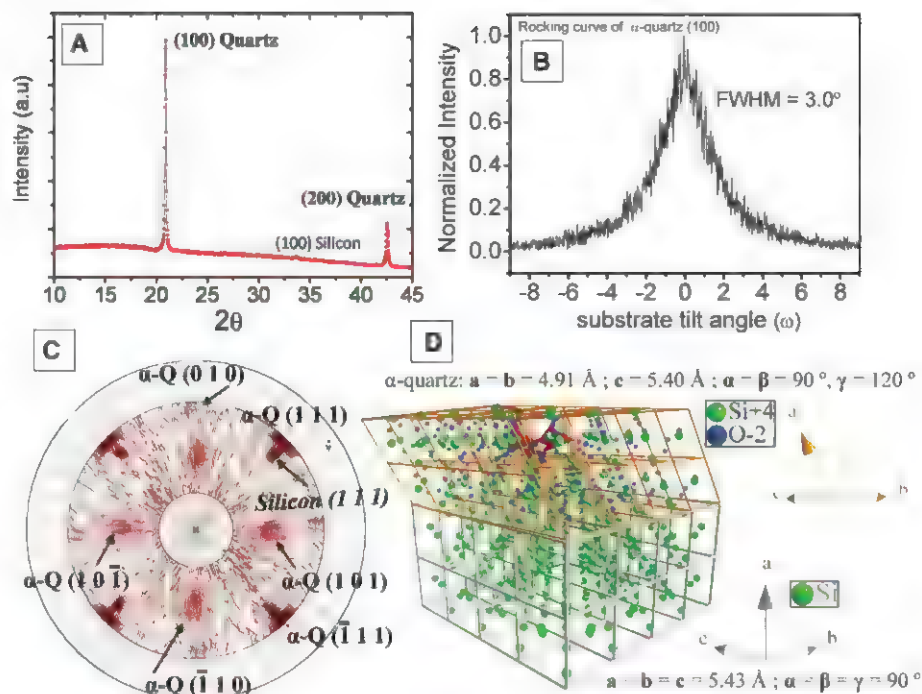


Fig. 4. Structural characterization of quartz films. (A to C) XRD Θ -2 Θ scan (A), rocking curve (B), and pole figure (C) of macroporous quartz films. (D) 3D model of the in-plane epitaxial relationship between the quartz film (in orange) and the silicon substrate (in gray) viewed along the [011] zone axis.

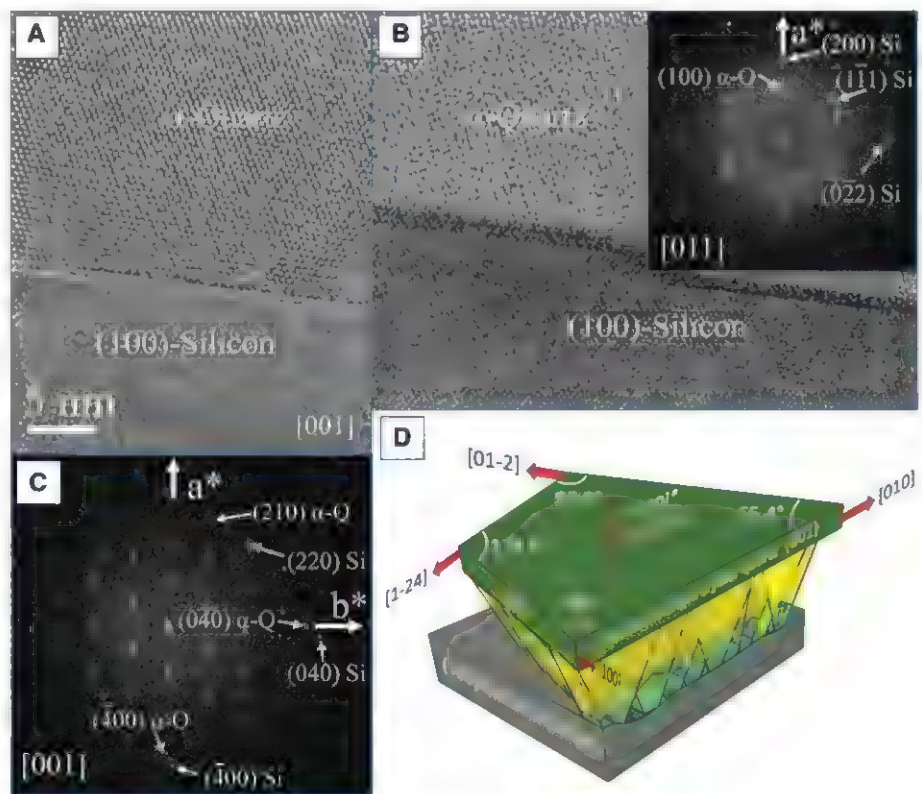


Fig. 5. Fine structural characterization of quartz films. (A and B) HRTEM images of the α -quartz-Si interface along [001] (A) and [011] (B) α -quartz zone axis. FFTs of (A) and (B) are shown in (C) and the inset of (B), respectively. The film and substrate spots are set apart, confirming the relaxation of the film. (D) Schematic representation of a quartz habit, displaying the macroscopic measured angles between the planar edges of quartz crystals and crystallographic directions that define the trapezoidal (100)_Q facets.

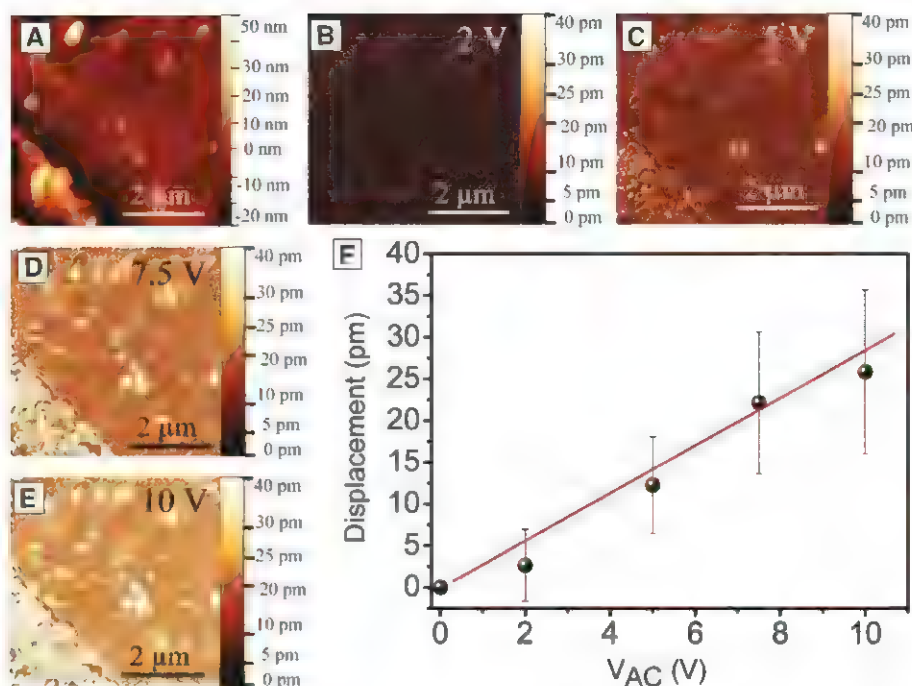


Fig. 6. Piezoelectric activity of quartz films. (A) AFM image of the topography and oscillating amplitudes obtained for the same film region under different tip-substrate voltages: (B) 2 V, (C) 5 V, (D) 7.5 V, and (E) 10 V. (F) The graph shows the linear dependence between the applied voltage and the mean deflection, reflecting the converse piezoelectric effect.

transform (FFT) patterns corroborate the epitaxial relationship previously established by XRD analyses and show that quartz films are epitaxially grown despite the relatively large lattice mismatch between b lattice parameters of both structures: $(b_{\text{SiO}_2} - b_{\text{Si}})/b_{\text{Si}} = -9\%$. Moreover, the splitting of the film and substrate FFT spots confirms the relaxation of the film (Fig. 5, A to C, and insert). It is worth noting that no trace of amorphous silica is observed at the interface; rather, HRTEM images reveal a sharp interface.

The largest piezoelectric response of α -quartz is observed along the $[100]_Q$ direction that, in our films, is at 30° normal from the substrate. Thus, we measured the piezoelectric effect by applying either a mechanical deformation (direct effect) or an electric field (converse effect) perpendicularly to the film. The direct load method (38) was used to detect the charging of a capacitor connected between the substrate and a rod-shaped electrode, which occurred when the latter exerted a pressure and elastically deformed the films (fig. S8). The converse piezoelectric effect was studied by piezoresponse force microscopy (39). Figure 6 shows images of the topography (Fig. 6A) and the cantilever oscillation amplitudes (Fig. 6, B to E) resulting from film surface displacements at the frequency of different AC voltages applied to the tip. The cantilever oscillation amplitude provides information about the film deformation and, as expected for the converse piezoelectric effect, is proportional to the applied voltage (Fig. 6F). From the slope of this curve, we can estimate the piezoelectric coefficient relating the strain to the electric field in the direction perpendicular to be

between 1.5 and 3.5 pm/V, which is in reasonable agreement with the 2.3 pm/V of the quartz d_{11} .

Finally, our synthetic approach based on sol-gel chemistry provides ready access and flexible production of textured piezoelectric thin films of low α -quartz, epitaxially grown on Si(100) substrates. Heating under atmospheric pressure in combination with strontium or barium (fig. S9) assists quartz nucleation and growth, making this approach deployable for large-scale production. Pore curvature as low as 40 nm is accommodated by the quartz nanocrystallites. Both the chemistry (i.e., templating agents and precursors) and processing (combining bottom-up and top-down nanofabrication techniques) can be incorporated into this process to engineer materials (12, 14). Finally, our work opens new avenues in the fields of sensors and information technologies through the fabrication of novel resonators, strain-coupled devices, or elements of THz optics.

References and Notes

1. J. Krim, D. H. Solina, R. Chiarello, *Phys. Rev. Lett.* **66**, 181 (1991).
2. M. V. Voinova, M. Jonson, B. Kasemo, *Biosens. Bioelectron.* **17**, 835 (2002).
3. C. Fredriksson, S. Kihlman, M. Rodahl, B. Kasemo, *Langmuir* **14**, 248 (1998).
4. C. A. Keller, B. Kasemo, *Biophys. J.* **75**, 1397 (1998).
5. R. Schumacher, *Angew. Chem. Int. Ed. Engl.* **29**, 329 (1990) [New Analytical Methods (40)].
6. S. Berg, M. Ruths, D. Johannsmann, *Rev. Sci. Instrum.* **74**, 3845 (2003).
7. L. Spassov, D. Y. Yankov, *Rev. Sci. Instrum.* **65**, 721 (1994).
8. P. Shumyatsky, R. R. Alfano, *J. Biomed. Opt.* **16**, 033001 (2011).
9. D. Doling, *J. Phys. Chem. Solids* **40**, 121 (1979).
10. F. Iwasaki, H. Iwasaki, *J. Cryst. Growth* **237–239**, 820 (2002).
11. A. Laschitsch, D. Johannsmann, *J. Appl. Phys.* **85**, 3759 (1999).

12. Y. Xia, G. M. Whitesides, *Annu. Rev. Mater. Sci.* **28**, 153 (1998).
13. C. Boissiere, D. Grosso, A. Chaumonnot, L. Nicole, C. Sanchez, *Adv. Mater.* **23**, 599 (2011).
14. C. Sanchez, C. Boissiere, D. Grosso, C. Laberty, L. Nicole, *Chem. Mater.* **20**, 682 (2008).
15. C. J. Brinker, G. W. Scherer, *Sol-Gel Science: The Physics and Chemistry of Sol-Gel Processing* (Academic Press, San Diego, ed. 1, 1990).
16. D. Grosso, *J. Mater. Chem.* **21**, 17033 (2011).
17. M. Okabayashi, K. Miyazaki, T. Kono, M. Tanaka, Y. Toda, *Chem. Lett.* **34**, 58 (2005).
18. X. Jiang, Y. B. Jiang, C. J. Brinker, *Chem. Commun.* **47**, 7524 (2011).
19. X. Jiang et al., *Chem. Commun.* **48**, 1293 (2012).
20. P. Bruhns, R. X. Fischer, *Eur. J. Mineral.* **12**, 615 (2000).
21. A. M. Venezia, V. La Parola, A. Longo, A. Martorana, *J. Solid State Chem.* **161**, 373 (2001).
22. V. G. Pol, A. Gedanken, J. Calderon-Moreno, *Chem. Mater.* **15**, 1111 (2003).
23. D. C. Altamirano-Juarez et al., *J. Phys. Chem. Solids* **62**, 1911 (2001).
24. N. Takahashi et al., *Chem. Mater.* **15**, 2889 (2003).
25. M. S. Chen, A. K. Santra, D. W. Goodman, *Phys. Rev. B* **69**, 155404 (2004).
26. M. Kundu, Y. Murata, *Appl. Phys. Lett.* **80**, 1921 (2002).
27. Z. Zhang et al., *Thin Solid Films* **516**, 3741 (2008).
28. L. Zhao et al., *Adv. Funct. Mater.* **17**, 1952 (2007).
29. S. Kar, S. Chaudhuri, *Solid State Commun.* **133**, 151 (2005).
30. D. Ito, N. Fujimura, T. Yoshimura, T. Ito, *J. Appl. Phys.* **93**, 5563 (2003).
31. Materials and methods are available as supplementary materials on Science Online.
32. P. Innocenzi, L. Malfatti, G. Solder-Ilia, *Chem. Mater.* **23**, 2501 (2011).
33. B.-L. Su, C. Sanchez, X.-Y. Yang, *Hierarchically Structured Porous Materials: From Nanoscience to Catalysis, Separation, Optics, Energy, and Life Science* (Wiley-VCH, Weinheim, 2011).
34. C. J. Brinker, Y. Lu, A. Sellinger, H. Fan, *Adv. Mater.* **11**, 579 (1999).
35. J. G. A. Rodriguez-Navarro, *Eur. J. Mineral.* **12**, 609 (2000).
36. D. P. Grigorov, *Ontogeny of Minerals* (IFST, Jerusalem, 1965).
37. M. Kubicek et al., *ACS Nano* **7**, 3276 (2013).
38. K. Lefki, G. J. M. Dormans, *J. Appl. Phys.* **76**, 1764 (1994).
39. J. A. Christman, R. R. Woolcott, A. I. Kington, R. J. Nemanich, *Appl. Phys. Lett.* **73**, 3851 (1998).

Acknowledgments: A.C.-G. acknowledges the financial support from COMPOSOL2 (Fond Unique Interministeriel dans le cadre du 9eme AAP) and IMPC for use of FEG-SEM facilities. A.C.-G. and G.L.D. acknowledge the Collège de France Fondation for material and partial financial support. This study was made possible by grants from Beatriu de Pinós and Fondation Pierre-Gilles de Gennes to L.P. and from Marie Curie Reintegration (PCIG09-GA-2011-294168) to M.G. We thank S. Scheuring, D. Montero, and M. Selmane for technical support. The HRTEM microscopy work was conducted in Laboratorio de Microscopias Avanzadas at the Instituto de Nanociencia de Aragon-Universidad de Zaragoza (LMA INA). The authors acknowledge the LMA-INA for offering access to their instruments and expertise. J.G. is grateful to C. Magen for help at LMA-INA. We thank G. Catalán for valuable discussions concerning PFM and A. Pérez del Pino and A. Gomez for their technical assistance in the PFM measurements. This research was partially supported by the Spanish Government (projects MAT2012-35324, CONSOLIDER Nanoselect CSD2007-00041, and an RYC-2009-04335 contract to M.G. and a JAE-CSIC contract to J.G.). This research was supported in part by Oak Ridge National Laboratory's Shared Research Equipment (ShaRE) User Facility, which is sponsored by the Scientific User Facility Division, Office of Basic Energy Sciences, U.S. Department of Energy. This work has been accepted as patent deposit number FR1257101.

Supplementary Materials

www.sciencemag.org/cgi/content/full/340/6134/827/DC1
Materials and Methods
Figs. S1 to S10

19 November 2012; accepted 18 April 2013
10.1126/science.1232968

Rationally Designed Complex, Hierarchical Microarchitectures

Wim L. Noorduin,^{1*} Alison Grinthal,¹ L. Mahadevan,^{1,2,3,4} Joanna Aizenberg^{1,2,3,5*}

The emergence of complex nano- and microstructures is of fundamental interest, and the ability to program their form has practical ramifications in fields such as optics, catalysis, and electronics. We developed carbonate-silica microstructures in a dynamic reaction-diffusion system that allow us to rationally devise schemes for precisely sculpting a great variety of elementary shapes by diffusion of carbon dioxide (CO_2) in a solution of barium chloride and sodium metasilicate. We identify two distinct growth modes and show how continuous and discrete modulations in CO_2 concentration, pH, and temperature can be used to deterministically switch between different regimes and create a bouquet of hierarchically assembled multiscale microstructures with unprecedented levels of complexity and precision. These results outline a nanotechnology strategy for “collaborating” with self-assembly processes in real time to build arbitrary tectonic architectures.

Natural patterns and shapes arise in innumerable ways on a range of scales and have fascinated artists and scientists alike (1, 2). Hierarchical nano- and microarchitectures not only offer insight into how complex forms can emerge from simple starting materials, but also underlie coloration (3), wetting (4), mechanics (5), and other phenomena seen in nature and may transform optics (6), catalysis (7–9), building construction, and many other technologies if we can find ways to create them synthetically. Using top-down lithography techniques (10), we can directly write and sculpt three-dimensional (3D) patterns into a variety of materials, but at small scales this hands-on control translates into a laborious, costly, and often insufficient approach. Self-assembly from the bottom up can generate diverse patterns through a much more complex evolution of forces than we could ever apply by hand (11); however, ceding control over all but the starting materials leaves little opportunity to fine-tune structures or control stages of hierarchical development, let alone rationally design arbitrary architectures. Strategies inspired by biomineralization have been explored as potential routes to controlling growth and self-assembly from the molecular level via tailored microenvironments, epitaxy, and inorganic or organic additives (12–21). Yet although these strategies have produced some interesting spherical, spiral, leaflike, and other shapes (22–29), the appearance of various forms in synthetic systems is often unexpected and not usually based on predictive mechanisms.

The vast majority of efforts to apply biomineralization principles to synthetic strategies have, like most nanoscale self-assembly techniques, fo-

cused primarily on defining the initial conditions or solution composition. Although this approach has certainly yielded useful insights, it is obvious that many complex patterns emerge specifically in response to a dynamic environment. For example, abrupt switches in marine shell patterning have been attributed to changes in conditions during growth (1); at a larger scale, bacteria form hierarchically structured communities by chemotactically responding to continuously changing chemical cues (30). This perspective not only highlights a major source of complexity and hierarchy currently missing from synthetic strategies, but also suggests that we might be able to actively shape self-assembling structures by manipulating the environment as they grow. This possibility is espe-

cially compelling for systems that develop through reaction-diffusion processes, where dynamic feedback between the reaction front and the solution is the central mechanism of pattern evolution (31–35). Such feedback mechanisms are not only proposed to explain a variety of natural forms, but they can also generate patterned precipitation in synthetic systems (36). We therefore explore whether mineralized forms can be precisely sculpted and hierarchically assembled into novel, arbitrary architectures through dynamic, rationally programmed modulations of the reaction solution.

In this work, we demonstrate how the responsive growth of BaCO_3 - SiO_2 structures toward or away from the bulk solution can be exploited to program a variety of “elementary” growth patterns. We derive sequences of simple, subtle modulations of CO_2 , pH, and temperature that serve as building strategies for intricate, user-defined microstructures of higher order. With the use of continuous and/or stepwise adjustments, we steer the precipitating reactants via precise sculpting and sequential combinatorial assembly of the developing shapes.

Hypothesis for Structure Evolution in a Field of Chemical Gradients

Our strategy for dynamically modulating structure evolution is based on the idea that the developing structure will be continuously shaped by a complex spatial field of overlapping chemical gradients, created by the interplay between the bulk solution, the reaction front, and potentially neighboring structures. We analyze this

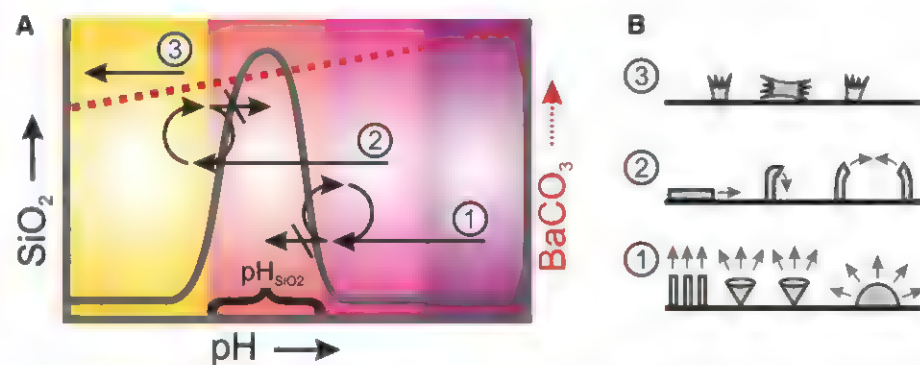


Fig. 1. Hypothesis for structure evolution in three growth regimes. Schematic representation of the rate of SiO_2 (37) (solid gray line) and BaCO_3 precipitation (dashed red line) in the range of pH ~8 to 12 (A) and anticipated shapes and growth directions (B) resulting from the three proposed growth regimes (see text for details). In all cases, growth will begin with the nucleation of BaCO_3 , which will lead to the local reduction of pH at the growth front. In regime 1, the associated pH drop brings the structures to the right side of the silica deposition range (denoted as pH_{SiO_2}), giving rise to the continuous coprecipitation of BaCO_3 and SiO_2 . The structures will grow most successfully away from one another and toward the solution where $\text{pH} > \text{pH}_{\text{SiO}_2}$, whereas other growth directions associated with lower pH become passivated by silica. Depending on the nucleation density, we expect the structures to “blossom” into stems, cones, and hemispherical shapes. In regime 2, the pH drop from carbonate deposition will lower the pH at the growth front to $\text{pH} < \text{pH}_{\text{SiO}_2}$, whereas the bulk solution remains more alkaline with $\text{pH} > \text{pH}_{\text{SiO}_2}$. In this case, any growth directions toward the higher pH bulk solution will cross the silica precipitation region and be blocked, such that the structures are expected to grow most successfully away from the solution, along the interface, or curl down and toward each other where pH remains below pH_{SiO_2} following the trail of produced acid. In regime 3, only BaCO_3 crystals are expected to form.

¹School of Engineering and Applied Sciences, Harvard University, Cambridge, MA 02138, USA. ²Wyss Institute for Biologically Inspired Engineering, Harvard University, Boston, MA 02115, USA. ³Kavli Institute for Bionano Science and Technology, Harvard University, Cambridge, MA 02138, USA. ⁴Department of Physics, Harvard University, Cambridge, MA 02138, USA. ⁵Department of Chemistry and Chemical Biology, Harvard University, Cambridge, MA 02138, USA.

*Corresponding author. E-mail: wnoord@seas.harvard.edu (W.L.N.); jaiz@seas.harvard.edu (J.A.)

growth process for the coprecipitation of SiO_2 and BaCO_3 in an alkaline aqueous solution containing Na_2SiO_3 and BaCl_2 , where precipitation is triggered by the diffusion of CO_2 . BaCO_3 deposition increases with increasing pH, whereas SiO_2 deposition takes place in a narrow, optimum pH_{SiO_2} range (Fig. 1A) (37), and mutual feedback between the two processes may create a reaction-diffusion scenario. We hypothesize that the pH-dependent feedback between BaCO_3 and SiO_2 deposition will lead to three distinct growth regimes, each with a characteristic set of morphologies, which can be evoked by small changes in the environment, as follows:

Regime 1) Starting with a high-pH bulk solution (region 1 in Fig. 1A), no silica deposition will take place, and the influx of CO_2 will trigger the precipitation of BaCO_3 , according to a simplified reaction: $\text{Ba}^{2+} + \text{CO}_2 + \text{H}_2\text{O} \rightarrow \text{BaCO}_3 + 2\text{H}^+$. The released H^+ will gradually lower the local pH at the growth front, until entering the pH range for silica precipitation, according to a simplified reaction: $\text{SiO}_3^{2-} + 2\text{H}^+ \rightarrow \text{SiO}_2 + \text{H}_2\text{O}$, which then shifts the reaction equilibrium and solubility back toward BaCO_3 precipitation, resulting in the continuous coprecipitation of BaCO_3 and SiO_2 (25). This sce-

nario will have several consequences for the developing structure: (i) Crystal growth will be passivated where silica precipitates, (ii) structures should grow most successfully toward the bulk solution where pH is above the range for silica deposition, and (iii) growth should be inhibited near the lowered pH of neighboring growth fronts. Depending on the nucleation density, different basic morphologies might then be expected: hemispheres at low nucleation densities, or cones and stem shapes at higher densities, where neighboring diffusion fields steer the structures away from each other toward regions of higher pH (Fig. 1B).

Regime 2) Lowering the initial bulk pH can generate a scenario in which the local pH is below the optimum pH for silica formation (pH_{SiO_2}), whereas the bulk pH is still above pH_{SiO_2} (region 2 in Fig. 1A). In this case, the local decrease in pH due to continuing BaCO_3 crystallization prevents, rather than promotes the formation of SiO_2 close to the growth front, whereas the influx of the bulk solution with $\text{pH} > \text{pH}_{\text{SiO}_2}$ brings the solution into the pH_{SiO_2} range and triggers the precipitation of SiO_2 that passivates growth. Structures will then be expected to grow most successfully away from the bulk solution, either along the interface to form

flat sheets or curling down and toward each other to preserve a low pH at the growth front (Fig. 1B).

Regime 3) If the pH of the bulk solution is below the pH_{SiO_2} range, only “normal” BaCO_3 structures should form (region 3, Fig. 1).

Testing Regime 1: Solution-Directed Growth of Stems, Vases, and Corals

As a first step toward testing the solution-dependent growth of structures in regime 1, we created a gradient of CO_2 concentrations by vertically positioning an aluminum plate or gold-coated glass substrate in a beaker containing an aqueous solution of BaCl_2 (19.1 mM) and Na_2SiO_3 (8.2 mM) at a pH of 11.8 and loosely covering the beaker to let CO_2 from the air diffuse into the system (Fig. 2A). The nucleation density of BaCO_3 , gradually decreases with depth, in accord with the decrease in CO_2 concentration. Within 2 hours, the nucleated BaCO_3 bundles develop into a dense forest of thin stems at the top of the substrate, where the CO_2 concentration is highest (Fig. 2A and fig. S1). At intermediate depths, the structures instead become vase-like and form coral-like hemispherical shapes toward the bottom. In all cases, the structures grow perpendicular to the substrate—that is, toward the bulk solution where $\text{pH} > \text{pH}_{\text{SiO}_2}$ —and veer away from each other. The basic morphologies and behavior are, thus, consistent with the solution-directed growth hypothesis proposed for regime 1. Yet at the same time, the intricate wall structures observed in the vases and corals provide another level of complexity within each of the basic shapes, supporting the idea that this growth mechanism also contains the seeds for more complex modulations.

Inspection by scanning electron microscopy (SEM) reveals that the walls have a constant thickness of $\sim 1 \mu\text{m}$, with a consistent thickening of stems and at the edges of the walls (Fig. 2B). The constant wall thickness suggests a 2D growth mechanism, in which precipitation merely occurs at the active top edges of the structures while being inhibited by silica at the sides. Selective dissolution of BaCO_3 using HCl (0.5 mol/L) leaves behind a hollow silica shell (fig. S2), further indicating that the silica mainly deposits on and selectively passivates the sides of the walls where the pH is lowest (Fig. 2C). This localized silica precipitation sets the thickness of the walls because the pH in the middle of the growth front is less buffered than closer to the sides where silica precipitation mainly occurs, allowing a new layer of BaCO_3 crystals to grow at the top of the walls. The increased thickness at the edges of the walls and stems is also consistent with solution-directed growth: These areas have a larger surface to accommodate the silica deposition, resulting in local thickening (Fig. 2B). The localized feedback also produces a uniform 2D growth front by dampening the formation of spontaneous protuberances. To directly demonstrate that the structures evolve toward the highest pH, we grew them in a continuous flow that increased the pH at the growth front using a microfluidic device. The

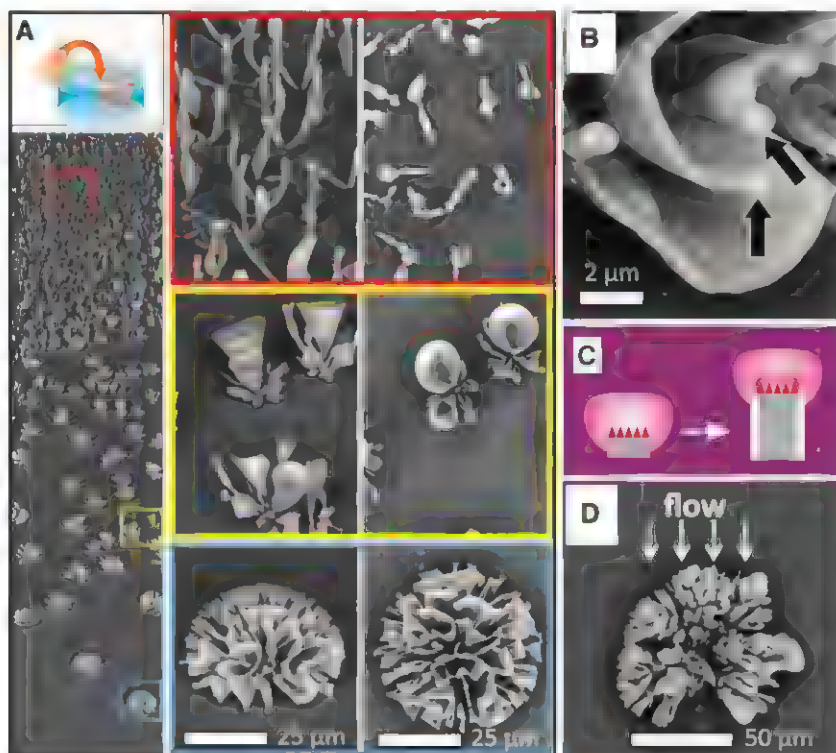


Fig. 2. Diversity of structures that grow in regime 1. (A) SEM image of a typical substrate vertically submerged in solution with an initial bulk pH of 11.8, showing a gradient of shapes (from top to bottom of the substrate: 1D stems, conical vases, and hemispherical coral-like structures). The enlarged side and top views of the structures in the red, yellow, and blue boxed regions are shown on the right. (B) High-magnification SEM image of a coral structure, showing the thickening of the sides of the walls (indicated by arrows). (C) Schematic of a 2D growth mechanism, in which the thickness of the walls and stems is fixed by the short-range buffering action of silica deposited on the walls (shown in white) that locally increases pH at the BaCO_3 growth front (the color scheme matches that in Fig. 1). (D) Top view of the coral structure grown in a flow in a microfluidic reactor. Directional growth toward the flow, where the pH is highest, is observed, consistent with the solution-directed growth behavior.

structures primarily grow against the flow along the interface (Fig. 2D), in the direction of the high-pH bulk solution.

This basic, relatively simple directed growth behavior thus enables both straightforward selection and continuous sculpting of the evolving structures into a diversity of well-controlled forms. For example, the wall thickness can be dynamically modulated by increasing and decreasing the flux of CO_2 . A temporary increase in CO_2 was imposed by opening the lid of the beaker, resulting in a thickening of the walls due to the increased carbonate deposition (Fig. 3A and fig. S3). This thickening occurs only at the growth edge, and the original wall and stem thickness is rapidly restored by the feedback mechanism when the lid is placed back on. As the growth rate is constant, we are able to use rhythmical fluctuations in the CO_2 concentration to produce well-defined series of ripples (Fig. 3B). This control over wall thickness further provides the means to prescribe the splitting and branching of the growth front. Specifically, if the wall thickness exceeds a critical size, the center of the growth front will not be sufficiently buffered by the silica deposition at the sides to continue growing, leading to a complete breakup of the growth front into new, separate growth fronts that branch away from each other (Fig. 3C). To reach such increased thicknesses, we performed experiments using SrCO_3 in place of BaCO_3 . SrCO_3 yields the same set of morphologies, but because its solubility is half that of BaCO_3 , a similar CO_2 pulse results in the precipitation of more carbonate and leads to a substantially greater thickening of the wall, inducing stems to open out into uniform vases (Fig. 3D). Perturbation of the thickness of the growth front by increased carbonate deposition can, thus, be swiftly restored to the original dimension by either slimming (Fig. 3A) or complete splitting of the front (Fig. 3C), depending on the precise magnitude of the perturbation.

In addition to directly modulating CO_2 or replacing BaCO_3 with SrCO_3 , the structures can also be finely sculpted by controlling the temperature or salt concentration of the bulk solution. Lowering the temperature provides an alternative means to increase the amount of available CO_2 , and we indeed observe a thickening of the walls (while preserving the overall shapes of the stems, vases, and corals) by simply cooling the solutions to 4°C (Fig. 3E). Adding NaCl increases the silica deposition rate (38) but leaves the BaCO_3 crystallization virtually unaffected (fig. S4). Again, this leads to a thickening of the walls to give similar structures, as shown in Fig. 3E. A variety of simple continuous modulations in the bulk solution can thus be used to dynamically steer the shape of the growing structures, allowing multiple levels of controlled sculpting.

Testing Regime 2: Further Diversity Through Inward-Directed Growth

When we shift to regime 2 by lowering the pH of the bulk solution to 11.2, we observe an entirely

different collection of shapes (Fig. 4A) (39). The basic shapes—including single and double spirals, as well as globular and leaflike structures—are consistent with the curling mode of growth and resemble those reported previously (25–28). In contrast to the pronounced gradient of structural variation observed in regime 1, here even a single set of bulk conditions gives rise to a tremendous diversity of forms that not only grow next to each other, but even appear together as part of composite structures. This diversity can be explained by considering how structures grow to avoid the passivating pH_{SiO_2} range: Whereas

in regime 1 the structures grow toward the bulk solution, where $\text{pH} > \text{pH}_{\text{SiO}_2}$, and away from neighbors, in regime 2 their growth appears inward, away from the bulk solution and toward their own and neighboring growth fronts, where $\text{pH} < \text{pH}_{\text{SiO}_2}$. In direct support of this mechanism, structures growing in a microfluidic reactor at pH 11.2 point away from the bulk solution (Fig. 4B), developing in the direction opposite that observed in regime 1 (Fig. 2D). This inward-directed growth can be expected to make the emerging shapes highly sensitive to small variations in local diffusion fields, driving a more intricate chemical

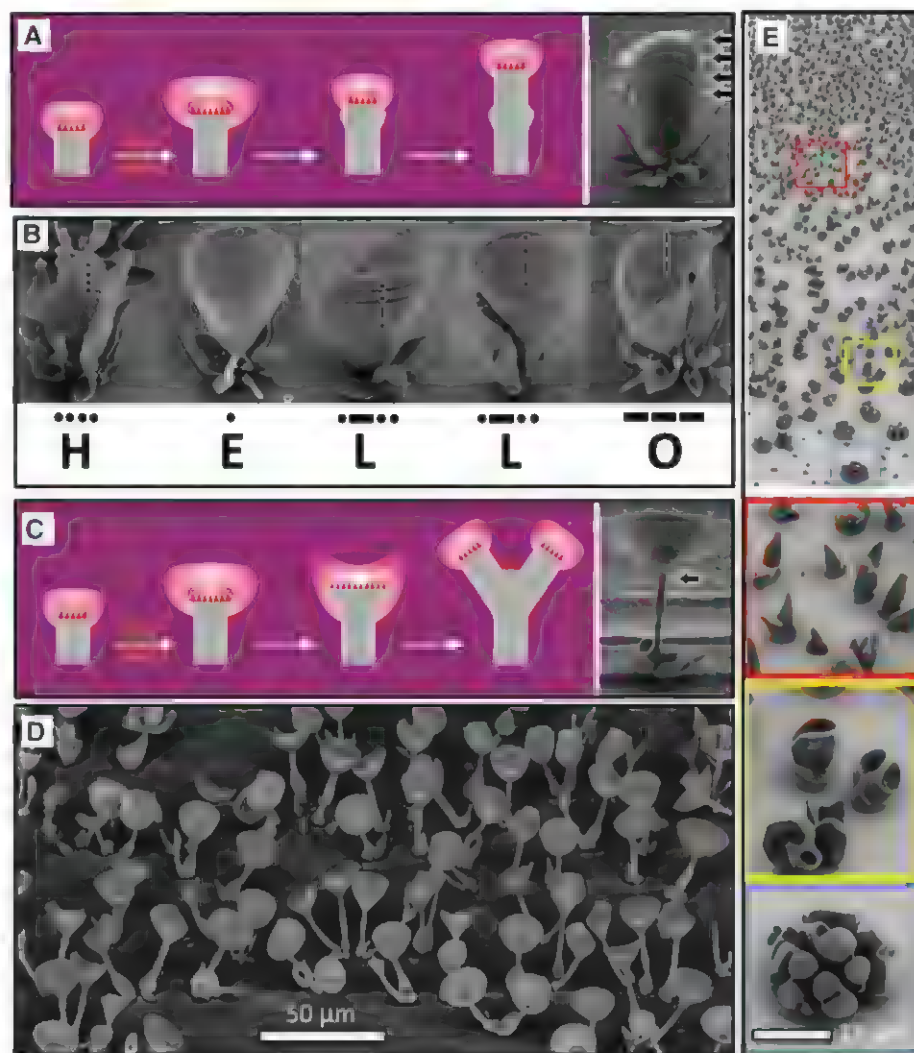


Fig. 3. Dynamically sculpting the growing stems, vases, and corals. (A) Schematic of the mechanism of restoration of the original, well-defined wall thickness after a temporary increase of the wall thickness is induced (by, for instance, a pulse of CO_2). The colors correspond to the pH regions in Fig. 1. (B) Experimental demonstration of (A). Rhythmical pulsing of CO_2 in the Ba-Si solution controllably produces ripples in the growing structures that can be used to write messages in Morse code. The "L" structures are from the same experiment; the other letters are made in separate experiments. (C) Schematic of the proposed mechanism of the splitting of the growth front to restore the original dimension, when the temporary increase of the wall thickness exceeds the dimension of the buffering front established by silica on the side walls. The arrow indicates a splitting point. (D) Experimental demonstration of splitting using a pulse of CO_2 into a Sr-Si solution, allowing sculpting stems into vases. (E) The structures can also be thickened, while preserving the overall morphologies, by increasing either the availability of CO_2 or the rate of the silica precipitation, which are achieved by lowering of the temperature (shown) or addition of NaCl , respectively.

interplay between nearby structures and different regions of their own surfaces.

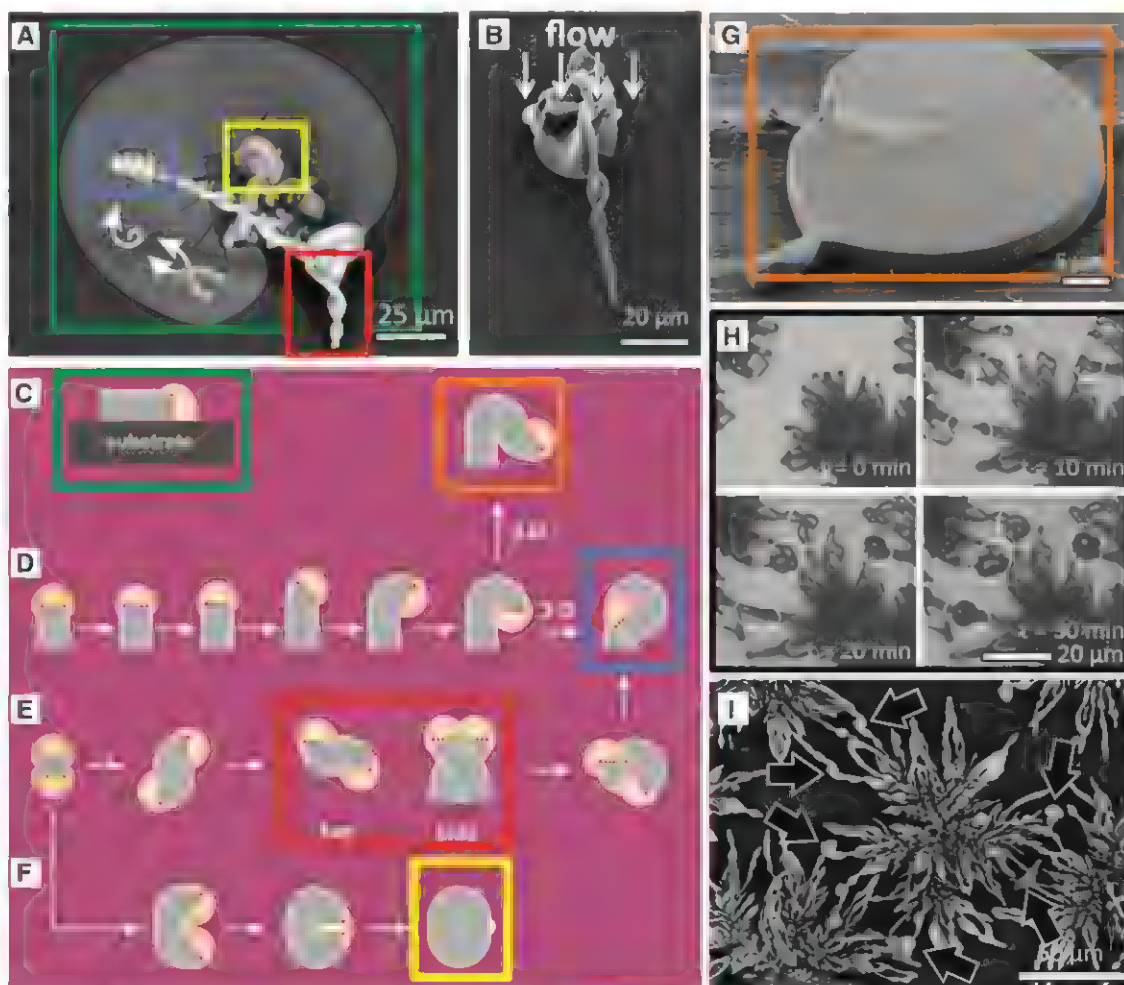
The simultaneously appearing basic shapes can each be understood by the inward-directed growth that characterizes regime 2 (Fig. 4, C to F; see fig. S5 for details): (i) Large leaflike structures covered with a mantle of silica (Fig. 4C) arise when the nucleated BaCO_3 crystals grow along the substrate, where the pH in the vicinity of the growth front remains sufficiently low ($\text{pH} < \text{pH}_{\text{SiO}_2}$) to prevent passivation by silica precipitation, whereas silica deposition occurs on top of the structure due to the flux of a more basic solution from the bulk. (ii) Single spirals form in response to perturbation of the growth front of the nucleated BaCO_3 crystals that results in a lower pH at one side of the front and a higher pH at the opposite side. The lowering of the local pH causes two complementary effects: growth toward the lower pH to remain in the region of $\text{pH} < \text{pH}_{\text{SiO}_2}$ and, conceivably, a slightly decreased BaCO_3 growth rate on the inner side of the curved structure. As the outer part continues growing and is passivated by silica, this further shields the inner part from the bulk solution, lowering the local pH

inside even more. The structure will continue to curl in this direction to give an increased curvature until the front is hampered by its own tail (Fig. 4D). To visualize this initial curling, we developed a method to grow quasi-2D structures by pinning the meniscus on the substrate (Fig. 4G). If we allow the structures to grow in 3D, the growth front continues to curl in the same direction, thereby following the acid that is produced by the previously formed part of the structure and generating a single spiral. This underlying part also shields the growth front from the bulk solution, comparable to the manner in which the substrate promotes growth of the leaves. (iii) Double spirals emerge when, instead of following its own tail, a growth front bends in the direction of the acid produced by a nearby BaCO_3 growth front. In this case, the two active sites follow each other's tails, making a double spiral (Fig. 4E). To confirm this cooperative growth mechanism, we grew a dense field of structures in regime 1 and subsequently lowered the pH to the curling growth mode. As can be observed from Fig. 4, H and I, the structures, which first grow away from each other and into the solution in regime 1, begin to

“sense” each other's active growth fronts, grow toward each other and away from the bulk, and finally merge to form single and double spirals in regime 2, in agreement with the hypothesis presented in Fig. 1. When one of the growth fronts of the double spiral catches up with the other one, they combine to form a single spiral with preservation of the chirality (Fig. 4, A and E). (iv) Finally, globular structures can be formed when two growth fronts crash into each other and merge together to become completely passivated by silica (Fig. 4F). The abundant acid that is released produces a local thickened scar on the silica mantle found on most globular structures (Fig. 4A).

The formation of spirals, double spirals, leaves, and globular shapes can thus be explained by growth-induced localized acid formation, which lowers the pH below the range for silica precipitation that passivates the growth, inducing structures to (i) grow most successfully away from the bulk solution and toward each other and (ii) curl as a result of the nonuniform growth rates that arise from the pH-dependent solubility (40). It is important to note that this mechanism can

Fig. 4. Diversity of structures that grow by inward-directed growth in regime 2. (A) SEM image of an exemplary BaCO_3 - SiO_2 structure grown at pH 11.2 containing a single spiral (blue rectangle), a double spiral (red rectangle), leaf shapes (green rectangle), and globular shapes (yellow rectangle). (B) Top view of a spiral grown in a flow, demonstrating directional growth away from the flow of bulk solution. (C) Leaf-like structures grow along the interface, away from the solution and become passivated on the top by a silica mantle. (D to F) Mechanisms of three curling modes, in which the structures curve away from the bulk solution and follow the trail of the acid produced at their own or neighboring growth fronts, resulting in the formation of single (D) and double (E) spirals and globular (F) structures (see text and supplementary materials for details). (G) Demonstration of the curling mode in a thin film of the solution that allows meandering only in 2D and eventually ceases when crashing into its own tail. (H to I) Optical microscopy time lapse series of a dense field of structures that initially (time $t = 0$ min) steer away from each other in regime 1 and then grow toward each other and merge upon lowering the pH to regime 2 to create spirals, as indicated by arrows in (I).



account for the full richness of observable forms and that it is principally different from a mechanics mechanism previously proposed to explain spiral formations (25).

Beyond Basic Shapes: Hierarchical Combinatorial Architectures

Because the morphology of the growing structures is responsive to the solution conditions and independent of the underlying form, a wide variety of different shapes can be stacked on top of each other by controlling the position, pH, temperature, and salt concentration in serial growth steps that distinctly allow for the formation of diverse higher-order architectures assembled hierarchically from the elementary building blocks.

Here, we provide only a few exemplary cases to illustrate the concept (Fig. 5 and figs. S6 to S8). When structures are grown sequentially in two different growth solutions, the second precipitation takes place preferentially at the active barium or strontium carbonate growth sites of the already-existing structures, showing no overgrowth of silica-passivated surfaces. We illustrate this by comparing the same structures before and after the second growth using SEM and confocal microscopy of dyed solutions (Fig. 5, A to C). By simply positioning the substrate at an angle relative to the first growth, we create a combinatorial matrix of reaction conditions that yield a large structural diversity with regions exhibiting well-defined hierarchical shapes on a single sample

(Fig. 5D). When the structures grown in the first step become overcoated with SiO_2 , these sites are passivated, so that the only nucleation sites available for the second precipitation are hidden in the cavities of the structure where the growth fronts split (Fig. 5, E and F). When the pH of the solution is reduced during the experiment from regime 2 to regime 3, spiral formations become overgrown by pure BaCO_3 bundles (Fig. 5G). Additionally, patterned substrates can be selectively decorated with structures (Fig. 5H). In all cases, the sculpted complex architectures show an unprecedented level of structural uniformity over large areas (see representative examples in Fig. 3D; Fig. 5, E and F; and figs. S6 to S8). Thus, the separate growth steps make it possible to create combinatorial, hybrid structures in which a judicious choice of the conditions is used to stack multiple shapes and sculpt continuously during the growth.

Conclusions

Sequential modulations of environmental conditions such as pH, temperature, and CO_2 concentration are used to modify local chemical fields that directly influence the growth front and control directional structure evolution. We identify two distinct and complementary growth modes: (i) a “blossoming” regime, in which the structures grow away from each other and toward the bulk solution to form stems, vases, and corals; and (ii) a “curling” regime, in which the growing fronts tend to shield themselves from the bulk solution by curling back toward themselves and each other to form spiral and leaf structures. A detailed understanding of the underlying buffering mechanisms allows us not only to program these elementary shapes, but also to dynamically sculpt and pattern evolving structures and assemble them inside or on top of each other to generate hierarchically assembled multiscale architectures with unprecedented levels of complexity and precision.

References and Notes

1. P. Ball, *The Self-Made Tapestry* (Oxford Univ. Press, Oxford, 1999).
2. D. W. Thompson, *On Growth and Form* (Cambridge Univ. Press, Cambridge, 1917); abridged edition, J. T. Bonner, Ed. (1961).
3. P. Vukusic, J. R. Sambles, *Nature* **424**, 852 (2003).
4. K.-H. Chu, R. Xiao, E. N. Wang, *Nat. Mater.* **9**, 413 (2010).
5. J. Aizenberg et al., *Science* **309**, 275 (2005).
6. J. K. Gansel et al., *Science* **325**, 1513 (2009).
7. J. Ge, J. Lei, R. N. Zare, *Nat. Nanotechnol.* **7**, 428 (2012).
8. Z. Bao et al., *Nature* **446**, 172 (2007).
9. B. Lim et al., *Science* **324**, 1302 (2009).
10. M. J. Madou, *Fundamentals of Microfabrication: The Science of Miniaturization* (CRC Press, Boca Raton, FL, 2002).
11. G. M. Whitesides, B. Grzybowski, *Science* **295**, 2418 (2002).
12. H. A. Lowenstam, S. Weiner, *On Biomimetic Mineralization* (Oxford Univ. Press, Oxford 1989).
13. P. Harting, *Q. J. Microsc. Sci.* **12**, 118 (1872).
14. J. J. Pagano, T. Bánsági Jr., O. Steinbock, *Angew. Chem. Int. Ed.* **47**, 9900 (2008).

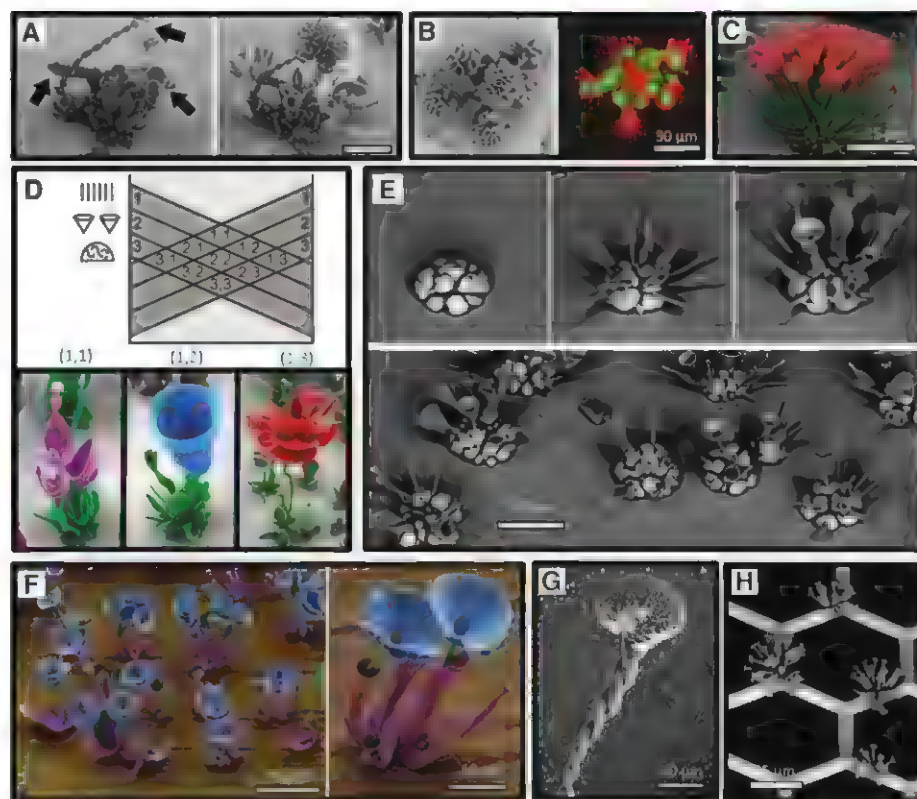


Fig. 5. Controlled synthesis of hierarchical complex structures. (A and B) $\text{BaCO}_3\text{-SiO}_2$ structures grown first in the solution containing fluorescein at pH 11.2 (regime 2) and then transferred to a solution containing rhodamine B at pH 11.8 (regime 1). Subsequent SEM images of the same structure (A) and confocal microscopy images (B) show that coral-like formations grow selectively on the active sites of the spirals [indicated by arrows in (A)], and no overgrowth occurs at the side walls of the previously formed shapes. (C) The SEM is false-colored, but represents the actual color of the structure composed of green $\text{SrCO}_3\text{-SiO}_2$ stems grown at pH 11.8 in the presence of fluorescein and then decorated with red, thick-walled $\text{BaCO}_3\text{-SiO}_2$ vases grown at 4°C in the presence of rhodamine B at pH 11.8. (D) Approach for making a combinatorial matrix of morphologies by changing the orientation of the substrate in distinct growth steps to stack different morphologies on top of each other. The SEMs of representative structures are false-colored to mark parts of the structure grown in different steps. (E) Multimaterial structure made in three steps: first, growing BaCO_3 corals that were thickened by addition of NaCl (top left) and, subsequently, inserting SrCO_3 stems (top center) and opening with a pulse of CO_2 (top right). The series is compiled from different structures. The bottom image is a large-area view. (F) False-colored SEMs showing a field of purple $\text{SrCO}_3\text{-SiO}_2$ vases containing $\text{SrCO}_3\text{-SiO}_2$ stems (green) that were subsequently opened with a CO_2 pulse (blue). (G) A spiral grown in regime 2 evolves into naked BaCO_3 crystals of regime 3 by lowering the pH of the bulk solution. (H) A transmission electron microscopy grid decorated with $\text{SrCO}_3\text{-SiO}_2$ stems that are opened with a CO_2 pulse. A larger variety of structures and overview images is provided in the supplementary materials (figs. S6 to S8).

15. J. H. E. Cartwright, J. M. García-Ruiz, M. L. Novella, F. Otálora, *J. Colloid Interface Sci.* **256**, 351 (2002).
16. C. Ritchie *et al.*, *Nat. Chem.* **1**, 47 (2009).
17. S. Mann, *Nature* **365**, 499 (1993).
18. S. Mann, G. A. Ozin, *Nature* **382**, 313 (1996).
19. G. Falini, S. Albeck, S. Weiner, L. Addadi, *Science* **271**, 67 (1996).
20. S. V. Patwardhan, S. J. Clarson, C. C. Perry, *Chem. Commun.* **2005**, 1113 (2005).
21. H. Y. Li, H. L. Xin, D. A. Muller, L. A. Estroff, *Science* **326**, 1244 (2009).
22. S.-H. Yu, H. Colfen, K. Tauer, M. Antonietti, *Nat. Mater.* **4**, 51 (2005).
23. L. A. Gower, D. A. Tirrell, *J. Cryst. Growth* **191**, 153 (1998).
24. S. D. Sims, J. M. Didymus, S. Mann, *J. Chem. Soc. Chem. Commun.* **1995**, 1031 (1995).
25. J. M. García-Ruiz, E. Melero-García, S. T. Hyde, *Science* **323**, 362 (2009).
26. J. M. García-Ruiz, J. L. Amoros, *J. Cryst. Growth* **55**, 379 (1981).
27. J. M. García-Ruiz *et al.*, *Science* **302**, 1194 (2003).
28. M. Kellermeier *et al.*, *Chemistry* **18**, 2272 (2012).
29. T. Terada, S. Yamabi, H. Imai, *J. Cryst. Growth* **253**, 435 (2003).
30. H. C. Berg, *E. coli in Motion* (Springer, New York, 2003).
31. A. M. Turing, *Philos. Trans. R. Soc. London Ser. B* **237**, 37 (1952).
32. I. Lengyel, I. R. Epstein, *Science* **251**, 650 (1991).
33. G. Ertl, *Science* **254**, 1750 (1991).
34. S. Kondo, T. Miura, *Science* **329**, 1616 (2010).
35. G. M. Whitesides, R. F. Ismagilov, *Science* **284**, 89 (1999).
36. B. A. Grzybowski, *Chemistry in Motion* (Wiley, Chichester, 2009).
37. C. J. Brinker, G. W. Scherer, *Sol-Gel Science* (Academic Press, London, 1990).
38. W. L. Marshall, J. M. Warakowski, *Geochim. Cosmochim. Acta* **44**, 915 (1980).
39. Our hypothesis suggests that the bulk solution in regime 2 is above the optimum pH for silica formation, whereas in the vicinity of the growth front, the localized acid formation lowers the pH below the optimum level: to precipitate silica on the active growth sites. We confirmed this localized pH gradient by monitoring $\text{BaCO}_3\text{-SiO}_2$ coprecipitation while deliberately adjusting the bulk pH (see supplementary materials).
40. We assume that the rate of the silica formation is slow enough to enter regime 2 before a layer of silica is formed

that locks the coprecipitation in regime 1. We verified this assumption by starting from regime 2 and increasing the rate of silica precipitation by adding 0.2 mM NaCl. As expected, we observe that the silica nucleation is now fast enough to not enter regime 2, but instead to grow thickened blossoming structures that correspond to regime 1.

Acknowledgments: We thank J. C. Weaver for advice with the SEM imaging, S. K. Y. Tang and R. Sadza for the microfluidic experiments, L. Hendriks for growing the structures in Fig. 5F, and A. J. Aizenberg for help with the manuscript. This work was supported by the NSF Materials Research Science and Engineering Centers under award no. DMR-0820484. W.L.N. thanks the Netherlands Organization for Scientific Research for financial support. EM was performed at Harvard's Center for Nanoscale Systems, supported by the NSF under award no. ECS-0335765.

Supplementary Materials
www.sciencemag.org/cgi/content/full/340/6134/832/DC1
Materials and Methods
Figs. S1 to S8

28 December 2012; accepted 19 March 2013
10.1126/science.1234621

Dual Molecular Signals Mediate the Bacterial Response to Outer-Membrane Stress

Santiago Lima,^{1*} Monica S. Guo,^{2*} Rachna Chaba,^{3†} Carol A. Gross,^{3,4} Robert T. Sauer^{1‡}

In Gram-negative bacteria, outer-membrane integrity is essential for survival and is monitored by the σ^E stress-response system, which initiates damage-repair pathways. One activating signal is unassembled outer-membrane proteins. Using biochemical and genetic experiments in *Escherichia coli*, we found that off-pathway intermediates in lipopolysaccharide transport and assembly provided an additional required signal. These distinct signals, arising from disruptions in the transport and assembly of the major outer-membrane components, jointly determined the rate of proteolytic destruction of a negative regulator of the σ^E transcription factor, thereby modulating the expression of stress-response genes. This dual-signal system permits a rapid response to dysfunction in outer-membrane biogenesis, while buffering responses to transient fluctuations in individual components, and may represent a broad strategy for bacteria to monitor their interface with the environment.

The outer membrane (OM) is essential for the survival of Gram-negative bacteria. In *Escherichia coli*, the σ^E stress-response sys-

tem recognizes signals indicative of OM dysfunction and triggers an adaptive response by activating the expression of gene products in-

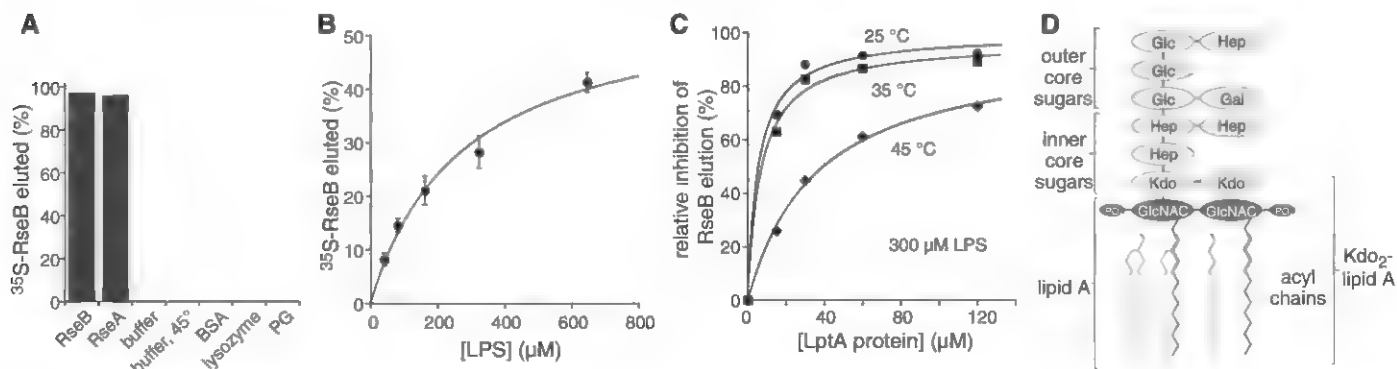
involved in the biogenesis, transport, and/or assembly of the lipopolysaccharides (LPSs), phospholipids, and outer-membrane proteins (OMPs) that make up the OM, and the proteases and chaperones that maintain or repair OM integrity (1, 2). In this system, the RseA and RseB regulatory proteins and the DegS and RseP inner-membrane (IM) proteases transmit the signal that activates the σ^E transcription factor (fig. S1). RseA, a single-pass IM protein, has a cytoplasmic domain that binds and inhibits σ^E and a periplasmic domain (RseA^P) that binds RseB (3–5). After stress, OMPs accumulate in the periplasm, and their C-terminal

¹Department of Biology, Massachusetts Institute of Technology, Cambridge, MA 02139, USA. ²Department of Biochemistry and Biophysics, University of California, San Francisco, CA 94158, USA. ³Department of Microbiology and Immunology, University of California, San Francisco, CA 94158, USA. ⁴Department of Cell and Tissue Biology, University of California, San Francisco, CA 94158, USA.

*These authors contributed equally to this work.

†Present address: Indian Institute of Science Education and Research–Mohali, Sector 81, Knowledge City, S.A.S. Nagar, Punjab 140306, India.

‡Corresponding author. E-mail: bobsauer@mit.edu



residues bind to DegS and activate cleavage of RseA^P (6), triggering a proteolytic cascade that frees σ^E to activate gene expression (1). However, a signal that inhibits RseB is also required, because RseB binding to RseA^P prevents activated DegS from cleaving RseA (4, 5, 7). The RseB-inhibition signal has not been characterized but may be related to LPS, because alterations in LPS structure

activate the σ^E response (8, 9). We tested and provide evidence here for a model in which intermediates in LPS transport and assembly are the second signal that activates σ^E .

LPS Antagonizes RseA-RseB Binding in Vitro

We developed an assay for ³⁵S-RseB dissociation from RseA^P-agarose and established that ³⁵S-RseB

was efficiently eluted by both unlabeled RseB and RseA^P but not by unrelated proteins or an abundant bacterial phospholipid (Fig. 1A). LPS purified from an *E. coli* K-12 strain also had RseB-elution activity (Fig. 1B), as did LPS variants purified from various mutant strains (figs. S2 and S3). LptA, a protein that is part of the periplasmic bridge that shuttles LPS from the IM to the OM (10), inhibited

Fig. 2. Lipid-A fragments disrupt RseA^P-RseB complexes. (A) Mass spectrometry and structure of the L-IIA fragment. (B) L-IIA and Kdo₂-L-IIA eluted ³⁵S-RseB from RseA^P-agarose (25°C). Data (mean ± SEM; *n* = 2) were fit to a Hill equation, giving *K*_{app} values of ~140 μM (L-IIA) and ~100 μM (Kdo₂-L-IIA). (C) Temperature dependence of LptA competition for Kdo₂-L-IIA (140 μM) elution of ³⁵S-RseB from RseA^P-agarose. Data are means ± SEM (*n* = 2). (D) L-IIA competed for RseB (3.5 μM) binding to fl-RseA^P (60 nM). Data (mean ± SD, *n* = 5) were fit to a competition equation (median effective concentration ~65 μM). (Inset) L-IIA did not change fl-RseA^P (60 nM) anisotropy. (E) After premixing RseB (5 μM) and fl-RseA^P (60 nM), dissociation was initiated by adding an equal volume of L-IIA (5 mM). The line is a single exponential fit (rate constant = 0.16 s⁻¹).

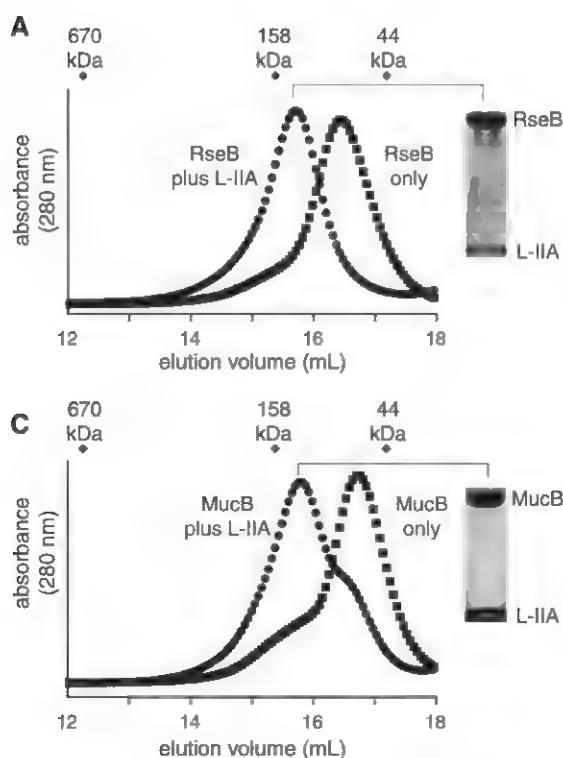
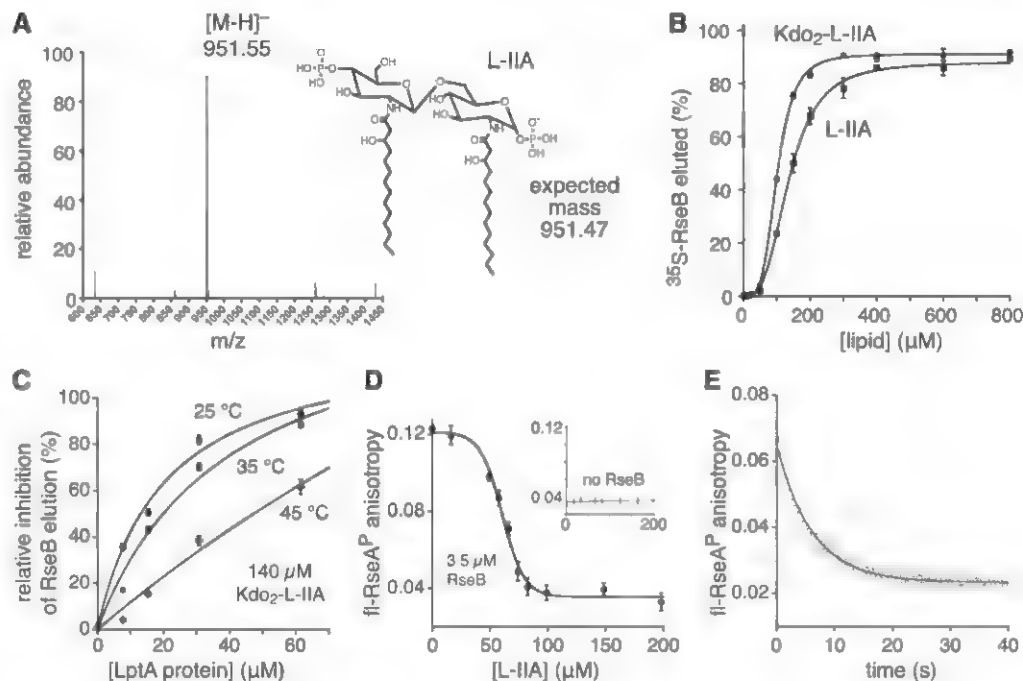


Fig. 3. Lipid-A fragments bind RseB/MucB and coactivate cleavage of RseA^P/MucA^P. (A) After adding L-IIA (2 mM) to RseB (180 μM), the protein eluted from a gel filtration column as expected for an RseB tetramer (~143 kD). SDS-polyacrylamide gel electrophoresis (SDS-PAGE) and silver staining of the "tetramer" peak fraction showed coelution of RseB and L-IIA. See fig. S6 for gels across the entire included volume. (B) SDS-PAGE assay of RseA^P (40 μM) degradation by DegS (4 μM trimer) in the presence or absence of RseB (40 μM monomer), OMP peptide (200 μM), and L-IIA (2 mM). (C) After adding L-IIA (2 mM), MucB (180 μM) largely eluted as a tetramer during gel filtration, although a dimeric shoulder was still evident. (D) L-IIA and Kdo₂-L-IIA eluted ³⁵S-MucB from MucA^P-agarose. Data (mean ± SD, *n* = 3) were fit to a Hill equation, giving *K*_{app} values of ~120 μM (L-IIA) and ~83 μM (Kdo₂-L-IIA). (E) SDS-PAGE assay of MucA^P (25 μM) degradation by AlgW (2 μM trimer) in the presence or absence of MucB (40 μM monomer), OMP peptide (75 μM), and L-IIA (2 mM).

LPS elution of RseB (Fig. 1C), indicating that RseB and LptA compete for LPS. RseB competed more efficiently at 45°C, a temperature that activates the cellular σ^E response, than at lower temperatures (Fig. 1C). Thus, altered competitive binding could contribute to σ^E activation in vivo.

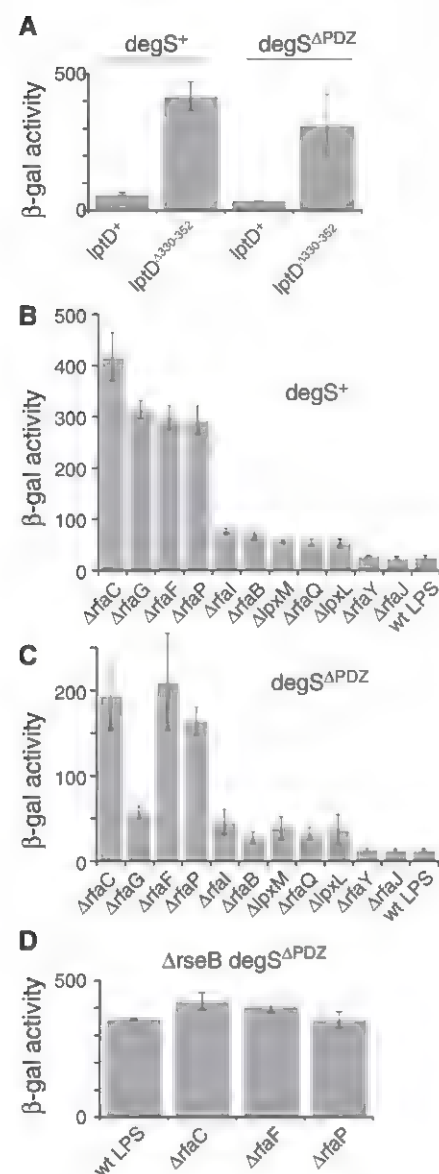


Fig. 4. Activation of a σ^E -dependent rpoHp3-LacZ reporter under nonstress conditions by LPS-biogenesis mutations. (A) σ^E activity was enhanced by *lptD*^{A330-352} in *degS*⁺ and *degS*^{APDZ} backgrounds. β -gal, β -galactosidase. (B) σ^E activity was enhanced in a *degS*⁺ strain by numerous LPS-biogenesis mutations (see fig. S9 for structures). (C) Same as (B) but *degS*^{APDZ}. *DegS*^{APDZ} has lower RseA-cleavage activity than OMP-activated *DegS* (18), probably accounting for the lower σ^E activities in (C) as compared to (B) (also see fig. S10). (D) σ^E activities were similar in Δ *rseB* *degS*^{APDZ} strains producing wild-type LPS and some of the strongest LPS-biosynthesis mutations from (C). In all panels, data are means \pm 1 SD ($n \geq 4$).

Minimal LPS Fragments Bind RseB and Facilitate Cleavage of RseA

We sought to test whether fragments of LPS containing lipid A or di-[keto-deoxyoctulosonate]-lipid A (Kdo₂-lipid-A; Fig. 1D) also bound RseB, but both molecules had very low solubilities, precluding the interpretation of biochemical studies. However, NaOH hydrolysis of lipid A or Kdo₂-lipid A, a treatment that partially removes acyl chains, improved solubility and allowed the purification of active fragments (called L-IIA and Kdo₂-L-IIA) with masses expected for the retention of two N-linked acyl chains but the loss of all four O-linked acyl chains (Fig. 2A and fig. S4). The activities of both fragments were similar (Fig. 2B), indicating that the Kdo sugars in Kdo₂-L-IIA are not essential for RseB elution. Derivatives of lipid A devoid of acyl chains had no RseB-elution activity. LptA also inhibited RseB elution by Kdo₂-L-IIA, with inhibition being less efficient at higher temperature (Fig. 2C). Thus, any LPS derivative that contains the phosphorylated *N*-acetylglucosamine (GlcNAc) disaccharide and *N*-linked acyl chains of the lipid-A moiety (colored dark gray in Fig. 1D) appears to bind RseB and displace RseA^P.

Although metabolically irrelevant, L-IIA and Kdo₂-L-IIA were useful LPS surrogates because they did not scatter light, permitting the use of fluorescence anisotropy to monitor RseB binding (4). L-IIA dissociated a complex of fluorescent RseA^P (fl-RseA^P) and RseB in a concentration-dependent manner but did not alter the anisotropy of fl-RseA^P alone (Fig. 2D), confirming competition between L-IIA and fl-RseA^P for RseB binding (fig. S5). Dissociation of the RseB-fl-RseA^P complex was complete within 30 s of addition of L-IIA (Fig. 2E), a time rapid enough to account for the kinetics of the cellular σ^E response after a stress treatment (11).

Purified RseB is a mixture of dimers and tetramers, with only the dimer binding RseA (4, 12). When we added L-IIA to freshly purified RseB dimers and re-chromatographed the mixture, most protein coeluted with L-IIA at an RseB-tetramer position (Fig. 3A). L-IIA alone eluted near the column salt volume (fig. S6). Thus, L-IIA binds directly to RseB, L-IIA complexes with RseB largely persist during the ~1 hour required for chromatography, and L-IIA binding stabilizes RseB in a tetrameric state that does not bind RseA.

We tested the effects of RseB, L-IIA, and OMP peptide on *DegS* cleavage of RseA^P in vitro (Fig. 3B). As expected (4–6), *DegS* alone did not cleave RseA^P, the addition of OMP peptide activated cleavage, and the further addition of RseB inhibited this cleavage. However, the addition of L-IIA to OMP peptide restored robust *DegS* cleavage of RseA^P in the presence of RseB. Other combinations did not restore cleavage. L-IIA alone did not activate *DegS*, confirming that it acts to inhibit RseB.

LPS Plays an Evolutionarily Conserved Role

Most γ and β proteobacteria have RseA, RseB, and *DegS* orthologs, with MucA, MucB, and AlgW being their functional equivalents in

Pseudomonas aeruginosa, a distant relative of *E. coli* (12). We tested the generality of our findings by examining the interaction of *E. coli* LPS fragments with the *P. aeruginosa* proteins. L-IIA largely converted MucB dimers to tetramers (Fig. 3C) and eluted ³⁵S-MucB from a MucA^P-affinity column (Fig. 3D), supporting conservation of an LPS-mediated displacement mechanism. L-IIA also allowed OMP-activated AlgW to cleave MucA in the presence of MucB (Fig. 3E). Thus, in both the *E. coli* and *P. aeruginosa* systems, an LPS molecule and OMP peptide mimic the signals that result in RseA/MucA cleavage in vivo by inactivating RseB/MucB and activating *DegS*/AlgW, respectively.

σ^E Activation by Wild-Type and Mutant LPS

Our results predict that increased periplasmic LPS should activate the cellular σ^E response. After synthesis on the IM, LPS is shuttled over an Lpt protein bridge and inserted into the OM by the LptD/E translocon at the distal end of the bridge (13–15). The *LptD*^{A330-352} variant has fewer functional bridges because of the loss of key disulfide bonds and should cause LPS accumulation in the periplasm (15–17). We found that the *lptD*^{A330-352} allele increased expression of a β -galactosidase reporter under σ^E transcriptional control in a strain requiring inhibition of RseB but not requiring an OMP signal (*degS*^{APDZ}) and in a strain requiring both inhibition of RseB and an OMP signal (*degS*⁺) (Fig. 4A and fig. S7). Although RseA cleavage neither requires nor is activated by OMPs in *degS*^{APDZ} cells, because the autoinhibitory PDZ domain of *DegS* is missing, RseB normally keeps σ^E activity low (4, 7, 18). Thus, increased σ^E activity in the *lptD*^{A330-352} *degS*^{APDZ} strain supports a model in which the accumulation of periplasmic LPS relieves RseB inhibition. The activation of σ^E in *lptD*^{A330-352} *degS*⁺ cells suggests that OMP intermediates also accumulate (6, 7), probably as a consequence of defects in LPS assembly. We also decreased the level of properly disulfide-bonded LptD by deleting the DsbA disulfide oxidoreductase (16, 17). Although the Δ *dsbA* mutation affects many proteins in addition to LptD, it increased σ^E activity in *degS*^{APDZ} and *degS*⁺ strains (fig. S8).

Using *degS*⁺ and *degS*^{APDZ} strains, we tested σ^E activity in a panel of 11 LPS-biosynthesis mutants to determine whether they relieved RseB inhibition and/or activated *DegS*. The mutant LPS variants all contained the minimal RseB-interaction motif (fig. S9). Nine mutants elevated σ^E activity in *degS*⁺ and *degS*^{APDZ} strains (Fig. 4, B and C), supporting a model in which activation is linked to LPS inhibition of RseB and to the generation of an OMP signal that activates *DegS*. In a Δ *rseB* *degS*^{APDZ} strain in which an OMP signal is not required and negative regulation by RseB is abrogated, the most strongly inducing LPS biosynthesis mutations did not further activate σ^E (Fig. 4D).

RseB as a Periplasmic LPS Sensor

Our results support a model in which LPS prevents RseB from blocking RseA cleavage. Intact LPS or LPS fragments containing a portion of the

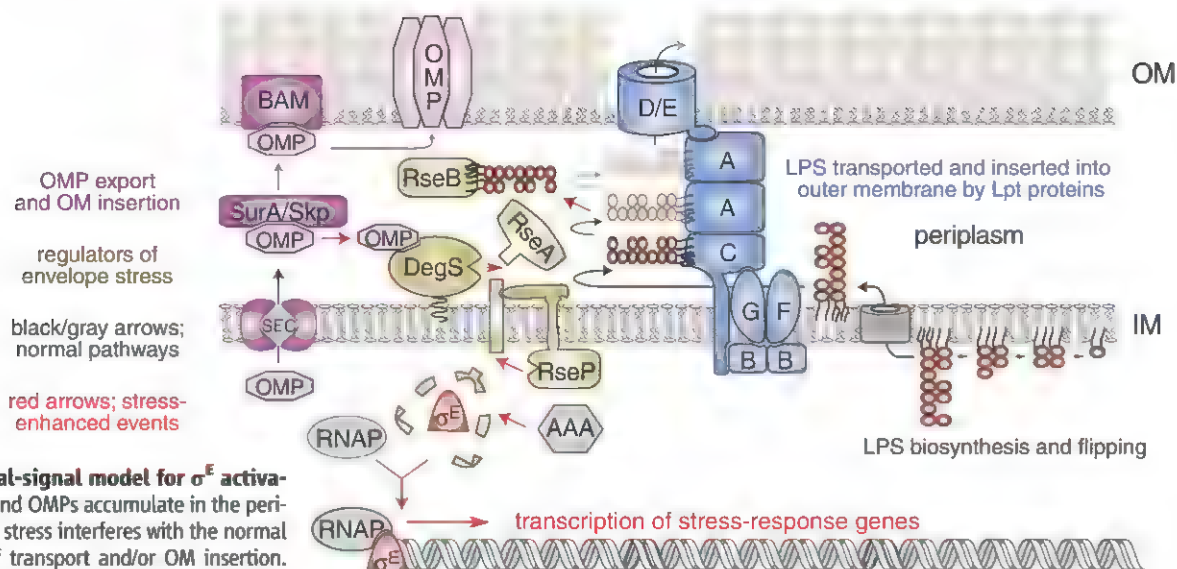


Fig. 5. Dual-signal model for σ^E activation. LPSs and OMPs accumulate in the periplasm when stress interferes with the normal pathways of transport and/or OM insertion. Periplasmic LPS binds RseB, freeing RseA to be cleaved by OMP-activated DegS, which initiates the σ^E stress response.

lipid-A scaffold bind RseB and release RseA, allowing its cleavage by DegS. Functionally, detection of part of the lipid-A moiety of LPS ensures that RseB can sense and respond to many mislocalized LPS species, including wild-type LPS, incompletely synthesized LPS molecules that reach the periplasm, and LPS variants lacking O-linked acyl chains or core sugars that support *E. coli* viability but decrease the ability of the OM to protect against cytotoxic agents.

Mutant LPS molecules with the fewest core sugars and phosphates activated σ^E to the highest levels in *rseB*⁺ cells (Fig. 4, B and C, and fig. S9). By analogy with the activation observed when LPS transport was disrupted by partially disabling LptD, we propose that these mutations disrupt synchrony between one or more discrete steps in LPS biosynthesis or transport or OM insertion in ways that increase periplasmic LPS (Fig. 5), which could transit to RseB either through free diffusion or hand-off. During exponential growth, the flux of LPS through the periplasm is $\sim 70,000$ molecules min^{-1} . Changes in the coordination of individual biogenesis and transport steps that diverted $\sim 10\%$ of these molecules would result in a $\sim 40 \mu\text{M min}^{-1}$ rise in periplasmic LPS (19). Likewise, environmental stress could affect the integrity or function of the Lpt machinery for LPS transport or OM insertion, causing periplasmic accumulation of LPS. Temperature stress might have additional direct effects. LptA, a key component of the transenvelope bridge (Fig. 5) (10, 15), competed less efficiently with RseB for binding to LPS at 45°C, suggesting that heat shock facilitates the transfer of LPS from LptA to RseB, providing a “feed-forward” mechanism for σ^E activation.

Dual-Signal Logic and σ^E Control

Two signals are required for DegS cleavage of RseA when RseB is present in vitro. An OMP signal activates proteolysis by DegS, whereas an

LPS signal prevents RseB from blocking the cleavage of RseA. The importance of both signals is also clear in certain genetic backgrounds in vivo. For example, mutations expected to increase periplasmic LPS activate the σ^E response in *degS*^{APDZ} cells, which require RseB inhibition but not OMP activation. Similarly, the expression of OMP signals alone is sufficient to strongly induce the σ^E response in Δ *rseB* cells (7). This requirement for dual signals is reminiscent of an “AND” operation in symbolic or digital logic.

σ^E activates the transcription of genes for the chaperones and machines that transport and insert both LPS and OMPs into the OM. Crosstalk between these pathways could add an additional layer of regulation (2, 13, 20, 21). If defects in LPS biogenesis created problems with OMP biogenesis and vice versa, then both signals needed to activate σ^E would be produced when either pathway is perturbed. Indeed, *rfaC*, *rfaF*, and *rfaP* LPS mutations activate σ^E in strains requiring only RseB inhibition (*degS*^{APDZ} *rseB*⁺, Fig. 4C), only OMP activation (*degS*⁺ Δ *rseB*, fig. S11), or both (*degS*⁺ *rseB*⁺, Fig. 4B). Supporting this idea, the OMPs of *rfaC*, *rfaF*, and *rfaP* strains have significantly reduced levels of OMPs (22–24), suggesting problems with OMP biogenesis. Conversely, the LptD component of the LPS translocon is transported and inserted into the OM by the same chaperones and machinery as other OMPs (16, 25), and thus defects in OMP biogenesis would soon lead to problems in LPS transport and assembly. Additionally, the combination of AND logic and cross-signaling permits the σ^E response to reflect the stress level. Low levels of off-pathway OMPs and LPS may be constantly present in the periplasm, because basal cleavage of RseA by DegS is essential for survival (26). Thus, transient increases in either signal would result in an increased but buffered response, whereas a full and metabolically expensive re-

sponse would be mounted only when RseB and DegS detect high concentrations of off-pathway LPS and OMPs, a condition indicative of extensive dysfunction in OM biogenesis.

Most unicellular organisms are enclosed by cell walls or envelopes that provide both a barrier to and an interface with the environment. These external structures are built from components that are synthesized in the cytosol but are assembled outside of the cytoplasmic membrane. Monitoring the flux of these molecules in the vicinity of the membrane, coupled with dual-signal logic to buffer spurious responses, may be a common regulatory strategy enabling precise homeostatic control of these critical barrier structures.

References and Notes

1. S. E. Ades, *Curr. Opin. Microbiol.* **11**, 535 (2008).
2. V. A. Rhodius, W. C. Suh, G. Nonaka, J. West, C. A. Gross, *PLoS Biol.* **4**, e2 (2006).
3. E. A. Campbell et al., *Mol. Cell* **11**, 1067 (2003).
4. B. O. Cezairliyan, R. T. Sauer, *Proc. Natl. Acad. Sci. U.S.A.* **104**, 3771 (2007).
5. D. Y. Kim, K. S. Jin, E. Kwon, M. Ree, K. K. Kim, *Proc. Natl. Acad. Sci. U.S.A.* **104**, 8779 (2007).
6. N. P. Walsh, B. M. Alba, B. Bose, C. A. Gross, R. T. Sauer, *Cell* **113**, 61 (2003).
7. R. Chaba et al., *Proc. Natl. Acad. Sci. U.S.A.* **108**, 2106 (2011).
8. C. Tam, D. Missiakos, *Mol. Microbiol.* **55**, 1403 (2005).
9. G. Klein, B. Lindner, W. Brabetz, H. Brade, S. Raina, *J. Biol. Chem.* **284**, 15369 (2009).
10. A. X. Tran, M. S. Trent, C. Whitfield, *J. Biol. Chem.* **283**, 20342 (2008).
11. S. E. Ades, I. L. Grigorova, C. A. Gross, *J. Bacteriol.* **185**, 2512 (2003).
12. B. O. Cezairliyan, R. T. Sauer, *Mol. Microbiol.* **72**, 368 (2009).
13. N. Ruiz, D. Kahne, T. J. Silhavy, *Nat. Rev. Microbiol.* **7**, 677 (2009).
14. E. Freinkman, S. S. Chng, D. Kahne, *Proc. Natl. Acad. Sci. U.S.A.* **108**, 2486 (2011).
15. E. Freinkman, S. Okuda, N. Ruiz, D. Kahne, *Biochemistry* **51**, 4800 (2012).
16. N. Ruiz, S. S. Chng, A. Hiniker, D. Kahne, T. J. Silhavy, *Proc. Natl. Acad. Sci. U.S.A.* **107**, 12245 (2010).

17. S. S. Chng *et al.*, *Science* **337**, 1665 (2012).
18. J. Sohn, R. A. Grant, R. T. Sauer, *Cell* **131**, 572 (2007).
19. Calculations assume 2×10^6 LPS molecules per *E. coli* cell, a doubling time of 30 min, and a periplasmic volume of 3×10^{-16} liters.
20. J. E. Mogensén, D. E. Otzen, *Mol. Microbiol.* **57**, 326 (2005).
21. C. L. Hagan, T. J. Silhavy, D. Kahne, *Annu. Rev. Biochem.* **80**, 189 (2011).
22. G. F. Ames, E. N. Spudich, H. Nikaïdo, *J. Bacteriol.* **117**, 406 (1974).
23. E. A. Austin, J. F. Graves, L. A. Hte, C. T. Parker, C. A. Schnaitman, *J. Bacteriol.* **172**, 5312 (1990).
24. H. Nikaïdo, *Microbiol. Mol. Biol. Rev.* **67**, 593 (2003).
25. D. Vertommen, N. Ruiz, P. Leverrier, T. J. Silhavy, J. F. Colet, *Proteomics* **9**, 2432 (2009).
26. B. M. Alba, H. J. Zhong, J. C. Pelayo, C. A. Gross, *Mol. Microbiol.* **40**, 1323 (2001).

Acknowledgments: We thank B. Cezairliyan, S. Chng, D. Kahne, C. Raetz, and D. Six for discussions and strains. Supported by NIH grants AI-16892 and GM-36278. S.L. was supported by an NIH postdoctoral fellowship (AI-084442). The

data reported in this paper are presented in the main text and supplementary materials.

Supplementary Materials

www.sciencemag.org/cgi/content/full/340/6134/83//DC1
Materials and Methods
Figs. S1 to S12
Table S1
References (27–32)

18 January 2013; accepted 25 March 2013
10.1126/science.1235358

REPORTS

Phase Diagram of the Topological Superfluid ^3He Confined in a Nanoscale Slab Geometry

L. V. Levitin,¹ R. G. Bennett,^{1*} A. Casey,¹ B. Cowan,¹ J. Saunders,^{1†} D. Drung,² Th. Schurig,² J. M. Parpia³

The superfluid phases of helium-3 (^3He) are predicted to be strongly influenced by mesoscopic confinement. However, mapping out the phase diagram in a confined geometry has been experimentally challenging. We confined a sample of ^3He within a nanofluidic cavity of precisely defined geometry, cooled it, and fingerprinted the order parameter using a sensitive nuclear magnetic resonance spectrometer. The measured suppression of the p-wave order parameter arising from surface scattering was consistent with the predictions of quasi-classical theory. Controlled confinement of nanofluidic samples provides a new laboratory for the study of topological superfluids and their surface- and edge-bound excitations.

At temperatures close to absolute zero, helium-3 (^3He) becomes a superfluid, a state of matter exhibiting macroscopic quantum coherence and characterized by dissipationless flow. A number of superfluid phases emerge that have a rich variety of broken symmetries and nontrivial momentum-space topologies (1–4). They provide model systems for unconventional superconductivity (5) and embody key paradigms of topological quantum matter (6, 7). The quantum liquid ^3He played the central role in the establishment of Landau Fermi liquid theory, which describes a degenerate system of mobile strongly interacting fermions as weakly correlated quasi-particles. Superfluidity in liquid ^3He arises from the formation of Cooper pairs, with relative orbital angular momentum $L = 1$ (p-wave) and total spin $S = 1$ (^3He has nuclear spin $1/2$). The Balian-Werthamer (B) phase is a time-reversal-invariant p-wave superfluid (8),

analogous to topological insulators and quantum spin Hall systems (9, 10). The Anderson-Brinkman-Morel (A) phase is a chiral p-wave superfluid, breaking time-reversal symmetry, and in the two-dimensional limit is analogous to integer quantum Hall systems (3) and related to the candidate topological superconductor Sr_2RuO_4 (6, 11).

Dimensional confinement into a film geometry of this model system for superconducting/superfluid p-wave order is predicted to give rise to considerable surface-induced distortions of the order parameter (12). The relevant confinement length scale is set by the diameter of the Cooper pair, $\xi_0 = \hbar v_F / 2\pi k_B T_c$, where v_F is the Fermi velocity, T_c is the superfluid transition temperature, \hbar is Planck's constant h divided by 2π , and k_B is the Boltzmann constant; $\xi_0 = 75$ nm at zero pressure, where $T_c = 0.9$ mK. The topological nature of the superfluids leads to Majorana (13) or Majorana-Weyl fermionic excitations at surfaces (14) or edges (3, 15) of the B and A phases respectively. The order parameter distortions and spectral weight of surface excitations are directly related and may be predicted by quasi-classical theory (16). Nevertheless, our understanding of the superfluid order of a ^3He film has remained limited, constrained by the difficulty in experimentally fingerprinting the order parameter of a film of precisely defined thickness; address-

ing this challenge is the central thrust of this Report.

In previous work, the superfluid flow of a thin liquid film over highly polished metal surfaces has been observed (17). The excitation of surface waves (third sound) (18) and torsional oscillator methods (19) have been used to determine the superfluid density as a function of film thickness. However, these methods crucially were unable to identify the pairing state. Moreover, achieving uniformity of the film and measuring the film thickness precisely are experimentally challenging.

These issues are addressed in our experiment by confining superfluid ^3He within a single nanofabricated cavity. The key control parameter, cavity height (which determines the film thickness), is fully characterized. We were able to cool such samples to well below 1 mK and interrogated them by means of nuclear magnetic resonance (NMR) in order to fingerprint the superfluid ^3He order parameter. We have developed an ultra-sensitive NMR spectrometer (20) to detect signals from this tiny sample. These technical steps represent a critical advance on previous NMR studies of confined ^3He , in which an ensemble of typically 1000 films within a stack of plastic sheets separated by spacer particles has been investigated (21), leading to an undesirably broad distribution of film thickness.

The sample geometry is shown in Fig. 1. We have investigated the pressure range from 0 to 5.5 bar, over which the Cooper pair diameter ξ_0 decreased by approximately a factor of two, providing pressure tuning of the effective confinement for a fixed cavity height D . The temperature dependence of the effective confinement is determined by the ratio of D to the temperature-dependent superfluid coherence length $\xi(T)$. The coherence length determines the scale of the recovery of the order parameter away from the surface and arises from the competition between condensation and order parameter gradient energies (12). In this work, we define $\xi_\Delta(T) = \hbar v_F / \Delta_B(T) \sqrt{10}$, where $\Delta_B(T)$ is the bulk B-phase gap, $\xi_\Delta(0) = 1.13\xi_0$, and $\xi_\Delta(T)$ diverges approaching T_c (22).

The p-wave superfluid order is represented as the amplitudes of pairs with projections of orbital and spin angular momentum $L_z, S_z \sim 1, 0, -1$; corresponding terms in the momentum-space pair-wavefunction $\Delta(\mathbf{p})$ have orbital part $(\hat{p}_x + i\hat{p}_y)$,

¹Department of Physics, Royal Holloway University of London, Egham, Surrey, TW20 0EX, UK. ²Physikalisch-Technische Bundesanstalt, Abbestrasse 2-12, D-10587 Berlin, Germany. ³Department of Physics, Cornell University, Ithaca, NY 14853, USA

*Present address: Isentropic Ltd, 7, Brunel Way, Segensworth East, Hampshire PO15 5TX, UK.

†Corresponding author. E-mail: j.saunders@rhul.ac.uk

$\sqrt{2}\hat{p}_x$, and $(-\hat{p}_x + i\hat{p}_y)$ and spin part $|\uparrow\uparrow\rangle, |\uparrow\downarrow\rangle + |\downarrow\uparrow\rangle/\sqrt{2}$, and $|\downarrow\downarrow\rangle$, respectively (3). Those pairs with orbital angular momentum in the plane of the cavity surface ($L_z = 0$) are completely suppressed at the surface (12). There is weaker or no suppression of pairs with orbital angular momentum parallel to the cavity surface normal $L_z = \pm 1$, depending on the nature of surface scattering. The spatial dependence of the components of the order parameter across the cavity is predicted within the framework of quasi-classical theory (23, 24).

The identification of the phases of superfluid ^3He is possible through NMR spectroscopy, which directly probes the spin degrees of freedom of the Cooper pairs (22). Although the condensation energy of Cooper pairing is invariant under relative rotation of the spin and orbital axes of the pairs, spin-orbit symmetry is broken by the nuclear dipole-dipole interaction of the paired fermions. This weak spin-orbit coupling energy leads to a frequency shift of the NMR spectrum with respect to the normal state and provides a signature of the superfluid order. This effect played the central role

in the identification of the phases of bulk superfluid ^3He shortly after their discovery (1).

At the pressure of 2.2 bar (Fig. 2), only the A phase is observed, with the order parameter $\Delta(\mathbf{p}) = \Delta(z)(\hat{p}_x + i\hat{p}_y)[|\uparrow\uparrow\rangle + |\downarrow\downarrow\rangle]$, where $\Delta(z)$ denotes that the gap has a spatial dependence across the cavity. This is a state with just the $S_z = \pm 1$ components of the spin triplet. The orbital angular momentum of all pairs is aligned and oriented normal to the cavity surface $\mathbf{l} = \pm \hat{z}$. The gap is suppressed with respect to the bulk A-phase gap for surfaces that scatter quasi-particles diffusively (randomly); specular scattering is predicted to eliminate this suppression (24). The static magnetic field $\mathbf{B}_0 = B_0\hat{z}$ orients the spins along \hat{z} , via the nuclear Zeeman energy, which for $B_0 = 32$ mT used in our experiment is larger than the spin-orbit coupling. This configuration maximizes the dipolar energy and gives rise to the observed negative frequency shift (25).

At 5.5 bar, on cooling through the superfluid transition, we first observed a similar A-phase signature, followed by a transition into a low-

temperature phase. This phase is predicted to be the planar-distorted B phase (23, 24), with order parameter $\Delta(\mathbf{p}) = \Delta_{||}(z)(-\hat{p}_x + i\hat{p}_y)|\uparrow\uparrow\rangle + \Delta_{||}(z)(\hat{p}_x + i\hat{p}_y)|\downarrow\downarrow\rangle + \Delta_{\perp}(z)\hat{p}_z[|\uparrow\downarrow\rangle + |\downarrow\uparrow\rangle]$, with all three components of the spin and orbital triplets; in the expression above, $L_z = S_z$. The bulk B phase is described by the above expression with isotropic gap: $\Delta_{\perp} = \Delta_{||}$. However, the cavity is predicted to induce a spatially dependent gap distortion: $\Delta_{\perp}(z) < \Delta_{||}(z)$. The order parameter component describing the $L_z = 0$ pairs changes sign upon quasi-particle reflection at the boundary, leading to the complete suppression of Δ_{\perp} approaching the walls and the formation of surface-bound states (26). Similar pair-breaking occurs in unconventional superconductors—for example, at the [110] surface of a cuprate superconductor with $d_{x^2-y^2}$ symmetry—for this reason (27).

Entering this phase, we found the sample in a state with either a positive (B₊) or negative (B₋) frequency shift; sometimes both signatures were observed at once, in which case, the sample is understood to comprise B₊ and B₋ domains. The two NMR signatures are attributed to different

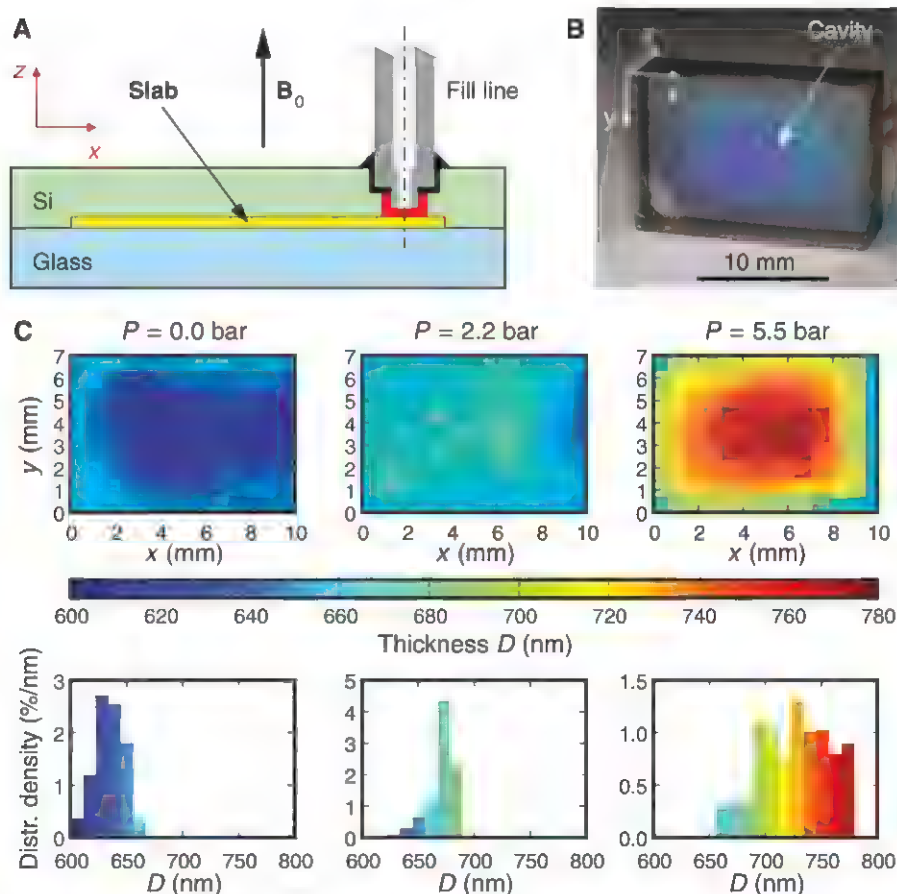


Fig. 1. Experimental cell providing confined geometry for ^3He . (A) Schematic diagram of cell filled with helium. The cell is fabricated from glass (blue) and silicon (green) wafers anodically bonded together. The unsupported cavity, of designed thickness 650 nm, is defined lithographically in the silicon wafer. A silver fill line (gray) is fitted with epoxy (black) through a hole drilled in the silicon. Yellow represents the slab of confined helium being investigated with NMR in a static field $B_0 = 32$ mT normal to the slab, and red is the small amount of bulk liquid around the mouth of the fill line also observed with the NMR spectrometer (22). (B) A photograph of the cell. (C) Slab thickness profiles and distributions determined at low temperatures and three sample pressures by means of optical interferometry.

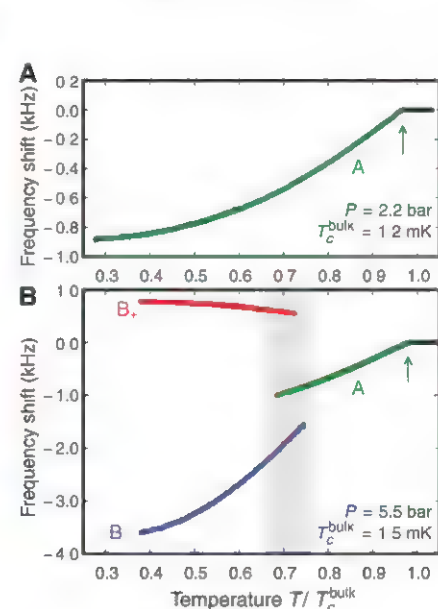


Fig. 2. NMR frequency shift signatures of superfluidity in the slab. (A) At 2.2 bar, a second-order phase transition (vertical arrow) is observed in the cavity between the normal state, in which the NMR precession occurs at the Larmor frequency, and the superfluid A phase, with a negative frequency shift. The superfluid transition temperature in the cavity is suppressed relative to that in bulk liquid T_c^{bulk} . (B) At 5.5 bar, there is also a first-order phase transition on cooling from the A phase to the planar-distorted B phase. The B phase has two possible configurations, B₊ and B₋, with positive and negative frequency shift, respectively. On cooling from the A phase, we observed either configuration or both, stochastically. The data are a compilation of several temperature sweeps. There is a region of coexistence of A and B phases around the A-B transition (gray). Data were obtained with diffuse walls.

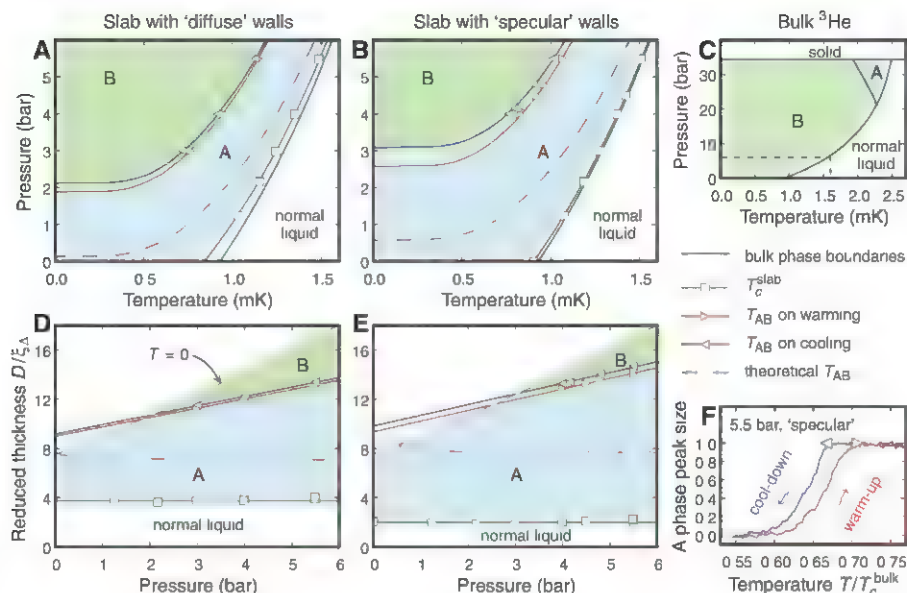


Fig. 3. Phase diagram of superfluid ^3He in the slab. (A and B) Phase diagram in the cavity with (A) diffuse and (B) specular walls. A-B phase boundary corresponds to the maximum cavity height at each pressure. (C) Bulk superfluid ^3He phase diagram (2) shown for comparison, in which the dashed region indicates the pressure range covered in plots (A) and (B). (D and E) Phase diagrams (A) and (B) respectively mapped into the reduced thickness $D/\xi_{\Delta}(T, P)$ versus pressure P plane (22) showing the boundary condition dependence of the superfluid transition temperature in the cavity T_c^{slab} and the A to planar-distorted-B transition temperature T_{AB} . The lines through the data are linear fits and are used to extrapolate the A-B phase boundary in the P - T plane in (A) and (B). The $T = 0$ value of $D/\xi_{\Delta}(T, P)$ is also shown (gray). The purple dashed line in (A) to (E) is the A-B phase boundary predicted by weak-coupling quasi-classical theory (30). (F) Signature of the A-B transition, from peak size of A-phase NMR line, on warming and cooling. The observed width of the transition is attributed to the slab thickness distribution. The features marked by triangles, observed on cooling and warming, are assigned to the maximum cavity thickness (22). Both cooling and warming data for the A-B transition are plotted in (A) to (E), placing bounds on the equilibrium transition temperature.

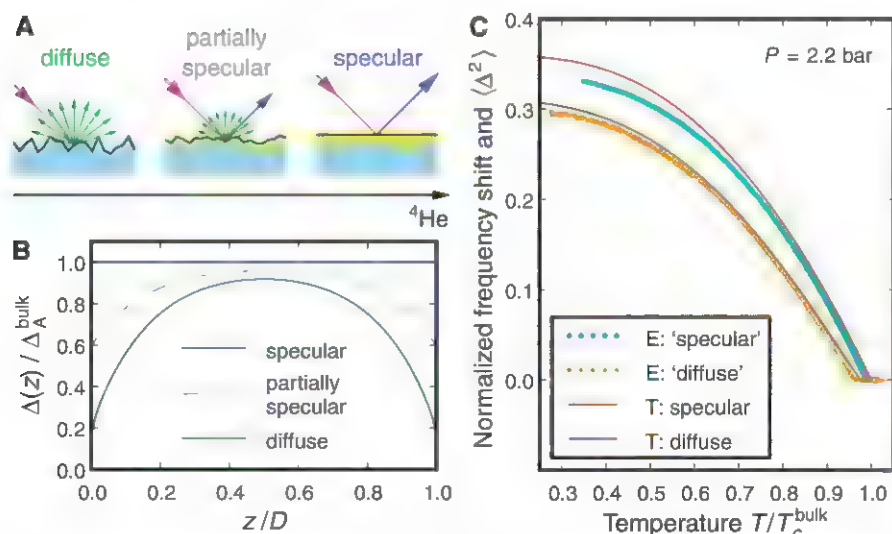


Fig. 4. Measured gap suppression in A phase and its dependence on boundary condition. (A) Quasi-particle scattering at boundary can be tuned from diffuse to specular by varying the thickness of a surface ^4He film (yellow). (B) Typical calculated A-phase gap profile for different boundaries (22–24). (C) Spatially averaged gap inferred from experimentally measured frequency shift (E) in comparison with results from quasi-classical theory (T) (24). The data are scaled so that the slope at T_c for specular scattering is unity (22).

relative spin-orbit orientations of the planar-distorted B phase (28). The positive shift corresponds to the orientation $L_z = -S_z$ presented above, for which both the nuclear Zeeman and spin-orbit energies are minimized. In the presence of confinement, the gap distortion induces an anisotropic magnetic susceptibility. As a result, a configuration of the B phase with $L_z = S_z$ may also be stabilized by the Zeeman energy, with order parameter $\Delta(\mathbf{p}) = \Delta_{\parallel}(z)(-\hat{p}_x + i\hat{p}_y)|\downarrow\downarrow\rangle + \Delta_{\parallel}(z)(\hat{p}_x + i\hat{p}_y)|\uparrow\uparrow\rangle + \Delta_{\perp}(z)\hat{p}_z[|\uparrow\downarrow\rangle + |\downarrow\uparrow\rangle]$. This state has a higher spin-orbit energy and a negative frequency shift. Because the planar-distorted B phase is nucleated at the first-order transition from the A phase, and the B- and B- configurations only differ energetically via the weak spin-orbit coupling energy, we observed an arbitrary distribution of B- and B- domains.

Confinement in the slab has a profound effect on the superfluid phase diagram (Fig. 3, A and B), as predicted theoretically (24, 29, 30). In bulk liquid ^3He in zero magnetic field, the equilibrium A phase exists only at high pressure, as a result of strong-coupling effects (Fig. 3C) (1, 2). Under confinement, a large area of the P - T plane at low pressures is opened up in which the A phase is stable. This arises from the weaker order parameter suppression of the A phase relative to the B phase owing to the absence of pairs with $L_z = 0$. The observed A-B transition occurs over a range of temperatures on both cooling and warming, arising from the distribution of cavity thickness. In addition, there is hysteresis between data taken on warming and cooling (Fig. 3F) that we tentatively attribute to pinning of the A-B boundary at scratches on the cell walls. The boundary conditions may be tuned in situ by plating the surface with ^4He because a thin superfluid ^4He layer is found to produce close to specular scattering (21). We have performed studies for two boundary conditions, denoted “diffuse” and “specular,” close to the diffuse and specular limits (22). We found that specular boundaries extend somewhat the region of stability of the A phase, as expected theoretically. They substantially reduce the suppression of the film superfluid transition temperature. The A-B phase boundary, mapped into the $D/\xi_{\Delta}(T, P)$ versus pressure plane (Fig. 3, D and E), reveals both a pressure-dependence and a shift relative to the predicted weak-coupling phase boundary (30). These observations are evidence for strong-coupling effects that persist to zero pressure.

We can measure the suppression of the A-phase gap, and its dependence on quasi-particle scattering boundary conditions, because the NMR frequency shift $|\Delta f| \propto \langle \Delta^2(z) \rangle$. Analysis of the frequency shift (Fig. 4) indicates good agreement with quasiclassical theory for the gap suppression by diffusely scattering walls (24) and demonstrates its predictive power.

Our results open the prospects for tailoring mesoscopic confinement and surface scattering both for the investigation of excitations in known topological superfluids and for the discovery of

new superfluid states. In particular, the environment may be optimized for the detection of Majorana fermions at the surface of $^3\text{He-B}$ and the Majorana-Weyl edge modes in chiral $^3\text{He-A}$ (31). Predicted new p-wave superfluids include a quasi-two-dimensional version of $^3\text{He-A}$ (a gapped $p_x + ip_y$ superfluid) (3) and a spatially modulated phase (32). Such experiments on dimensionally confined superfluid ^3He provide flexible model systems, when coupled with quasi-classical theory, for understanding topological superfluidity. This is likely to have considerable impact on the emerging field of topological quantum matter.

References and Notes

1. A. J. Leggett, *Rev. Mod. Phys.* **47**, 331 (1975).
2. D. Vollhardt, P. Wölfe, *The Superfluid Phases of ^3He* (Taylor & Francis, London, UK, 1990).
3. G. Volovik, *Exotic Properties of Superfluid ^3He* (World Scientific, Singapore, 1992).
4. G. Volovik, *The Universe in a Helium Droplet* (Oxford Univ. Press, London, 2002).
5. M. R. Norman, *Science* **332**, 196 (2011).
6. X.-L. Qi, S.-C. Zhang, *Rev. Mod. Phys.* **83**, 1057 (2011).
7. J. E. Moore, *Nature* **464**, 194 (2010).
8. R. Roy, <http://arxiv.org/abs/0803.2868>.
9. X.-L. Qi, T. L. Hughes, S. Raghu, S.-C. Zhang, *Phys. Rev. Lett.* **102**, 187001 (2009).
10. A. P. Schnyder, S. Ryu, A. Furusaki, A. W. W. Ludwig, *Phys. Rev. B* **78**, 195125 (2008).
11. A. P. Mackenzie, Y. Maeno, *Rev. Mod. Phys.* **75**, 657 (2003).
12. V. Ambegaokar, P. G. de Gennes, D. Rainer, *Phys. Rev. A* **9**, 2676 (1974).
13. F. Wilczek, *Nat. Phys.* **5**, 614 (2009).
14. S. B. Chung, S.-C. Zhang, *Phys. Rev. Lett.* **103**, 235301 (2009).
15. M. Stone, R. Roy, *Phys. Rev. B* **69**, 184511 (2004).
16. J. W. Serene, D. Rainer, *Phys. Rep.* **101**, 221 (1983).
17. S. Steel, J. P. Harrison, P. Zawadzki, A. Sachrajda, *J. Low Temp. Phys.* **95**, 759 (1994).
18. A. M. R. Schechter, R. W. Simmonds, R. E. Packard, J. C. Davis, *Nature* **396**, 554 (1998).
19. J. Xu, B. C. Crooker, *Phys. Rev. Lett.* **65**, 3005 (1990).
20. L. V. Levitin *et al.*, *Appl. Phys. Lett.* **91**, 262507 (2007).
21. M. R. Freeman, R. S. Germain, E. V. Thuneberg, R. C. Richardson, *Phys. Rev. Lett.* **60**, 596 (1988).
22. Materials and methods are available as supplementary materials on Science Online.
23. Y. Nagato, M. Yamamoto, K. Nagai, *J. Low Temp. Phys.* **110**, 1135 (1998).
24. A. B. Vorontsov, J. A. Sauls, *Phys. Rev. B* **68**, 064508 (2003).
25. A. I. Ahonen, M. Krusius, M. A. Paalanen, *J. Low Temp. Phys.* **25**, 421 (1976).
26. L. J. Buchholtz, G. Zwirgagl, *Phys. Rev. B* **23**, 5788 (1981).
27. C.-R. Hu, *Phys. Rev. Lett.* **72**, 1526 (1994).
28. Yu. M. Bunkov, G. E. Volovik, *Sov. Phys. JETP* **76**, 794 (1993).
29. L. H. Kjälman, J. Kurkijärvi, D. Rainer, *J. Low Temp. Phys.* **33**, 577 (1978).
30. Y. Nagato, K. Nagai, *Physica B* **284-288**, 269 (2000).
31. J. A. Sauls, *Phys. Rev. B* **84**, 214509 (2011).
32. A. B. Vorontsov, J. A. Sauls, *Phys. Rev. Lett.* **98**, 045301 (2007).

Acknowledgments: We thank S. Dimov, B. Ilic, and S. S. Verbridge for assistance with cell construction at Cornell Nano Fabrication Facility; S. T. Boogert and A. Bosco for advice and loan of equipment for optical thickness measurement; and M. Eschrig for critically reading the manuscript. This work was supported by Engineering and Physical Sciences Research Council grants EP/C52287/1, EP/E0541129/1, and EP/J022004/1, NSF grants DMR 0806629 and DMR-120991; and European Microkelvin Consortium (FP7 grant agreement 228464). We dedicate this paper to the memory of Professor Robert C. Richardson (1937–2013), who inspired this research.

Supplementary Materials

www.sciencemag.org/cgi/content/full/340/6134/841/DC1
Materials and Methods

Figs. S1 to S14

Table S1

References (33–49)

4 December 2012; accepted 11 March 2013

10.1126/science.1233621

3D Computational Imaging with Single-Pixel Detectors

B. Sun,^{1*} M. P. Edgar,¹ R. Bowman,^{1,2} L. E. Vittert,³ S. Welsh,¹ A. Bowman,³ M. J. Padgett¹

Computational imaging enables retrieval of the spatial information of an object with the use of single-pixel detectors. By projecting a series of known random patterns and measuring the backscattered intensity, it is possible to reconstruct a two-dimensional (2D) image. We used several single-pixel detectors in different locations to capture the 3D form of an object. From each detector we derived a 2D image that appeared to be illuminated from a different direction, even though only a single digital projector was used for illumination. From the shading of the images, the surface gradients could be derived and the 3D object reconstructed. We compare our result to that obtained from a stereophotogrammetric system using multiple cameras. Our simplified approach to 3D imaging can readily be extended to nonvisible wavebands.

Computational imaging based on projected patterns is an alternative technique to conventional imaging and removes the need for a spatially resolving detector. Instead, this form of computational imaging infers the scene by correlating the known spatial information of a changing incident light field with the total reflected (or transmitted) intensity. For example, two copies of a randomly generated light field can be made with a beam splitter; one copy of the light field interacts with the object and a non-spatially resolving detector, and the other copy is

recorded with a camera. Aggregating the correlations between the two detectors yields an image even though the light striking the camera has never interacted with the object. This phenomenon, called ghost imaging, has been demonstrated in both the quantum and classical regimes (1–9).

Such imaging systems can be simplified by using a device capable of generating computer-programmable random light fields, which obviates the requirement for the beam splitter and the camera because knowledge of the light field is held in the computer memory. This type of system was initially called computational ghost imaging (10) but is similar in approach to more standard computational imaging systems, which use projected light patterns [albeit usually highly structured (11, 12)]. We also note that the use of projected patterns is related to the field of single-

pixel cameras (13), where the programmable component is used to filter the detected, rather than illuminating, light.

In both single-pixel cameras and computational imaging systems, inverting the known random patterns and the measured intensities is a computational problem. A number of sophisticated algorithms have been developed over the years to improve the signal-to-noise ratio (SNR) for different systems (14, 15), but with appropriate normalization (16) a simple iterative algorithm was adopted for this experiment.

Previous experiments in single-pixel computational imaging (9, 14, 16) were restricted to relatively small (less than 10 cm) two-dimensional (2D) images, mainly of 2D template objects or 2D outlines of 3D objects. In the present work, we capture the 3D spatial form of an object by using several single-pixel detectors in different locations. A 2D image is derived from each detector but appears as if it is illuminated differently from the others. Comparing the shading information in the images allows the surface gradient and hence the 3D form of the surface to be reconstructed.

The experimental setup (Fig. 1) consists of a digital light projector to illuminate objects with random binary light patterns, four spatially separated single-pixel photodetectors to measure the intensity of the reflected light, an analog-to-digital converter to digitize the photodetector signals, and a computer to generate the random speckle pattern as well as perform 3D reconstructions of the test object.

The digital light projector comprises a red, green, and blue light-emitting diode illumination source and a digital micromirror device (DMD) to generate the structured illumination

¹Scottish Universities Physics Alliance, School of Physics and Astronomy, University of Glasgow, Glasgow G12 8QQ, UK.

²Department of Physics, Cavendish Laboratory, University of Cambridge, Cambridge CB3 0HE, UK. ³School of Mathematics and Statistics, University of Glasgow, Glasgow G12 8QQ, UK.

*Corresponding author. E-mail: b.sun.1@research.gla.ac.uk

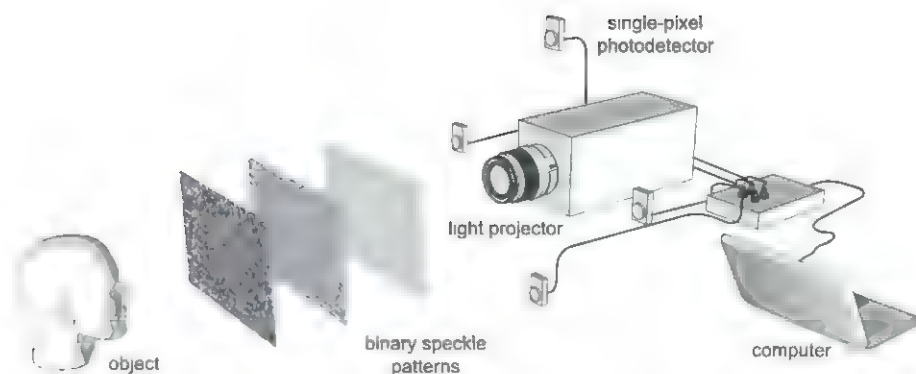


Fig. 1. Experimental setup used for 3D surface reconstructions. The light projector illuminates the object (head) with computer-generated random binary speckle patterns. The light reflected from the object is collected on four spatially separated single-pixel photodetectors. The signals from the photodetectors are measured and used to reconstruct a computational image for each photodetector.

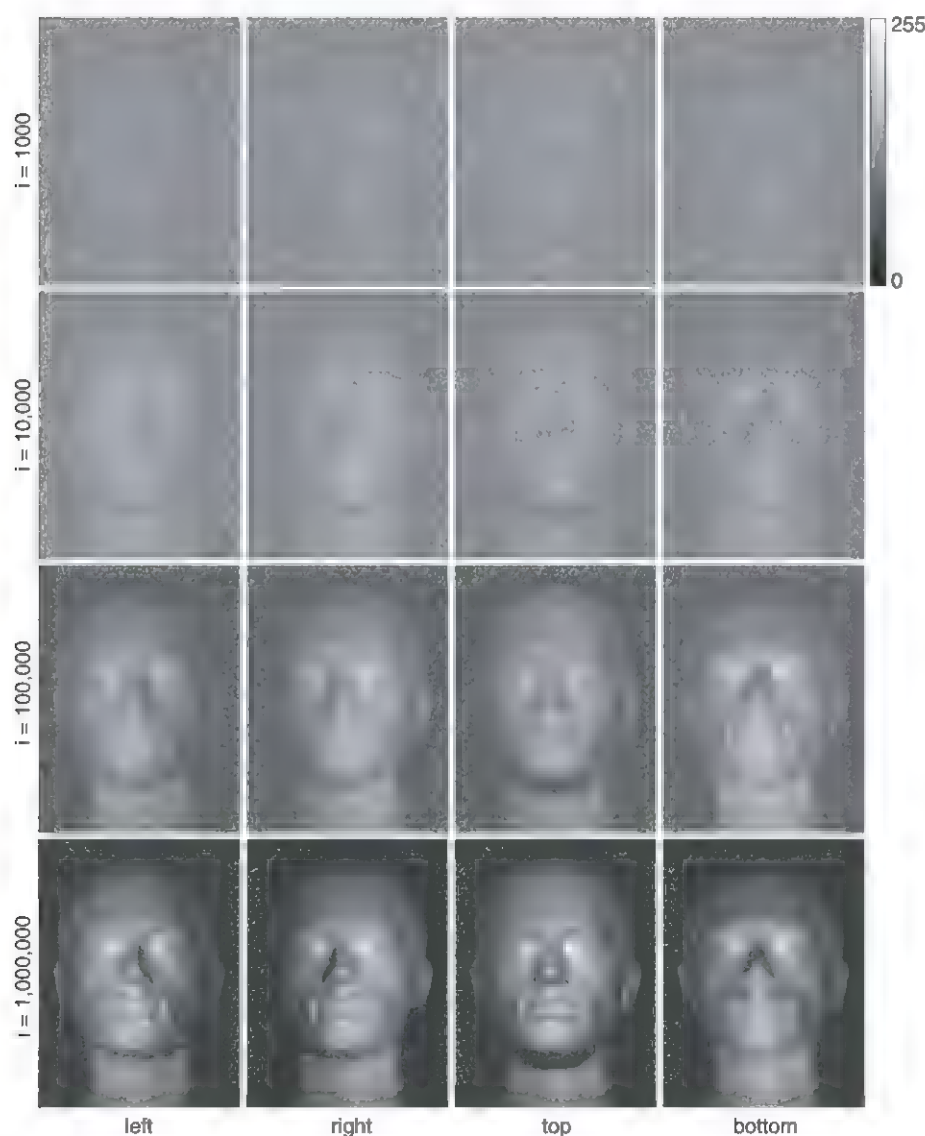


Fig. 2. Source images from the four single-pixel detectors from 1000 to 1 million iterations. The images from each photodetector are reconstructed using an iterative algorithm (described in the text). The spatial information in each image is identical; however, the apparent illumination source is determined by the location of the relevant photodetector, indicated underneath. No postprocessing has been applied to the images. The scale refers to the relative intensity of the images (in arbitrary units, 0 to 255).

(see supplementary materials). Note that the large operational bandwidth of the DMD (300 nm to 2 μ m) enables the use of this technique at other wavelengths that are potentially unsuitable for existing imaging technologies.

The projected patterns are randomly distributed binary patterns, with a black-to-white ratio of 1:1, that are projected onto the object. The life-sized mannequin head is positioned about 1 m from the lens so that it fits within the projected pattern. Four spatially separated single-pixel photodetectors are positioned in the plane of the lens, separated by 500 mm and each pointing toward a common point on the object to record the back-scattered light. For every binary pattern projected, the corresponding object intensity is measured by each photodetector, and the data are fed to a computer algorithm.

DMD-based projectors create color images by displaying 24 binary images (bit planes) per frame in quick succession. By alternating between a binary pattern and its inverse in subsequent bit planes, we can demodulate the measured signal at the frequency of the bit plane projection (1440 Hz) to isolate the backreflected signal from light sources at other frequencies such as room lighting. Because the speckle pattern has equal numbers of black and white pixels, the measured signals for each pattern can be normalized; this has been shown to improve the SNR of the final reconstruction (16).

In all iterative techniques, a 2D representation of the object is reconstructed by averaging the product of the measured photodetector signal and the incident pattern over many patterns. A sequence of M binary patterns, $P_i(x, y)$, are reflected from the object, giving a sequence of measured signals S_i . The 2D reconstruction $I(x, y)$, which provides an estimate of the object, can be stated as

$$I(x, y) = \langle (S_i - \langle S_i \rangle) (P_i(x, y) - \langle P_i(x, y) \rangle) \rangle \quad (1)$$

where angle brackets denote an ensemble average for M iterations, $(1/M)\sum$.

Using Eq. 1, we obtain 2D reconstructions of the object for each of the four photodetectors. Because all the images are derived from the same set of projected patterns, the (x, y) locations of the features in each image are identical. However, the intensity distribution in each image is different, because the apparent lighting of the object is dependent on the location of the detector used to record the backscattered light (optical imaging systems are reciprocal; see supplementary materials). Thus, in contrast to imaging systems based on multiple cameras, the perspective of the single-pixel detector does not render geometrical distortion to the object being imaged.

Depth information of a scene is normally lost in a 2D image, but there are instances where it can be inferred using a technique called "shape from shading" (SFS) (17, 18). From a single image with one source of illumination, this method

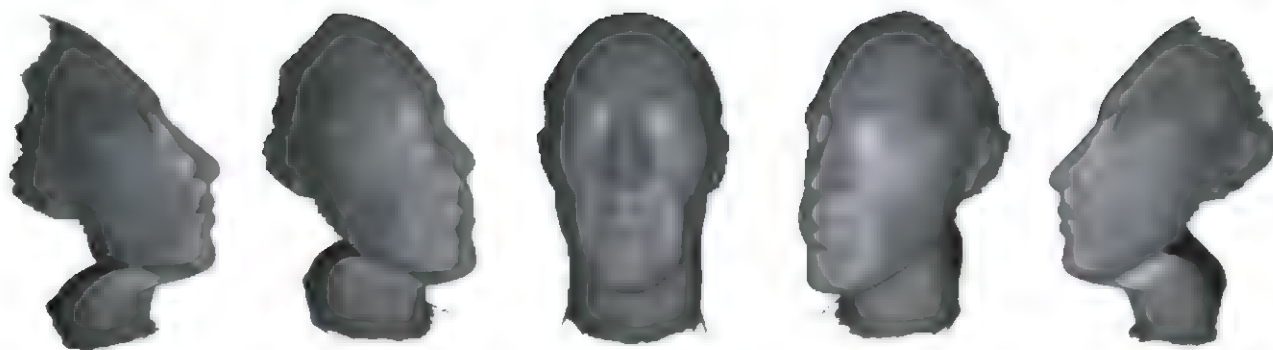


Fig. 3. 3D reconstruction of the object. Rendered views of the reconstructed facial surface derived by integration of the surface normal data and overlaid with the reflectivity data (see movie S1).

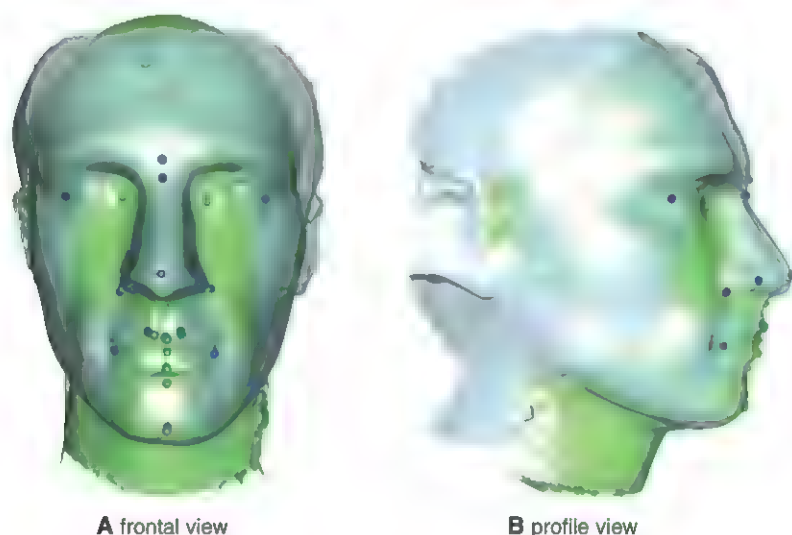


Fig. 4. Comparison between computational imaging and a stereophotogrammetric imaging system. Computational imaging (green) and stereophotogrammetric (blue) reconstructions of the mannequin head, from frontal (A) and profile (B) viewpoints, are shown with anatomical landmarks (color-coded green and blue, respectively) added.

relies on the shading caused by geometrical features to reveal the depth of the scene. Many SFS methods assume that the object exhibits uniform Lambertian (matte) reflectance and that a single light source is located at infinity, such that the incoming lighting vector is constant across the surface of the object. The test objects used in our experiment exhibit Lambertian reflectance (see supplementary materials) and so this assumption is valid. An alternative technique, called photometric stereo (19, 20), adopts the same assumptions but uses multiple images, each with a different illumination and taken from the same viewpoint, similar to the types of images retrieved by our 3D computational imaging system.

The intensity of a pixel (x, y) in the image obtained from the i th detector can be expressed as

$$I_i(x, y) = I_s \alpha(d_i \cdot \hat{n}) \quad (2)$$

where I_s is the source intensity, α is the surface reflectivity, \hat{d}_i is the unit detector vector pointing from the object to the detector, and \hat{n} is the sur-

face normal unit vector for the object. Thus, for N images, we can write Eq. 2 as

$$I(x, y) = I_s \alpha(D \cdot \hat{n}) \quad (3)$$

where D is an array containing the unit detector vectors and I is an array containing the corresponding image intensities. For any pixel (x, y), the unit surface normal is

$$\hat{n} = \frac{1}{I_s \alpha(D^{-1} \cdot I)} \quad (4)$$

and the surface albedo (reflectivity) is

$$\alpha = D^{-1} \quad (5)$$

From these surface normals, calculated for each pixel, it is possible to determine the gradient between adjacent pixels, from which we obtain the surface geometry by integration. Because we record four images, the problem becomes overconstrained; the surface normals represent only two degrees of freedom per pixel. We can thus remove our assumption of uniform reflectivity and

recover an estimate of the surface albedo α at the same time as finding the object's shape.

The gradients are integrated to find the shape of the object, starting at the center and working outward. The height of the surface at a given point can be estimated from a nearest-neighbor point using the height of that point and the gradient of the surface. Because the center of each pixel is associated with the measured gradient data, we use the mean of the gradient at the nearest-neighbor pixel and the gradient at the pixel to be evaluated. For each point where the height is being estimated, the value used is the mean of the estimates from each nearest neighbor.

After the integration has been performed to provide an initial estimate of the object's shape, an optimization step refines the shape, where the cost function is the sum of the squared differences between the gradients of the reconstructed surface and the gradients recovered from the photometric stereo measurement. As described above, it is possible to estimate the height of a pixel on the basis of the height and gradient at each of its neighboring pixels. Our simple optimization works one pixel at a time, each iteration setting the pixel's height such that it matches the mean estimate from each of its nearest neighbors. In the case of a pixel that is surrounded by other pixels with height estimates, this corresponds to setting the Laplacian of the reconstructed height field equal to the Laplacian calculated from the measured gradient data. In the case of pixels at the edge of the object, this is equivalent to assuming that the gradient measured perpendicular to the edge of the object is accurate. These two criteria are suggested by Horn (20). Because the optimal value for any given pixel can be calculated quickly (in both cases it is a linear operation), millions of iterations could be carried out in a few minutes, corresponding to approximately 100 passes over each pixel on average.

Once the algorithm had been appropriately calibrated by imaging flat and spherical surfaces (with the same surface material and reflective properties), accounting for changes of the lighting vector for different pixels across the object plane,

the system was tested for objects with geometric complexity. One object investigated was a life-size white polystyrene mannequin head, with approximate dimensions 190 mm × 160 mm × 250 mm. Using the 2D images shown in Fig. 2, we calculated for each pixel the reflectivity, the surface normals, the surface gradient, and the estimated depth as prescribed by our model. A standard 3D graphic package was then used to visualize this profile, overlaid with the reflectivity data, as illustrated in Fig. 3.

To quantify the accuracy of our approach, we compared the 3D reconstruction of the test object with a 3D image captured from a stereophotogrammetric camera system. This latter system uses a matching algorithm on the 2D images from multiple cameras to recover the distance map of an object from the cameras. The accuracy of this system with facial shapes is well documented (21) to have a root mean square error (RMSE) on the order of 1 mm for central facial locations, but the error can rise substantially (2 cm) at side locations where the surface normals are close to perpendicular to the line of sight.

To compare the facial profiles measured by the two systems, we characterized the shapes according to well-defined facial locations (22): nose tip, mouth corners, etc. Figure 4 shows two sets of 21 such anatomical landmarks superimposed on these facial images by a trained observer. After lateral and angular registration and subsequent depth scaling, the RMSE of our 3D computational imager is found to be slightly below 4 mm. In common with camera-based stereophotogrammetry, the observed error is greater toward the edge of the object, around the ears and upper

forehead. The increased error is a consequence of the projected pattern expanding at greater depth and highlights one limitation of the system. Our approach to minimizing this effect is to use a lens with suitable focal length for projection (see supplementary material).

Beyond showing that high-quality images of real-life objects can be captured using a single-pixel photodetector, our experiment demonstrates that by using a small number of single-pixel detectors, computational imaging methods can yield 3D images. An important difference between our technique and the multiple-camera approach is that a single projector determines the spatial resolution of the system, removing issues of pixel alignment associated with multiple cameras. Furthermore, reversing the fundamental imaging process allows for the use of simpler, less expensive detectors. The operational bandwidth of the system is limited not by the efficiency of a pixelated imaging detector but instead by the reflectivity of the DMD used for light projection, whose efficiency extends well beyond the visible spectrum. The development of such technology—for example, the use of a broadband white light source—could enable computational imaging systems to become a cheaper alternative for applications in 3D and multispectral imaging.

References and Notes

1. T. B. Pittman, Y. H. Shih, D. V. Strekalov, A. V. Sergienko, *Phys. Rev. A* **52**, R3429 (1995).
2. D. V. Strekalov, A. V. Sergienko, D. N. Klyshko, Y. H. Shih, *Phys. Rev. Lett.* **74**, 3600 (1995).
3. R. S. Bennink, S. J. Bentley, R. W. Boyd, *Phys. Rev. Lett.* **89**, 113601 (2002).
4. A. Gatti, E. Brambilla, M. Bache, L. A. Lugiato, *Phys. Rev. A* **70**, 013802 (2004).

5. A. Valencia, G. Scarcelli, M. D'Angelo, Y. Shih, *Phys. Rev. Lett.* **94**, 063601 (2005).
6. F. Ferri et al., *Phys. Rev. Lett.* **94**, 183602 (2005).
7. B. Jack et al., *Phys. Rev. Lett.* **103**, 083602 (2009).
8. J. H. Shapiro, R. W. Boyd, *Quantum Inf. Process* **11**, 949 (2012).
9. Y. Bromberg, O. Katz, Y. Silberberg, *Phys. Rev. A* **79**, 053840 (2009).
10. J. H. Shapiro, *Phys. Rev. A* **78**, 061802 (2008).
11. M. S. Mermelstein, thesis, Massachusetts Institute of Technology (1999).
12. J. Ryu, S. S. Hong, B. K. P. Horn, D. M. Freeman, M. S. Mermelstein, *Appl. Phys. Lett.* **88**, 171112 (2006).
13. M. F. Duarte et al., *IEEE Signal Process. Mag.* **25**, 83 (2008).
14. O. Katz, Y. Bromberg, Y. Silberberg, *Appl. Phys. Lett.* **95**, 131110 (2009).
15. F. Ferri, D. Magatti, L. A. Lugiato, A. Gatti, *Phys. Rev. Lett.* **104**, 253603 (2010).
16. B. Sun, S. S. Welsh, M. P. Edgar, J. H. Shapiro, M. J. Padgett, *Opt. Express* **20**, 16892 (2012).
17. B. K. P. Horn, *Artif. Intell.* **8**, 201 (1977).
18. M. J. Brooks, B. K. P. Horn, *Shape from Shading* (MIT Press, Cambridge, MA, 1989).
19. R. J. Woodham, *Opt. Eng.* **19**, 191139 (1980).
20. B. K. P. Horn, *Robot Vision* (MIT Press, Cambridge, MA, 1986).
21. B. Khambay et al., *Br. J. Oral Maxillofac. Surg.* **46**, 27 (2008).
22. L. G. Farkas, *Anthropometry of the Head and Face* (Raven Press, New York, 1994).

Acknowledgments: Supported by the Royal Society and the Wolfson Foundation (M.J.P.) and by the UK Engineering and Physical Sciences Research Council. B.S. and M.P.E. thank D. Giovannini for useful discussions. All authors contributed equally to this work and to the writing of the manuscript.

Supplementary Materials

www.sciencemag.org/cgi/content/full/340/6134/844/DC1
Materials and Methods
Supplementary Text
Figs. S1 to S3
Movie S1

26 December 2012; accepted 28 March 2013
10.1126/science.1234454

Computationally Assisted Identification of Functional Inorganic Materials

Matthew S. Dyer,¹ Christopher Collins,¹ Darren Hodgeman,¹ Philip A. Chater,¹ Antoine Demont,¹ Simon Romani,² Ruth Sayers,¹ Michael F. Thomas,³ John B. Claridge,¹ George R. Darling,¹ Matthew J. Rosseinsky^{1*}

The design of complex inorganic materials is a challenge because of the diversity of their potential structures. We present a method for the computational identification of materials containing multiple atom types in multiple geometries by ranking candidate structures assembled from extended modules containing chemically realistic atomic environments. Many existing functional materials can be described in this way, and their properties are often determined by the chemistry and electronic structure of their constituent modules. To demonstrate the approach, we isolated the oxide $\text{Y}_{2.24}\text{Ba}_{2.28}\text{Ca}_{3.48}\text{Fe}_{7.44}\text{Cu}_{0.56}\text{O}_{21}$, with a largest unit cell dimension of over 60 angstroms and 148 atoms in the unit cell, by using a combination of this method and experimental work and show that it has the properties necessary to function as a solid oxide fuel-cell cathode.

The identification and synthesis of functional materials is a substantial challenge for both experiment and theory, especially for complex crystalline materials (those containing many atoms of different elements in distinct geometries). There are a vast number of arrange-

ments of the atoms in the unit cell of a complex structure that need to be adequately sampled for structural identification and prediction (1). Different theoretical approaches to this problem have been developed; some involve an unbiased search through the different atomic arrangements (2–7),

whereas others use existing chemical knowledge and understanding to reduce the number of arrangements considered (8–14).

In describing complex solid-state structures, it is customary to break them down in terms of modules or fragments and their combinations (15). Structural units—such as blocks, rods, or layers (as shown in Fig. 1, A and B, for two different structural families)—derived from archetypal structures are combined by structure-building operators. Within this approach, the combination of two or more layers from different crystal structures, a concept known as polysomatism (16), has proved powerful. The diverse families described as polysomatic series in terms of layers include heterogeneous structural series of intermetallics (17); light-element networks, such as the aluminum carbonitrides (18) (Fig. 1A); mineral families (19), such as the sapphires (20) and biopyrroles (16); and accretional series within

¹Department of Chemistry, University of Liverpool, Crown Street, Liverpool L69 7ZD, UK. ²Centre for Materials and Structures, School of Engineering, The Quadrangle, University of Liverpool, Brownlow Hill, Liverpool L69 3GH, UK. ³Department of Physics, University of Liverpool, Liverpool L69 7ZL, UK.

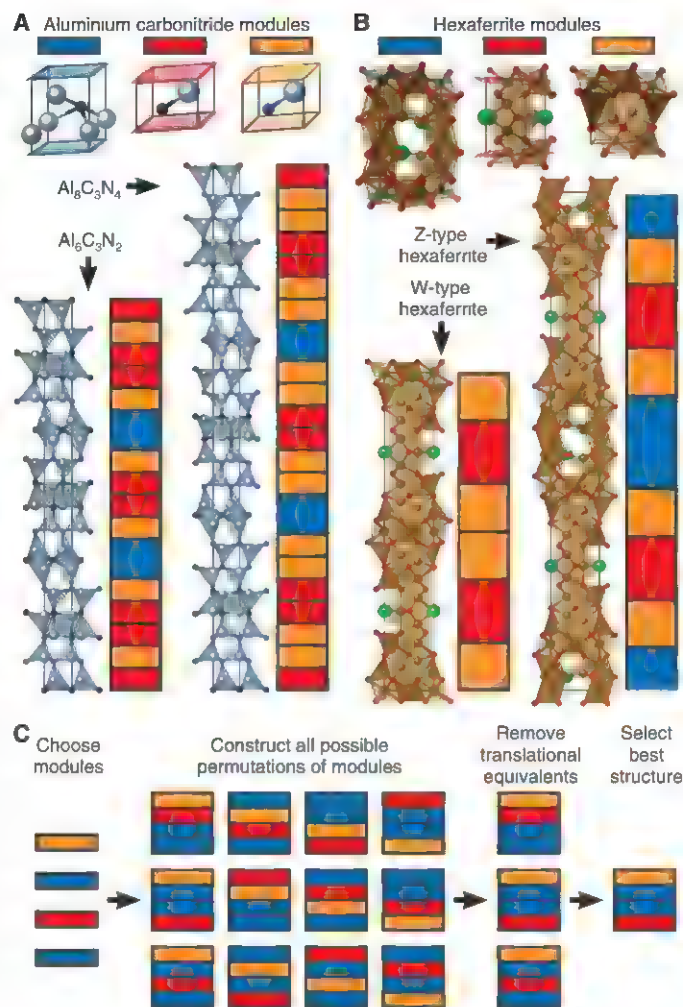
*Corresponding author. E-mail: m.j.rosseinsky@liverpool.ac.uk

the perovskite family (21), including Aurivillius and Dion-Jacobson phases, and families of hexagonal perovskites (22). It is possible to envisage polysomatic series using larger layers, including the complex ferrites (Fig. 1B), some of the largest-volume functional inorganic structures known (23). The functional behavior can be directly controlled by the constituent layers; for example, lone pair-based fluorite-like layers in the Aurivillius series can produce high-temperature ferroelectricity, whereas the Ba-containing R and T blocks (red and blue, respectively, in Fig. 1B) in the hexaferrites impose large magnetic anisotropy (24).

We use the combination of layers in the extended module materials assembly (EMMA) approach adopted here to identify new candidate structures as outlined in Fig. 1C. First, a set of extended layers (modules) must be chosen. Next, the number of times each module appears within a single repeated unit cell is selected. At this point, all possible permutations of the modules within the unit cell are created by using chosen structure-building operators. The present examples used translation along the long axis and inversion symmetry; however, other symmetry operations could be included. The number of candidate structures is reduced by removing duplicates of the same cyclical stacking sequence. Those remaining are ranked according to some suitable selection criteria to give the most promising candidates for experimental synthesis. We initially ranked a large number of structures by using energies obtained from a preliminary structural relaxation by classical force-field methods (25) (although any cost function suitable for the system under study could be used). The relative stabilities of the best candidates were evaluated quantitatively by using ab initio calculations (25). The extended modules encode bonding information directly into the candidate structures, mainly creating structures in which atoms are in chemically sensible environments where the use of force fields is valid. There is no conceptual limit to the nature or size of the modules, although we have concentrated on one-atom-thick metal oxide layers in this study. A practical limit exists on the number of modules within a single repeat, because the total number of permutations becomes very large with more than 15 to 20 modules. This limitation could be circumvented by searching through possible permutations with use of methods such as evolutionary algorithms (5, 7). Finite computational resources will also limit the overall size of the generated unit cell (a product of the number of modules and their individual sizes).

The perovskite ABO_3 structure can be described by stacking AO rock-salt and BO_2 square-layer modules that contain large A and smaller transition-metal B cations. There are a large number of possible superstructures derived by coupled cation-site and anion-vacancy ordering, such as $YBa_2Ca_2Fe_5O_{13}$, which functions as a solid oxide fuel-cell (SOFC) cathode (26). We select anion vacancy-containing modules to construct superstructures containing Fe^{3+} ions. Such units afford

Fig. 1. Assembling structures with extended modules. (A) A modular description of the aluminum carbonitride structural family. Modules of composition Al_2C (blue), AlC (red), and AlN (orange) are used to describe the extended structures of $Al_6C_3N_2$ and $Al_8C_3N_4$ (23). Atoms are colored as follows: light blue, Al; black, C; and dark blue, N. Al-C/N tetrahedra are shaded in light blue to guide the eye. (B) A modular description of the hexaferrite structural family. Modules of composition $Ba_2Fe_8O_{14}$ (T block, blue), $(BaFe_6O_{13})^{2-}$ (R block, red), and $(Fe_6O_8)^{2+}$ (S block, orange) are used to describe the extended structures of W- and Z-type hexaferrites (32). Atoms are colored as follows: green, Ba; brown, Fe; and red, O. Fe-O polyhedra are shaded in brown to guide the eye. (C) A schematic outlining the EMMA method of constructing and screening possible structures arising from extended modular units. In this case, four layered units are chosen, with two equivalent units. All 12 permutations of these units are built into structures, of which three are unique under translational symmetry. These three are tested, and the best structure chosen.



both electronic conductivity and oxide ion transport, which are required for functionality as an SOFC cathode. We validated the EMMA approach by reproducing the structure of this material. By generating a set of structures that use $2Y_4 + 4Ba_4O_4 + 4Ca_4O_4 + 2Fe_4O_4 + 8Fe_4O_8$ modules (Fig. 2A) in a cell of dimensions $2a_p$ by $2a_p$ by $10a_p$, where $a_p \approx 3.9$ Å is the dimension of an ABO_3 unit cell, we obtained 14,190 structures with 184 atoms per unit cell. The $AO_{1/8}$ and $BO_{2/8}$ ($0 \leq \Delta \leq 1$) modules were permuted separately. For each permuted arrangement of $AO_{1/8}$ and $BO_{2/8}$ modules, a candidate structure was constructed by stacking alternate $AO_{1/8}$ and $BO_{2/8}$ modules. During the initial relaxation (25), 7628 structures failed to converge because of poor starting geometries and were rejected. The three structures shown in Fig. 2C are significantly lower in energy than the others (Fig. 2B), with an energetic spread of only 0.02 eV per formula unit (FU, here $YBa_2Ca_2Fe_5O_{13}$) and a separation in energy of 0.15 eV per FU to the next structure; the experimental $YBa_2Ca_2Fe_5O_{13}$ structure is the second most stable. These four most stable struc-

tures were then relaxed by using density functional theory (DFT) (25) to improve the energetics. The most stable structure by 0.09 eV per FU using DFT (Fig. 2D) corresponds to the known experimental structure for $YBa_2Ca_2Fe_5O_{13}$, demonstrating that the EMMA approach can correctly identify a known structure.

We experimentally explored the partial substitution of 7% Cu^{2+} for Fe^{3+} in order to increase the electronic conductivity of $YBa_2Ca_2Fe_5O_{13}$ and therefore improve its performance as an SOFC cathode. This resulted in a multiphase sample, suggesting that other phases are accessible near this composition. One phase gave a powder x-ray diffraction pattern with Bragg reflections indicative of an $8a_p$ repeat and an energy-dispersive x-ray spectroscopy (EDX)-derived cation composition of $Y_{2.1(2)}Ba_{1.8(2)}Ca_{4.1(2)}Fe_{7.4(2)}Cu_{0.6(2)}$ (the estimated standard error in units of the last quoted decimal place is shown in parentheses). We attempted to identify the structure of this phase by the EMMA method, which targeted the idealized compositions $Y_2Ba_2Ca_4Fe_8O_{21}$ and $Y_2Ba_2Ca_4Fe_{7.5}Cu_{0.5}O_{21}$

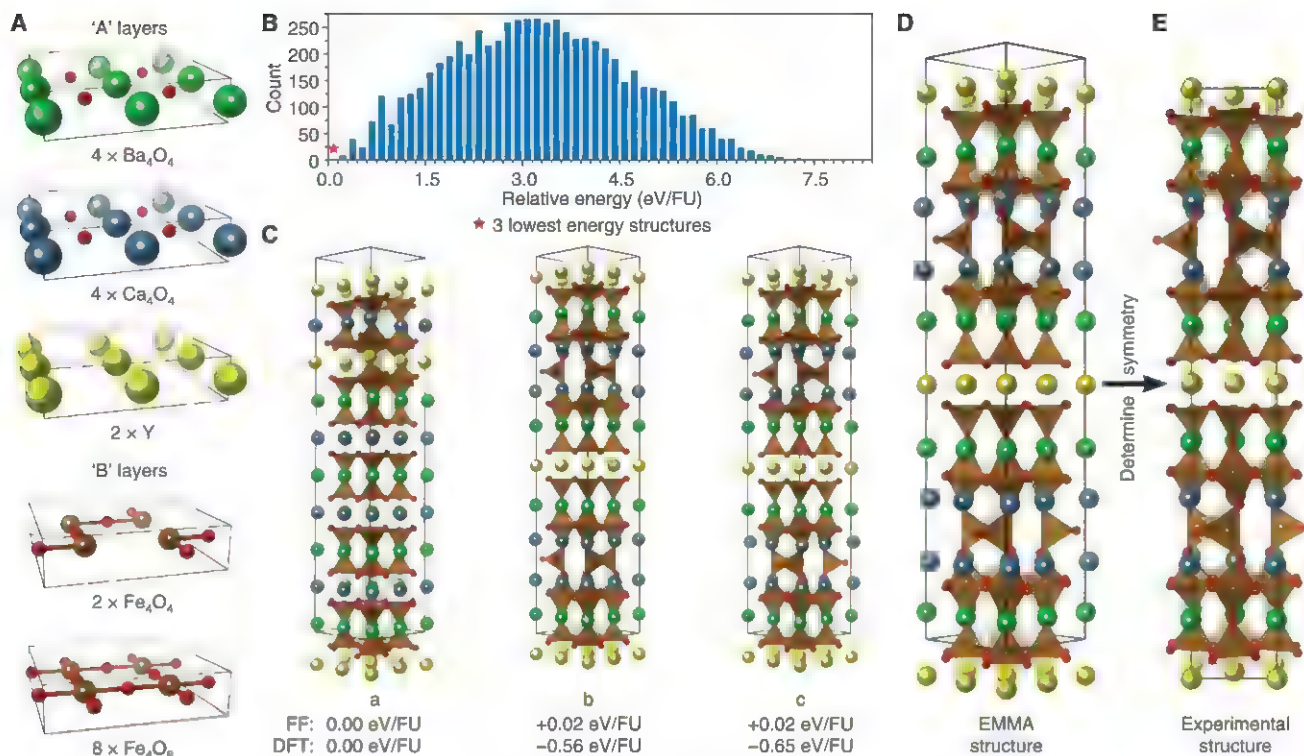
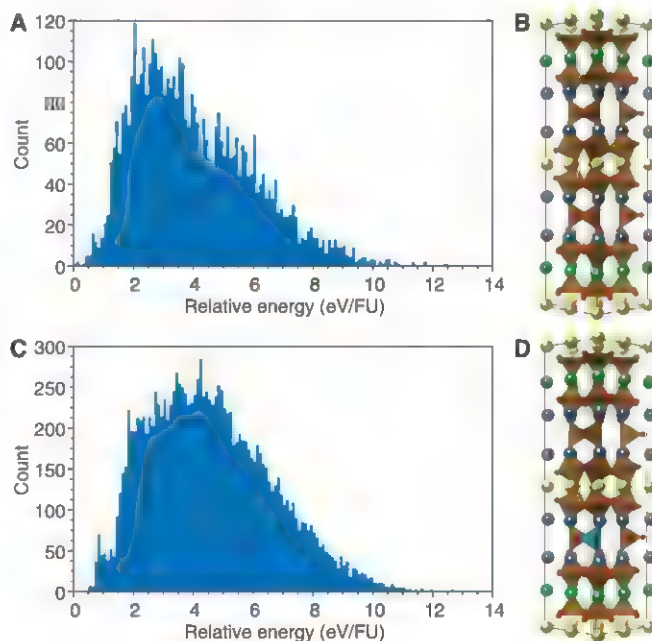


Fig. 2. The $10a_p$ structure of $\text{YBa}_2\text{Ca}_2\text{Fe}_5\text{O}_{13}$. (A) The A- and B-site layered units used as the base structural modules throughout this work, (B) a graph showing the force-field energies of all calculated structures, (C) the three lowest-energy structures predicted from force-field calculations and their

relative energies calculated by using both force-fields and DFT, (D) the lowest-energy structure from EMMA, and (E) the refined experimental structure. Atoms are colored as follows: yellow, Y; green, Ba; blue, Ca; brown, Fe; and red, O.

Fig. 3. EMMA calculations on structures with an $8a_p$ repeat. The energies of structures with the composition $\text{Y}_2\text{Ba}_2\text{Ca}_4\text{Fe}_8\text{O}_{21}$ with converged force-field calculations are plotted in (A), and those with composition $\text{Y}_2\text{Ba}_2\text{Ca}_4\text{Fe}_{7.5}\text{Cu}_{0.5}\text{O}_{21}$ are plotted in (C). The most stable $\text{Y}_2\text{Ba}_2\text{Ca}_4\text{Fe}_8\text{O}_{21}$ and $\text{Y}_2\text{Ba}_2\text{Ca}_4\text{Fe}_{7.5}\text{Cu}_{0.5}\text{O}_{21}$ structures are shown in (B) and (D), respectively. Atoms are colored as follows: yellow, Y; green, Ba; blue, Ca; brown, Fe; light blue, Cu; and red, O.



(Fig. 3). These are candidate $\text{Fe}^{3+}/\text{Cu}^{2+}$ compositions based on eightfold multiples of the basic ABO_3 perovskite formula unit with repeat dimension a_p ($8a_p$). By using these target compositions and a box of dimensions $2a_p$ by $2a_p$ by $8a_p$ (where $a_p \approx 3.9$ Å) that accommodates mul-

tiples orderings of the cations on the basis of the target composition, we generated 6300 structures for $\text{Y}_2\text{Ba}_2\text{Ca}_4\text{Fe}_8\text{O}_{21}$ with use of three chemically sensible choices of modules, expanded from those used for $\text{YBa}_2\text{Ca}_2\text{Fe}_5\text{O}_{13}$ in which the constituent modules were already known. The module

sets each included $2\text{Ba}_4\text{O}_4 + 4\text{Ca}_4\text{O}_4 + 5\text{Fe}_4\text{O}_8$ modules and then a combination of either $2\text{Y}_4 + \text{Fe}_4\text{O}_4 + 2\text{Fe}_4\text{O}_8$, $\text{Y}_4 + \text{Y}_4\text{O}_4 + 2\text{Fe}_4\text{O}_4 + \text{Fe}_4\text{O}_8$, or $2\text{Y}_4\text{O}_4 + 3\text{Fe}_4\text{O}_4$ modules. The three sets of modules place the oxygen vacancies in different combinations of Y_4 and Fe_4O_4 layers, allowing for flexibility in the final structures while using chemical intuition to guide the initial location of oxygen vacancies. A total of 17,640 structures for $\text{Y}_2\text{Ba}_2\text{Ca}_4\text{Fe}_{7.5}\text{Cu}_{0.5}\text{O}_{21}$ were constructed by using $2\text{Ba}_4\text{O}_4 + 4\text{Ca}_4\text{O}_4 + 2\text{Y}_4 + 5\text{Fe}_4\text{O}_8 + \text{Fe}_4\text{O}_4 + 2\text{Fe}_3\text{CuO}_8$ modules, with Cu atoms at different locations within the two Fe_3CuO_8 modules.

After initial relaxation of the structures (Fig. 3), one $\text{Y}_2\text{Ba}_2\text{Ca}_4\text{Fe}_{7.5}\text{Cu}_{0.5}\text{O}_{21}$ structure was 0.42 eV per FU more stable than all others (Fig. 3D). We relaxed the 20 lowest-energy structures at this composition by using DFT, confirming that the predicted lowest-energy structure is the same from both force-field and DFT calculations. The same lowest-energy structure was also found for $\text{Y}_2\text{Ba}_2\text{Ca}_4\text{Fe}_8\text{O}_{21}$ (Fig. 3B). We note that extensive relaxation of local structure and cell dimensions away from the initial module-constrained structures was observed at the force-field stage, suggesting that considerable movement away from the starting structures is possible and reducing the bias in the prediction because of our original choice of modules (fig. S1). However, the lowest-energy structure was only found by using one of the three sets of starting modules for $\text{Y}_2\text{Ba}_2\text{Ca}_4\text{Fe}_8\text{O}_{21}$,

which illustrates the need to consider a variety of different starting modules to ensure identification of the optimal final structures.

In parallel with the EMMA calculations, the experimental phase diagram was investigated by synthesis at similar compositions (Fig. 4F). Synthesis of $\text{Y}_2\text{Ba}_2\text{Ca}_4\text{Fe}_{7.5}\text{Cu}_{0.5}\text{O}_{21}$ generated a polyphasic material containing a perovskite-derived phase with the apparent $8a_p$ repeat (fig. S2).

Competing phases observed in this system were two $10a_p$ phases related to $\text{YBa}_2\text{Ca}_2\text{Fe}_5\text{O}_{13}$, a $3a_p$ $\text{Sr}_2\text{LaFe}_3\text{O}_8$ -related structure (27), $\text{YCa}_4\text{Fe}_5\text{O}_{13}$, and Y_2O_3 . Isolation of the target compound in phase-pure form suitable for structure refinement and property characterization requires experimental optimization of the global composition and synthesis conditions (25) through a classical phase-diagram study (Fig. 4F) to afford compound **1**, with the

nominal composition $\text{Y}_{2.24}\text{Ba}_{2.28}\text{Ca}_{3.48}\text{Fe}_{7.44}\text{Cu}_{0.56}\text{O}_{21}$ [EDX-derived cation composition $\text{Y}_{2.07(15)}\text{Ba}_{2.49(20)}\text{Ca}_{3.44(5)}\text{Fe}_{7.63(18)}\text{Cu}_{0.37(7)}$]. Selected area electron diffraction (SAED) (25) evaluation of this sample revealed that the longest axis in the unit cell is a $16a_p$ repeat derived from body-centering superposition of the $8a_p$ blocks (Fig. 4J and fig. S3). A compound with the same $16a_p$ repeat but without any Cu in the material, **2**, has been synthesized as

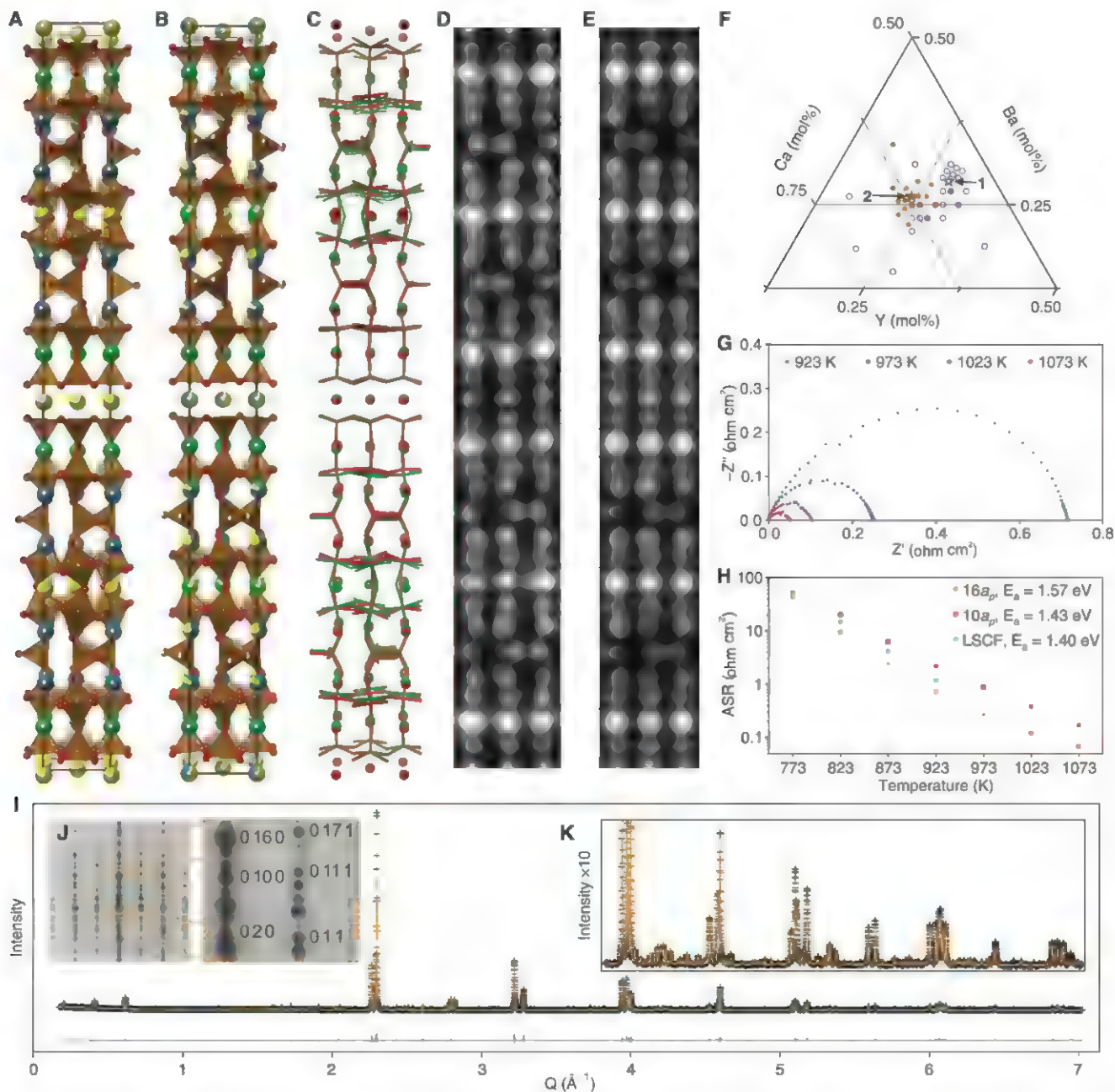


Fig. 4. The $16a_p$ structure. (A) The $16a_p$ structure as predicted by EMMA is compared with (B) the refined structure of **1**. Atoms are colored as follows: yellow, Y; green, Ba; blue, Ca; brown, Fe/Cu; and red, O. (C) Overlaid EMMA (green) and refined experimental (red) structures. (D) Observed and (E) calculated HAADF-STEM images of the $16a_p$ phase. (F) Compositional phase diagram showing the compositions investigated to isolate **1** (open blue circles) and **2** (solid brown circles). The compositions of **1** and **2** are highlighted with a star. (G) A Z-Z* plot showing cathode performance of **1** in a symmetrical cell on a GDC electrolyte at

temperatures between 923 and 1073 K. (H) ASR values obtained at temperatures between 773 and 1073 K for **1** compared to literature values reported for $10a_p$ (26) and LSCF (31). E_a , activation energy. (I) Refined x-ray diffraction data (25) showing observed (black crosses), calculated (orange line), and difference (gray line) data as a function of Q , the momentum transfer. Tabulated crystallographic data can be found in table S1 and refined neutron powder diffraction data in fig. S13. An electron diffraction pattern of **1** showing the $16a_p$ repeat (J) and an enlarged high- Q region of the diffraction data (K) are shown inset.

part of a polyphasic sample at a nominal composition of $Y_{1.95}Ba_{2.1}Ca_{3.95}Fe_8O_{21}$ (fig. S4). A second series of EMMA calculations were performed on materials with the composition $Y_2Ba_2Ca_4Fe_8O_{21}$ in the enlarged $16a_p$ repeat, adding an inversion center to generate the body centering observed by SAED on the experimental compound to reduce the number of total permutations of modules. By using the experimental SAED results to inform the EMMA procedure, we reduced over 10^8 possible structures with $16a_p$ repeats to a restricted set of 47,040 candidate structures that have body centering in agreement with experiment (25).

The final predicted $16a_p$ structure from EMMA (Fig. 4A) contains five elements with a 61 Å longest repeat. The $16a_p$ structure consists of nine crystallographically distinct cation sites. There are four Fe sites in three different coordination environments: one square pyramidal (S_q), two octahedral (O_h), and one tetrahedral (T_d). Y cations occupy two 8-coordinate sites (between S_q Fe layers and between O_h Fe layers), whereas the larger Ba cations occupy a 12-coordinate site (between S_q and O_h Fe layers). Ca cations occupy two chemically similar 8-coordinate sites (between O_h and T_d Fe layers). The total B-site stacking sequence can be represented as $S_qO_hT_dO_hT_dO_hS_q$. We note that the $16a_p$ structure is related to the lowest-energy $8a_p$ structure found in the first set of calculations by the addition of body centering; the smaller $8a_p$ unit cell dimensions still allowed sufficient complexity for the observed local chemical environments of each ion to emerge.

The symmetrically unconstrained $16a_p$ structure from EMMA was transformed into the experimentally (SAED) determined symmetry of *Imma* (fig. S5) and used as a starting point for Rietveld refinement with combined x-ray and neutron powder diffraction data collected on the experimentally synthesized phase 1 (Fig. 4I) (25). During the course of the refinement, the phase composition was changed from the idealized EMMA $16a_p$ composition of $Y_2Ba_2Ca_4Fe_8O_{21}$ to that of $Y_{1.24}Ba_{2.28}Ca_{3.48}Fe_{7.44}Cu_{0.56}O_{21}$. The experimentally determined structure from Rietveld refinement closely resembles the EMMA-predicted structure (Fig. 4, B and A, respectively), with complete preservation of the predicted Fe coordination environments. The determined A-site distribution shows the same majority cation ordering as predicted by EMMA but with significant cation mixing between layers, which is both made necessary by the difference between the EMMA composition and the experimental composition and expected because of entropy considerations at the synthesis temperature. The fractional cation occupancies can be modeled by swapping the cations on the A sites in the EMMA-derived structure and using finite temperature Monte Carlo sampling (25, 28). The similarities between the predicted and refined structures are notable (Fig. 4C). The diffraction-based long-range average structure was observed in shorter length-scale high-angle annular dark field scanning transmission electron microscopy (HAADF-STEM) (25) im-

aging of 1 (Fig. 4D), which was in good agreement with a simulated HAADF-STEM image of the refined structure (Fig. 4E and fig. S6). Mössbauer spectroscopy (25) also confirmed that the structure contains only Fe^{3+} in O_h , S_q , and T_d environments in a 2:1:1 ratio, in agreement with the calculated and refined experimental structures (fig. S7) and iodometric titrations (25).

The $16a_p$ material 1 has the structural and electronic prerequisites for mixed ionic and electronic conduction because of the presence of open-shell Fe^{3+} and anion vacancies, which was directly encoded in the choice of EMMA modules, suggesting its application as an SOFC cathode. It showed good kinetic stability, with no detectable decomposition after heating at 950°C for 5 hours. No reactivity was observed with typical electrolytes $Ce_{0.8}Sm_{0.2}O_{2-\delta}$ (SDC), $Ce_{0.9}Gd_{0.1}O_{2-\delta}$ (GDC), and $La_{0.9}Sr_{0.1}Ga_{0.8}Mg_{0.2}O_{3-\delta}$ at common intermediate temperature (IT)-SOFC operating and processing temperatures of 1023 and 1223 K, respectively (fig. S8). The $16a_p$ material 1 shows an improved stability to the state-of-the-art barium-rich cathode material, $Ba_{0.5}Sr_{0.5}Co_{0.8}Fe_{0.2}O_{3-\delta}$ (BSCF), which decomposes to a hexagonal phase (29) and reacts with SDC (30) under the same conditions used in the reactivity and stability tests. Symmetrical cells were fabricated by screen-printing porous cathode layers on both faces of a dense GDC electrolyte disc, and the resulting area-specific resistance (ASR) value of 0.27 ohm cm^2 at 973 K compares well with the common IT-SOFC cathode $La_{0.6}Sr_{0.4}Co_{0.2}Fe_{0.8}O_{3-\delta}$ (LSCF, 0.46 ohm cm^2) (31) and the layered $10a_p$ $YBa_2Ca_2Fe_5O_{13}$ cathode (0.88 ohm cm^2) (26) (Fig. 4H). dc conductivity measurements are shown in fig. S9. The EMMA method has therefore identified a structure that has experimentally demonstrated functionality as an SOFC cathode material.

Compounds 1 and 2 are likely to be metastable at temperatures below ~1250 K, based on both experimental and computational evidence. To produce phase-pure 1 ($16a_p$), it is necessary to quench from the synthesis temperature (fig. S10); slow cooling produces a mixed phase sample containing a significant proportion of $10a_p$. Calculated enthalpies of reaction at 0 K based on DFT predict that $Y_2Ba_2Ca_4Fe_8O_{21}$ ($16a_p$) is less stable than a multiphase assemblage of $YFeO_3$ + $Ca_2Fe_2O_5$ + $YBa_2Ca_2Fe_5O_{13}$ ($10a_p$). Finite temperature effects must be included to explain the synthesis of 1 and 2 (supplementary text). In a complex compositional range of this type, reaction conditions often have a controlling influence on phase stability, leading to the conclusion that a practical target is to develop computation to assist rather than to direct the synthesis of such complex phases. Nevertheless, we have demonstrated the use of EMMA in searching a phase diagram to find new structures, by investigating the (Y, Ba, Ca, Fe^{3+} , O) phase diagram for layered phases with $7a_p$ long-axis repeats (supplementary text and fig. S11).

By including an initial bias toward the use of specific modules, EMMA provides a compro-

mise between exhaustive approaches, which seek to sample all of phase space, and the need to predict complex structures. It can identify candidate structures for compositionally and structurally complex inorganic materials, given a reasonable choice of starting modules. Furthermore, the large set of ranked structures generated by EMMA contains a wealth of information, which can be analyzed further to gain more general understanding (supplementary text and fig. S12). The modular approach adopted in EMMA allows desired functional properties to be built into the predicted structures; the selection of modules containing the relevant chemical bonding known to give rise to functional behavior in other materials allows the targeting of specific functions.

References and Notes

1. C. W. Lehmann, *Angew. Chem. Int. Ed.* **50**, 5616 (2011).
2. C. R. A. Catlow, A. N. Cormack, F. Theobald, *Acta Crystallogr. B* **40**, 195 (1984).
3. R. Martoňák, A. Laio, M. Parrinello, *Phys. Rev. Lett.* **90**, 075503 (2003).
4. M. A. Neumann, F. J. J. Leusen, J. Kendrick, *Angew. Chem. Int. Ed.* **47**, 2427 (2008).
5. A. R. Oganov, Y. M. Ma, A. O. Lyakhov, M. Valke, C. Gatti, *Rev. Mineral. Geochem.* **71**, 271 (2010).
6. M. A. C. Wevers, J. C. Schön, M. Jansen, *J. Solid State Chem.* **136**, 233 (1998).
7. S. M. Woodley, P. D. Battle, J. D. Gale, C. R. A. Catlow, *Phys. Chem. Chem. Phys.* **1**, 2535 (1999).
8. O. Delgado-Friedrichs, A. W. M. Dress, D. H. Huson, J. Klinowski, A. L. Mackay, *Nature* **400**, 644 (1999).
9. A. Le Bail, *J. Appl. Crystallogr.* **38**, 389 (2005).
10. C. Fischer, K. J. Tibbets, D. Morgan, G. Ceder, *Nat. Mater.* **5**, 641 (2006).
11. O. Levy, G. L. W. Hart, S. Curtarolo, *J. Am. Chem. Soc.* **132**, 4830 (2010).
12. C. Mellot Drazmeks, J. M. Newsam, A. M. Gorman, C. M. Freeman, G. Ferey, *Angew. Chem. Int. Ed.* **39**, 2270 (2000).
13. X. Zhang, V. Stevanović, M. d'Avezac, S. Lany, A. Zunger, *Phys. Rev. B* **86**, 014109 (2012).
14. P. Piquini, P. A. Graf, A. Zunger, *Phys. Rev. Lett.* **100**, 186403 (2008).
15. J. Lima-de-Faria, E. Hellner, F. Liebau, E. Makovicky, E. Parthe, *Acta Crystallogr. A* **46**, 1 (1990).
16. J. B. Thompson, *Am. Mineral.* **63**, 239 (1978).
17. E. I. Gladyshevskii, I. I. Zalutskii, G. T. Tivanchuk, *Vysn. L'viv. Univ. Ser. Khim.* **14**, 9 (1972).
18. G. A. Jeffrey, V. Wu, *Acta Crystallogr.* **20**, 538 (1966).
19. G. Ferraris, E. Makovicky, S. Merlino, *Crystallography of Modular Materials* (Oxford Univ. Press, Oxford, 2004).
20. B. B. Zvyagin, S. Merlino, *Z. Kristallogr.* **218**, 210 (2003).
21. R. H. Mitchell, *Perovskites: Ancient and Modern* (Almaz, Thunder Bay, Canada, 2002).
22. J. Darriet, M. A. Subramanian, *J. Mater. Chem.* **5**, 543 (1995).
23. I. Orlov, L. Palatinus, A. Arakcheeva, G. Chapuis, *Acta Crystallogr. B* **63**, 703 (2007).
24. Ü. Özgür, Y. Alivov, H. Morkoç, *J. Mater. Sci. Mater. Electron.* **20**, 789 (2009).
25. Materials and methods are available as supplementary materials on Science Online.
26. A. Demont et al., *Chem. Mater.* **22**, 6598 (2010).
27. P. D. Battle, T. C. Gibb, P. Lightfoot, *J. Solid State Chem.* **84**, 237 (1990).
28. M. O. Zacate, R. W. Grimes, *Philos. Mag. A* **80**, 797 (2000).
29. S. Svarcová, K. Wiik, J. Tolchard, H. J. M. Bouwmeester, T. Grande, *Solid State Ion.* **178**, 1787 (2008).
30. K. Wang et al., *J. Power Sources* **179**, 60 (2008).
31. V. Dusastre, J. A. Kilner, *Solid State Ion.* **126**, 163 (1999).
32. J. Smi, H. P. J. Wijn, Eds., *Ferrites* (Wiley, New York, 1959).

Acknowledgments: This work is funded by the European Research Council (ERC Grant agreement 227987 RLUCIM). It was carried out with the support of the Diamond Light

Source (DLS) and ISIS. We thank C. Tang, J. Parker, and S. Thompson for assistance in using beamline I11 (DLS) and A. Daoud-Aladine for assistance in using the High Resolution Powder Diffractometer (HRPD, ISIS). CCDC 887926 contains the supplementary crystallographic data for this paper. These data can be obtained free of charge via www.ccdc.cam.ac.uk/data_request/cif, by e-mailing data_request@ccdc.cam.ac.uk, or by contacting the Cambridge Crystallographic Data Centre, 12, Union Road, Cambridge CB2 1EZ, UK; fax: +44 1223 336033. We also thank M.S. Islam (Department of Chemistry, University of Bath) for helpful discussion with regards to

fitting force-field parameters. Via our membership of the United Kingdom's HPC Materials Chemistry Consortium, which is funded by Engineering and Physical Sciences Research Council (EPSRC) (EP/F067496), this work made use of the facilities of HECToR, the United Kingdom's national high-performance computing service, which is provided by UoEHPC Limited at the University of Edinburgh, Cray Incorporated and NAG Limited, and funded by the Office of Science and Technology through EPSRC's High End Computing Programme. We thank EPSRC for studentships for C.C. and D.H. M.J.R. is a Royal Society Research Professor.

Supplementary Materials

www.sciencemag.org/cgi/content/full/science.1226558/DC1
Materials and Methods
Supplementary Text
Figs. S1 to S13
Table S1
References (33–53)

26 June 2012; accepted 14 March 2013
Published online 11 April 2013;
10.1126/science.1226558

A Reconciled Estimate of Glacier Contributions to Sea Level Rise: 2003 to 2009

Alex S. Gardner,^{1,2*} Geir Moholdt,³ J. Graham Cogley,⁴ Bert Wouters,^{5,6} Anthony A. Arendt,⁷ John Wahr,^{5,8} Etienne Berthier,⁹ Regine Hock,^{7,10} W. Tad Pfeffer,¹¹ Georg Kaser,¹² Stefan R. M. Ligtenberg,¹³ Tobias Bolch,^{14,15} Martin J. Sharp,¹⁶ Jon Ove Hagen,¹⁷ Michiel R. van den Broeke,¹³ Frank Paul¹⁴

Glaciers distinct from the Greenland and Antarctic Ice Sheets are losing large amounts of water to the world's oceans. However, estimates of their contribution to sea level rise disagree. We provide a consensus estimate by standardizing existing, and creating new, mass-budget estimates from satellite gravimetry and altimetry and from local glaciological records. In many regions, local measurements are more negative than satellite-based estimates. All regions lost mass during 2003–2009, with the largest losses from Arctic Canada, Alaska, coastal Greenland, the southern Andes, and high-mountain Asia, but there was little loss from glaciers in Antarctica. Over this period, the global mass budget was -259 ± 28 gigatons per year, equivalent to the combined loss from both ice sheets and accounting for $29 \pm 13\%$ of the observed sea level rise.

Global estimates of glacier mass changes have traditionally been based on the extrapolation of local geodetic and glaciological measurements. These records indicate increasing mass loss in recent decades (1–3). However, a recent study (4) using Gravity Recovery and Climate Experiment (GRACE) sat-

ellite gravimetry from 2003 to 2010 suggests that global glacier mass wastage is much less than previously thought (1, 5). To investigate this discrepancy, we recalculated existing results from glaciological extrapolation and GRACE to a common spatial and temporal reference that we compare with independent altimetric estimates from the Ice, Cloud, and land Elevation Satellite (ICESat). We provide estimates of regional mass budgets for glaciers peripheral to the Greenland and Antarctic Ice Sheets and for the glaciers of high-mountain Asia (HMA), based on elevation changes from ICESat.

For regional glacier analyses, we relied on the Randolph Glacier Inventory (RGIv3 (6)), a globally complete digital database of glacier coverage. It defines 19 glacier regions that contain a total glacierized area of $\sim 729,400$ km² (circa 2000; Fig. 1 and Table 1). Deriving regional and global mass budgets from glaciological and local geodetic measurements is complicated, because the set of measured glaciers is sparse for many regions and can be biased toward smaller land-terminating glaciers (7). Monitoring of glacier mass change on a global scale using satellite gravimetry or altimetry has only become possible with the launch of the GRACE and ICESat satellites in early 2002 and 2003, respectively. The ICESat mission ended in October 2009, giving a 6-year overlap with GRACE from October 2003 to October 2009, during which we are able to com-

pare results from all three methods. Unless otherwise stated, all the mass budgets on which we relied (8–10) have been updated to cover this common time span over the RGI regions, with no changes to the original methods. All reported estimates are accompanied by 95% confidence intervals (CIs).

We recalculated recent GRACE glacier mass-change estimates (4, 11) with updated mascons (table S1). We also made alternative GRACE estimates of glacier mass changes by expanding the methods of Wouters *et al.* (12), which were originally developed to retrieve mass changes for the Greenland Ice Sheet and Arctic glaciers (12–14), to all glacierized regions (table S2). Both analyses use monthly time-variable GRACE gravity-field solutions produced by the University of Texas Center for Space Research: The Wouters *et al.* approach used product Release 5, and the updated Jacob *et al.* estimates (4) used product Release 4. The two analyses give a total mass budget for all glaciers outside Greenland and Antarctica of -170 ± 32 Gt year⁻¹ and -166 ± 37 Gt year⁻¹, respectively. The two GRACE estimates also agree well on a regional scale (11), so for the remaining analysis we averaged them and refer to the combined result as JW12. The averaged gravimetric estimate is half as negative as a more conventional estimate (2), based on spatial interpolation of glaciological and local geodetic measurements (hereafter referred to as glaciological records). This method yields a mass budget of -329 ± 121 Gt year⁻¹ (we refer to these results as C09). If we include glaciers peripheral to the Greenland and Antarctic Ice Sheets, C09 gives a total estimate for all glaciers of -491 ± 200 Gt year⁻¹ which is comparable to an earlier estimate (-402 ± 95 Gt year⁻¹) of glacier mass loss for 2006, also determined from extrapolation of local glaciological records (1). Here we address the large discrepancies between gravimetric and glaciological estimates region by region and compare them with estimates from ICESat laser altimetry where available.

Peripheral glaciers in Antarctica (15) and Greenland (16) account for about 30% of the global glacier area, but until recently there have been no published region-wide estimates for our study period. We present an analysis of elevation changes along ICESat near-repeat tracks, using a plane-fitting technique that accounts for the local surface slope (8). We used surface elevations from the GLA12 and GLA06 altimetry products Release 533, with standard saturation correction applied and no correction for potential intercampaign

¹Graduate School of Geography, Clark University, Worcester, MA 01610, USA. ²Department of Atmospheric, Oceanic and Space Science, University of Michigan, Ann Arbor, MI 48109, USA. ³Institute of Geophysics and Planetary Physics, Scripps Institution of Oceanography, La Jolla, CA 92093, USA. ⁴Department of Geography, Trent University, Peterborough, Ontario K9J 7B8, Canada. ⁵Department of Physics, University of Colorado at Boulder, Boulder, CO 80309, USA. ⁶Bristol Glaciology Centre, School of Geographical Science, Bristol BS8 1SS, UK. ⁷Geophysical Institute, University of Alaska Fairbanks, Fairbanks, AK 99775, USA. ⁸Cooperative Institute for Research in Environmental Sciences, University of Colorado at Boulder, Boulder, CO 80309, USA. ⁹Centre National de la Recherche Scientifique, Université de Toulouse, LEGOS, 14 Avenue E. Belin, 31400 Toulouse, France. ¹⁰Department of Earth Sciences, Uppsala University, SE-751 05 Uppsala, Sweden. ¹¹Institute of Arctic and Alpine Research, University of Colorado at Boulder, Boulder, CO 80309, USA. ¹²Institute of Meteorology and Geophysics, Universität Innsbruck, A-6020 Innsbruck, Austria. ¹³Utrecht University, Institute for Marine and Atmospheric Research Utrecht, 3508 TA Utrecht, Netherlands. ¹⁴Department of Geography, University of Zurich, CH-8057 Zurich, Switzerland. ¹⁵Institut für Kartographie, Technische Universität Dresden, D-01062 Dresden, Germany. ¹⁶Department of Earth and Atmospheric Sciences, University of Alberta, Edmonton, Alberta T6G 2E3, Canada. ¹⁷Department of Geosciences, University of Oslo, Box 1047 Blindern, N-0316, Oslo, Norway.

*Corresponding author. E-mail: agardner@clarku.edu

biases (11). In Antarctica, we corrected elevation changes for variations due to change in the firm density, using a firm pack model with a horizontal resolution of ~ 27 km (17, 18). We attributed residual volume changes after these firm corrections to changes in glacier ice and converted them

to mass changes, using a density of 900 ± 17 kg m $^{-3}$. The Antarctic peripheral glaciers (133,200 km 2) have not changed much in total mass (-6 ± 10 Gt year $^{-1}$), which is in contrast to earlier modeling estimates for 1961–2004 (19). There are, however, subregional examples of both loss (Ant-

arctic Peninsula Islands, -7 ± 4 Gt year $^{-1}$) and gain (Ellsworth Land Islands, 3 ± 4 Gt year $^{-2}$). For Greenland we lack firm pack model simulations and instead rely on estimates of the firm area and the bulk density of the firm volume change (11). We estimate a total mass budget of -38 ± 7 Gt

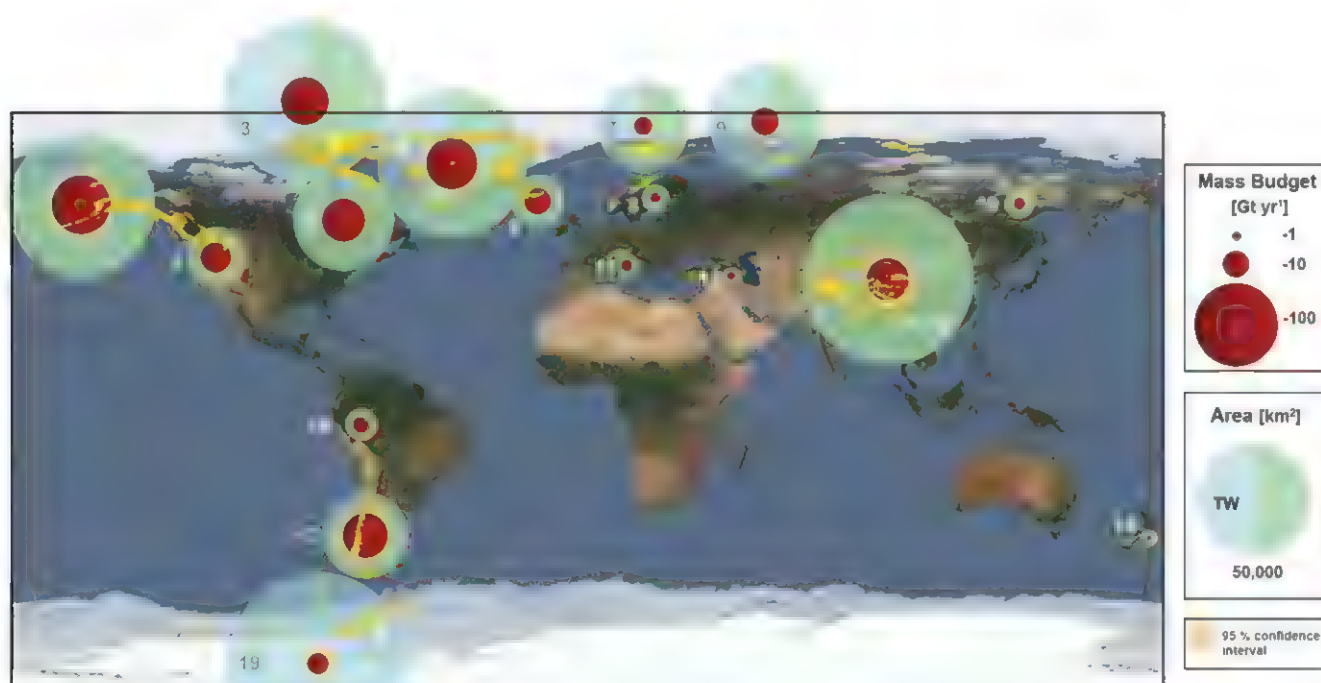


Fig. 1. Regional glacier mass budgets and areas. Red circles show 2003–2009 regional glacier mass budgets, and pale blue/green circles show regional glacier areas with tidewater basin fractions (the extent of

ice flowing to termini in the ocean) in blue shading (Table 1). Peach-colored halos surrounding red circles show the 95% CI in mass change estimates, but can only be seen in regions that have large uncertainties.

Table 1. Regional areas and mass budgets. Regional breakdown of total and tidewater glacier basin area, best estimate of mass budget for 2003–2009 with the 95% CI, and methods selected as most suitable for estimating glacier mass change. G, GRACE; I, ICESat; gl, glaciological.

	Region	Total area (km 2)	Tidewater area (km 2)	Mass budget (kg m $^{-2}$ year $^{-1}$)	Mass budget (Gt year $^{-1}$)	Method	Ref.
1	Alaska	87,100	11,900	-570 ± 200	-50 ± 17	G	New, (4, 9, 10)
2	Western Canada/United States	14,600	0	-930 ± 230	-14 ± 3	gl	(2)
3	Arctic Canada north	104,900	48,800	-310 ± 40	-33 ± 4	I, G	New, (4, 13)
4	Arctic Canada south	40,900	3,000	-660 ± 110	-27 ± 4	I, G	New, (4, 13)
5	Greenland	89,700	31,300	-420 ± 70	-38 ± 7	I	New
6	Iceland	11,100	0	-910 ± 150	-10 ± 2	G, gl	New, (2, 4)
7	Svalbard	34,000	14,900	-130 ± 60	-5 ± 2	I, G	New, (4, 8)
8	Scandinavia	2,900	0	-610 ± 140	-2 ± 0	gl	(2)
9	Russian Arctic	51,600	33,400	-210 ± 80	-11 ± 4	I, G	New, (4, 14)
10	North Asia	3,400	0	-630 ± 310	-2 ± 1	gl	(2)
11	Central Europe	2,100	0	-1060 ± 170	-2 ± 0	gl	(2)
12	Caucasus and Middle East	1,100	0	-900 ± 160	-1 ± 0	gl	(2)
13–15	HMA	118,200	0	-220 ± 100	-26 ± 12	I, G	New, (4)
16	Low latitudes	4,100	0	-1080 ± 360	-4 ± 1	gl	(2)
17	Southern Andes	29,400	7,000	-990 ± 360	-29 ± 10	G	New, (4, 25)
18	New Zealand	1,200	0	-320 ± 780	0 ± 1	gl	(2)
19	Antarctic and sub-Antarctic	133,200	130,200	-50 ± 70	-6 ± 10	I	New
	Total, excluding Greenland and Antarctic	506,600	119,000	-420 ± 50	-215 ± 26		
	Global total	729,400	280,500	-350 ± 40	-259 ± 28		

year⁻¹ for the Greenland peripheral glaciers (89,700 km²). All subregions experienced significant thinning [Fig. 2 (11)], except for the Flade Isblink Ice Cap, Greenland's largest ice cap (20). Our estimate is consistent with a recently published estimate of -28 ± 11 Gt year⁻¹ for the period 2003–2008 that was determined from ICESat data using methods comparable to ours but assuming a larger firn area and lower bulk density for the firn volume change (21). We do not include this estimate in our analysis, as it does not cover the full 2003–2009 period. ICESat-based estimates are less negative than C09 in both Greenland and Antarctica (Fig. 3), but only significantly different in Antarctica, where the C09 estimate is 100 Gt year⁻¹ more negative. The cause of the disagreement is discussed after our assessment of regional mass changes.

Outside of Greenland and Antarctica, there are four high-latitude regions with published glacier mass budgets from ICESat (2003–2009) that we can compare with the C09 and JW12 estimates: Arctic Canada north (13) (-37 ± 7 Gt year⁻¹), Arctic Canada south (13) (-24 ± 6 Gt year⁻¹), Svalbard (8) (-5 ± 1 Gt year⁻¹), and the Russian Arctic (14) (-10 ± 4 Gt year⁻¹). Summing mass budgets for these four regions gives an ICESat estimate of -75 ± 10 Gt year⁻¹, a JW12 estimate of -78 ± 12 Gt year⁻¹, and a C09 estimate of -116 ± 52 Gt year⁻¹. Regional errors are considered uncorrelated for ICESat and JW12, but fully correlated for C09. ICESat and GRACE agree well in all regions, whereas C09 is considerably more negative, although error bounds usually overlap [Fig. 3 (11)].

The two remaining large (>5000 km²) high-latitude regions, Alaska and Iceland, have no

published mass budgets from ICESat. Alaska mass-budget estimates from C09 and JW12 are 72 ± 22 Gt year⁻¹ and 42 ± 11 Gt year⁻¹, and two other GRACE estimates give mass budgets of -54 ± 26 Gt year⁻¹ and -61 ± 22 Gt year⁻¹ (9, 10). Although estimates have overlapping error bounds, there is still considerable spread in the mean values. For Iceland, the C09 and JW12 estimates of glacier mass change of -9 ± 2 Gt year⁻¹ and -11 ± 3 Gt year⁻¹ agree well.

The largest glacierized region outside the Arctic and Antarctic is HMA. Glacier changes in this region are spatially heterogeneous and not well known (22). Himalayan and Hindu Kush glaciers have recently been found to be losing mass (23), whereas the glaciers in the Karakoram are in near balance (24). For complete comparison with JW12 and C09, we analyzed ICESat altimetry for

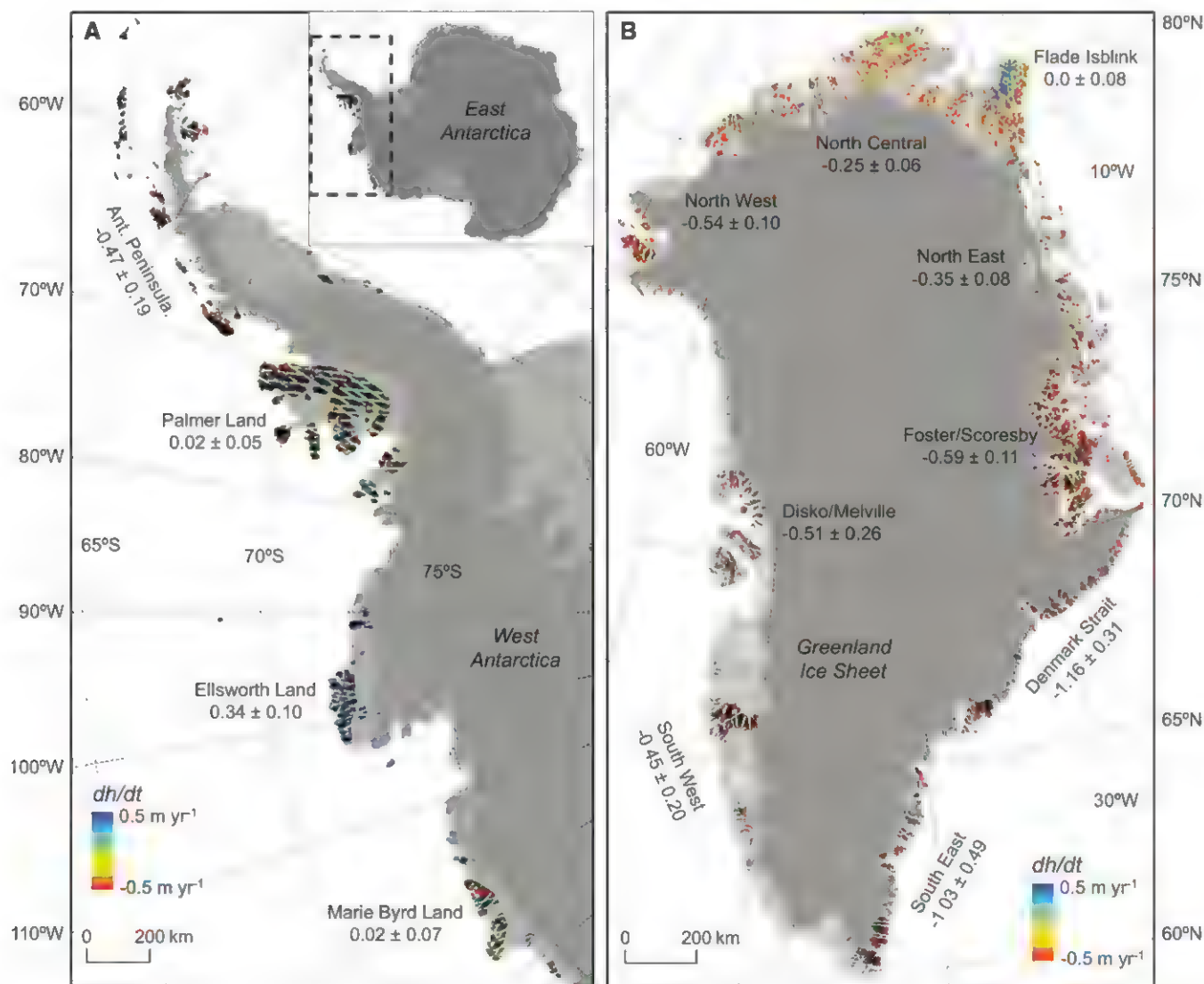


Fig. 2. Elevation changes for glaciers peripheral to the ice sheets. Elevation change rates (dh/dt) between October 2003 and October 2009 for peripheral glaciers in (A) West Antarctica and (B) Greenland. Gray shadings from black to white show glaciers, ice sheets, ice shelves, land surfaces, and ocean, respectively. West Antarctica contains 85% of the

peripheral glacier cover in Antarctica. The remaining glaciers are found on scattered islands around East Antarctica (11%, inset map) and on remote sub-Antarctic islands (4%, not shown). Text labels define a set of subregions with accompanying average elevation change rates in m year⁻¹ (table S4). Uncertainties give the 95% CI.

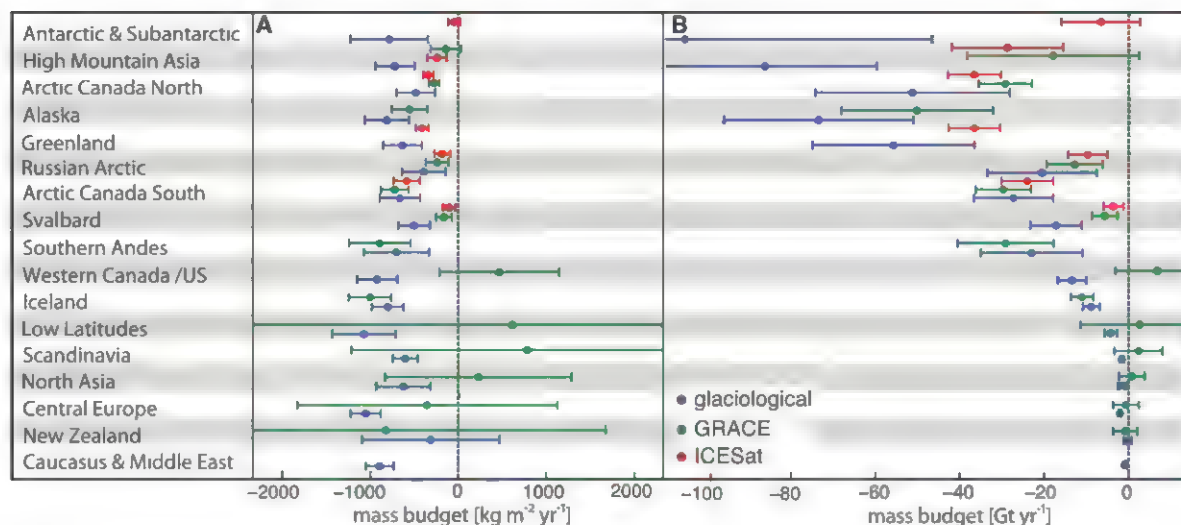


Fig. 3. Comparison of regional glacier mass-budget estimates. Regional estimates of glacier mass change for 2003–2009 in (A) $\text{kg m}^{-2} \text{year}^{-1}$ and (B) Gt year^{-1} . Estimates are as assessed by ICESat (8, 13, 14) and GRACE [JW12

(9, 10)] and from interpolation of glaciological records (2) with an updated measurement data set for 2003–2009 (glaciological). Regions are arranged from top to bottom by total glacierized area. Uncertainties give the 95% CI.

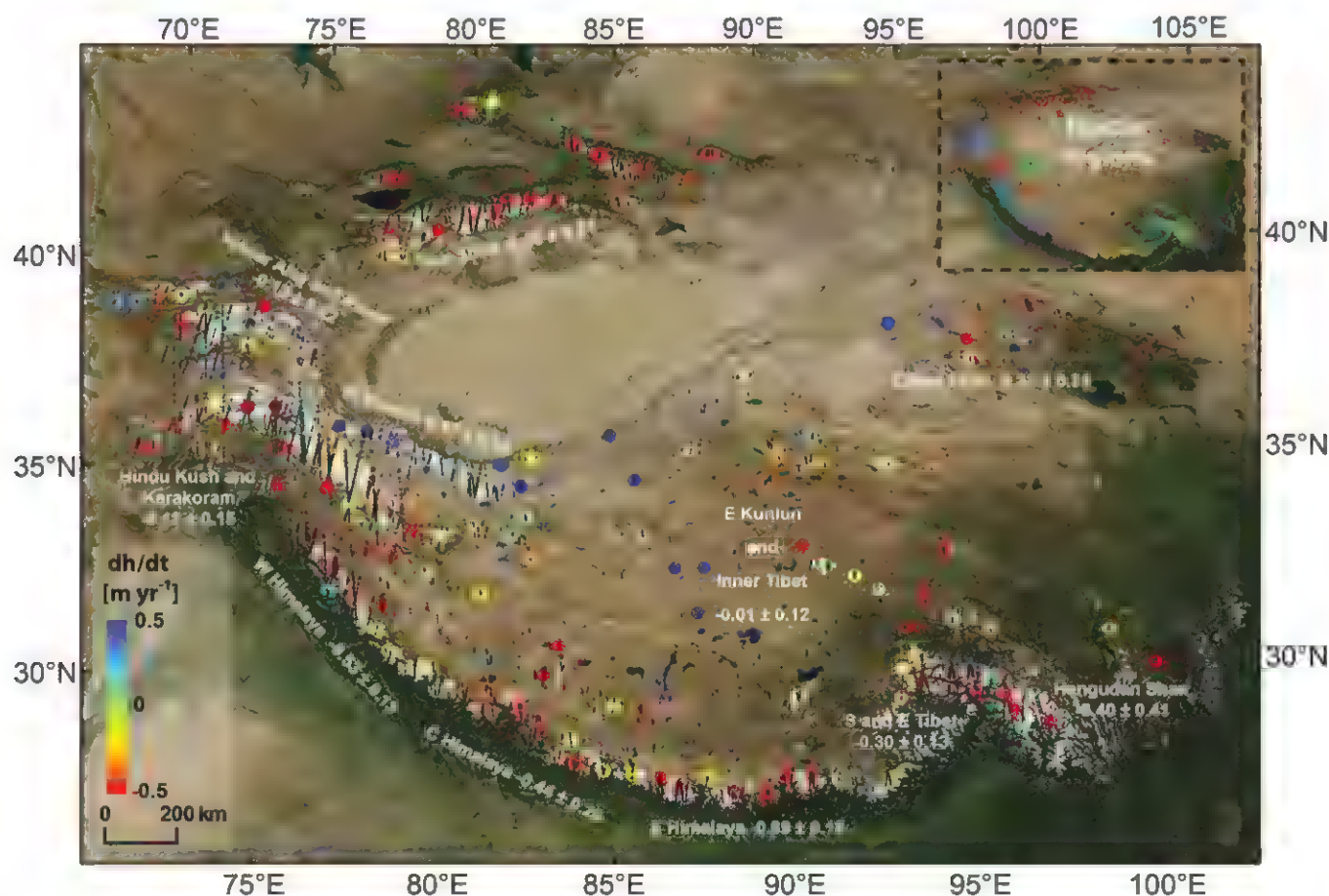


Fig. 4. Elevation changes for high-mountain Asia glaciers. Averaged elevation change rates (dh/dt) between October 2003 and October 2009 for high-mountain Asia. Each colored dot represents an independent spatial average of a minimum of 50 dh/dt observations within a radius of 50 km.

ICESat ground tracks over glaciers are shown with thin black lines. The inset image and text labels define a set of subregions for which we have estimated area-averaged elevation changes (shown here in m year^{-1} together with their uncertainties) and mass budgets (table S5). Uncertainties give the 95% CI.

the entire HMA using two approaches: a modification of the method of Moholdt and others (8); and methods similar to those of Kääb and others (23), whose analysis was restricted to about half of the glacierized area in HMA (11). Both approaches use an elevation model from the Shuttle Radar Topography Mission to correct for topographic differences between ICESat points. The results confirm a heterogeneous pattern of elevation change [Fig. 4 (11)], with most rapid thinning (<-0.4 m year⁻¹) in the south (Himalaya) and north (Tien Shan), moderate rates of thinning (~ -0.3 m year⁻¹) in eastern and southern Tibet, and near balance (-0.12 to $+0.16$ m year⁻¹) in the western and central portions of the region (Pamir, Karakoram, and western Kunlun). We converted volume changes to mass changes using a density of 900 kg m⁻³ and summed the subregional estimates (table S5) to obtain a total HMA mass budget of -29 ± 13 Gt year⁻¹. This estimate shows significant mass loss and is within the error bounds of JW12 (-19 ± 20 Gt year⁻¹). Both satellite-based estimates are significantly less negative than C09 (-86 ± 26 Gt year⁻¹).

The two remaining large (>5000 km²) glacierized regions are the southern Andes (including Patagonia) and western Canada/United States. For the southern Andes, the mass-budget estimates of JW12 (-29 ± 10 Gt year⁻¹) and C09 (-21 ± 11 Gt year⁻¹) agree relatively well with another GRACE estimate (-26 ± 12 Gt year⁻¹; 2003–2009) (25) and with estimates for a longer time period from the analysis of multitemporal digital elevation models for the three major icefields in the region (-28 ± 3 Gt year⁻¹; 2000–2011/12) (26–28). The comparison is more troublesome in western Canada/United States, where C09 gives

a net loss of -14 ± 3 Gt year⁻¹ and JW12 gives a net gain of $+7 \pm 10$ Gt year⁻¹. The only previous estimate (29) of glacier mass change for this region, based on differencing of digital elevation models, yielded mass loss at -8 ± 4 Gt year⁻¹ during 1985–2000 (excluding subregions that are part of the Alaska region as defined by RGI). The C09 estimate for the same period (-9 ± 2 Gt year⁻¹) agrees well with Schiefer and others (29), and glaciological records indicate that the most recent decade has seen accelerated glacier loss. This suggests that C09 performs satisfactorily in this region and that JW12 may not adequately separate the glacier mass signal from other mass changes in the region.

The remaining six small regions (glacier area <5000 km² each) contain only 2% of Earth's glaciers by area (Table 1). The JW12 gravimetric estimates of glacier mass change for these regions have larger uncertainties than the glaciological estimates (Fig. 3), and there are no concurrent regional-scale measurements of elevation changes, because ICESat track coverage is insufficient for reliable estimation. These sparsely glacierized regions all have a relatively high density of glaciological records (table S3), and we therefore expect C09 to perform satisfactorily here. Summing all six regions gives a C09 estimate of -12 ± 4 Gt year⁻¹ and a JW12 estimate of $+4 \pm 16$ Gt year⁻¹.

Our assessment shows that ICESat and GRACE estimates of mass change for large glacierized regions agree well and that estimates derived from the interpolation of glaciological records can be substantially more negative (Fig. 3). This suggests that the database of glaciological records is negatively biased. To investigate this bias, we extracted subsamples of ICESat elevation change data within 100 km of the C09 glaciological measurements in the five regions where both data sets are available. These ICESat subsamples reveal that the neighborhoods of the glaciological measurements are typically thin-

ning more rapidly than the regional mean (Fig. 5). Forty-one of the 49 glacier neighborhoods had rates of thinning higher than their respective regional averages (fig. S9). Across the five regions, which account for 75% of the global glacierized area, the area-weighted difference between the regional mean and the elevation changes in the C09 neighborhoods is -0.43 m year⁻¹, which would translate to a large global mass-budget bias of -201 Gt year⁻¹ for 2003–2009. Thus, glaciers with glaciological measurements tend to be located in subregions where mass loss is greater than in their region as a whole, and this sampling bias is probably the major source of the discrepancy between C09 and the satellite-based estimates.

For our consensus estimate of global glacier mass wastage, GRACE and ICESat estimates are favored for all regions that have glacierized area greater than 5000 km², except western Canada/United States. In the latter region, and in six smaller regions where the density of in situ measurements is relatively high and the GRACE uncertainty exceeds ± 1000 kg m⁻² year⁻¹, we take C09 as the best estimate of mass change. C09 also has a relatively high measurement density for Iceland, so we included it in the method-averaged estimate for Iceland. On the basis of this synthesis, we estimate that Earth's glaciers had a mass budget for 2003–2009 of -215 ± 26 Gt year⁻¹ when peripheral glaciers in Greenland and Antarctica are excluded, and -259 ± 28 Gt year⁻¹ when peripheral glaciers are included (Table 1).

Compared to longer-term global estimates from 1960–1961 to 2004–2005, our consensus mass budget is slightly less negative than three of four previous studies (2, 19, 30) but more negative than the fourth (3). This could imply that there has been no increase in glacier mass loss in the most recent decade, but this conflicts with the glaciological records themselves (Fig. 6) and with repeat geodetic measurements (13, 25, 31–33).

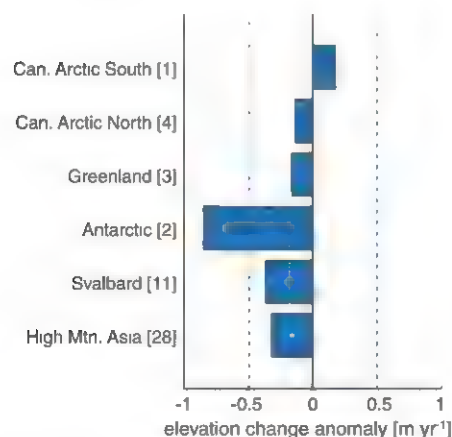


Fig. 5. Possible bias due to sparse spatial coverage of glaciological records. ICESat-derived elevation change anomalies between neighborhoods of glaciological and local geodetic measurements and averages over their RGI regions. Each neighborhood is centered on a measured glacier and has a radius of 100 km. Each region name is followed by its number of measured glaciers during the 2003–2009 period. Negative values indicate that neighborhoods of glaciological records experienced thinning at higher rates than the regional average.

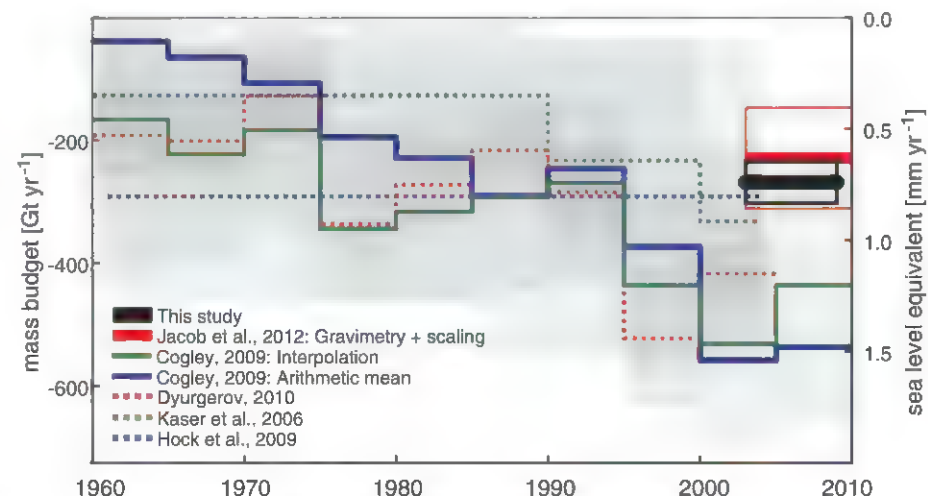


Fig. 6. Global estimates of glacier mass change. All estimates have been multiplied by the ratio of the total glacier area used in this study, 729,400 km², to that used in each source. 95% CIs are shown for all estimates except the arithmetic averages of C09 (2), which have formal errors in the range from 410 to 1520 Gt year⁻¹. The two C09 estimates are determined from an updated set of glaciological records using the methods of Cogley (2).

We instead suggest that most previous assessments have overestimated global mass losses because of the interpolation of sparse glaciological measurements that are not representative for the largest glacierized regions. We can only demonstrate this negative bias for the 2003–2009 period, but it has long been suspected for earlier periods as well (34, 35). This calls for a reexamination of previous global estimates based on the interpolation of glaciological records, which will probably lead to a downward revision of the estimated total contribution of glaciers to sea level rise over the past century.

Our consensus estimate of glacier mass wastage between 2003 and 2009 implies a sea-level contribution of 0.71 ± 0.08 mm of sea level equivalent (SLE) year⁻¹, accounting for $29 \pm 13\%$ of the observed sea level rise for the same period (11). The total glacier mass loss is comparable to a recent estimate for the whole of Greenland and Antarctica (36) (peripheral glaciers + ice sheets) for the period 2003–2008. To avoid double counting, we subtracted our estimates for peripheral glacier mass loss from this total to obtain a total ice-sheet mass budget of -289 ± 49 Gt year⁻¹ (11) and a total land ice (all glaciers + ice sheets) mass budget of -545 ± 57 Gt year⁻¹, amounting to a sea level rise of 1.50 ± 0.16 mm of SLE year⁻¹ which is $60 \pm 19\%$ of the total global sea level rise (11).

References and Notes

1. M. F. Meier *et al.*, *Science* **317**, 1064 (2007).
2. J. G. Cogley, *Ann. Glaciol.* **50**, 96 (2009).
3. G. Kaser, J. G. Cogley, M. B. Dyurgerov, M. F. Meier, A. Ohmura, *Geophys. Res. Lett.* **33**, L19501 (2006).
4. T. Jacob, J. Wahr, W. T. Pfeffer, S. Swenson, *Nature* **482**, 514 (2012).
5. J. A. Church *et al.*, *Geophys. Res. Lett.* **38**, L18601 (2011).
6. A. Arendt *et al.*, *Randolph Glacier Inventory: A Dataset of Global Glacier Outlines Version: 2.0* (Global Land Ice Measurements from Space, Digital Media, Boulder, CO, 2012).
7. M. Zemp, M. Hoelzle, W. Haeberli, *Ann. Glaciol.* **50**, 101 (2009).
8. G. Moholdt, C. Nuth, J. O. Hagen, J. Kohler, *Remote Sens. Environ.* **114**, 2756 (2010).
9. I. Sasgen, V. Klemann, Z. Martinec, *J. Geodyn.* **59–60**, 49 (2012).
10. S. B. Luthcke, A. A. Arendt, D. D. Rowlands, J. J. McCarthy, C. F. Larsen, *J. Glaciol.* **54**, 767 (2008).
11. Materials and methods are available in the supplementary materials on Science Online.
12. B. Wouters, D. Chambers, E. J. O. Schrama, *Geophys. Res. Lett.* **35**, L20501 (2008).
13. A. S. Gardner *et al.*, *Nature* **473**, 357 (2011).
14. G. Moholdt, B. Wouters, A. S. Gardner, *Geophys. Res. Lett.* **39**, L10502 (2012).
15. A. B. Iss, R. Hock, J. G. Cogley, *Ann. Glaciol.* **54**, 191 (2013).
16. P. Rastner *et al.*, *Cryosphere* **6**, 1483 (2012).
17. H. D. Pritchard *et al.*, *Nature* **484**, 502 (2012).
18. S. R. M. Ligtenberg, M. M. Helsen, M. R. van den Broeke, *Cryosphere* **5**, 809 (2011).
19. R. Hock, M. de Waul, V. Radic, M. Dyurgerov, *Geophys. Res. Lett.* **36**, L07501 (2009).
20. E. J. Rinne *et al.*, *J. Geophys. Res.* **116**, F03024 (2011).
21. T. Bolch *et al.*, *Geophys. Res. Lett.* **40**, 875 (2013).
22. T. Bolch *et al.*, *Science* **336**, 310 (2012).
23. A. Käb, E. Berthier, C. Nuth, J. Gardelle, Y. Arnaud, *Nature* **488**, 495 (2012).
24. J. Gardelle, E. Berthier, Y. Arnaud, *Nat. Geosci.* **5**, 322 (2012).
25. E. R. Ivins *et al.*, *J. Geophys. Res.* **116**, B02043 (2011).
26. M. J. Willis, A. K. Melkonian, M. E. Pritchard, J. M. Ramage, *Remote Sens. Environ.* **117**, 184 (2012).
27. M. J. Willis, A. K. Melkonian, M. E. Pritchard, A. Rivera, *Geophys. Res. Lett.* **39**, L17501 (2012).
28. A. K. Melkonian *et al.*, *Cryosphere Discuss.* **6**, 3503 (2012).
29. E. Schiefer, B. Menounos, R. Wheate, *Geophys. Res. Lett.* **34**, L16503 (2007).
30. M. Dyurgerov, M. F. Meier, R. L. Armstrong, *Mass Balance of Mountain and Sub-Polar Glaciers Outside the Greenland and Antarctic ice sheets: Supplement to*

Occasional Paper No. 55 (Institute of Arctic and Alpine Research, University of Colorado, Boulder, CO, 2005).

31. E. Berthier, E. Schiefer, G. K. C. Clarke, B. Menounos, F. Remy, *Nat. Geosci.* **3**, 92 (2010).
32. E. Rignot, A. Rivera, G. Casassa, *Science* **302**, 434 (2003).
33. A. S. Gardner, G. Moholdt, A. Arendt, B. Wouters, *Cryosphere* **6**, 1103 (2012).
34. M. B. Dyurgerov, M. F. Meier, *Arct. Alp. Res.* **29**, 379 (1997).
35. J. G. Cogley, W. P. Adams, *J. Glaciol.* **44**, 315 (1998).
36. A. Shepherd *et al.*, *Science* **338**, 1183 (2012).

Acknowledgments: We thank K. Matsuo, M. Huss, T. Jacob, A. Käb, S. Luthcke, A. Willsman, M. Willis, and I. Sasgen for updated or early access to regional estimates of glacier mass change, M. Flanner, T. Jacob, and S. Swenson for helping with analysis of the hydrologic models; A. Bliss, N. Molg, C. Nuth, P. Rastner, M. Willis, and G. Wolken for providing regional areas of ocean-terminating glacier basins; J. Lenaerts and J. van Angelen for providing RACMO2 output for Greenland and Antarctica; J. Box and C. Chen for making available Greenland Ice Sheet snowline estimates; G. A. R. Riva, and P. Stocchi for providing glacial isostatic adjustment models, and C. Starr and the NASA/Goddard Space Flight Center Scientific Visualization Studio for help with Fig. 1. This work was supported by funding to A.S.G. and M.J.S. from the Natural Sciences and Engineering Research Council of Canada, G.M. from NASA award NNX09AE52G, B.W. from a Marie Curie International Outgoing Fellowship within the 7th European Community Framework Programme (FP7-PEOPLE-2011-IOF-301260), E.B. from the TOSCA program of the French Space Agency (CNES), R.H. from NASA grants NNX11AF41G and NNX11A023G and NSF grant ANT-1043649, G.K. from Austrian Science Fund (FWF) grant P25362-N26, T.B. from the Deutsche Forschungsgemeinschaft (DFG, BO 3199/2-1), and F.P. from European Space Agency project *glaciers_cci* (4000101778/10/I-AM).

Supplementary Materials

www.sciencemag.org/cgi/content/full/340/6134/852/DC1
Materials and Methods

Figs. S1 to S10

Tables S1 to S5

References

26 December 2012; accepted 7 March 2013

10.1126/science.1234532

Inhibition of PRC2 Activity by a Gain-of-Function H3 Mutation Found in Pediatric Glioblastoma

Peter W. Lewis,¹ Manuel M. Müller,² Matthew S. Koletsky,¹ Francisco Cordero,³ Shu Lin,⁴ Laura A. Banaszynski,¹ Benjamin A. Garcia,⁴ Tom W. Muir,² Oren J. Becher,³ C. David Allis^{1*}

Sequencing of pediatric gliomas has identified missense mutations Lys27Met (K27M) and Gly34Arg/Val (G34R/V) in genes encoding histone H3.3 (*H3F3A*) and H3.1 (*HIST3H1B*). We report that human diffuse intrinsic pontine gliomas (DIPGs) containing the K27M mutation display significantly lower overall amounts of H3 with trimethylated lysine 27 (H3K27me3) and that histone H3K27M transgenes are sufficient to reduce the amounts of H3K27me3 in vitro and in vivo. We find that H3K27M inhibits the enzymatic activity of the Polycomb repressive complex 2 through interaction with the EZH2 subunit. In addition, transgenes containing lysine-to-methionine substitutions at other known methylated lysines (H3K9 and H3K36) are sufficient to cause specific reduction in methylation through inhibition of SET-domain enzymes. We propose that K-to-M substitutions may represent a mechanism to alter epigenetic states in a variety of pathologies.

Somatic mutations in genes encoding proteins that modify chromatin dynamics frequently contribute to tumorigenesis (1). Mutations in subunits of the Polycomb repressive complex 2 (PRC2) are often associated with tu-

mor progression (2). PRC2 normally helps maintain epigenetic gene silencing and X chromosome inactivation through enzymatic di- and trimethylation of K27 on histone H3 (3). In addition to enzymatic machinery, histone H3 missense mu-

tations in pediatric gliomas represent direct evidence that alterations of the histones themselves can promote cancer. In two pediatric brain cancers, diffuse intrinsic pontine gliomas (DIPGs) and supratentorial glioblastoma multiforme (GBMs), 60% of patients studied exhibited one of two mutually exclusive mutations in either *H3F3A*, one of two genes encoding the histone H3 variant H3.3, or *HIST3H1B*, one of several genes encoding H3.1 (4–6). The K27M mutation occurring in either *H3F3A* or *HIST3H1B* was observed in nearly 80% of DIPGs, and 22% of non-brain stem gliomas (6).

We sought to determine whether DIPG samples that contain the K27M mutation exhibit global changes in key regulatory histone modifications. Immunoblots with antisera raised against the K27M substitution (fig. S1A) indicated the presence of

¹Laboratory of Chromatin Biology and Epigenetics, The Rockefeller University, New York, NY 10065, USA. ²Department of Chemistry, Princeton University, Princeton, NJ 08544, USA. ³Departments of Pediatrics and Pathology, Preston Robert Tisch Brain Tumor Center, Duke University Medical Center, Durham, NC 27710, USA. ⁴Department of Biochemistry and Biophysics, Perelman School of Medicine, University of Pennsylvania, Philadelphia, PA 19104, USA.

*Corresponding author. E-mail: alliscd@rockefeller.edu

H3 K27M protein in DIPG samples containing *H3F3A* (H3.3) or *HIST3H1B* (H3.1) alleles (Fig. 1A). DIPG tumors containing H3K27M mutations exhibited both a decrease in H3 with trimethylated lysine 27 (H3K27me3) and a modest increase in amounts of H3 with acetylated lysine 27 (H3K27ac) by immunoblot with modification-specific antisera (Fig. 1, A and C). Quantification of H3K27me3 by immunohistochemistry demonstrated that K27M mutant DIPGs contained significantly less H3K27me3 than non-K27M mutant DIPGs (Fig. 1D). The H3.1/3 K27M protein is 3.63% (± 0.33) to 17.61% (± 1.11) of total H3 in human DIPG samples, as measured by quantitative mass spectrometry (fig. S1B). Two histone modifications related to transcription and/or activation (H3K4me3 and H3K36me3) were similar in DIPG samples regardless of tumor genotype, which could be used to argue that global changes in posttranslational modifications were specific to H3K27. Using a platelet-derived growth factor (PDGF)-induced brain stem glioma model to characterize this mutation in vivo (7), we found that transgenic H3.3K27M was sufficient to increase H3K27ac and to significantly reduce H3K27me3 (Fig. 1, B to D). Expression of H3.3K27M with p53 loss in nestin progenitors of the neonatal mouse brain stem was not sufficient to generate gliomas but did induce proliferating ectopic cell clusters in 72% (21

out of 29) of the mice (fig. S1C), whereas expression of the wild-type H3.3 with p53 loss ($n = 8$) in nestin progenitors of the neonatal mouse brain stem did not result in the induction of ectopic proliferating cell clusters (fig. S1D).

To investigate the mechanism by which H3K27M decreased overall H3K27me3, we generated stable human embryonic kidney-293T (HEK293T) cell lines that express FLAG- and hemagglutinin (HA) epitope-tagged wild-type histone H3.3 or K27M and G34R/V mutants, which contributed to about 1% of total cellular histone H3, as measured by immunoblot. Cells expressing the H3K27M mutant histone exhibited a profound reduction in H3K27me2/3, with little changes in the amounts of H3K4me3 or H3K36me3 (Fig. 2A). This reduction was specific to the H3K27M mutation, as amounts of H3K27me2/3 remained unchanged in H3.3G34R/V transgenic cell lines. We did not observe change in the amounts of PRC2 complex components in H3.3K27M, PDGF-induced glioblastoma cell lines (fig. S2A).

The heterozygous and invariant nature of the lysine-to-methionine mutation at residue 27 in nearly 80% of pediatric DIPGs strongly suggests that this specific amino acid substitution imparts a unique gain-of-function to the mutant histone. To further test the specificity of this substitution, we performed a

survey of all amino acid substitutions at H3K27. Nearly all substitutions had little effect, if any, on the amounts of K27me3, with the exception of methionine, and to a lesser extent isoleucine (Fig. 2B).

The global reduction in H3K27me2/3 suggested that the H3K27M transgene reduced methylation on endogenous wild-type H3 histones. Indeed, purified heterotypic mononucleosomes (1:1 ratio of H3.3-FLAG-HA: endogenous H3.3), oligonucleosomes containing H3K27M, or wild-type oligonucleosomes from K27M-expressing cells displayed a marked decrease in H3K27me3 on the endogenous H3 protein (fig. S2B). Concomitantly, these nucleosomes exhibited a modest increase in the acetylation of H3K27 (H3K27ac) on the untagged H3 in the heterotypic K27M nucleosomes (Fig. 2C), and, similar to the modification pattern observed on mononucleosomes, oligonucleosome arrays showed elevated H3K27ac when they contained H3.3K27M (Fig. 2D).

We investigated amounts of H3K36me3 in cell lines carrying H3.3G34R/V mutations to determine whether these mutations behave similarly to H3K27M. Although overall amounts of H3K36me3 remained unchanged in H3.3G34R/V cell lines, a marked loss of H3K36me3 was exclusive to the epitope-tagged H3.2/3 of purified mono- or oligonucleosomes (Fig. 2, B and C). The epitope-

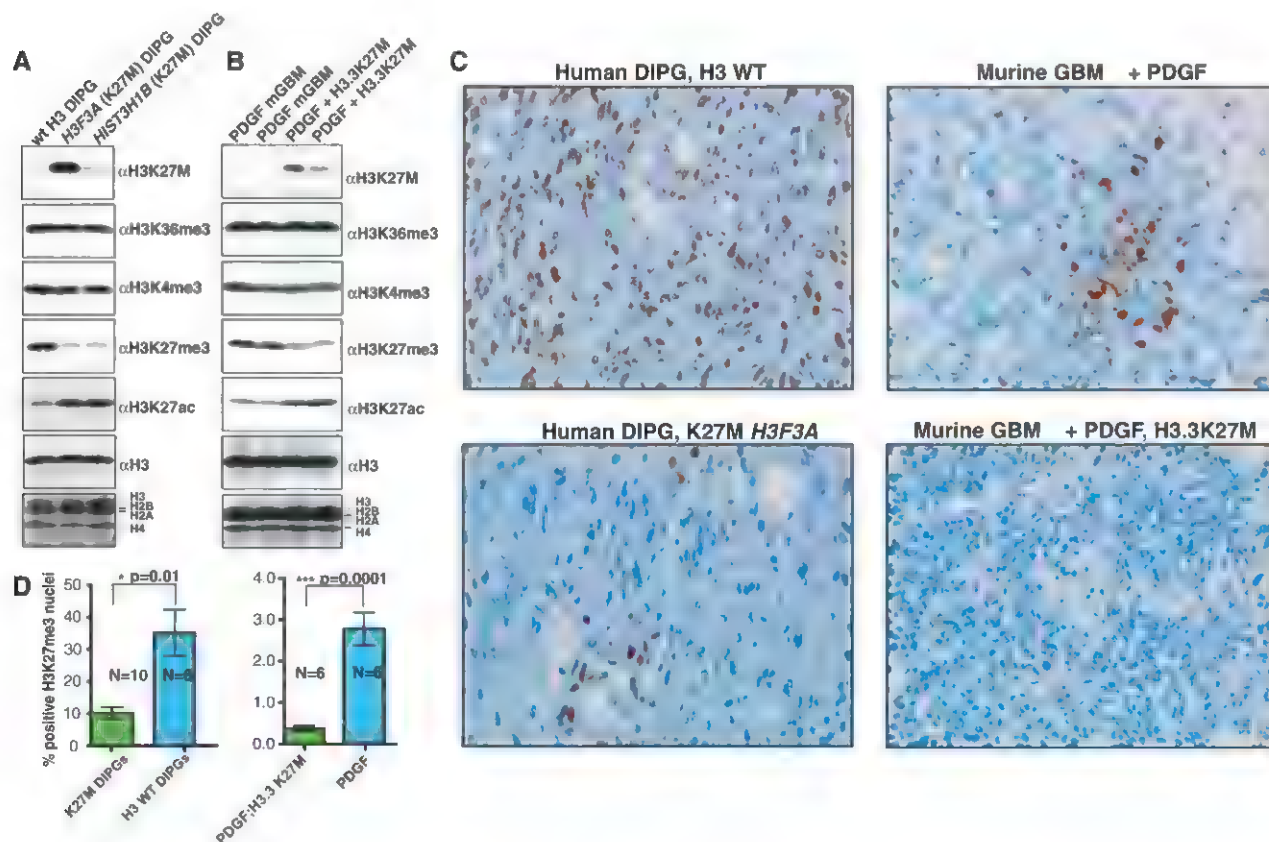


Fig. 1. Histones extracted from human DIPG containing *H3F3A* K27M (H3.3) or *HIST3H1B* K27M (H3.1) mutations exhibit decreased H3K27me3. (A) Immunoblots of acid-extracted histones from DIPGs of different indicated H3 genotypes. **(B)** Immunoblots of histones from PDGF-induced gliomas with

and without the H3.3K27M transgene. **(C)** Immunohistochemistry of H3K27me3 in human or murine gliomas containing wild-type H3.3 or H3.3K27M. **(D)** Immunohistochemistry quantification of nuclei staining positive for H3K27me3 ($P = 0.01$ for human DIPG, and $P = 0.0001$ for murine gliomas with the unpaired t test).

tagged H3 exhibited a decrease in K36me2 (~2.7-fold) and K36me3 (~18.5-fold) on the G34R/V mutants, compared with wild type, as measured by mass spectrometry (fig. S2C). Heterotypic H3.3 G34R or G34V mononucleosomes were methylated to a lesser extent by recombinant SETD2 in vitro, which indicated that nonglycine residues at position 34 on the substrate peptide decreases SETD2 methylation at K36 (fig. S2, D and E).

H3K27me3 peptides allosterically stimulate PRC2 methyltransferase activity on nucleosome substrates (8, 9), and we found that incubation of 10 or 100 μ M of H3K27me3 peptide strongly stimulated PRC2 activity toward mononucleosome or oligonucleosome templates (Fig. 3A). Heterotypic H3K27M mono- or oligonucleosomes containing H3K27M (fig. S3, A and B) were methylated to a lesser extent than wild-type nucleosome substrates when purified human PRC2 was used (Fig. 3A and fig. S3C). This reduction in PRC2-dependent signal was unique to chromatin containing H3K27M, as heterotypic K27A, K27R, or K27Q mononucleosomes showed no decrease in methylation on the endogenous histone (Fig. 3B).

The reduced methylation on nucleosome templates suggested that the K27M peptide might interfere with PRC2 activity normally stimulated by H3K27me3. Incubation of K27M peptide in trans decreased PRC2 activity on wild-type nu-

cleosomes to below the no-peptide signal (Fig. 3C), whereas the unmodified or K27ac peptide exhibited little stimulation relative to no-peptide control (Fig. 3C). The H3K27M peptide reduced PRC2-dependent methylation by 6.2-fold at 45 μ M as measured by scintillation counting (Fig. 3D). Peptide titration showed that μ M concentrations of H3K27M, but not the K27ac peptide, could inhibit PRC2-dependent methyltransferase activity in a dose-dependent manner (Fig. 3E and fig. S3, D and E).

We synthesized biotinylated H3 peptides carrying either the diazine-containing methionine isostere L-photo-Met at position 27 (peptide 1) or a benzophenylalanine residue at position 31 that retains the K27M mutation (peptide 2) (fig. S4, F and G). Upon irradiation, both peptides cross-linked effectively to the EZH2 subunit and less so to the AEBP2 and EED subunits (Fig. 4A and fig. S4E), which suggested that K27M peptides inhibit PRC2 through interaction with the EZH2 active site. Although the EED subunit is needed for enzymatic activity and K27me3 allosteric activation (8), we did not observe interaction between EED and H3K27M peptides by surface plasmon resonance or peptide pull-down assays (fig. S4, A to D). We additionally found the K27M peptide could inhibit a PRC2 complex that contained a mutant EED (Y365A) that cannot interact with K27me3 (fig. S5A).

Titration of K27M peptide to in vitro methylation reactions revealed a median inhibitory concentration (IC_{50}) of 5.9 μ M [95% confidence interval (CI) of 1.10 to 6.42]. To evaluate whether the thioether moiety of methionine was required for inhibition of PRC2, a norleucine derivative (K27Nle) was prepared. The K27Nle variant proved to be an even better inhibitor of PRC2 (Fig. 4B) (IC_{50} for K27Nle = 0.85 μ M) (95% CI: 0.57 to 1.27) (fig. S6A). Peptides containing Lys²⁷ replaced by Ile inhibited PRC2 to a lesser extent than K27M (IC_{50} for K27I = 8.9 μ M) (95% CI: 4.12 to 11.2), whereas Lys²⁷ replaced by Leu had no inhibitory effect on the amounts of H3K27me3 in vivo or PRC2 in vitro (Fig. 4C and fig. S6, B to D). Thus, a long, hydrophobic residue suffices for EZH2 binding, and methionine—and to a slightly lesser extent isoleucine—represents the ideal biochemically accessible choices.

SET domain histone methyltransferases contain several highly conserved aromatic residues that serve in substrate binding and catalysis. The Tyr⁶⁴¹ residue in EZH2 is hypothesized to restrict higher-order lysine methylation by acting as a steric gatekeeper (10, 11). Recombinant Y641N EZH2-containing PRC2 was less sensitive to inhibition by the H3K27M peptide compared with wild-type PRC2 (Fig. 4, D to F, and fig. S6, E and F), which furthers the argument that hydrophobic

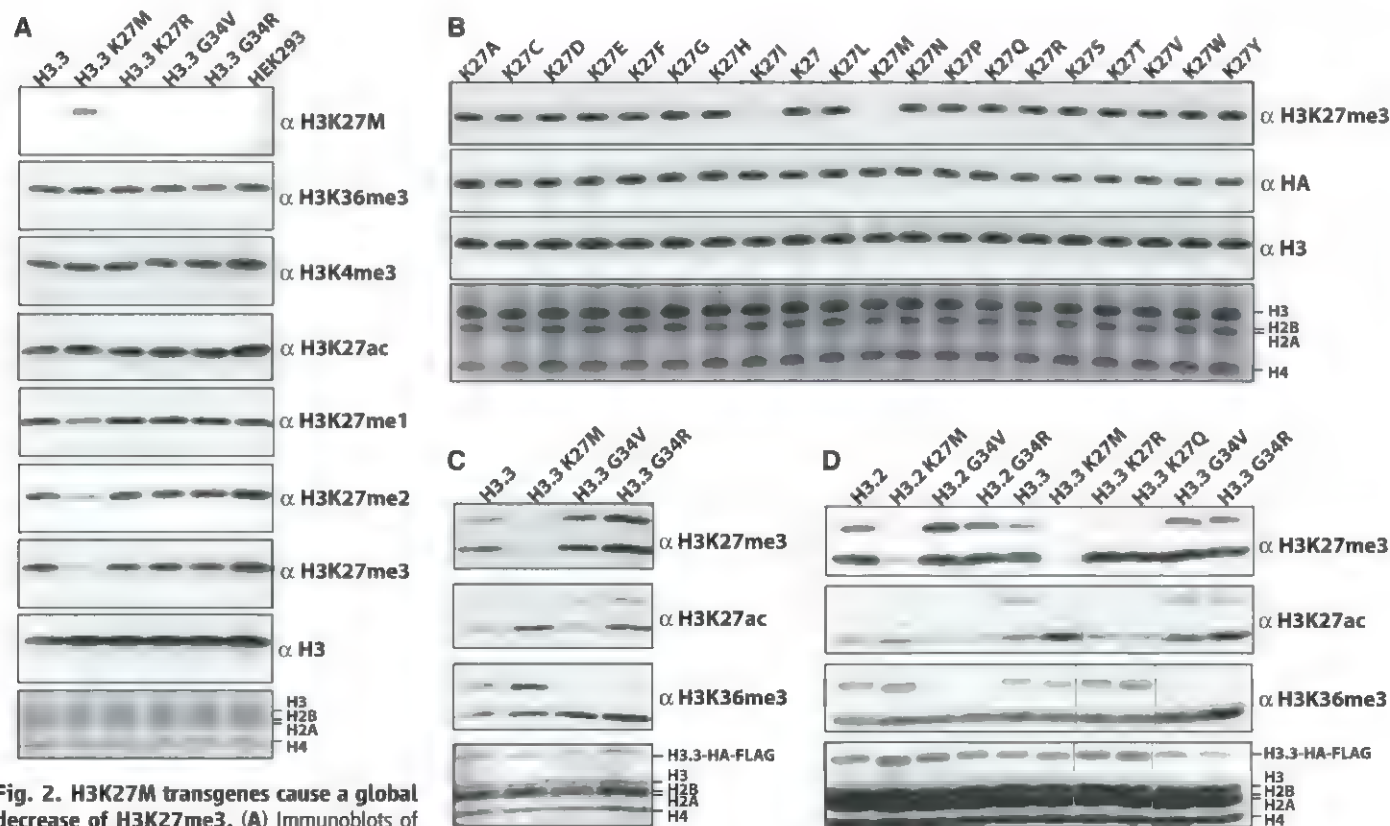


Fig. 2. H3K27M transgenes cause a global decrease of H3K27me3. (A) Immunoblots of whole-cell extract from lentivirus-transduced 293T cells expressing the indicated H3.3 transgenes. (B) Immunoblots of whole extract from H3.3 K27-to-X transduced 293T cells. The antibody against HA (anti-HA) blot shows the relative H3.3 transgene amounts. (C) Immunoblots of anti-HA-immunoprecipitated heterotypic H3.3 K27M or G34R/V mononucleosomes from

the indicated H3.3 transgenic 293T cell lines. (D) Immunoblots of anti-HA-immunoprecipitated oligonucleosomes (>95% of four to five nucleosomes in length, with a median of two to three nucleosomes) from the indicated H3.3 transgenic 293T cell lines (vertical black lines indicate where control lanes were removed for clarity).

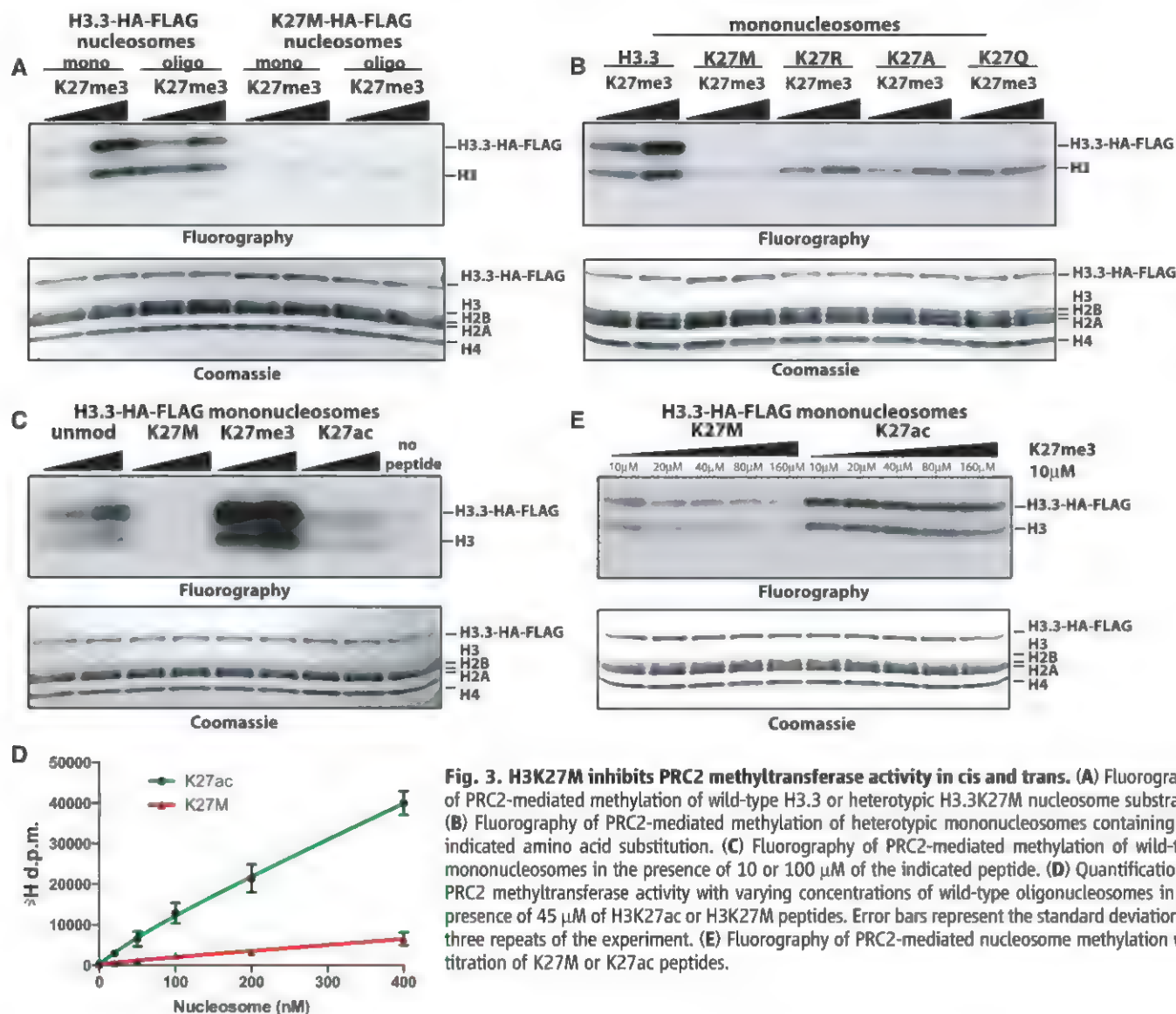


Fig. 3. H3K27M inhibits PRC2 methyltransferase activity in cis and trans. (A) Fluorography of PRC2-mediated methylation of wild-type H3.3 or heterotypic H3.3K27M nucleosome substrates. (B) Fluorography of PRC2-mediated methylation of heterotypic mononucleosomes containing the indicated amino acid substitution. (C) Fluorography of PRC2-mediated methylation of wild-type mononucleosomes in the presence of 10 or 100 μ M of the indicated peptide. (D) Quantification of PRC2 methyltransferase activity with varying concentrations of wild-type oligonucleosomes in the presence of 45 μ M of H3K27ac or H3K27M peptides. Error bars represent the standard deviation for three repeats of the experiment. (E) Fluorography of PRC2-mediated nucleosome methylation with titration of K27M or K27ac peptides.

interactions between the methionine side chain and aromatic residues in the EZH2 active site are important for K27M inhibition of PRC2.

We tested whether the highly conserved active sites of other SET-domain proteins may be similarly sensitive to methionine substitution at their cognate peptidyl-lysine substrate by constructing H3.3 transgenes containing methionine at K4, K9, and K36 (12). H3K9M and H3K36M transgenes decrease overall amounts of H3K9me2/3 and H3K36me2/3, respectively (Fig. 4G and fig. S7A). Although H3K4M transgenes did not diminish overall amounts of H3K4me2/3, the lack of reduction in methylation may be a consequence of reported inhibition of LSD1/2 histone H3K4me3 demethylases by H3K4M peptides (13). Histone H3K9M(1–20) peptides effectively inhibit recombinant histone H3K9 methyltransferases SUV39H1 and G9a (Fig. 4H) [IC_{50} for K9M = 2.2 μ M for SUV39H1 (95% CI: 1.7 to 2.6); IC_{50} for K9M = 3.6 μ M for G9a (95% CI: 2.1 to 5.9)] (fig. S7, B and C). These data argue that the H3K9-specific

SET-domain inhibition likely causes the reduction of H3K9me2/3 in H3.3K9M-expressing cells.

To determine whether the chromatin context of K-to-M mutants is important for in vivo inhibition of trimethylation, we placed the H3 tail (amino acids 1 to 42) onto the core domain (amino acids 23 to 102) of histone H4-HA-FLAG. H3K9me3 was reduced in cells expressing the K9M H3-H4 hybrid (fig. S8A). However, K27M and K36M failed to reduce H3K27me3 and H3K36me3 when expressed in the context of H3-H4 hybrid transgenes (fig. S8, B, C, and D). These results argue that SET-domain protein interactions with non-N-terminal nucleosomal surfaces are important for the full inhibitory activity of some K-to-M, but not all, mutants in vivo.

In summary, the data shown here provide compelling evidence that a missense histone mutation can dramatically alter nuclear biochemical processes through a gain-of-function mechanism. Moreover, our data indicate that K-to-M mutations target the active sites of diverse SET domain-

containing methyltransferases and, thereby, effectively compete with substrate binding and turnover. Notably, in their proper chromosomal context, K-to-M mutant histones that make up only a few percent of total histones suffice to prevent global methylation at their cognate residues. This reduction in histone methylation is expected to disrupt positive-feedback loops that contribute to the regulation of PRC2 and thus to enhance the inhibitory effect of mutant histones. We propose a model whereby aberrant epigenetic silencing through H3K27M-mediated inhibition of PRC2 activity promotes gliomagenesis. The broadly adaptable, yet highly specific, inhibition of SET-domain proteins through K-to-M mutation offers the intriguing possibility of other etiological missense mutations in histones. Additionally, our work has uncovered a potentially useful mechanism to exclusively inhibit individual SET-domain methyltransferases, and conceivably other chromatin-modifying enzymes, implicated in a variety of malignancies.

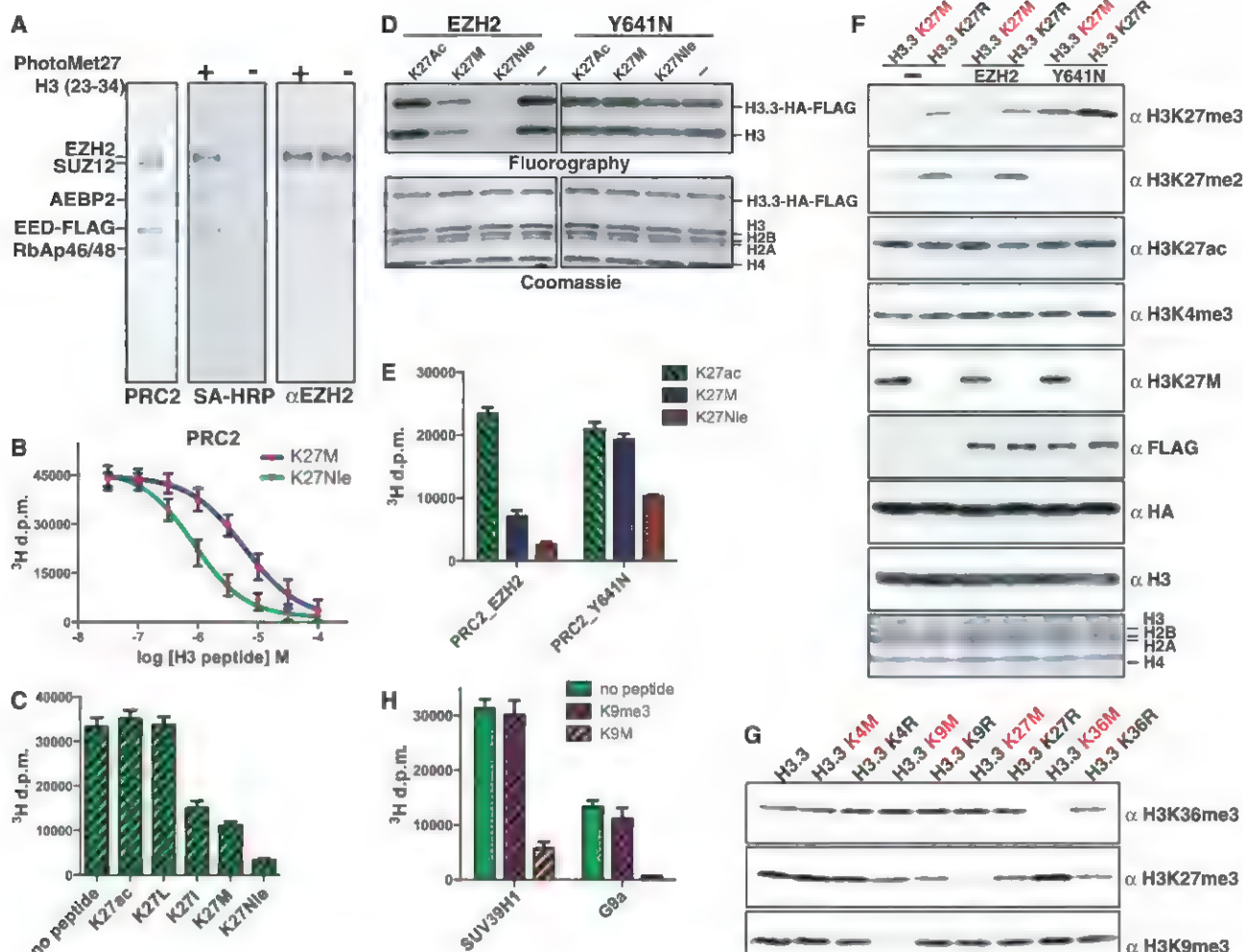


Fig. 4. H3K27M-mediated inhibition of PRC2 occurs through interaction with EZH2. (A) Coomassie gel of purified PRC2 cross-linked to peptide 1 (fig. S4F) and immunoblots with streptavidin–horseradish peroxidase (SA-HRP) or antibody against EZH2. (B) IC_{50} measurement for methionine or nortecine substitution at K27. Titration reactions of H3.3K27M or K3.3K27Nle peptides with 70 ng PRC2 and 0.8 μg wild-type oligonucleosomes. Error bars represent the standard deviation of five repeats. (C) Quantification of PRC2 methyltransferase activity in the presence of 50 μM of H3 peptides (18 to 37) containing K27acetyl, K27Leu, K27Ile, K27Met, or K27Nle. Error bars represent standard deviation of three repeats. (D) Fluorography of methyltransferase reactions with wild-type or EZH2-Y641N PRC2 on wild-type H3.3 nucleosomes in the presence of 50 μM H3 peptides (18 to 37) with K27acetyl, K27Met, or K27Nle. Error bars represent the standard deviation of three repeats. (E) Quantification of methyltransferase activity of reactions in (D). Error bars represent the standard deviation of five repeats. (F) Immunoblots of 293T cells expressing the indicated EZH2 and H3.3 transgenes. The anti-HA blot shows relative H3.3 transgene amounts, and the anti-FLAG shows the relative EZH2 or Y641N amounts. (G) Immunoblots of whole-cell extract from transduced 293T cells expressing the indicated H3.3 transgenes. The arrows to the right of the total H3 blot point to the transgenic histone (red) or endogenous wild-type histone (black). (H) Quantification of histone methyltransferase activity on H3 peptides (1 to 20) by SUV39H1 or G9a in the presence of 10 μM H3K9me3 or H3K9M or no peptide. Error bars represent the standard deviation for five repeats.

References and Notes

1. S. J. Eassey, C. D. Allis, P. W. Lewis, *Science* **331**, 1145 (2011).
2. J. A. Simon, C. A. Lange, *Mutat. Res.* **647**, 21 (2008).
3. R. Margueron, D. Reinberg, *Nature* **469**, 343 (2011).
4. D. A. Khuong-Quang et al., *Acta Neuropathol.* **124**, 439 (2012).
5. J. Schwartzentruber et al., *Nature* **482**, 226 (2012).
6. G. Wu et al., *Nat. Genet.* **44**, 251 (2012).
7. O. J. Becher et al., *Cancer Res.* **70**, 2548 (2010).
8. R. Margueron et al., *Nature* **461**, 762 (2009).
9. C. Xu et al., *Proc. Natl. Acad. Sci. U.S.A.* **107**, 19266 (2010).
10. D. B. Yap et al., *Blood* **117**, 2451 (2011).

11. C. J. Sneeringer et al., *Proc. Natl. Acad. Sci. U.S.A.* **107**, 20980 (2010).
12. S. D. Taverna, H. Li, A. J. Ruthenburg, C. D. Allis, D. J. Patel, *Nat. Struct. Mol. Biol.* **14**, 1025 (2007).
13. A. Karytinos et al., *J. Biol. Chem.* **284**, 17775 (2009).

Acknowledgments: B.A.G. acknowledges funding from NIH Innovator grant (DP2OD007447), Office of the Director, NIH. O.J. B. is supported by the U.S. Department of Defense; The Pediatric Brain Tumor Foundation; and the Damon Runyon, Rory David Deutsch, and Cristian Rivera Foundations. C.D.A. acknowledges funding from NIH (GM040922) and Starr Cancer Consortium

(grant SCC I6-A614). We thank D. Reinberg for reagents, and EMD Millipore for its role in H3K27M antibody generation.

Supplementary Materials

www.sciencemag.org/cgi/content/full/science.1232245/DC1
Materials and Methods
Supplementary Text
Figs. S1 to S8
Reference (14)

1 November 2012; accepted 12 March 2013
Published online 28 March 2013;
10.1126/science.1232245

Invasive Harlequin Ladybird Carries Biological Weapons Against Native Competitors

Andreas Vilcinskas,^{1,3*†} Kilian Stoecker,^{2,3†} Henrike Schmidtberg,³ Christian R. Röhrich,³ Heiko Vogel⁴

Invasive species that proliferate after colonizing new habitats have a negative environmental and economic impact. The reason why some species become successful invaders, whereas others, even closely related species, remain noninvasive is often unclear. The harlequin ladybird *Harmonia axyridis*, introduced for biological pest control, has become an invader that is outcompeting indigenous ladybird species in many countries. Here, we show that *Harmonia* carries abundant spores of obligate parasitic microsporidia closely related to *Nosema thompsoni*. These microsporidia, while not harming the carrier *Harmonia*, are lethal pathogens for the native ladybird *Coccinella septempunctata*. We propose that intraguild predation, representing a major selective force among competing ladybird species, causes the infection and ultimate death of native ladybirds when they feed on microsporidia-contaminated *Harmonia* eggs or larvae.

Human activities, particularly international trade, promote the spread of invasive species that cause extensive economic losses and negatively affect native species. Several factors can play a role in the invasive success of such species, including the lack of predators, short generation times, and the ability to disperse rapidly and adapt easily to new habitats (1, 2). However, the principles that allow some species to become successful invaders, whereas most (even if closely related) do not, remain poorly understood (3). Invaders can be released from native,

coevolved pathogens, but they face other pathogens in their new environments, suggesting that the ability to mount strong antimicrobial defenses may promote invasive success (4). Yet enhanced immunity can be costly and, therefore, can be traded off against other traits such as growth and reproduction (5, 6). We used the harlequin ladybird *Harmonia axyridis* (a native species in central Asia) as a model to explore the potential role of immunity in invasion biology. This species has been introduced into many countries as a biological control agent against aphids and other insect

pests but is now causing severe problems because it successfully outcompetes native ladybird species in many areas (7).

We recently showed that, in contrast to native ladybird species in Europe, the *Harmonia* hemolymph contains strong and constitutive antibacterial activity throughout development. We attributed this activity to harmonine, a secondary metabolite that accumulates to high levels in the hemolymph. The broad-spectrum activity of this alkaloid compound is demonstrated by its ability to inhibit even human pathogens such as *Mycobacterium tuberculosis* and *Plasmodium falciparum*, making it a promising lead for the development of new anti-infective drugs (8). Constitutive harmonine activity may help *Harmonia* to deal with pathogens encountered in new habitats, whereas native ladybirds are more susceptible to infection (9).

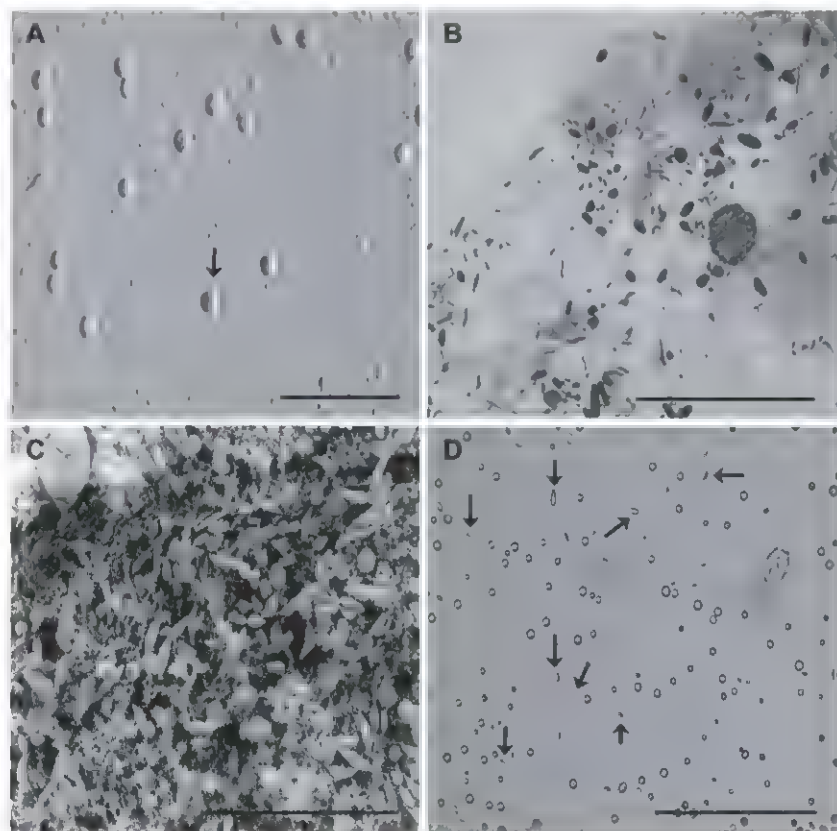
Independently, harmonine has been proposed as a chemical defense compound protecting *Harmonia* eggs and larvae from predation by native ladybird species (10). Kajita *et al.* reported that

¹Institute of Phytopathology and Applied Zoology, Heinrich-Buff-Ring 26-32, Justus-Liebig-University of Giessen, D-35392 Giessen, Germany. ²Bundeswehr Institute of Microbiology, Neuherbergstrasse 11, D-80937 Munich, Germany. ³Fraunhofer Institute of Molecular Biology and Applied Ecology, Winchesterstrasse 2, 35394 Giessen, Germany. ⁴Max-Planck-Institute of Chemical Ecology, Hans-Knoell-Strasse 8, D-07745 Jena, Germany.

*Corresponding author. E-mail: andreas.vilcinskas@agr.uni-giessen.de

†These authors contributed equally to this work.

Fig. 1. Microscopy studies of microsporidia. (A) Light microscopy image showing the high concentration of microsporidia (small objects) between the larger hemocytes (arrow) in *Harmonia* hemolymph. Scale bar, 50 μ m. (B) Semithin sections of hemolymph tissue confirm the presence of microsporidia, among which some exhibit extruded polar tubes (circles). Extrusion of polar tubes occurred during fixation. Scale bar, 20 μ m. (C) Scanning electron microscopy image of microsporidia in the *Harmonia* hemolymph, showing the high load of spores. Scale bar, 20 μ m. (D) Light microscopy image showing microsporidia (arrows) between yeastlike cells and larger hemocytes in dying *Coccinella* beetles 7 days post-inoculation. Scale bar, 20 μ m.



the ingestion of *Harmonia* eggs by native *Coccinella septempunctata* beetles caused mortality, but the reciprocal situation was nonlethal. In agreement with our previous report (8), they detected high concentrations of harmonine in *Harmonia* eggs and concluded that this compound protects the invasive ladybird from intraguild predation (10), which is a major selective force among competing ladybird species (11).

Here, we report that the injection of *Harmonia* hemolymph—but not synthetic harmonine alone, even in high concentrations (fig. S1)—can kill *Coccinella* beetles, making it unlikely that the mortality caused by feeding on *Harmonia* eggs is caused by the presence of harmonine. It is therefore apparent that the mortality in *Coccinella* beetles is caused by another component found in the hemolymph of *Harmonia*.

Light microscopy revealed the presence of abundant microsporidia among the hemocytes in *Harmonia* hemolymph (Fig. 1A) (see supplementary materials and methods). Microsporidia are obligate parasites that replicate within eukaryotic cells after penetrating the plasma membrane with an extruded polar tube. Semithin sections of hemolymph tissue confirmed the presence of microsporidia, among which some exhibited extruded polar tubes (Fig. 1B). We used scanning electron microscopy to document the high abundance of microsporidia in the hemolymph of *Harmonia* (Fig. 1C). Despite the abundance of spores, we did not find any *Harmonia* beetles that were killed by the parasites in our rearing. The low physiological activity of the microsporidia is further supported by the absence of microsporidial gene expression when analyzing the transcriptome of *Harmonia* eggs and beetles (12). These data suggest that the microsporidia are present in a physiologically inactive

spore stage and do not harm their host, perhaps because it has acquired tolerance or resistance.

We identified the microsporidia by amplifying the small-subunit ribosomal RNA (rRNA) genes using a variety of previously described primer sets (13), resulting in the specific amplification of the partial microsporidial 16S rRNA gene. The determined sequence identity ($\geq 99\%$) placed the *Harmonia*-associated microsporidia within the *Nosema/Vairimorpha* clade, with *Nosema thomsoni* as the closest relative (14). This assay confirmed the presence of *Nosema*-like microsporidia in all *Harmonia* beetles of all populations sampled, as well as in eggs and larvae, suggesting vertical transmission. All attempts to coculture the microsporidia with different insect cell lines (Sf9, Sf21, *Drosophila* S2, High Five) failed.

Given that (i) *Coccinella* beetles are killed by feeding on *Harmonia* eggs and larvae, but the reciprocal situation is not lethal (10), and (ii) harmonine does not affect *Coccinella* beetles, even at high concentrations, we propose that native ladybird species may be lethally infected by the microsporidia carried by *Harmonia* when they feed on its eggs and larvae. To test this hypothesis, we collected hemolymph samples from *Harmonia* and isolated the microsporidia by repeated centrifugation and washing steps. We divided the purified microsporidia into two portions, one of which was heat-inactivated and used for control injections.

All *Coccinella* beetles injected with live microsporidia isolated from *Harmonia* died within 2 weeks (Fig. 2), whereas the majority of control beetles injected with either the heat-inactivated microsporidia or the buffer alone survived. Control injections with cell-free hemolymph samples from *Harmonia* lacking microsporidia and

hemocytes did not result in enhanced mortality (fig. S4). This observation and the analysis of injected samples by SDS-polyacrylamide gel electrophoresis (fig. S2) and mass spectrometry ruled out the possibility that the mortality was caused by thermolabile toxins in the hemolymph of *Harmonia*. Further, we determined the presence of microsporidia in dying *Coccinella*, but not in control beetles (Fig. 1D and fig. S3). We concluded that the microsporidia carried by *Harmonia* were lethal but required some time to infect and replicate within *Coccinella*.

The high abundance of tolerated microsporidia in *Harmonia* hemolymph and their ability to kill *Coccinella* beetles support our hypothesis that these parasites contribute to the dominance of *Harmonia* over native species. Obviously, native ladybirds such as *Coccinella* do not share with *Harmonia* the ability to suppress microsporidial replication. It remains to be seen whether or not harmonine (8) and/or the tremendous spectrum of antimicrobial peptides discovered in *Harmonia* (12) contribute to its tolerance or resistance against microsporidia. Our data also provide a candidate mechanism to explain why the decline in native ladybird numbers is associated with intraguild predation (11). The presence of microsporidia in *Harmonia* may function like a biological weapon, in accordance with the novel weapons theory (15).

References and Notes

1. R. N. Mack et al., *Ecol. Appl.* **10**, 689 (2000).
2. P. Alpert, *Biol. Invasions* **8**, 1523 (2006).
3. D. A. Wardle, R. D. Bardgett, R. M. Callaway, W. H. Van der Putten, *Science* **332**, 1273 (2011).
4. K. A. Lee, K. C. Klasing, *Trends Ecol. Evol.* **19**, 523 (2004).
5. P. Schmid-Hempel, *Annu. Rev. Entomol.* **50**, 529 (2005).
6. A. Vilcinskas, *J. Insect Physiol.* **59**, 123 (2013).
7. H. Roy, H. Wajnberg, *BioControl* **53**, 1 (2008).
8. C. R. Röhrich et al., *Biol. Lett.* **8**, 308 (2012).
9. H. E. Roy, P. M. J. Brown, P. Rothery, R. L. Ware, M. E. N. Majerus, *BioControl* **53**, 265 (2008).
10. Y. Kajita, J. J. Obyrsky, J. I. Slogett, K. F. Haynes, *Oecologia* **163**, 313 (2010).
11. M. M. Gardiner, M. E. O'Neal, D. A. Landis, *PLoS ONE* **6**, e23576 (2011).
12. A. Vilcinskas, K. Mukherjee, H. Vogel, *Proc. R. Soc. B* **280**, 20122113 (2013).
13. L. M. Weiss, C. R. Vossbrinck, in *The Microsporidia and Microsporidiosis*, M. Wittner, L. M. Weiss, Eds. (American Society for Microbiology Press, Washington, DC, 1999), vol. 4, pp. 129–171.
14. The partial microsporidial 16S rRNA sequence has been deposited in the public database GenBank under accession no. KC596023.
15. R. M. Callaway, W. M. Ridenour, *Front. Ecol. Environ.* **2**, 436 (2004).

Acknowledgments: We acknowledge project funding provided by the excellence initiative of the Hessian Ministry of Science and Art via the LOEWE research focus "Insect Biotechnology." We thank J. Löffl for critical reading and R. M. Twyman for editing of the manuscript.

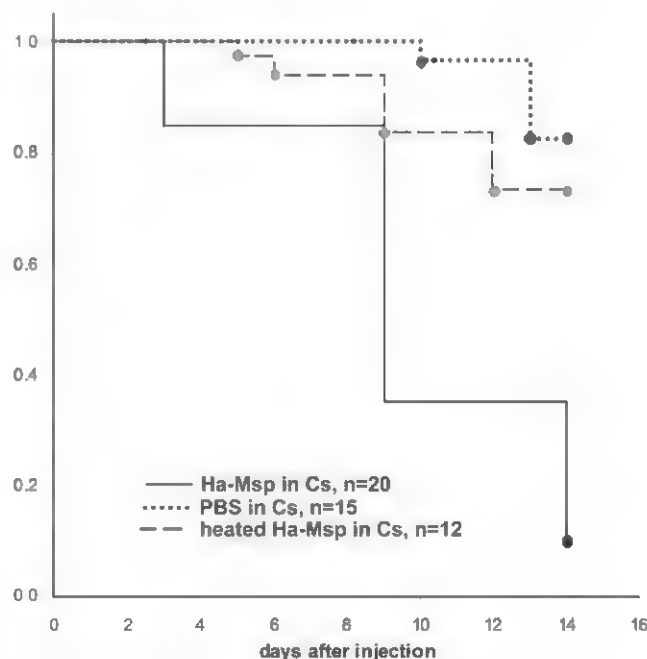
Supplementary Materials

www.sciencemag.org/cgi/content/full/340/6134/862/DC1
Materials and Methods
Figs. S1 to S4
Tables S1 to S3
References (16, 17)

13 December 2012; accepted 28 March 2013
10.1126/science.1234032

Fig. 2. Survival after injection.

Coccinella beetle survival rate (y axis) analysis after transfer of microsporidia isolated from the hemolymph of *Harmonia* (Ha-Msp in Cs), calculated by Kaplan Meier survival analysis log-rank test. *Coccinella* beetles were injected with living microsporidia (solid line). Control injections with either heat-inactivated microsporidia (heated Ha-Msp) isolated from *Harmonia* (dashed line) or PBS alone (dotted line) showed statistically significant differences ($P < 0.05$), indicating that mortality of *Coccinella* is predominantly caused by living microsporidia. Circles indicate where animals have been taken out of the experiment to control the presence of microsporidia in the hemolymph. Cs, *Coccinella septempunctata*; PBS, phosphate-buffered saline.



Nuclear Actin Network Assembly by Formins Regulates the SRF Coactivator MAL

Christian Baarlink, Haicui Wang, Robert Grosse*

Formins are potent activators of actin filament assembly in the cytoplasm. In turn, cytoplasmic actin polymerization can promote release of actin from megakaryocytic acute leukemia (MAL) protein for serum response factor (SRF) transcriptional activity. We found that formins polymerized actin inside the mammalian nucleus to drive serum-dependent MAL-SRF activity. Serum stimulated rapid assembly of actin filaments within the nucleus in a formin-dependent manner. The endogenous formin mDia was regulated with an optogenetic tool, which allowed for photoreactive release of nuclear formin autoinhibition. Activated mDia promoted rapid and reversible nuclear actin network assembly, subsequent MAL nuclear accumulation, and SRF activity. Thus, a dynamic polymeric actin structure within the nucleus is part of the serum response.

Formins are actin nucleation and elongation factors that assemble linear actin filaments (1–3). The formins mDia1 and mDia2 can be detected in the nucleus, and mDia2 is exported in an exportin 1 (CRM1)-dependent manner (4, 5). However, whether formins have a function in the nucleus is unclear. Immunoblotting for endogenous proteins revealed the presence of mDia1 and mDia2, as well as β -actin, in nuclear fractions; nevertheless, the absence of α -tubulin demonstrated that the fractions were not contaminated with cytoplasmic content (Fig. 1A). When compartmentalization of FLAG-labeled mDia2 was examined by using leptomycin B (LMB) to block CRM1, we observed nuclear accumulation within 5 min (Fig. 1B), which suggests rapid mDia2 nuclear shuttling.

Actin dynamics directly control activation of serum response factor (SRF), a transcription factor essential for early embryogenesis (6), through the cofactor megakaryocytic acute leukemia protein MAL (also known as MRTF-A or MKL1) (7). This occurs via release of actin-MAL interactions for nuclear accumulation of MAL (8). MAL-SRF-dependent transcription is critical for numerous cytoskeletal processes, such as cell contraction, adhesion, and motility (7). MAL is also regulated through actin inside the nucleus, although the underlying mechanism is unclear (8). We hypothesized that nuclear mDia participates in this process. To compare the abilities of cytoplasmic and nuclear mDia to activate MAL-SRF, we fused a CRM1-dependent nuclear export signal (NES) to a constitutively active version of mDia1 (Dia1ct) that displays predominant nuclear localization (9). Nuclear mDia-driven SRF activity was at least as potent as its cytoplasmic counterpart (fig. S1, A and B). To confirm nuclear activity of Dia1ct, we compared actin assembly rates from cytoplasmic and nuclear fractions from

Dia1ct-expressing cells. Only Dia1ct-expressing nuclear extracts displayed increased actin assembly over mock transfections (fig. S1C). We then assessed whether nuclear formin-mediated SRF regulation requires actin dynamics by expressing a nonpolymerizable R62D actin mutant (in which aspartic acid replaces arginine 62) fused to a nuclear localization signal (NLS) (10). Indeed, Dia1ct could not induce SRF activity in cells expressing R62D actin, while the SRF-VP16 fusion protein was unaffected (fig. S1D). Of note, nuclear confined Dia1ct increased the expression of the SRF target genes vinculin, SRF, and Acta2 comparable to levels of a constitutively active Δ N-MAL (11) (fig. S1E). To characterize the impact of cytoplasmic versus nuclear Dia1ct on MAL-SRF, we analyzed SRF activity under increasing amounts of NLS-actin. Only nuclear mDia could efficiently counteract increased concentrations of nuclear G-actin for SRF activity (Fig. 1C), which suggested that nuclear actin polymerization promotes G-actin re-

lease from MAL. Indeed, endogenous MAL interaction with NLS-actin was efficiently perturbed in the presence of nuclear Dia1ct but not NES-Dia1ct (fig. S1F). Furthermore, Dia1ct-expressing cells displayed a highly organized nuclear actin network (fig. S2) in contrast to expression of a nuclear localized VCA-domain, a known activator of Arp2/3 (fig. S2E) (12). We then inhibited mDia selectively in the nuclear compartment by fusing an NLS to dominant-negative mDia (13). This construct, dn.Dia-NLS, which efficiently localized and exclusively functioned in the nucleus (fig. S1G), robustly interfered with serum-induced SRF activity but did not affect the actin-independent mutant Δ N-MAL (Fig. 1D). Consistently, replacement of endogenous mDia2 with a derivative unable to enter the nucleus could not fully restore serum-induced SRF activity (fig. S3). Thus, nuclear function of mDia2 is required to efficiently activate SRF by serum.

Physiological nuclear actin network assembly has not been reported in mammalian cell culture, although the presence of monomeric actin in the nucleus is well documented (14–16). Given the predominance of cytoplasmic actin over nuclear actin, we fused an NLS to the F-actin probe LifeAct, tagged with green fluorescent protein (GFP), to restrict detection to the nuclear compartment. In serum-starved cells, LifeAct-GFP-NLS displayed a diffuse fluorescence signal (Fig. 2A). When cells were stimulated with 20% serum, we observed the rapid assembly of an endogenous nuclear actin network within 15 s (Fig. 2A and movie S1). This was confirmed by glutaraldehyde fixation and phalloidin staining on cells with no ectopic protein expression (Fig. 2B and fig. S4). Serum-induced nuclear actin assembly was abrogated by combined small interfering RNA (siRNA) treatment against mDia1 and mDia2 (Fig. 2B). Serum-stimulated actin polymerization, as well as its mDia dependency, was further confirmed by actin

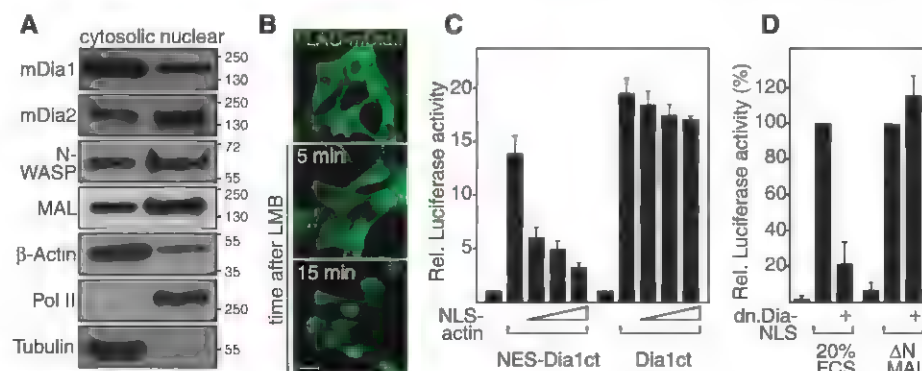


Fig. 1. Nuclear mDia effects on MAL-SRF transcriptional activity. (A) Subcellular fractions were immunoblotted for endogenous proteins as indicated. Numbers indicate molecular mass (kD). (B) NIH3T3 cells stably expressing FLAG-mDia2 were treated with 20 nM LMB before fixation. FLAG-immunolabeling reveals nuclear accumulation of mDia2 over time. Scale bar, 20 μ M. (C) Nuclear formin negotiates inhibition of MAL by nuclear actin. Cells were transfected with the MAL-SRF reporter 3DA.Luc to assess effects on SRF. SRF activity was measured after expression of nuclear Dia1ct or cytoplasmic NES-Dia1ct with increasing amounts of NLS-actin (0.1, 0.3, and 0.5 μ g). Results are means \pm SD ($n = 3$). (D) SRF activity from serum (fetal calf or bovine serum, FCS)— or Δ N-MAL-stimulated cells in the absence or presence of dn. Dia-NLS to suppress endogenous mDia in the nucleus. Results are means \pm SD ($n = 3$).

Institute of Pharmacology, Biochemical-Pharmacological Center (BPC), University of Marburg, Germany.

*Corresponding author. E-mail: robert.grosse@staff.uni-marburg.de

Fig. 2. Dynamics, serum-responsiveness, and mDia-dependence of nuclear actin assembly.

(A) Live NIH3T3 cells transfected with LifeAct-GFP-NLS (25 ng/6-well) were kept in serum-free medium for 24 hours and monitored before and during serum (FCS) stimulation. Individual frames reveal LifeAct-GFP-NLS probed endogenous F-actin distribution at indicated time points. Scale bar, 10 μ m. See also movie S1. (B) Depletion of endogenous mDia impairs nuclear actin filament formation. NIH3T3 cells were treated with siRNA against mDia1 and mDia2, kept in serum-free medium for 16 hours before stimulation with 20% FCS for 20 s and instant glutaraldehyde fixation. Probing endogenous F-actin by using fluorescently labeled phalloidin reveals native nuclear actin filaments in 72% of control siRNA-treated cells and 7% of cells silenced for both mDia1 and mDia2 (>30 cells per condition). Scale bar, 10 μ m. DAPI, 4',6'-diamidino-2-phenylindole. See also fig. S4. (C and D) The capacity of nuclear extracts to stimulate actin assembly was quantified by using pyrenyl-actin assembly assays. Results are shown as means \pm SD ($n = 3$). (C) NIH3T3 cells were starved for 16 hours and instantly lysed at indicated time points after stimulation with 20% FCS. After subcellular fractionation, equal amounts of nuclear extracts were measured in pyrenyl-actin assembly assays (see also fig. S5G). (D) Serum-stimulated nuclear actin assembly is mDia-dependent. Nuclear extracts, obtained directly after serum-stimulation, were subdivided to compare the effects of addition of either dimethyl sulfoxide or the mDia-inhibitor K216-0385 (compound 2.4) on actin assembly. Results are means \pm SD ($n = 3$). DMSO, dimethyl sulfoxide.

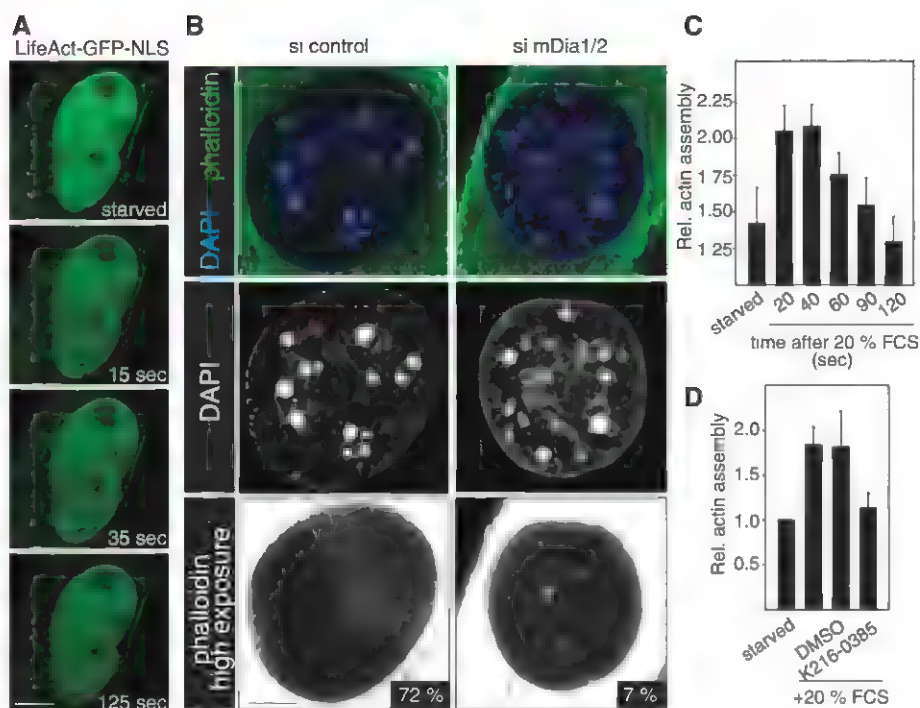
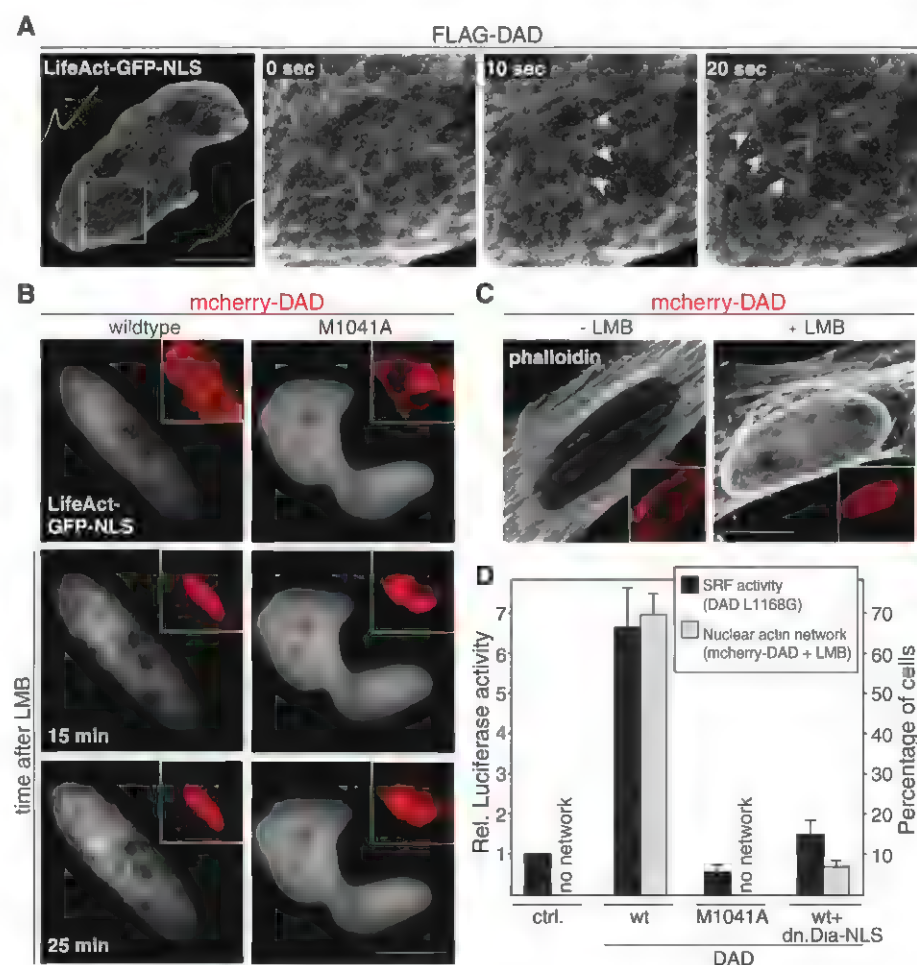


Fig. 3. Activation of nuclear formins and effects on actin network assembly and dynamics for SRF activity. (A) Live HeLa cells expressing LifeAct-GFP-NLS together with FLAG-tagged mDia2-DAD were monitored over time. Individual frames at higher magnification (white rectangle) reveal newly formed actin filaments (arrow heads) and dynamics at indicated time points in seconds (movie S2). Scale bar, 10 μ m. Yellow lines delineate cell borders. (B) Spatiotemporal induction of a nuclear actin network by localized release of autoinhibited endogenous mDia through mCherry-DAD derivatives, as indicated, monitored using LifeAct-GFP-NLS. Nuclear accumulation of mCherry-DAD variants (shown in insets) was mediated by LMB addition, as indicated (movie S3). Scale bar, 10 μ m. (C) HeLa cells expressing mCherry-DAD were treated with or without LMB (20 nM for 60 min) before fixation and staining of endogenous F-actin by using fluorescently labeled phalloidin. Scale bar, 10 μ m. (D) Nuclear mDia2-DAD stimulates SRF and nuclear actin network formation. SRF activation by nuclear trapped DAD-L1168G was compared with the ability of nuclear accumulated DAD (mCherry-DAD + LMB) to induce nuclear actin network formation in the presence or absence of dn.Dia-NLS to inhibit endogenous mDia in the nucleus. Image examples are shown in fig. S7.



assembly assays on nuclear fractions and by using a small-molecule inhibitor (17) to block mDia1 and mDia2 activity (Fig. 2, C and D). Consistently, RNA interference of mammalian mDia1 or mDia2 also inhibited basal actin assembly rates of nuclear extracts, whereas knockdown of the formin FHOD1 or inhibition of Arp2/3 had no effect (fig. S5 and S6).

mDia2 activity is controlled through autoinhibition mediated by the key residue M1041 in the diaphanous autoregulatory domain (DAD) (18, 19). To spatially activate endogenous mDia2 in the nucleus, we made use of DAD expression as a tool to release mDia autoinhibition (fig. S7A) (19). Cells expressing the DAD construct had a nuclear actin network that was constantly and dynamically reorganized over time (Fig. 3A and movie S2). We also observed what appeared to be bending or buckling of filaments, suggesting that the assembled filaments might be under tension and organized into a distinct network spanning the nucleus. We subsequently assessed this process of endogenous formin activation in a spatiotemporal manner. A NES-like sequence within the mDia2-DAD region requires residue Leu¹¹⁶⁸ (fig. S7A) (4). This allowed us to rapidly accumulate mCherry-DAD in the nucleus after adding LMB to monitor the de novo generation of

nuclear actin filaments. Nuclear translocation of DAD readily induced the formation of an actin filament network inside the nucleus (Fig. 3B and movie S3), which was confirmed by phalloidin staining in the absence of LifeAct (Fig. 3C). No actin network could be detected when a mutated M1041A-DAD was translocated that is unable to release endogenous mDia autoinhibition (Fig. 3B). We then asked whether endogenous nuclear formins can activate SRF. We generated a NES mutant of mDia2-DAD (DAD-L1168G) for continuous nuclear accumulation and mDia activation (fig. S7B). Expression of this mutant activated MAL-SRF, whereas the double mutant DAD-L1168G/M1041A defective in diaphanous inhibitory domain (DID) binding did not (Fig. 3D). This effect was abrogated by the presence of dn.Dia-NLS, which also blocked endogenous nuclear actin network production by mDia activation through mCherry-DAD (Fig. 3D and fig. S7C). Thus, nuclear mDia activation is necessary for actin assembly and MAL-SRF activity, and under certain circumstances, it can be sufficient.

Next, we devised an optogenetic tool to activate endogenous formins in the nucleus of living cells, which circumvented the requirement for serum stimulation or LMB treatment. We generated, screened, and characterized fusions of

the LOV (light, oxygen, or voltage) J α -domain of *Avena sativa* phototropin-1 (AsLOV2) (20) to mDia2-DAD (LOV-DAD) to achieve release of endogenous mDia2 autoinhibition and subsequent SRF activity upon 400- to 500-nm illumination (fig. S8). To restrict this construct to the nucleus, we introduced the point mutation L1168G into the NES-like sequence of mDia2-DAD and fused it to an NLS to obtain nuc.LOV-DAD (fig. S8G). Illumination of cells expressing mCherry-nuc.LOV-DAD rapidly formed a nuclear actin cytoskeleton (Fig. 4A). Actin filaments disassembled when illumination was paused and were rebuilt in response to a second round of illumination (Fig. 4A). Cells expressing mCherry-nuc.LOV-DAD also showed MAL nuclear accumulation, as well as SRF activity, when exposed to blue light, which was dependent on the light-sensitive residue C450 in nuc.LOV-DAD and the presence of mDia1/2 (Fig. 4, B to D). Thus, photoactivation of endogenous mDia in the nucleus promotes nuclear actin polymerization and MAL-SRF activity.

Here, we have observed the regulated assembly of nuclear actin filaments in mammalian cells. This nuclear actin network was serum-responsive, mDia-dependent, and formed upon activation of mDia. Indeed, endogenous formin

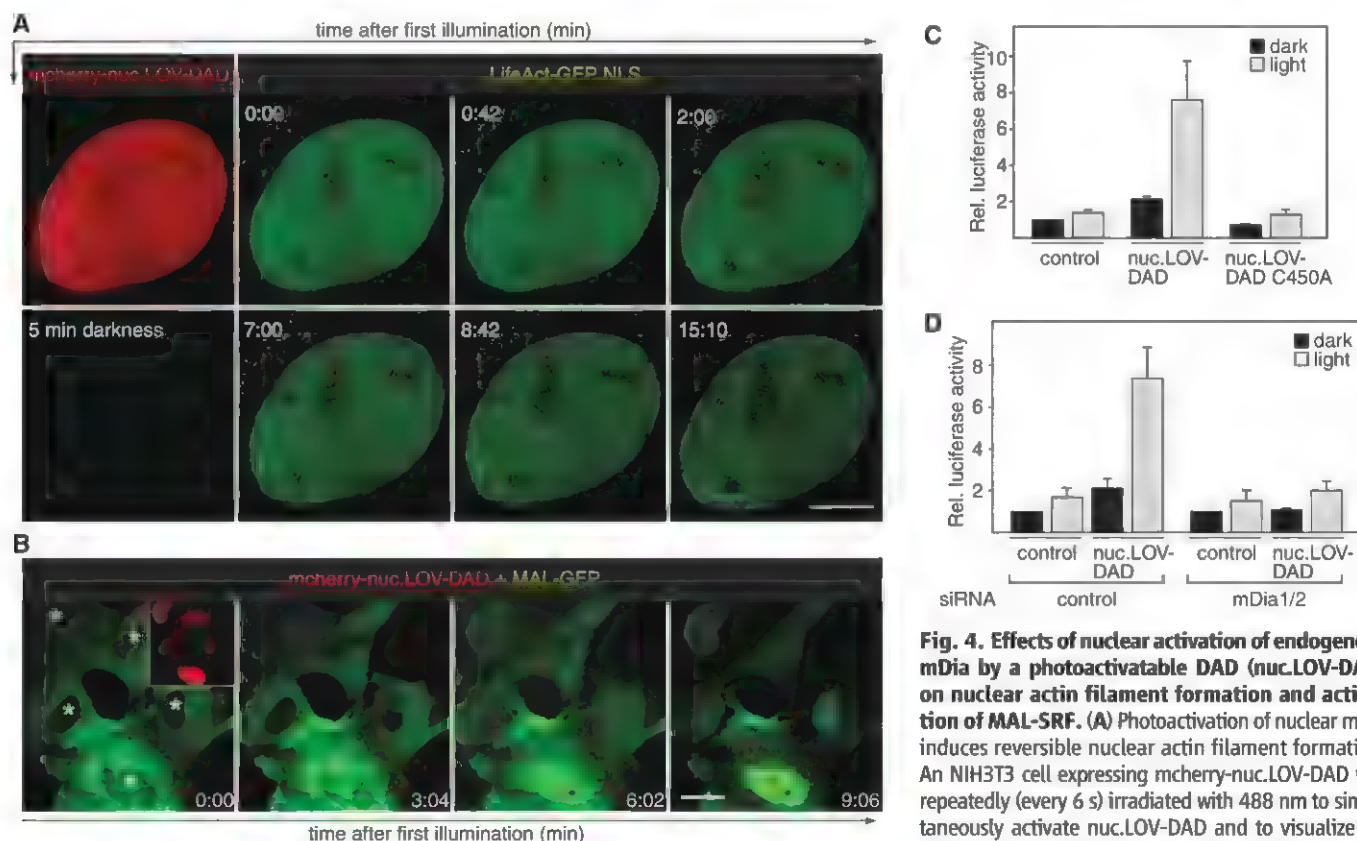


Fig. 4. Effects of nuclear activation of endogenous mDia by a photoactivatable DAD (nuc.LOV-DAD) on nuclear actin filament formation and activation of MAL-SRF. (A) Photoactivation of nuclear mDia induces reversible nuclear actin filament formation. An NIH3T3 cell expressing mCherry-nuc.LOV-DAD was repeatedly (every 6 s) irradiated with 488 nm to simultaneously activate nuc.LOV-DAD and to visualize redistribution of LifeAct-GFP-NLS. Scale bar, 5 μ m. **(B)**

Photoactivation of nuclear mDia triggers nuclear accumulation of MAL. HeLa cells expressing MAL-GFP together with mCherry-nuc.LOV-DAD were irradiated with blue light (every 2 s) to simultaneously photoactivate nuc.LOV-DAD and to follow redistribution of MAL-GFP over time. Note the nuclear accumulation of MAL-GFP (white asterisks). Scale bar, 10 μ m. **(C)** Stimulation of SRF activity by photoactivation of nuc.LOV-DAD in contrast to the light-insensitive nuc.LOV-DAD C450A as assessed by reporter gene assays. Results are means \pm SD ($n = 3$). **(D)** SRF activation by nuc.LOV-DAD photoactivation is sensitive to mDia1/2 siRNA treatment. Results are means \pm SD ($n = 4$).

autoinhibition was released inside the nucleus, which suggests that nuclear formin regulation is dynamically and tightly controlled. Thus, the entire process from actin polymerization to SRF-dependent gene expression can occur in the nucleus. Moreover, nuclear formin function represents an integral part of the physiological serum response.

References and Notes

1. C. Baarjnk, D. Brandt, R. Grosse, *Cell* **142**, 172, 172e1 (2010).
2. J. Faix, R. Grosse, *Dev. Cell* **10**, 693 (2006).
3. S. H. Zigmond, *Curr. Opin. Cell Biol.* **16**, 99 (2004).
4. T. Miki et al., *J. Biol. Chem.* **284**, 5753 (2009).
5. T. Stüven, E. Hartmann, D. Görlach, *EMBO J.* **22**, 5928 (2003).
6. S. Arsenian, B. Weinhold, M. Oelgeschläger, U. Rütger, A. Nordheim, *EMBO J.* **17**, 6289 (1998).
7. E. N. Olson, A. Nordheim, *Nat. Rev. Mol. Cell Biol.* **11**, 353 (2010).
8. M. K. Varthainen, S. Guettler, B. Larijani, R. Treisman, *Science* **316**, 1749 (2007).
9. S. J. Copeland et al., *J. Biol. Chem.* **282**, 30120 (2007).
10. S. Stern et al., *J. Neurosci.* **29**, 4512 (2009).
11. F. Miralles, G. Posern, A.-I. Zaromytidou, R. Treisman, *Cell* **113**, 329 (2003).
12. S. B. Padrick, M. K. Rosen, *Annu. Rev. Biochem.* **79**, 707 (2010).
13. J. W. Copeland, R. Treisman, *Mol. Biol. Cell* **13**, 4088 (2002).
14. R. S. Gieni, M. J. Hendze, *Biochem. Cell Biol.* **87**, 283 (2009).
15. B. M. Jockusch, C.-A. Schoenenberger, J. Stetefeld, U. Aebi, *Trends Cell Biol.* **16**, 391 (2006).
16. M. K. Varthainen, *FEBS Lett.* **582**, 2033 (2008).
17. T. J. Gauvin, J. Fukui, J. R. Peterson, H. N. Higgs, *Biochemistry* **48**, 9327 (2009).
18. D. R. Kovar, *Curr. Opin. Cell Biol.* **18**, 11 (2006).
19. A. S. Alberts, *J. Biol. Chem.* **276**, 2824 (2001).
20. S. M. Harper, L. C. Neil, K. H. Gardner, *Science* **301**, 1541 (2003).

Acknowledgments: We thank J. V. Small for advice on rapid actin fixation, L. O. Essen and C. Taxis for advice on using the LOV-domain, M. Innocenti for mDia2 antibodies, B. Di Ventura for critical reading of the manuscript, and laboratory members for discussions. This work was funded by grants from the Deutsche Forschungsgemeinschaft (GR 2111/2-1 and SFB 593) and the Deutsche Krebsstiftung e.V. (108293) to R.G. The data presented in this manuscript are tabulated in the main paper and in the supplementary materials.

Supplementary Materials

www.sciencemag.org/cgi/content/full/science.1235038/DC1

Materials and Methods

Figs. S1 to S8

References (21–24)

Movies S1 to S4

11 January 2013; accepted 26 March 2013

Published online 4 April 2013;

10.1126/science.1235038

Wnt Stabilization of β -Catenin Reveals Principles for Morphogen Receptor-Scaffold Assemblies

Sung-Eun Kim,^{1*} He Huang,^{1,*†} Ming Zhao,^{2*} Xinjun Zhang,¹ Aili Zhang,^{2,4} Mikhail V. Semonov,^{1,‡} Bryan T. MacDonald,¹ Xiaowu Zhang,⁵ Jose Garcia Abreu,^{1,3} Leilei Peng,² Xi He^{1,5}

Wnt signaling stabilizes β -catenin through the LRP6 receptor signaling complex, which antagonizes the β -catenin destruction complex. The Axin scaffold and associated glycogen synthase kinase-3 (GSK3) have central roles in both assemblies, but the transduction mechanism from the receptor to the destruction complex is contentious. We report that Wnt signaling is governed by phosphorylation regulation of the Axin scaffolding function. Phosphorylation by GSK3 kept Axin activated ("open") for β -catenin interaction and poised for engagement of LRP6. Formation of the Wnt-induced LRP6-Axin signaling complex promoted Axin dephosphorylation by protein phosphatase-1 and inactivated ("closed") Axin through an intramolecular interaction. Inactivation of Axin diminished its association with β -catenin and LRP6, thereby inhibiting β -catenin phosphorylation and enabling activated LRP6 to selectively recruit active Axin for inactivation reiteratively. Our findings reveal mechanisms for scaffold regulation and morphogen signaling.

Signaling by secreted Wnt morphogens governs developmental, homeostatic, and pathological processes by regulating β -catenin stability and represents a critical target for cancer and disease therapeutics (1, 2). Without Wnt stimulation, cytosolic β -catenin concentrations are kept low because a "destruction complex" assembled by the Axin scaffold binds to β -catenin, Adenomatous polyposis coli (APC), casein kinase-1 α (CK1 α), and glycogen synthase

kinase-3 (GSK3), and promotes phosphorylation of β -catenin by CK1 α and GSK3, thus ensuring β -catenin ubiquitination and degradation (1–3). Upon Wnt stimulation, a receptor complex on the cell surface is formed between Frizzled (Fz) and low-density lipoprotein receptor-related protein 6 (LRP6), resulting in phosphorylation and activation of LRP6 and its recruitment of Axin (4–7). Assembly of the Fz-LRP6 complex and associated Dishevelled (Dvl) and the Axin destruction complex, referred to collectively as the LRP6 signaling complex (signalosome), inhibits phosphorylation of β -catenin, thereby causing its stabilization (6–10). The mechanism by which LRP6 activation leads to β -catenin stabilization remains enigmatic (1, 2, 11).

Axin is a phosphoprotein central to assemblies of both destruction (12, 15) and signaling complexes (4–10), and it becomes dephosphorylated upon Wnt stimulation (16, 17). We generated an antibody, Ab-pS497/500 (fig. S1, A to C), for Axin phosphorylated at serines 497 and 500, which are GSK3 phosphoryl-

ation sites in vitro (18). Axin phosphorylation at S497/S500 was decreased within 15 to 30 min of Wnt3a treatment of mouse L fibroblasts (Fig. 1A), embryonic fibroblasts (fig. S1D), and human embryonic kidney (HEK) 293T cells (Fig. 1, C and D). Wnt-induced dephosphorylation of Axin likely reflects the counterbalance between GSK3 and a protein phosphatase (PP) such as PP1, whose catalytic subunit, PP1c, was identified in an RNA interference screen in *Drosophila* cells as a requirement for Wnt/ β -catenin signaling (19). Through a functional cDNA overexpression screen in HEK293T cells, we identified PP1c, one of the three PP1c genes in the human genome (20), as an activator of the Wnt/ β -catenin signaling reporter TOP-Flash (fig. S2A). PP1c overexpression decreased phosphorylation of Axin but not of LRP6 (Fig. 1B); a pharmacological PP1 inhibitor, Tautomycin (TM), prevented Wnt-induced dephosphorylation of Axin without affecting LRP6 phosphorylation (Fig. 1C and fig. S3).

PP1 has pleiotropic roles, and its specificity is conferred by hundreds of PP1c-binding proteins (20). Inhibitor-2 (I2, or PPP1R2) is a specific inhibitor of PP1c (20). Overexpression of I2 countered Wnt3a-induced Axin dephosphorylation (without affecting LRP6 phosphorylation) and β -catenin stabilization (Fig. 1D and fig. S2B), inhibited Wnt3a- or PP1c-activated TOP-Flash (fig. S2, C and D), and antagonized β -catenin stabilization by an activated LRP6 (fig. S2E). Depletion of the endogenous I2 with short hairpin RNAs (shRNAs) resulted in accumulation of β -catenin and increased TOP-Flash (Fig. 1E and fig. S2F). A morpholino antisense-oligonucleotide (MO) that targets *Xenopus* I2 mRNA and blocked I2 protein synthesis caused deficiency in *Xenopus* head development and reduced anterior marker expression, which were restored by human I2 mRNA injection or knock-down of β -catenin (Fig. 1F and fig. S4). Thus, I2 antagonizes Wnt/ β -catenin signaling and participates in vertebrate anteriorization, which requires Wnt pathway inhibition (21).

Recent models of Wnt signaling (22, 23) have overlooked Axin phosphorylation, and one

¹F. M. Kirby Center, Boston Children's Hospital, Harvard Medical School, Boston, MA 02115, USA. ²College of Optical Sciences, University of Arizona, Tucson, AZ 85721, USA. ³Instituto de Ciencias Biomédicas, Universidade Federal do Rio de Janeiro, Rio de Janeiro, Brazil. ⁴School of Biomedical Engineering, Jiaotong University, Shanghai, China. ⁵Cell Signaling Technology, Danvers, MA 01923, USA.

*These authors contributed equally to this work.

†Present address: Department of Pathology, University of Buffalo, Buffalo, NY 14203, USA

‡Present address: Veterans Administration Hospital and Department of Pathology, Boston University, Bedford, MA 01730, USA

§Corresponding author. E-mail: xi.he@childrens.harvard.edu

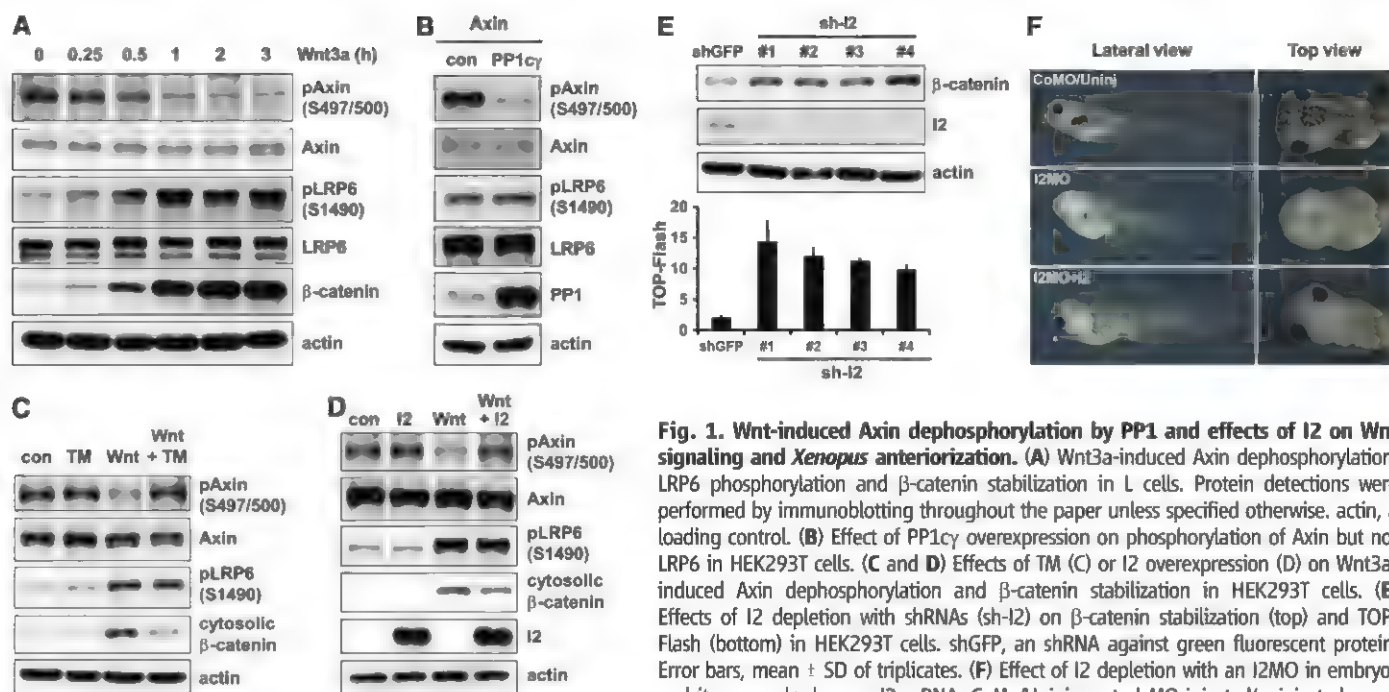


Fig. 1. Wnt-induced Axin dephosphorylation by PP1 and effects of I2 on Wnt signaling and *Xenopus* anteriorization. (A) Wnt3a-induced Axin dephosphorylation, LRP6 phosphorylation and β -catenin stabilization in L cells. Protein detections were performed by immunoblotting throughout the paper unless specified otherwise. actin, a loading control. (B) Effect of PP1cy overexpression on phosphorylation of Axin but not LRP6 in HEK293T cells. (C and D) Effects of TM (C) or I2 overexpression (D) on Wnt3a-induced Axin dephosphorylation and β -catenin stabilization in HEK293T cells. (E) Effects of I2 depletion with shRNAs (sh-I2) on β -catenin stabilization (top) and TOP-Flash (bottom) in HEK293T cells. shGFP, an shRNA against green fluorescent protein. Error bars, mean \pm SD of triplicates. (F) Effect of I2 depletion with an I2MO in embryos and its rescue by human I2 mRNA. CoMo/Uninj, control MO-injected/uninjected.

argued that Wnt/LRP6 signaling maintains an intact Axin destruction complex without inhibiting β -catenin phosphorylation (22). We reevaluated this critical issue. We found that in multiple Wnt-responsive cells, the rate of β -catenin phosphorylation was suppressed under Wnt stimulation (fig. S5) as reported (3, 24), and this correlated with Axin dephosphorylation.

Association of Axin and β -catenin is the cornerstone binary interaction within the destruction complex. Coimmunoprecipitation (co-IP) of endogenous proteins showed that the amount of β -catenin associated with Axin appeared to be unchanged or decrease after 0.5 hours of Wnt treatment but to increase after 2 hours (fig. S6, A and B). However normalization to the amount of cytosolic β -catenin made it clear that Wnt stimulation weakened the interaction between β -catenin and Axin (Fig. 2, A and B, left panels). We estimated that the dissociation constant (K_d) of Axin- β -catenin association was increased by Wnt3a (fig. S6C), signifying a weaker interaction. Indeed, Axin from extracts of Wnt3a-treated cells exhibited reduced capability to associate with β -catenin in an *in vitro* binding assay (Fig. 3A) (17). Such diminished Axin- β -catenin association observed *in vitro* and *in vivo* correlated with, and appeared to be attributable to, Axin dephosphorylation by PP1, because it could be partially restored by I2 overexpression or TM treatment (Fig. 3, A to C). For β -catenin coimmunoprecipitated with Axin from Wnt3a-treated cells, the amount of phosphorylation relative to that of β -catenin was reduced (Fig. 2, A and B, middle panels; and fig. S6, A and B), implying a diminished rate of β -catenin phosphorylation in the Axin complex in Wnt-treated cells. Association of Axin with GSK3 remained

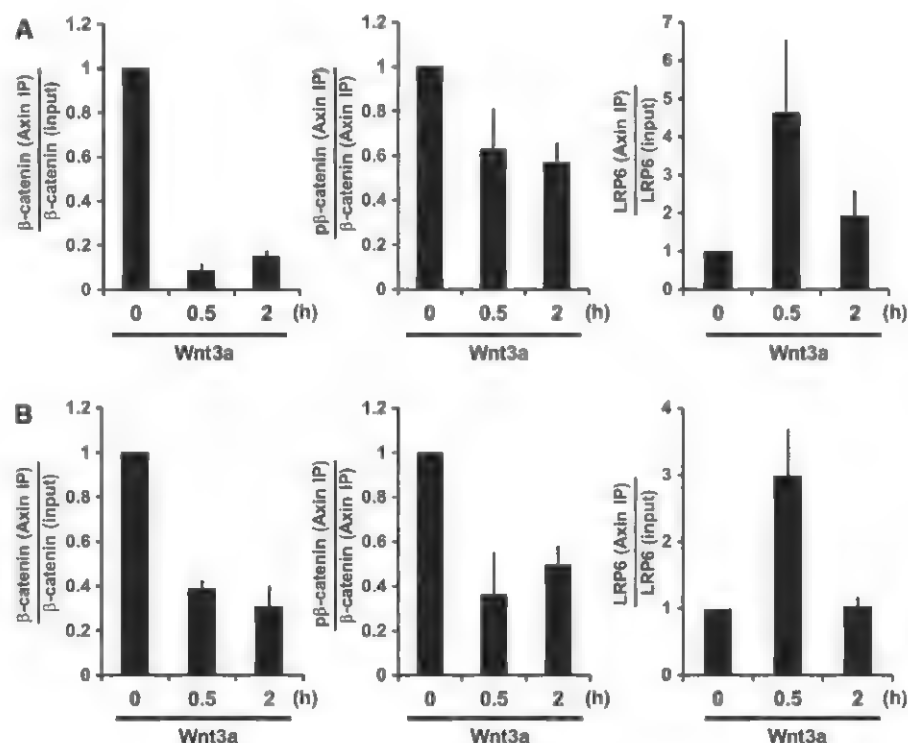


Fig. 2. Wnt regulation of Axin- β -catenin and Axin-LRP6 association, and of β -catenin phosphorylation in the Axin complex. (A and B) Quantifications of Wnt3a effects on ratios of Axin-associated β -catenin versus input β -catenin (left), Axin-associated phospho- β -catenin versus Axin-associated β -catenin (middle), and Axin-associated LRP6 versus total LRP6 (right) in L (A) and HEK293T (B) cells. Error bars, mean \pm SEM of triplicates.

constant regardless of Wnt treatment (fig. S6, A and B) (22, 25). Thus, Wnt signaling inhibits Axin- β -catenin association and β -catenin phosphorylation, consistent with earlier findings

(3, 17), kinetic modeling (24), and the prevailing model (1, 11, 14, 15) (see fig. S6C).

Wnt-induced phosphorylation of LRP6 recruits Axin to assemble the signaling complex

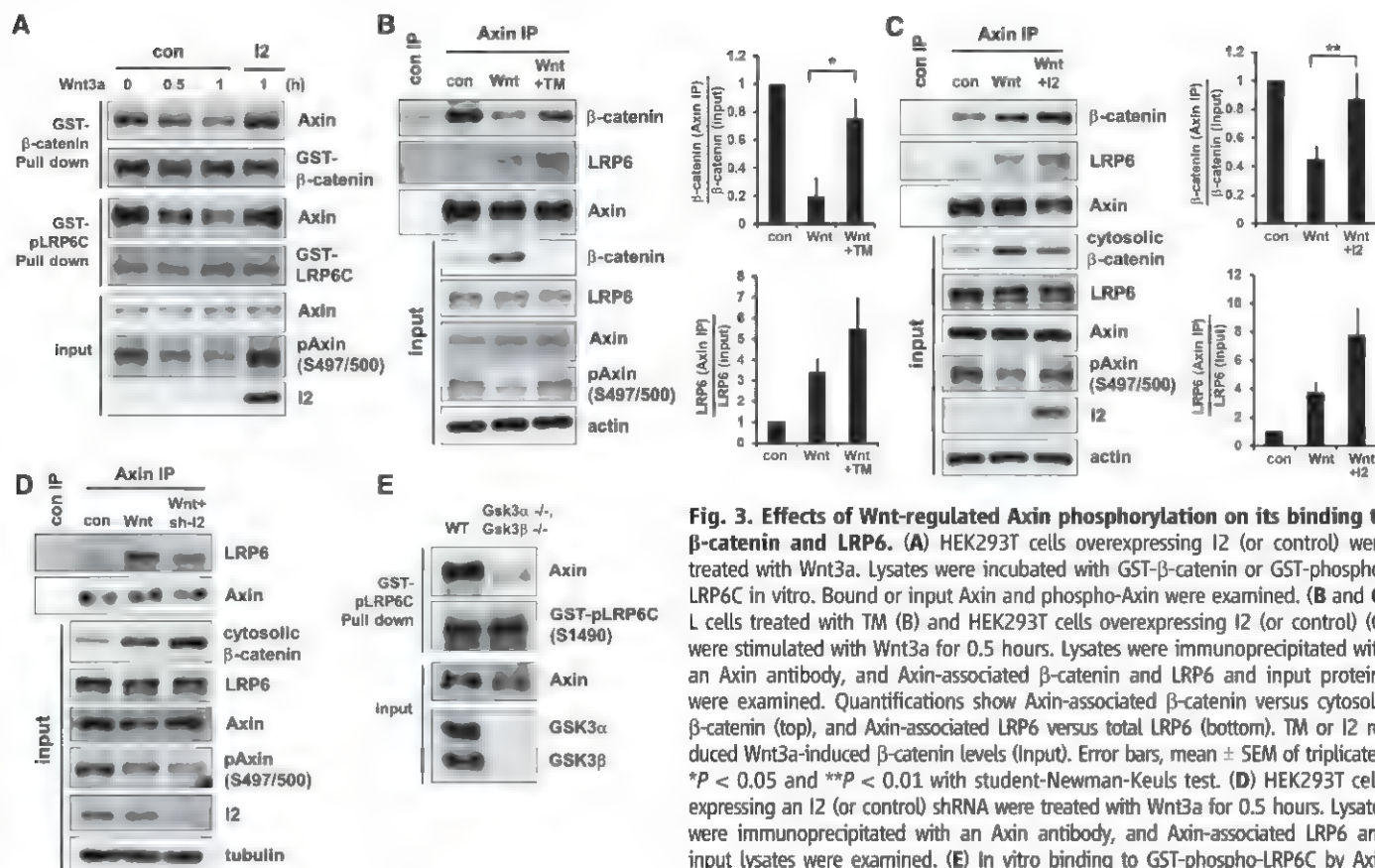


Fig. 3. Effects of Wnt-regulated Axin phosphorylation on its binding to β-catenin and LRP6. (A) HEK293T cells overexpressing I2 (or control) were treated with Wnt3a. Lysates were incubated with GST-β-catenin or GST-phospho-LRP6C in vitro. Bound or input Axin and phospho-Axin were examined. (B and C) L cells treated with TM (B) and HEK293T cells overexpressing I2 (or control) (C) were stimulated with Wnt3a for 0.5 hours. Lysates were immunoprecipitated with an Axin antibody, and Axin-associated β-catenin and LRP6 and input proteins were examined. Quantifications show Axin-associated β-catenin versus cytosolic β-catenin (top), and Axin-associated LRP6 versus total LRP6 (bottom). TM or I2 reduced Wnt3a-induced β-catenin levels (Input). Error bars, mean ± SEM of triplicates. *P < 0.05 and **P < 0.01 with student-Newman-Keuls test. (D) HEK293T cells expressing an I2 (or control) shRNA were treated with Wnt3a for 0.5 hours. Lysates were immunoprecipitated with an Axin antibody, and Axin-associated LRP6 and input lysates were examined. (E) In vitro binding to GST-phospho-LRP6C by Axin from lysates of WT or Gsk3α^{-/-};Gsk3β^{-/-} mouse embryonic stem cells. Bound or input Axin was examined.

(5–7). Intriguingly, co-IP of endogenous proteins showed that Wnt-induced association of LRP6 and Axin was prominent at 0.5 hours but diminished after 2 hours (Fig. 2, A and B, right panels; and fig. S6, A and B), despite persistence of phospho-LRP6 (fig. S5). The diminished binding between phospho-LRP6 and Axin appeared to result from Axin dephosphorylation by PP1, because the binding was enhanced by I2 overexpression or TM treatment (Fig. 3, B and C) and reduced by I2 depletion (Fig. 3D). Axin from extracts of Wnt3a-treated cells showed reduced capability to associate with phospho-LRP6 in an in vitro binding assay (fig. S7A), and this reduction appeared to result from Axin dephosphorylation by PP1 because it was prevented by I2 overexpression (Fig. 3A). Complementarily, Axin from extracts of cells treated with a pharmacological GSK3 inhibitor, BIO or SB216763, or of Gsk3α^{-/-};Gsk3β^{-/-} cells (26), had minimal association with phospho-LRP6 (Fig. 3E and fig. S7B). Thus, phosphorylation of Axin by GSK3 enhanced, whereas dephosphorylation of Axin by PP1 diminished, Axin's ability to associate with phospho-LRP6 (and β-catenin), implying that activated LRP6 selectively recruits the phosphorylated form of Axin that is active in β-catenin association and degradation.

The above results imply that Axin may undergo a phosphorylation-dependent conforma-

tional change. Axin is an intrinsically disordered protein with individual partner-binding domains (fig. S8A) (14, 15). Axin's β-catenin binding domain (Axin-BCD) associated, in vitro and when overexpressed in cells, with Axin DIX domain (Axin-DIX) but not homologous Dvl2 DIX domain (Dvl-DIX) (Fig. 4A and figs. S8B and S9), reflecting a specific and direct interaction. Phosphorylation of Axin-BCD by GSK3 in vitro inhibited BCD-DIX binding (Fig. 4A and fig. S8C). Therefore, there may be an intramolecular BCD-DIX interaction that is prevented upon Axin phosphorylation by GSK3, providing an explanation for how phosphorylation of Axin enhances its association with β-catenin and phospho-LRP6. Indeed Axin intra- and intermolecular interactions appeared to be mutually exclusive because β-catenin and Axin-DIX competed for binding to Axin-BCD (Fig. 4B and fig. S10A). A positively charged histidine-rich region of BCD (figs. S9, S10B, and S11) and a negatively charged loop of DIX (figs. S12A and S13) participated in BCD-DIX interaction, which appeared to be disrupted by negative charges generated in BCD through phosphorylation by GSK3 (figs. S10, C and D, and S11). Axin(SD4), which contains phosphomimetic aspartic acid substitutions of four serines (including S497 and S500) in BCD (fig. S11), and Axin(DA), which contains alanine substitutions

of acidic residues in DIX (fig. S13), were each expected to have a weaker intramolecular interaction (figs. S10D and S12A) and were indeed more effective in inhibiting Wnt/β-catenin signaling than the wild-type (WT) Axin (Fig. 4C). Axin(SA4), which contains alanine substitutions of the four serines in BCD (fig. S11) and was predicted to have a stronger intramolecular interaction (fig. S10C), was less effective in inhibiting Wnt/β-catenin signaling (Fig. 4C). These results support a model that Axin "autoinhibits" through the BCD-DIX intramolecular interaction. Live cell FRET (fluorescence resonance energy transfer) imaging corroborated this model by demonstrating a Wnt3a-induced proximity of Axin's carboxyl DIX to its amino terminus (figs. S14 to S17), likely through Axin dephosphorylation.

We propose a Wnt signaling model (Fig. 4D) that appears to unify findings on the two Axin complexes mediating LRP6 signaling and β-catenin destruction. Without Wnt, Axin is associated with and phosphorylated by GSK3 and is in an activated ("open") conformation for β-catenin binding and phosphorylation and poised for engagement of LRP6 (Fig. 4D). With Wnt, LRP6 undergoes Fz/Dvl-dependent phosphorylation and recruits the active Axin destruction complex to form the signaling complex, in which GSK3 bound to Axin is inhibited by phospho-LRP6

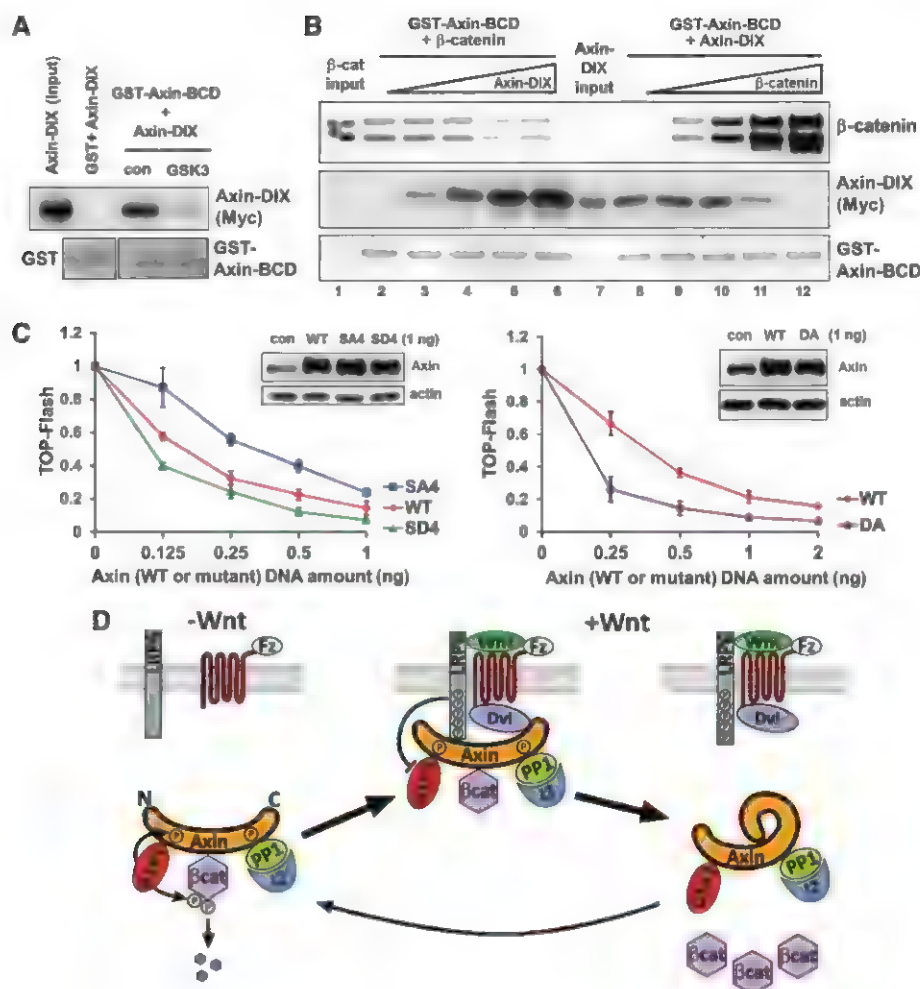


Fig. 4. A phosphorylation-regulated Axin intramolecular interaction and a Wnt signaling model. (A) Association of Axin-DIX with GST-Axin-BCD and its inhibition by GSK3 phosphorylation of Axin-BCD. (B) Competition of β -catenin association with GST-Axin-BCD by Axin-DIX (lanes 1 to 6) and vice versa (lanes 7 to 12). Purified recombinant proteins were used in these *in vitro* assays. Axin-DIX or β -catenin was detected by immunoblotting and GST or GST-Axin-BCD by Ponceau staining [(A) and (B)]. The lower band of β -catenin (B) was a proteolytic fragment. (C) Comparisons of Axin(SD4), Axin(SA4), and Axin(DA) with Axin in antagonizing Wnt-induced TOP-Flash in HEK293T cells. *x* axes represent DNA doses transfected. Error bars, mean \pm SD of triplicates. Note larger TOP-Flash differences at lower overexpression doses. Insets show levels of overexpressed Axin at the 1 ng dose and that of endogenous Axin (con). (D) An "Axin inactivation" model for Wnt stabilization of β -catenin. APC and CK1 α were omitted for clarity. See text and fig. S18.

(27–29), leading to inhibition of β -catenin phosphorylation and tipping the balance toward Axin dephosphorylation by PP1. Dephosphorylated Axin adopts an inactivated ("closed") conformation through intramolecular autoinhibition and becomes incompetent for association with β -catenin or phospho-LRP6, leading to disassembly of destruction and signaling complexes (Fig. 4D). Phospho-LRP6 is thus freed for another round of recruitment of phosphorylated-activated Axin for inactivation while ignoring dephosphorylated-inactivated Axin, and the steps likely reiterate to keep β -catenin phosphorylation suppressed. Wnt-induced biphasic assembly and disassembly of the LRP6 signaling complex appear to enable phospho-LRP6 to inactivate Axin in a "catalytic" manner, underlying Wnt stabiliza-

tion of β -catenin in broad component stoichiometries. GSK3 acts as an "assembler" of destruction (16–18) and signaling complexes (4, 6, 8–10) through phosphorylation of Axin and LRP6, whereas PP1 dephosphorylates Axin (19) to disassemble both complexes while leaving phospho-LRP6 unperturbed for continuous signaling. Our model further explains β -catenin stabilization kinetics. Elevating levels of β -catenin, by competing against Axin intramolecular autoinhibition, could promote reassembly of the Axin-GSK3- β -catenin complex and counter its disassembly by Wnt (Fig. 4D), thereby plateauing when equilibrium is achieved. This implies a safeguard mechanism by which rising concentrations of β -catenin could trigger its own degradation to avoid excessive accumulation. Axin

represents a scaffold with an on/off switch controlled through a ligand- and phosphorylation-dependent intramolecular interaction, which additionally could serve as a feedback sensor of target (β -catenin) concentrations. Similar scaffold functions could occur in other pathways as highlighted by yeast Ste5 (30).

References and Notes

1. B. T. MacDonald, K. Tamai, X. He, *Dev. Cell* **17**, 9 (2009).
2. H. Clevers, R. Nusse, *Cell* **149**, 1192 (2012).
3. C. Liu et al., *Cell* **108**, 837 (2002).
4. J. Mao et al., *Mol. Cell* **7**, 801 (2001).
5. K. Tamai et al., *Mol. Cell* **13**, 149 (2004).
6. X. Zeng et al., *Nature* **438**, 873 (2005).
7. G. Davidson et al., *Nature* **438**, 867 (2005).
8. J. Bilic et al., *Science* **316**, 1619 (2007).
9. X. Zeng et al., *Development* **135**, 367 (2008).
10. T. Schwarz-Romond, C. Metcalfe, M. Bienz, *J. Cell Sci.* **120**, 2402 (2007).
11. C. Metcalfe, M. Bienz, *J. Cell Sci.* **124**, 3537 (2011).
12. S. Ikeda et al., *EMBO J.* **17**, 1371 (1998).
13. J. Behrens et al., *Science* **280**, 596 (1998).
14. D. Kimelman, W. Xu, *Oncogene* **25**, 7482 (2006).
15. J. L. Stamos, W. L. Weiss, *Cold Spring Harb. Perspect. Biol.* **5**, a007898 (2013).
16. H. Yamamoto et al., *J. Biol. Chem.* **274**, 10681 (1999).
17. K. Willert, S. Shibamoto, R. Nusse, *Genes Dev.* **13**, 1768 (1999).
18. E. Jho, S. Lomvardas, F. Costantini, *Biochem. Biophys. Res. Commun.* **266**, 28 (1999).
19. W. Luo et al., *EMBO J.* **26**, 1511 (2007).
20. D. M. Virshup, S. Shenolikar, *Mol. Cell* **33**, 537 (2009).
21. C. Niehrs, *Nat. Rev. Genet.* **5**, 425 (2004).
22. V. S. W. Li et al., *Cell* **149**, 1245 (2012).
23. V. F. Taelman et al., *Cell* **143**, 1136 (2010).
24. A. R. Hernandez, A. M. Klein, M. W. Kirschner, *Science* **338**, 1337 (2012).
25. A. J. Valvezan, F. Zhang, J. A. Diehl, P. S. Klein, *J. Biol. Chem.* **287**, 3823 (2012).
26. B. W. Doble, S. Patel, G. A. Wood, L. K. Kockentz, J. R. Woodgett, *Dev. Cell* **12**, 957 (2007).
27. G. Wu, H. Huang, J. Garcia Abreu, X. He, *PLoS ONE* **4**, e4926 (2009).
28. C. S. Cselenyi et al., *Proc. Natl. Acad. Sci. U.S.A.* **105**, 8032 (2008).
29. S. Piao et al., *PLoS ONE* **3**, e4046 (2008).
30. J. G. Zalatan, S. M. Coyle, S. Rajan, S. S. Sidh, W. A. Lim, *Science* **337**, 1218 (2012).

Acknowledgments: We thank Y. Wu for the BCD2 construct; X. Yu for figs. S11 and S13; B. Doble and J. Woodgett for Gsk3-null mouse embryonic stem cells; A. Klein, M. Kirschner, T. Schwarz, J.-h. Wang, and X.H. laboratory members for comments; and M. Lin, B. Yu, M. Wan, X. Cao, and W. Wei for help. S.-E.K. and H.H. were supported partially by postdoctoral fellowships from National Research Foundation of Korea (KRF 2009 357 C00096) and Canadian Institute of Health Research, respectively. J.G.A. was funded partially by the National Council for Scientific and Technological Development (CNPq, Brazil) as a visiting scientist to the X.H. laboratory. L.P. acknowledges support by NIH (R01EB008737 and R01EB015481). X.H. acknowledges support by NIH (R01 GM074241) and Boston Children's Hospital Intellectual and Developmental Disabilities Research Center (P30 HD 18655).

Supplementary Materials

www.sciencemag.org/cgi/content/full/science.1232389/DC1
Materials and Methods
Figs. S1 to S18
References (31–39)

5 November 2012; accepted 19 March 2013
Published online 11 April 2013;
10.1126/science.1232389

Activation of the Yeast Hippo Pathway by Phosphorylation-Dependent Assembly of Signaling Complexes

Jeremy M. Rock,^{1,2} Daniel Lim,¹ Lasse Stach,³ Roksana W. Ogradowicz,³ Jamie M. Keck,^{4*} Michele H. Jones,⁴ Catherine C. L. Wong,⁵ John R. Yates III,⁵ Mark Winey,⁴ Stephen J. Smerdon,³ Michael B. Yaffe,¹ Angelika Amon^{1,2,†}

Scaffold-assisted signaling cascades guide cellular decision-making. In budding yeast, one such signal transduction pathway called the mitotic exit network (MEN) governs the transition from mitosis to the G₁ phase of the cell cycle. The MEN is conserved and in metazoans is known as the Hippo tumor-suppressor pathway. We found that signaling through the MEN kinase cascade was mediated by an unusual two-step process. The MEN kinase Cdc15 first phosphorylated the scaffold Nud1. This created a phospho-docking site on Nud1, to which the effector kinase complex Dbf2-Mob1 bound through a phosphoserine-threonine binding domain, in order to be activated by Cdc15. This mechanism of pathway activation has implications for signal transmission through other kinase cascades and might represent a general principle in scaffold-assisted signaling.

Signaling complex assembly must be tightly controlled in both space and time. The use of protein scaffolds and phosphorylation-dependent protein-protein interactions is central to this spatiotemporal control. The mitotic exit network (MEN) is a conserved guanosine triphosphatase (GTPase) signaling cascade that governs exit from mitosis (1, 2). During anaphase, MEN signaling complexes assemble at spindle pole bodies (SPBs) (3, 4) to trigger exit from mitosis and to couple this cell cycle transition with nuclear position (5). The Ras-like GTPase Tem1 and the Polo protein kinase Cdc5 coordinately recruit the Hippo-like kinase Cdc15 to SPBs (3). Once localized to SPBs, Cdc15 is activated to phosphorylate the kinase Dbf2 and its coactivator Mob1 (6). Phosphorylation activates Dbf2-Mob1, which then promotes the release of the MEN effector protein phosphatase Cdc14 from the nucleolus, resulting in exit from mitosis (2).

Scaffold proteins serve as assembly platforms for kinase cascades and may function as signaling insulators (7). Our results show that, rather than functioning as a passive platform onto which MEN components assemble, the SPB-resident MEN scaffold Nud1 is a dynamic participant in MEN signal transmission. Nud1 is a phosphoprotein and its phosphorylation increases during mitosis (fig. S1, A to C, and table S1) (8–10). We generated a *NUD1* allele in which the 38

high-confidence mitotic phosphorylation sites and 4 lower-confidence sites were mutated to alanine (henceforth *nud1-42A*). The *nud1-42A*

protein was stable and localized to SPBs, but phosphorylation during mitosis was reduced (fig. S1, B to D).

To examine the effects of the *nud1-42A* allele on MEN activity, we introduced the allele into a strain expressing the temperature-sensitive *nud1-44* allele under the control of the galactose-inducible and glucose-repressible *GAL1-10* promoter. *GAL-nud1-44 nud1-42A* cells, like MEN loss-of-function mutants, arrested in late anaphase with inactive Dbf2-Mob1 and nucleolar-restricted Cdc14 under conditions in which *nud1-44* is inactive (Fig. 1, A and B, and fig. S1, E and F). Thus, *nud1-42A* cells are defective in MEN signaling.

Localization of the MEN components Tem1, Cdc15, Dbf2, and Mob1 to SPBs is essential for Dbf2-Mob1 activation and requires *NUD1* (3, 4, 11). Localization of Nud1, Bfa1 [a Tem1 GTPase-activating protein (GAP) complex component], Tem1, and Cdc15 was normal in *nud1-42A* cells (12) (fig. S2, A to D), but Mob1 and Dbf2 were absent from SPBs (fig. S2, E and F). *nud1-42A* cells also harbored mispositioned anaphase spindles and detached astral microtubules (fig. S1F).

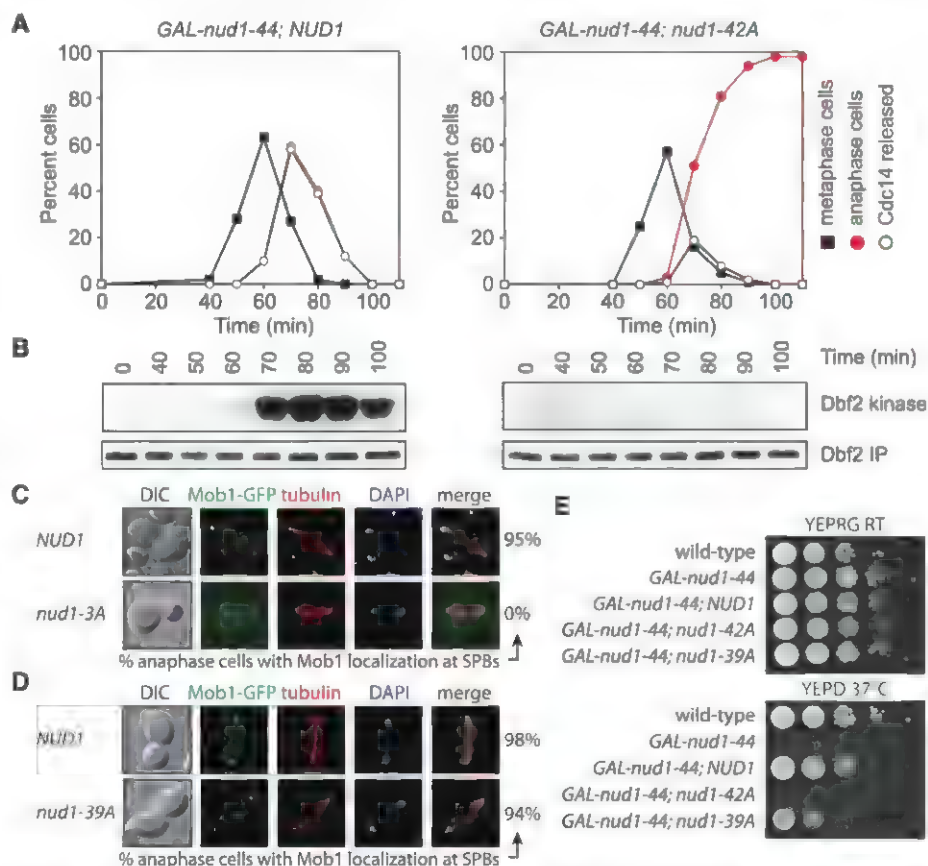


Fig. 1. Dbf2-Mob1 recruitment to SPBs and MEN activation requires Nud1 phosphorylation. (A and B) Dbf2 kinase activity and cell cycle progression in *GAL-nud1-44 NUD1* (A29878) and *GAL-nud1-44 nud1-42A* (A29881) cells. Cells were arrested in G₁ with α -factor and released under conditions in which *nud1-44* is inactive (12). (C) Mob1 localization in anaphase *NUD1* (A29453) and *nud1-3A* (A31169) cells. (D) Mob1 localization in anaphase *NUD1* (A24631) and *nud1-39A* (A31477) cells. DAPI, 4',6-diamidino-2-phenylindole; DIC, differential interference contrast. (E) Growth of 10-fold serial dilutions of A2587, A29248, A29685, A29500, and A32295 cells on YEP plates containing either galactose and raffinose (YEPG) or glucose (YEPD) (12).

¹David H. Koch Institute for Integrative Cancer Research, Massachusetts Institute of Technology, Cambridge, MA 02139, USA. ²Howard Hughes Medical Institute, Massachusetts Institute of Technology, Cambridge, MA 02139, USA. ³Division of Molecular Structure, MRC National Institute for Medical Research, The Ridgeway, London NW7 1AA, UK. ⁴Department of Molecular, Cellular, and Developmental Biology, UCB 347, University of Colorado, Boulder, CO 80309, USA. ⁵Department of Chemical Physiology, Scripps Research Institute, La Jolla, CA 92037, USA.

*Present address: Division of Hematology and Medical Oncology and OHSU Knight Cancer Institute, Oregon Health and Science University, Portland, OR 97239, USA.

†Corresponding author. E-mail: angelika@mit.edu

Thus, the *nud1-42A* allele is defective in recruitment of Dbf2-Mob1 to SPBs and astral microtubule anchorage (11).

Further analyses (12) (fig. S3, A to C) revealed that Nud1 T78 was especially critical for MEN signaling, with two additional residues, S53 and S63, contributing to this function. A *NUD1* allele carrying alanine substitutions of S53, S63, and T78 (*nud1-3A*; table S1) caused an anaphase arrest when overexpressed in the presence of wild-type *NUD1* (fig. S3C) and failed to restore viability to cells expressing the *GAL-nud1-44* allele grown under restrictive conditions (fig. S3D). The anaphase delay caused by a *NUD1* allele that included the S53A and S63A mutations but not T78A was minor (fig. S3C). Replacing S53, S63, and T78 with residues that mimic phosphorylation (Asp or Glu) disrupted Nud1 function (12), precluding us from examining the consequences of constitutive phosphorylation of these residues. S53, S63, and T78 are conserved across fungal orthologs (fig. S4). Thus, these residues may have similarly important roles in other fungal species.

Localization of Mob1 to SPBs was disrupted in *nud1-3A* cells as it was in *nud1-42A* cells (Fig.

1C), but astral microtubule organization was not affected (fig. S5A). In contrast, a *NUD1* allele in which all mitotic phosphorylation sites were mutated to alanine with the exception of S53, S63, and T78 (*nud1-39A* allele; table S1) facilitated normal Mob1 localization and restored viability to cells expressing the *GAL-nud1-44* allele under restrictive conditions (Fig. 1, D and E). *nud1-39A* cells did exhibit a 2-min delay in exit from mitosis (fig. S5B), suggesting that other phosphorylation sites in Nud1 play a very minor role in MEN activation. *nud1-39A* cells also harbored mispositioned anaphase spindles and detached astral microtubules (fig. S5, A, C, and D). The spindle positioning and astral microtubule anchoring defect of *nud1-39A* cells was suppressed by forcing localization of the astral microtubule anchor Spc72 to SPBs (fig. S5E), suggesting that *nud1-39A* cells are defective in Spc72 recruitment. Indeed, Spc72 localization to SPBs was impaired in *nud1-39A* cells (fig. S5F). These results distinguish the two Nud1 functions: MEN activation and astral microtubule anchorage.

Next, we sought to identify the kinase(s) that phosphorylates Nud1 S53, S63, and T78. Cdc15 is a likely candidate because it, like Nud1 phos-

phorylation, is essential for Dbf2-Mob1 SPB localization (fig. S6) (13). Mob1 coimmunoprecipitated with Nud1 in anaphase-arrested cells in which *CDC15* is active (*cdc14-3* cells) but not in cells in which *CDC15* is inactive (*cdc14-3 cdc15-2* cells; Fig. 2A). Cdc15 kinase activity was also sufficient for localization of Dbf2-Mob1 to SPBs. Constitutive targeting of Cdc15 to SPBs by fusing *CDC15* to the SPB (*CDC15-SPB*) (3) led to recruitment of Dbf2-Mob1 to SPBs soon after expression of *CDC15-SPB* and induced premature phosphorylation of Nud1 (Fig. 2B and fig. S7). To directly test whether Cdc15 phosphorylates Nud1 in vivo, we raised phospho-specific antibodies to S53, S63, and T78 (fig. S8). The antibodies bound to wild-type Nud1 only in anaphase cells (Fig. 2C). T78 phosphorylation depended on *CDC15*, S63 phosphorylation was partially dependent, and S53 phosphorylation was not (Fig. 2D). Consistent with this, premature targeting of Cdc15 to SPBs was sufficient to cause phosphorylation of Nud1 T78 and S63, but not S53 (Fig. 2E). In vitro, Cdc15 phosphorylated a recombinant N-terminal fragment of Nud1 (amino acids 1 to 150) but not the *nud1-3A* protein (Fig. 2F). Thus, Cdc15 phosphorylates

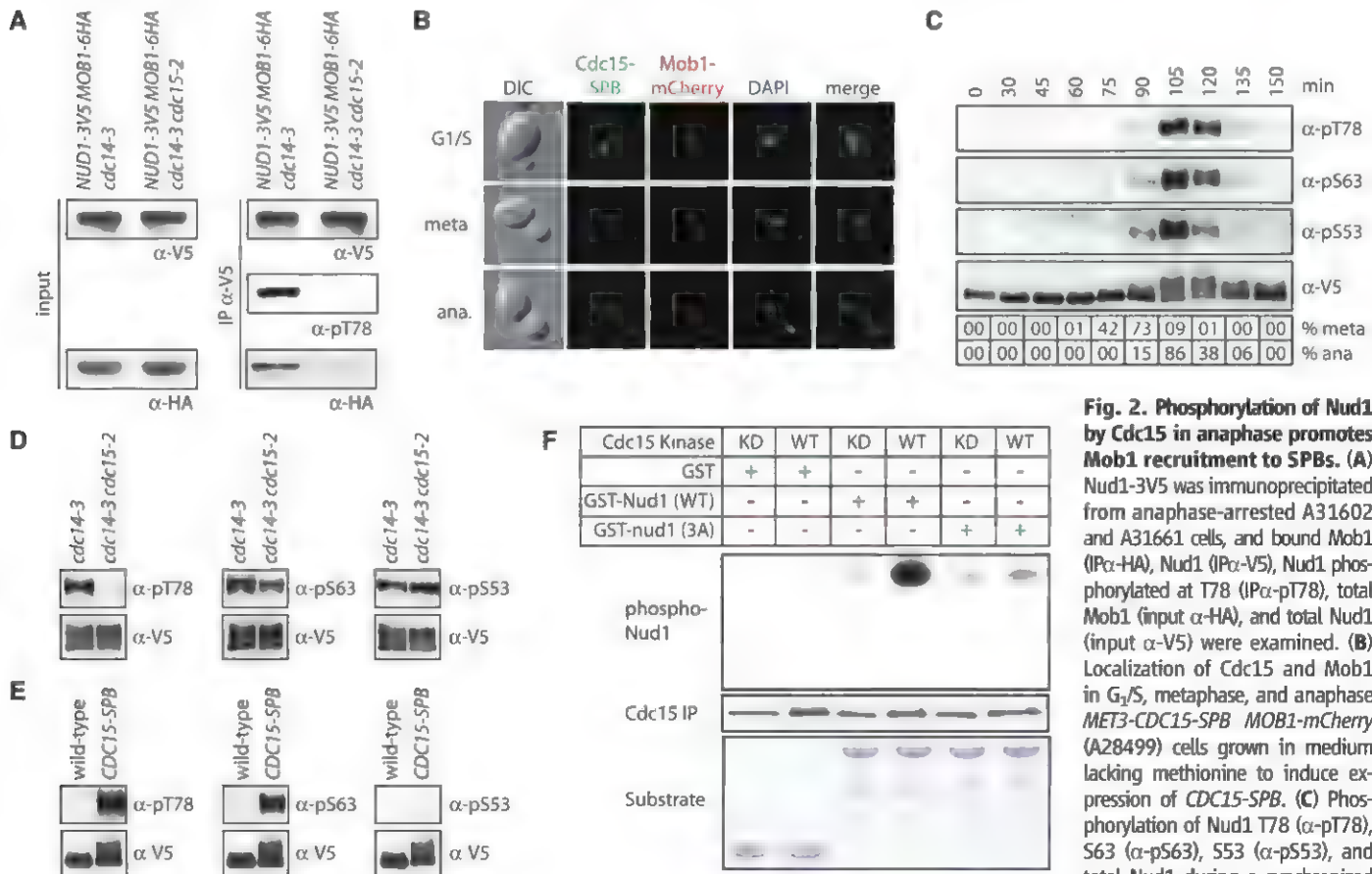


Fig. 2. Phosphorylation of Nud1 by Cdc15 in anaphase promotes Mob1 recruitment to SPBs. (A) Nud1-3V5 was immunoprecipitated from anaphase-arrested A31602 and A31661 cells, and bound Mob1 (IP α -HA), Nud1 (IP α -V5), Nud1 phosphorylated at T78 (IP α -pT78), total Mob1 (input α -HA), and total Nud1 (input α -V5) were examined. (B) Localization of Cdc15 and Mob1 in G₁/S, metaphase, and anaphase *MET3-CDC15-SPB MOB1-mCherry* (A28499) cells grown in medium lacking methionine to induce expression of *CDC15-SPB*. (C) Phosphorylation of Nud1 T78 (α -pT78), S63 (α -pS63), S53 (α -pS53), and total Nud1 during a synchronized cell cycle (A24513). Percent meta-

phase (% meta) and anaphase (% ana) cells are shown. (D) Phosphorylation of Nud1 as in Fig. 2C in anaphase-arrested *NUD1-3V5 cdc14-3* (A29851) and *NUD1-3V5 cdc14-3 cdc15-2* (A31661) cells. (E) Phosphorylation of Nud1 as in Fig. 2C in S-phase-arrested *NUD1-3V5* (A24513) and *NUD1-3V5 MET3-CDC15-SPB* (A31422) cells (12). *CDC15-SPB* expression was induced as in Fig. 2B. (F) Phosphorylated Nud1, immunoprecipitated Cdc15 [Cdc15 IP; wild type (WT): A24957; kinase-dead (KD): A30371], and GST fusion protein substrate added to the kinase reaction (Substrate) are shown.

Nud1 on residues T78 and S63 during anaphase to promote binding of Dbf2-Mob1 to Nud1.

Mob1 bound to SPBs in the absence of Dbf2 (Fig. 3A), but Dbf2 did not bind to SPBs in the absence of Mob1 (Fig. 3B). This observation, together with the finding that Mob1 and Nud1 form a complex in a *CDC15*-dependent manner (Fig. 2A), suggests that Mob1 binds Nud1 in a phosphorylation-dependent manner. To test this, we assayed the interaction of recombinant Mob1 with Nud1 phosphopeptides in vitro. Glutathione *S*-transferase (GST)-Mob1 (amino acids 79 to 314) that contains the conserved Mob1 core but not the N terminus unique to yeast (14) preferentially bound to phosphorylated T78 Nud1 peptides (Fig. 3C). Oriented peptide library screening (12) revealed that Mob1 displayed a preference for Y or F in the -2 position and preferred aliphatic, hydrophobic, or R residues in the +1 to +4 positions. The Nud1 protein sequence surrounding T78 shows features consistent with these results (fig. S9, A to C). We measured binding of GST-Mob1 to filter-bound peptides predicted to be optimal ligands on the basis of the peptide library screening. Mob1 bound to these optimal peptides in a phosphorylation-specific manner (Fig. 3D). The binding of Mob1 to the optimal ligand was stronger than that to the Nud1 pT78 peptide (dissociation constant K_d of 174 nM and 2.4 μ M, respectively; fig. S9, D and E). These values are similar to those observed for the interaction of FHA phosphopeptide binding domains with their optimal and physiologic peptides (15, 16). Thus, Mob1 directly binds Nud1 T78 in a phosphorylation-dependent manner.

We attempted to crystallize human (hMob1) and yeast Mob1 as complexes with the Nud1

pT78 and optimal phosphopeptides. Of these combinations, hMob1 bound to the peptide TVARIYHpsVVRYAPS yielded crystals of sufficient quality for structure determination and refinement at a resolution of 2.1 Å (table S4). The phosphopeptide binds across a shallow pocket on the Mob1 surface (Fig. 4A and fig. S10A). The structural basis for selection of aromatic residues in the pSer/pThr -2 position (fig. S9, A and B) is explained by the packing of the phenolic side chain of Tyr -2 against the aliphatic portion of K84. In yeast Mob1, this lysine is substituted by a proline, which would also make favorable van der Waals interactions. Discrimination for small- to medium-sized hydrophobic residues at the +1 and +2 positions is also explained by their interactions with a largely conserved hydrophobic depression on the Mob1 surface.

The structure explains the phospho-dependence of Mob1 binding through extensive interactions of the phosphoserine with three basic residues (K132, R133, and R136) that form part of a positively charged pocket located on the face opposite to that of the Dbf2-interacting surface. In yeast Mob1, three structurally equivalent arginine residues, R253, R254, and R257, form the conserved basic pocket and directly coordinate a sulfate ion derived from the crystallization mother liquor (Fig. 4B and fig. S10B) (14). Thus, the Mob1 protein family contains a distinct class of phosphoserine-threonine binding domains.

To test whether these arginine residues are important for Mob1 binding to Nud1, we assayed the interaction of GST-mob1-R253A,R254A,R257A (henceforth mob1-3RA) with phosphopeptides. The mob1-3RA protein was properly folded (fig. S11A), but failed to interact with

Nud1 pT78 peptides (Fig. 4C). Thus, the basic pocket of Mob1 mediates phosphopeptide binding. Phosphopeptide binding was also essential for Mob1 function in vivo. The mob1-R→A proteins interacted with Dbf2 (fig. S11B) but did not localize to SPBs (Fig. 4D and fig. S11C) nor support viability (Fig. 4E and fig. S11D). Furthermore, these cells lacked Dbf2 kinase activity and failed to release Cdc14 from the nucleolus or to exit from mitosis (Fig. 4F). This cell cycle arrest was not suppressed by a dominant, constitutively active Dbf2 allele (*DBF2-Hy4*; fig. S11E) (17). Thus, even if the defect in Dbf2 activation is corrected in *mob1-3RA* cells, the failure of mob1-3RA to bind phosphopeptides and presumably target Dbf2 to its relevant substrates results in an inability to exit from mitosis. Indeed, the phosphopeptide binding property of Mob1 may also be critical for targeting Dbf2-Mob1 to its substrates. Mob1 binds experimentally verified phosphorylation sites in the Dbf2-Mob1 substrate Hof1 (fig. S12) (18).

Our results show that MEN signaling requires an unusual two-step process (Fig. 4G). Rather than directly activating its downstream kinase Dbf2-Mob1, Cdc15 first creates phospho-docking sites on the MEN scaffold Nud1. Nud1 phosphorylation recruits Dbf2-Mob1 to SPBs followed by Cdc15-dependent activation of Dbf2-Mob1. As Cdc15 alone is sufficient to activate Dbf2-Mob1 in vitro (6), why do cells use a two-step mechanism for Dbf2-Mob1 activation? A two-step scaffold-assisted mechanism of activating downstream kinases may afford many advantages. In addition to allowing for greater regulatory power, this mechanism mitigates the "biphasic effect" in which scaffold proteins can exhibit concentration-

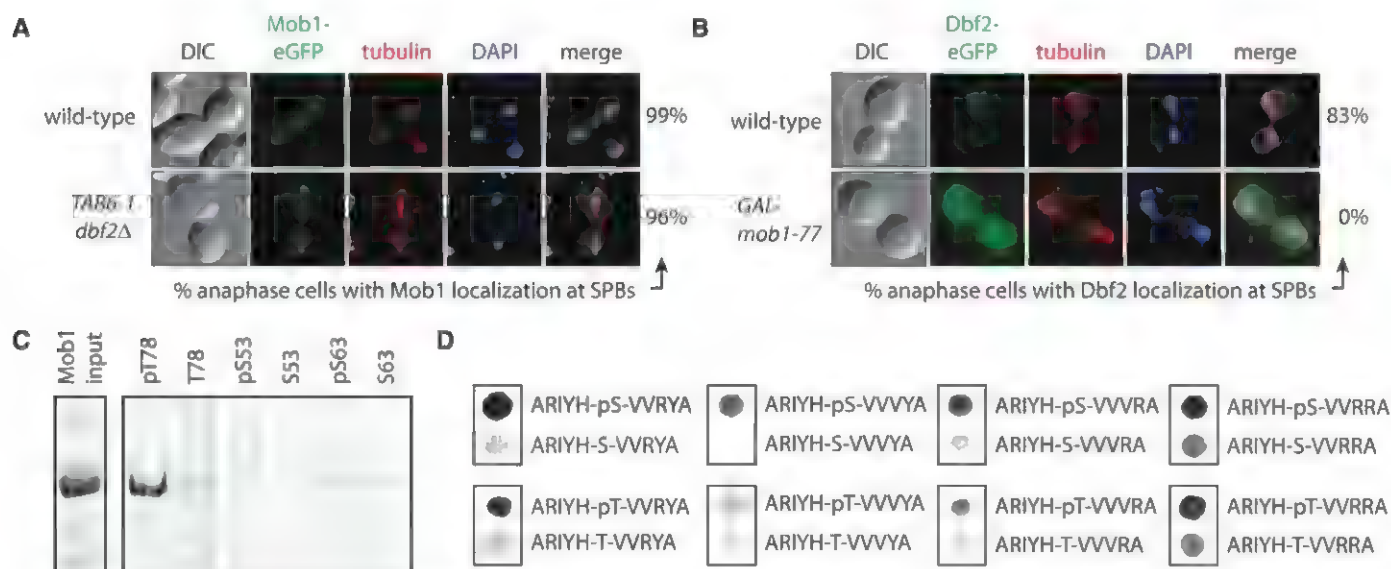


Fig. 3. Phosphorylation-dependent binding of Mob1 to Nud1. (A) Mob1 localization in anaphase *MOB1-eGFP* (A24631) and *MOB1-eGFP dbf2Δ* *TAB6-1* (A32656) cells. *TAB6-1* is a dominant active *CDC14* allele that was necessary to keep *dbf2Δ* cells alive (20). (B) Dbf2 localization in anaphase *DBF2-eGFP* (A29921) and *DBF2-eGFP GAL-mob1-77* (A32654) cells. eGFP, enhanced green

fluorescent protein. (C) Bead-bound phosphorylated (pT78, pS53, or pS63) or nonphosphorylated (T78, S53, or S63) Nud1 peptides were incubated with GST-Mob1 and input and eluates analyzed. (D) Binding of GST-Mob1 to an array of peptide spots. Abbreviations for the amino acid residues are as follows: A, Ala; H, His; I, Ile; R, Arg; S, Ser; T, Thr; V, Val; and Y, Tyr.

dependent titration effects (19). Increasing concentrations of scaffold proteins initially favor interaction of partner proteins but, at higher concentrations, will sequester partner proteins into separate complexes. The dependency of

terminal kinase binding on scaffold phosphorylation may ensure that terminal kinases only engage in complexes in which their upstream kinases are bound and active. Such a protective mechanism predicts that MEN signaling ought

to be resistant to the overexpression of individual signaling components, and this is what we observe (fig. S13).

A two-step mechanism may also facilitate signal transmission and effector activation at

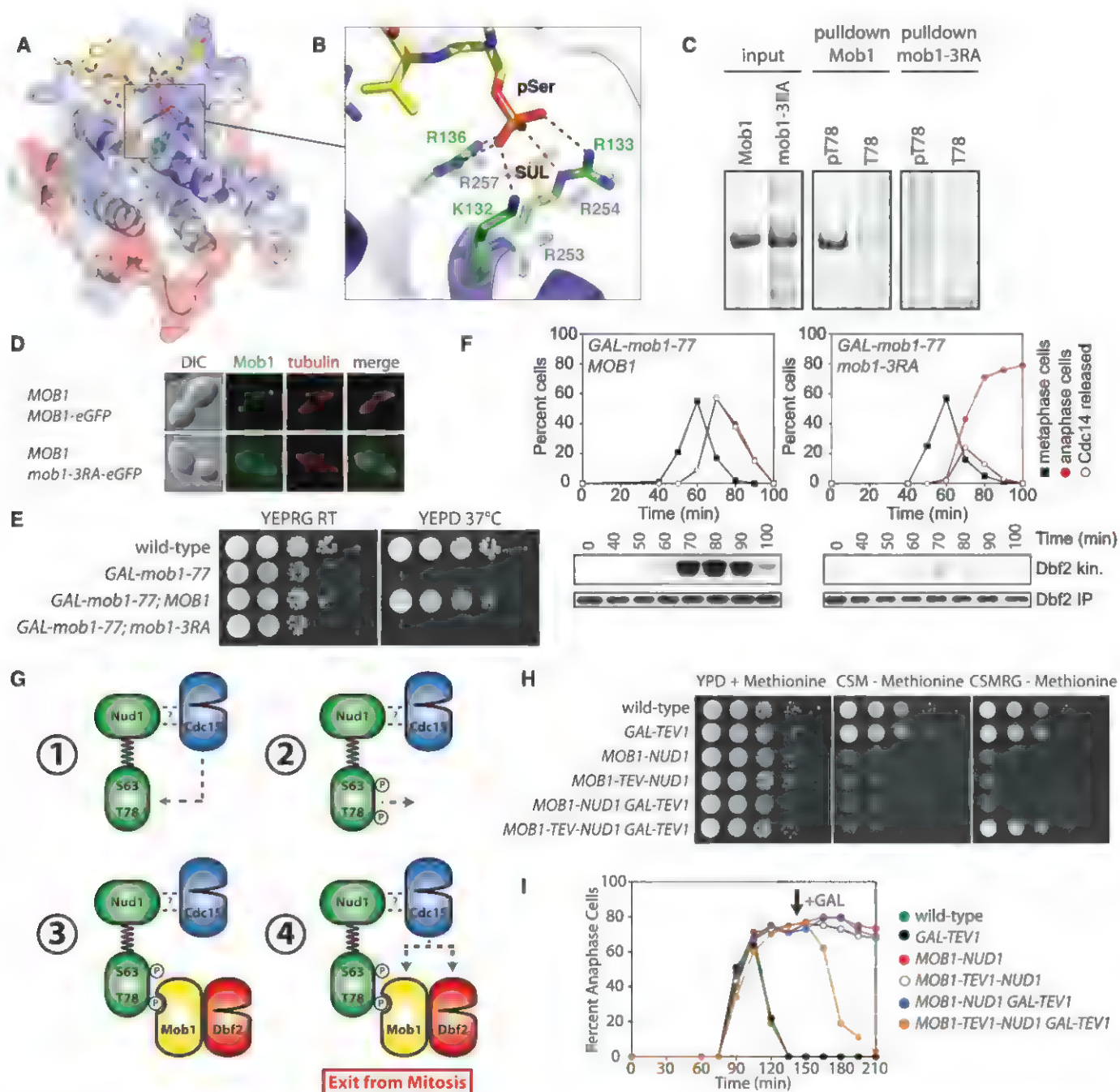


Fig. 4. Mob1 binding to phospho-Nud1 through a conserved basic pocket. (A) Structure of the hMob1-phosphopeptide complex. The peptide is shown as yellow sticks and hMob1 is shown in ribbon representation overlaid with a transparent electrostatic potential surface. Surface electrostatic potential between -10 kT (red) and +10 kT (blue) is shown. (B) View of the basic pocket of Mob1. pSer is coordinated by hMob1 K132, R133, and R136, and the SO_4^{2-} ion by yeast Mob1 R253, R254, and R257. (C) Binding of phosphorylated (pT78) or nonphosphorylated (T78) Nud1 peptides to GST-Mob1 or GST-mob1-3RA as in Fig. 3C. (D) Mob1 localization in anaphase A3150 and A31504 cells. (E) Growth of A2587, A32452, A32586, and A32589 cells on YEPRG and

YEPRG plates as in Fig. 1E. (F) Dbf2 kinase activity and cell cycle progression in MOB1 GAL-mob1-77 (A32818) and mob1-3RA GAL-mob1-77 (A32823) cells grown as in Fig. 1A. (G) Model for Dbf2-Mob1 activation. (H) Growth of A2587, A5588, A32336, A33289, A33551, and A33285 cells on YEPRG+Methionine, CSM-methionine+glucose, or CSM-methionine+raffinose and galactose (CSMRG) plates as in Fig. 1E. (I) Anaphase kinetics in A1411, A33291, A32668, A33549, A33287, and A33283 cells. Cells were arrested in G₁ with α -factor in YEPRaff+Methionine medium and released into CSM-methionine+raffinose medium to induce expression of the Mob1-Nud1 fusion. Galactose was added (arrow) to induce expression of GAL-TEV1.

distinct sites in the cell. Dbf2-Mob1 activated by Cdc15 at SPBs must phosphorylate Cdc14 in the nucleolus. This predicts that the Mob1-Nud1 interaction must be dynamic. In agreement, fusion of *MOB1* to *NUD1* (*MOB1-NUD1*) resulted in the constitutive localization of Dbf2 to SPBs (fig. S14, A and B) but, despite the proper localization pattern, did not restore viability to *mob1-77* cells at restrictive conditions (fig. S14C). Indeed, expression of *MOB1-NUD1* was lethal in wild-type cells because Cdc14 could not be released from the nucleolus (fig. S14, D to F). This lethality appears to result from failure of Dbf2-Mob1 to dissociate from SPBs because a Mob1-Nud1 fusion in which Mob1 could be proteolytically released from Nud1 restored proper MEN regulation (Fig. 4, H and I). Furthermore, lethality caused by expression of *MOB1-NUD1* was not suppressed by expression of a dominant, constitutively active Dbf2-HyA allele (fig. S14G), indicating that even hyperactive Dbf2 that cannot dissociate from SPBs is not functional. During MEN signaling, dynamic interaction between Mob1 and Nud1 may be achieved by Cdc15 first generating a high-affinity scaffold docking site for Dbf2-Mob1. Phosphorylation of Dbf2-Mob1 by Cdc15 could then, in addition to activating the kinase, decrease affinity to the

Nud1 scaffold, thereby promoting the dissociation of Dbf2-Mob1 from SPBs.

In this study, we have uncovered a distinct mechanism of scaffold-assisted activation of a kinase cascade. We propose that the two-step activation of terminal kinases may be a common feature of scaffold-assisted signaling that provides a potentially general means to avoid the biphasic effect and organize signaling pathways in which the site of pathway activation differs from the essential site of action.

References and Notes

1. A. Hergovitch, B. A. Hemmings, *Semin. Cell Dev. Biol.* **23**, 794 (2012).
2. F. Stegmeier, A. Amon, *Annu. Rev. Genet.* **38**, 203 (2004).
3. J. M. Rock, A. Amon, *Genes Dev.* **25**, 1943 (2011).
4. M. Valerio-Santiago, F. Monje-Casas, *J. Cell Biol.* **192**, 599 (2011).
5. A. K. Caydas, G. Pereira, *Exp. Cell Res.* **318**, 1421 (2012).
6. A. S. Mah, J. Jang, R. J. Deshaies, *Proc. Natl. Acad. Sci. U.S.A.* **98**, 7325 (2001).
7. M. C. Good, J. G. Zalatan, W. A. Lim, *Science* **332**, 680 (2011).
8. H. Maekawa, C. Priest, J. Lechner, G. Pereira, E. Schiebel, *J. Cell Biol.* **179**, 423 (2007).
9. C. J. Park et al., *Eukaryot. Cell* **7**, 444 (2008).
10. J. M. Keck et al., *Science* **332**, 1557 (2011).
11. U. Grunberg, K. Campbell, C. Simpson, J. Grindlay, E. Schiebel, *EMBO J.* **19**, 6475 (2000).
12. Materials and methods are available as supplementary materials on Science Online.

13. C. König, H. Maekawa, E. Schiebel, *J. Cell Biol.* **188**, 351 (2010).
14. S. Mrkobrada, L. Boucher, D. F. Ceccarelli, M. Tyers, F. Sicheri, *J. Mol. Biol.* **362**, 430 (2006).
15. D. Durocher et al., *Mol. Cell* **6**, 1169 (2000).
16. Z. Ding et al., *Biochemistry* **46**, 2684 (2007).
17. M. Geymonat, A. Spanos, G. de Bettignies, S. G. Sedgwick, *J. Cell Biol.* **187**, 497 (2009).
18. A. E. Elia, L. C. Cantley, M. B. Yaffe, *Science* **299**, 1228 (2003).
19. A. Levchenko, J. Bruck, P. W. Sternberg, *Proc. Natl. Acad. Sci. U.S.A.* **97**, 5818 (2000).
20. W. Shou et al., *Mol. Cell* **8**, 45 (2001).

Acknowledgments: We thank I. Cheeseman, F. Solomon, and the Amon lab for comments and E. Schiebel for reagents. Coordinates and structure factors for the hMob1-phosphopeptide complex have been deposited with the Protein Data Bank (PDBID: 4JIZ). Supported by the NIH (GM056800 to A.A.; CA112967 and ES015339 to M.B.Y.; P41 RR011823 to J.R.Y. III and T. N. Davis, principal investigator; and GM51312 to M.W.); MRC UK (U117584228) to S.J.S.; MRC centenary fellowship to L.S.; NIH F32 GM086038 to J.M.K.; and NSF Predoctoral Fellowship to J.M.R. A.A. is an investigator of the Howard Hughes Medical Institute.

Supplementary Materials

www.sciencemag.org/cgi/content/full/science.1235822/DC1
Materials and Methods
Figs. S1 to S14
Tables S1 to S4
References

29 January 2013; accepted 13 March 2013
Published online 11 April 2013;
10.1126/science.1235822

ATAXIN-2 Activates PERIOD Translation to Sustain Circadian Rhythms in *Drosophila*

Chunghun Lim* and Ravi Allada†

Evidence for transcriptional feedback in circadian timekeeping is abundant, yet little is known about the mechanisms underlying translational control. We found that ATAXIN-2 (ATX2), an RNA-associated protein involved in neurodegenerative disease, is a translational activator of the rate-limiting clock component PERIOD (PER) in *Drosophila*. ATX2 specifically interacted with TWENTY-FOUR (TYF), an activator of PER translation. RNA interference-mediated depletion of *Atx2* or the expression of a mutant ATX2 protein that does not associate with polyadenylate-binding protein (PABP) suppressed behavioral rhythms and decreased abundance of PER. Although ATX2 can repress translation, depletion of *Atx2* from *Drosophila* S2 cells inhibited translational activation by RNA-tethered TYF and disrupted the association between TYF and PABP. Thus, ATX2 coordinates an active translation complex important for PER expression and circadian rhythms.

Daily oscillations of gene expression underlie time-keeping in animals (1). A transcriptional feedback network of core clock genes drives circadian transcription, whereas posttranslational modification of the clock genes is important for precise timing of the clock (2). Emerging evidence suggests that other modes of posttranscriptional regulation play more pivotal

roles in clock mechanisms than previously appreciated (3–5). Yet the molecular mechanisms of this important facet of the clock remain to be elucidated. The product of the *Drosophila* gene *twenty-four* (*tyf*) is required for the efficient translation of the core clock protein PERIOD (PER) (6). *tyf* mutants display weak behavioral rhythms with decreased abundance of PER specifically in pacemaker neurons. TYF associates with polyadenylate [poly(A)]-binding protein (PABP) as well as with *per* RNA. TYF can activate translation of reporter RNAs in vitro. TYF lacks known functional domains, including RNA-binding domains. We used a proteomic strategy to identify the fly homolog of

the neurodegenerative disease gene ATAXIN-2 (ATX2) as a translational coactivator of TYF.

TYF can stimulate translation when tethered to a reporter RNA (6). We used an RNA-tethering assay in *Drosophila* S2 cells to map a domain necessary and sufficient for such activation to the C-terminal 290 amino acids of TYF (Fig. 1A, TYF-C5). To identify components that interact with this domain, we affinity-purified TYF complexes in S2 cells. Two proteins specifically associated with TYF-C5 and full-length TYF (Fig. 1, B and C, arrows). Mass spectrometric analyses identified the larger and smaller molecular-size proteins as ATX2 and PABP, respectively. We confirmed that TYF-C5 was necessary and sufficient to specifically associate with ATX2 and PABP (Fig. 1D).

Polyglutamine expansion in human ATX2 (also ATXN2) leads to neurodegenerative diseases such as spinocerebellar ataxia type 2 (SCA2) (7–9) or an increased risk of amyotrophic lateral sclerosis and Parkinsonism (10, 11). ATX2 associates with polyribosomes through its N-terminal like-Sm (Lsm) and like-Sm-associated (LsmA) domains or C-terminal poly(A)-binding protein-interacting motif 2 (PAM2) domain (12, 13). The ATX2-PABP interaction is conserved from yeast to human (12–14). TYF and PABP separately bound to different regions of ATX2 in a ribonuclease-insensitive manner (figs. S1 and S2A). Deletion of the PAM2 region abolished binding of PABP but not TYF to ATX2 (fig. S2A). A PABP-independent interaction of TYF with ATX2 was also observed in extracts of fly heads (fig. S2B). To test the function of the ATX2-TYF interaction, we generated

Department of Neurobiology, Northwestern University, Evanston, IL 60208, USA.

*Present address: School of Nano-Bioscience and Chemical Engineering, Ulsan National Institute of Science and Technology, Ulsan 689-798, Republic of Korea.

†Corresponding author. E-mail: r-allada@northwestern.edu

transgenic flies expressing wild-type TYF or a mutant lacking the ATX2-binding domain (TYFΔC5). TYF transgenes were expressed in clock neurons by *timeless* (*tim*)-Gal4 (15). We verified the TYF C5 domain-dependent association of TYF with ATX2 and PABP (Fig. 1E). *Pigment-dispersing factor* (*Pdf*)-expressing neurons govern free-running locomotor rhythms (16–18). Expression of full-length TYF but not TYFΔC5 in PDF neurons restored rhythmicity in *tyf* mutants, and the extent of this effect depended on transgenic insertion (Fig. 2A and table S1). We excluded the possibility of positional effects of different transgenic insertions because TYF-V5 and TYFΔC5-V5 transgenes were inserted into the same genomic locus (*attP40*). Reduced amounts of PER in PDF neurons of *tyf* mutants were also rescued by expression of full-length TYF but not TYFΔC5 (Fig. 2, B and C), confirming the importance of the ATX2-binding C5 domain.

TYF associates with clock gene mRNAs, especially *per* and *tim* (6). Loss of the ATX2-binding domain did not affect this RNA association (Fig. 2D), suggesting that neither ATX2 nor PABP tethers TYF to RNA. Given that full-length and mutant TYF comparably associated with target

RNAs, TYFΔC5 lacking the activation domain might act as a dominant negative. Indeed, TYFΔC5 overexpression in wild-type flies compromised locomotor rhythms for up to a 31-hour period (Fig. 2A and fig. S3). Amounts of PER were reduced in cells overexpressing TYFΔC5 (Fig. 2C), whereas PER overexpression restored long-period rhythms in TYFΔC5-overexpressing flies (fig. S3), consistent with the idea that the ATX2-binding domain is crucial for TYF-dependent translation of PER.

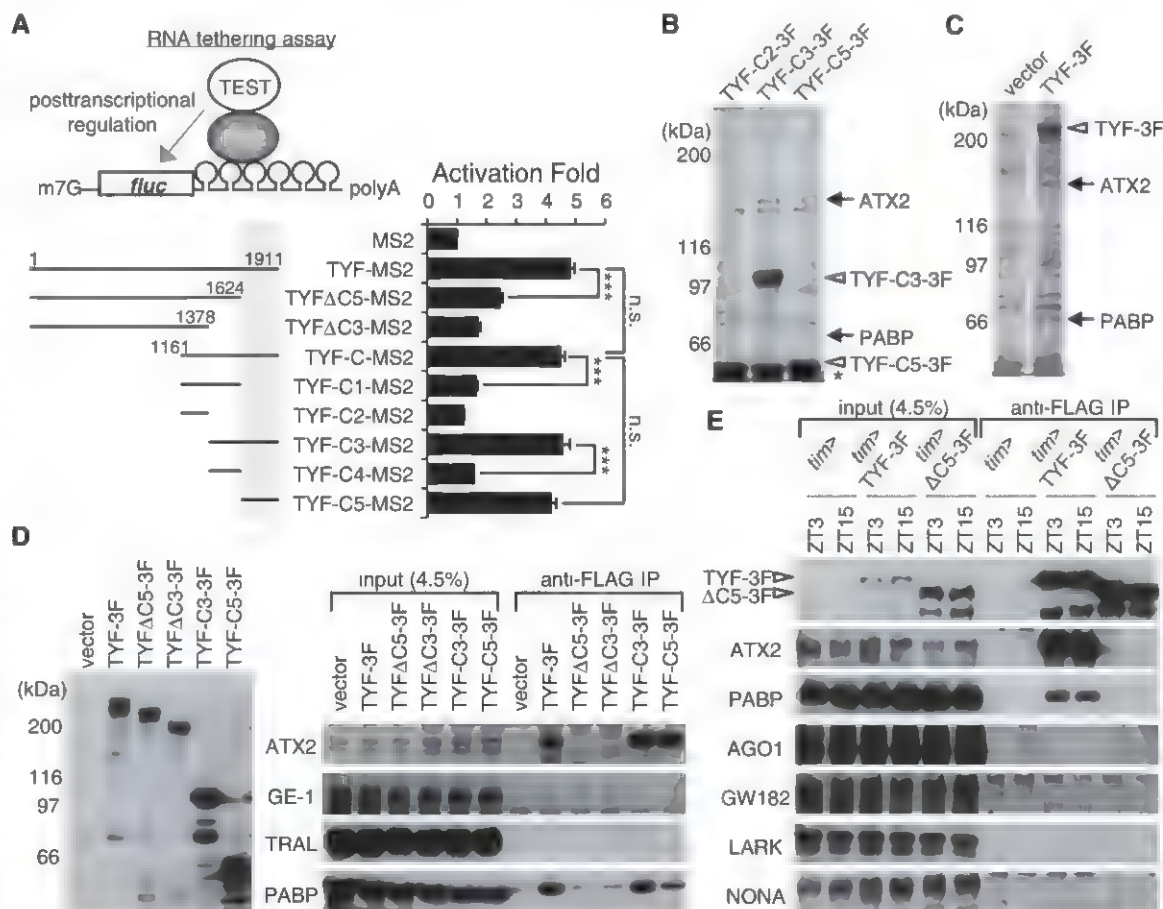
If ATX2 is important for TYF function, reductions in *Atx2* should cause circadian phenotypes similar to those in *tyf* mutant flies. Because homozygous *Atx2* mutants do not live to adulthood (19), we decreased *Atx2* expression with RNA interference (RNAi). Abundance of ATX2 was specifically reduced in the *Atx2* RNAi flies (fig. S4). Depletion of *Atx2* from PDF neurons by RNAi resulted in a long-period rhythm in constant dark (Fig. 3A and fig. S5). Normal rhythm was partially restored by overexpression of wild-type ATX2, consistent with the idea that RNAi acts through depletion of *Atx2* (fig. S5). A heterozygous *Atx2* mutation, *Atx2*[06490] (19), further reduced rhythmicity because of RNAi

(fig. S6). Overexpression of PER also suppressed this period phenotype (fig. S5), indicating that effects of *Atx2* RNAi were mediated via PER.

Expression of *Atx2* RNAi with the stronger *Pdf*-Gal4 driver along with the RNAi-enhancing *dcr2* transgene suppressed rhythms (Fig. 3A and fig. S7), mimicking *tyf* mutant phenotypes. Peak amounts of PER in *Atx2* RNAi flies were only ~30% of those in wild-type PDF neurons, whereas TIM was little affected (Fig. 3B). We observed reduced abundance of PER and severe behavioral arrhythmicity when *Atx2* RNAi was expressed with *tim*-GAL4 (figs. S8 and S9). The RNAi effects on clock proteins TIM or VRILLE were not as evident as on PER (fig. S9). Also, the PER effects were absent in head extracts, because they are absent in *tyf* mutants (fig. S4B). Strong depletion of *Atx2* by *tim*-Gal4 led to abnormal PDF neuron projections (fig. S10). However, no morphological changes were observed after depletion of *Atx2* by *Pdf*-Gal4, consistent with *Atx2* function in adult rhythms (fig. S10). The strongest effects of *tyf* and *Atx2* on PER are in PDF neurons, suggesting that these pacemaker neurons might have distinct posttranscriptional mechanisms necessary for pacemaker function. These

Fig. 1. Association of ATX2 and PABP with the TYF activation domain. (A) Deletion analyses of the C-terminal TYF activation domain (TYF-C5, highlighted by a gray box) in a RNA-tethering assay.

Drosophila S2 cells were transfected with firefly luciferase (*luc*) reporter containing MS2-binding sites, *renilla* luciferase (*rluc*) reporter, and expression vector for each TYF-MS2 fusion protein. FLUC activity was normalized to RLUC activity. Activation was calculated by normalizing to the value with MS2 control. Data represent average \pm SEM ($n = 4$ to 6). n.s., not significant at the 0.05 level; *** $P < 0.001$ as determined by one-way analysis of variance (ANOVA), Tukey post hoc test. (B and C) Each of the 3 \times FLAG-tagged TYF domains or full-length TYF was immunoprecipitated from S2 cell extracts. Bound proteins were visualized in polyacrylamide gel by Coomassie staining (B) or by silver staining (C). Asterisk indicates the heavy chain of antibody to FLAG. (D) Each of the 3 \times FLAG-tagged TYF domains (left) was immunoprecipitated from S2 cell extracts. Bound proteins were probed with specific antibodies (right). IP, immunoprecipitate. (E) 3 \times FLAG-tagged full-length TYF or TYFΔC5 was expressed in all clock neurons by



tim-Gal4 driver (*tim*>). Adult flies were collected at Zeitgeber time (ZT) 3 and ZT15 during a light-dark cycle (lights on at ZT0; lights off at ZT12). Proteins from head extracts were immunoprecipitated with anti-FLAG affinity gels. Bound proteins were analyzed as in (D).

data demonstrate specific effects of *Atx2* on PER expression and circadian behavior, consistent with other studies indicating some target specificity of *Atx2* effects (12, 14, 19–21).

We examined genetic interactions between *Atx2* and *tyf* to see whether they operate in the same pathway. We did not observe additive effects of *Atx2* knockdown and *tyf* mutation on period lengthening and rhythmicity (fig. S11), but poor rhythms make it difficult to accurately assess period length. Therefore, we quantified rhythm phase in constant dark (fig. S12). The offset phase of evening activity peaks was delayed in animals depleted of *Atx2* and in *tyf* mutants, reflecting their lengthened periods. However, the RNAi effects were not additive when combined with *tyf* mutants. The heterozygous *Atx2*[06490] mutation modestly enhanced the period lengthening caused by overexpression of TYFΔC5 but did

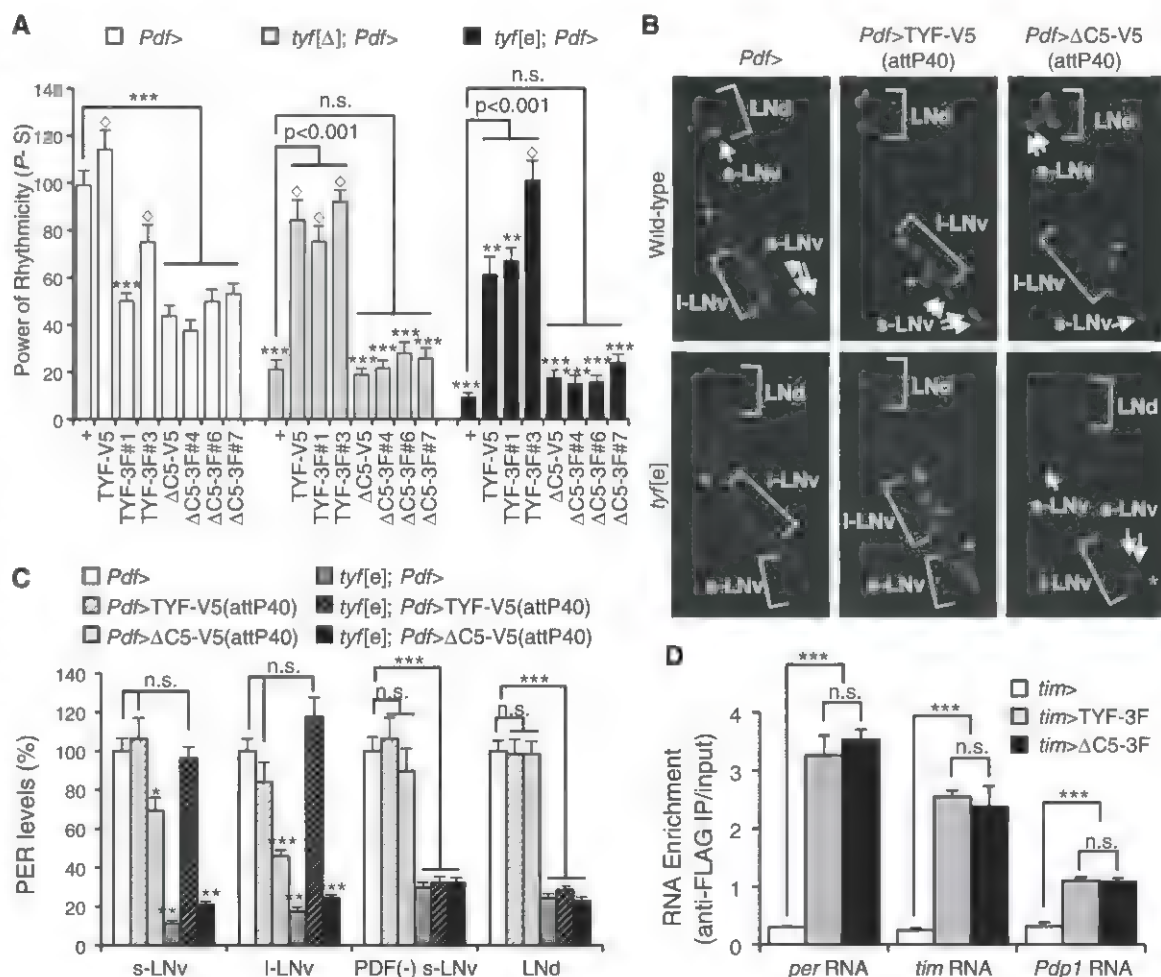
not affect period length in wild type (fig. S13), indicating that TYFΔC5 sensitizes TYF function to reduced *Atx2*. These interactions between *tyf* and *Atx2* genetic manipulation are consistent with their participation in a common genetic pathway controlling circadian period.

To test whether *Atx2* effects, like those of *tyf*, might reflect an association with *per* RNA, we immunoprecipitated epitope-tagged ATX2 overexpressed in all clock neurons. ATX2 not only associated with *per* RNA, but it bound with a small preference for *per* RNA over most clock transcripts except *cycle* (Fig. 3C). Time-dependent changes in abundance of immunoprecipitated RNA largely mirrored changes in the amounts of oscillating input RNAs (fig. S14). We did not observe rhythms in the abundance of ATX2 protein in head extracts (fig. S15), but rhythms may have been masked by constitutive ATX2 expres-

sion or activity in nonclock cells. The preferential association of ATX2 with *per* RNA may contribute to its specific activation of PER expression, although other mechanisms are likely to have larger specific effects on PER translation and expression.

The RNA-binding activity of ATX2 depends on its interaction with PABP but not TYF, because deletion of the PAM2 domain, but not *tyf* mutation, abolished its association with clock RNAs (Fig. 3C). Indeed, overexpression of ATX2 lacking the PAM2 domain in PDF neurons caused arrhythmic circadian behaviors (fig. S16 and table S2) and dampening in PER oscillations (fig. S17) similar to those observed in the *Atx2* RNAi flies. ATX2 lacking the PAM2 domain may interact with TYF, thereby dominantly inhibiting endogenous ATX2 activity and PER translation. These data confirm a role for the ATX2-PABP complex in vivo.

Fig. 2. Requirement of ATX2-binding domain for TYF function in vivo. (A) Epitope-tagged TYF or TYFΔC5 was expressed in PDF neurons of wild-type (white bars) or *tyf* mutant flies (gray and black bars) by *Pdf*-Gal4 driver (*Pdf*>). V5-tagged transgenes (TYF-V5 and ΔC5-V5) were inserted into the same genomic locus (attP40), and 3×FLAG-tagged transgenic lines (TYF-3F and ΔC5-3F) were independently generated by random insertions. Locomotor rhythmicity under constant dark cycles was measured by power (P) minus significance (S) values. Data represent average ± SEM (n = 24 to 68). n.s., not significant at the 0.05 level; ♦, not significant; **P < 0.01, ***P < 0.001 to the Gal4 control in wild type as determined by one-way ANOVA, Tukey post hoc test. Comparisons between other lines are indicated. (B) Adult fly brains were dissected at ZT0 during a light-dark cycle (lights on at ZT0; lights off at ZT12) and immunostained



with an antibody against PER. PER-expressing lateral neurons (LNs) were imaged with a 60× oil objective lens and further classified by costaining with antibody against PDF. LNd, dorsal LN; I-LNv, large ventral LN; s-LNv, small ventral LN. Asterisk indicates PDF-negative s-LNv. (C) PER levels in each clock neuron group were quantified and normalized to the values of the Gal4 control (*Pdf*>, set as 100%). Data represent average ± SEM (n = 10 to 12). n.s., not significant at the 0.05 level; *P < 0.05, ***P < 0.001 to the Gal4 controls (white bars) as determined by one-way ANOVA, Tukey post hoc

test. (D) 3×FLAG-tagged TYF or TYFΔC5 was expressed in all clock neurons by *tim*-Gal4 (*tim*>). Adult flies were collected at ZT15, and proteins from head extracts were immunoprecipitated with anti-FLAG affinity gels. Bound RNAs were analyzed by quantitative real-time reverse transcription polymerase chain reaction (RT-PCR) in triplicate. RNA enrichment was calculated by normalizing RNA levels in each IP to input levels. Data represent average ± SEM (n = 3). n.s., not significant at the 0.05 level; ***P < 0.001 as determined by one-way ANOVA, Tukey post hoc test.

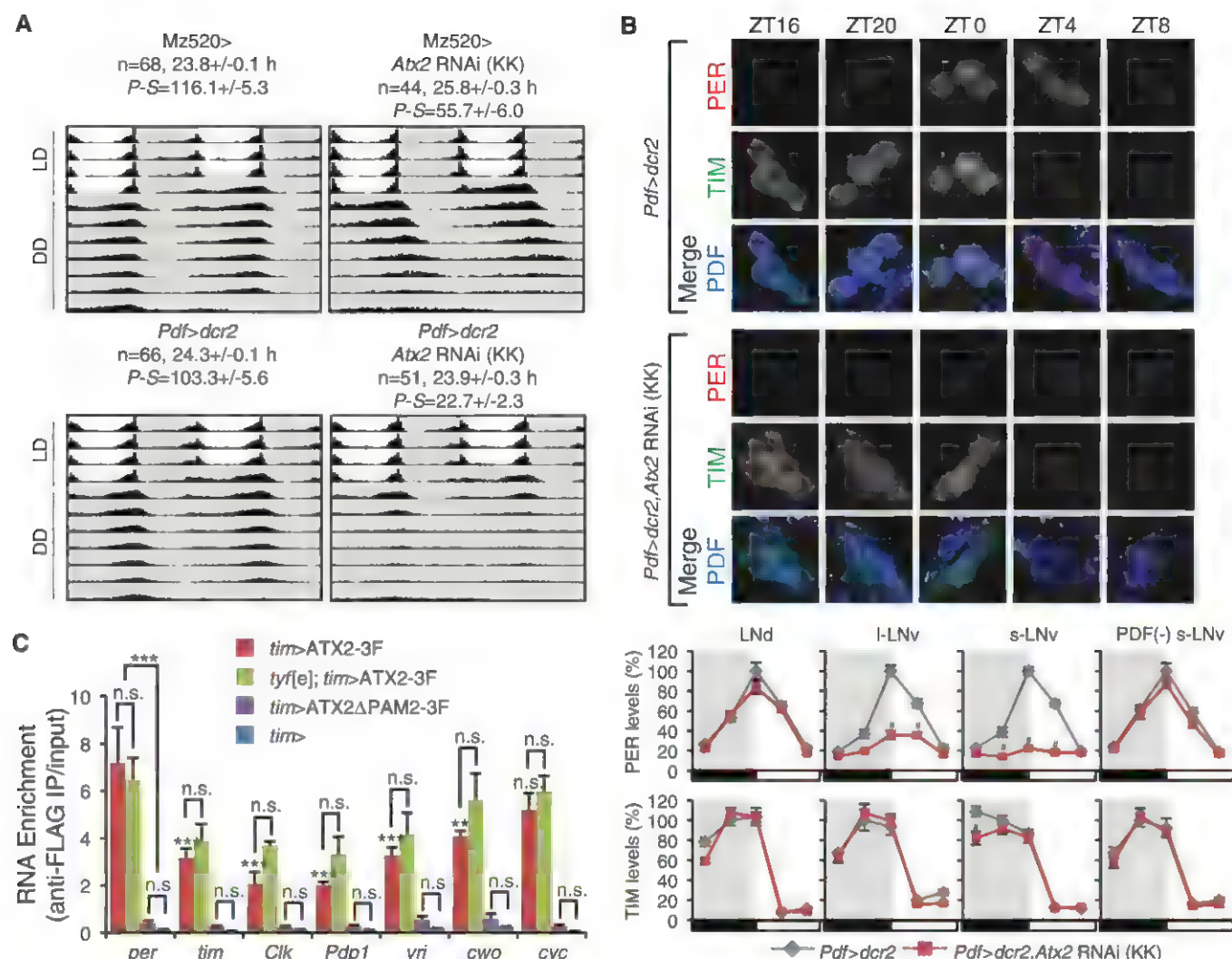


Fig. 3. *Atx2* RNAi mimics circadian phenotypes in *tyf* mutant flies. (A) An *Atx2* RNAi transgene (KK) was overexpressed in PDF neurons by Mz520-Gal4 (Mz520>, top) or *Pdf*-Gal4 along with RNAi-enhancing *dcrc2* transgene (*Pdf*>*dcrc2*, bottom). Averaged actograms during light-dark (LD) and constant dark (DD) cycles are double-plotted. Genotypes, number of flies tested, period (hour), and power of rhythmicity [as measured by power (*P*)—significance (*S*) values] under DD cycles are shown. Data represent average ± SEM. **(B)** Adult fly brains were dissected at various time points under a LD cycle (lights on at ZT0; lights off at ZT12) and immunostained with antibodies against PER, TIM, and PDF. Abundances of PER and TIM in each group of LNs were quantified and normalized to the values of the Gal4 control at peak time points (*Pdf*>*dcrc2*, set as 100%) as in Fig. 2, B and C. Representative confocal images from small

ventral LNs are shown at the top. Data represent average ± SEM (*n* = 9 to 10). **P* < 0.001 to the Gal4 control (*Pdf*>*dcrc2*) at each time point as determined by one-way ANOVA, Tukey post hoc test. PDF(-), PDF-negative. **(C)** Either 3×FLAG-tagged ATX2 or PAM2 deletion (ATX2ΔPAM2-3F) was expressed in all clock neurons of wild-type or *tyf* mutant (*tyf*[e]) flies by *tim*-Gal4 (*tim*>). Adult flies were collected at ZT15, and proteins from head extracts were immunoprecipitated with anti-FLAG affinity gels. Bound RNAs were analyzed by quantitative real-time RT-PCR using each gene-specific primer set in triplicate. RNA enrichment was calculated by normalizing amounts of RNA in each IP to input amounts. Data represent average ± SEM (*n* = 3 to 6). n.s., not significant at the 0.05 level; ***P* < 0.01, ****P* < 0.001 to the *per* RNA enrichment in *tim*>ATX2-3F flies as determined by one-way ANOVA, Tukey post hoc test.

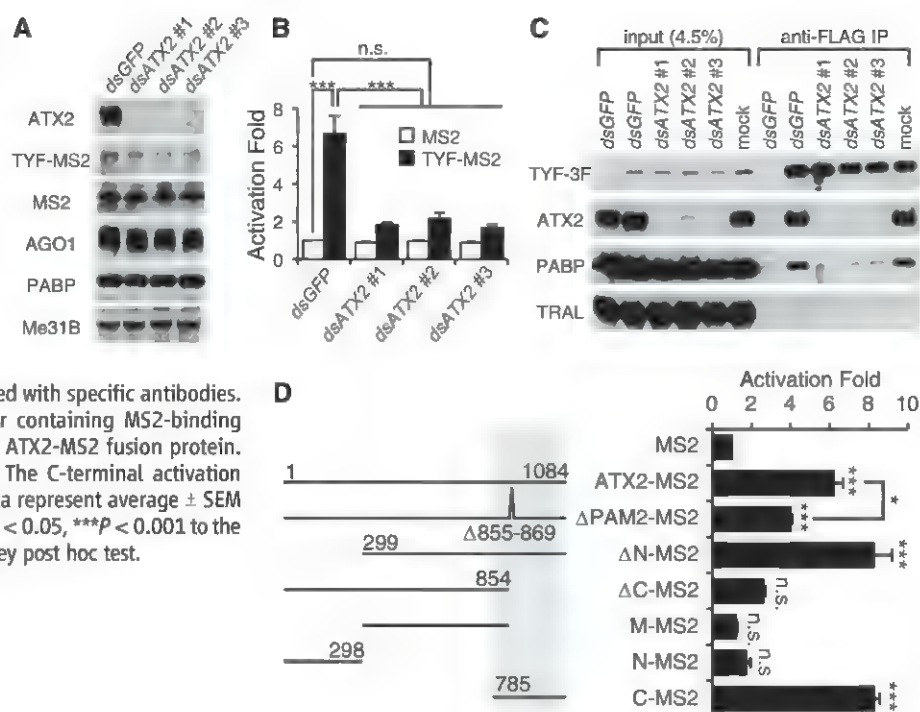
We used RNA-tethering assays with gene-specific depletion in S2 cells to further understand the mechanistic basis of *Atx2* effects. Expression of endogenous ATX2 in S2 cells was silenced in cells incubated with each of three double-stranded RNAs (dsRNAs) targeting different *Atx2* regions (Fig. 4A). Depletion of *Atx2* suppressed reporter activation by RNA-tethered TYF (TYF-MS2) (Fig. 4B) but not baseline reporter expression. Moreover, *Atx2* depletion blocked the interaction of TYF with PABP (Fig. 4C). Thus ATX2 appears to be required for TYF activation as well as PABP recruitment to the TYF-containing protein complex. A direct RNA-tethering of ATX2 induced re-

porter activation comparably to TYF-MS2 (Fig. 4D, ATX2-MS2). A deletion of the PABP-binding PAM2 domain partially decreased ATX2-MS2 activity, indicating PABP-dependent and -independent mechanisms for ATX2 (13). This translation activation function of ATX2 contrasts with its role in microRNA (miRNA)-mediated gene silencing (21–23). Depletion of miRNA-induced silencing complex (miRISC) components (24, 25) or Me31b, a RNA helicase that may mediate silencing effects by ATX2 (21–23), had no significant effect on activation of ATX2 or TYF (fig. S18). We failed to detect miRISC components in complex with TYF (Fig. 1E) and observed only a weak,

PABP-dependent interaction of ARGONAUTE1 with ATX2 (fig. S2B). Thus, our studies reveal that ATX2 functions as a translational activator by coordinating a translationally competent complex including TYF, PABP, and *per* mRNA.

Individuals bearing SCA2 disease mutations in human *Atx2* show disturbed rapid eye movement (REM) sleep even before the onset of ataxia symptoms (26, 27), and REM sleep is tightly regulated by the circadian clock (28). Given the high conservation of both circadian clock components in general and ATX2 in particular, we propose that mammalian *Atx2* homologs may also participate in circadian clock function.

Fig. 4. ATX2 as a posttranscriptional coactivator of TYF. (A and B) S2 cells were treated with dsRNAs for control (*dsGFP*) or *Atx2* gene (*dsATX2*) and subsequently transfected with fluc reporter containing MS2-binding sites, ruc reporter, and expression vector of MS2 (white bars) or TYF-MS2 (black bars) for the RNA-tethering assay. Specific depletion of endogenous ATX2 was confirmed by immunoblotting (A). A dual-luciferase reporter assay (B) was performed as in Fig. 1A. Data represent average \pm SEM ($n = 3$). n.s., not significant at the 0.05 level; *** $P < 0.001$ as determined by one-way ANOVA, Tukey post hoc test. (C) The 3 \times FLAG-tagged full-length TYF was immunoprecipitated from control or *dsATX2*-treated S2 cells. Bound proteins were probed with specific antibodies. (D) S2 cells were cotransfected with fluc reporter containing MS2-binding sites, ruc reporter, and expression vector for each ATX2-MS2 fusion protein. Reporter activation was calculated as in Fig. 1A. The C-terminal activation domain of ATX2 was highlighted by a gray box. Data represent average \pm SEM ($n = 3$ to 11). n.s., not significant at the 0.05 level; * $P < 0.05$, *** $P < 0.001$ to the MS2 control as determined by one-way ANOVA, Tukey post hoc test.



References and Notes

- C. J. Doherty, S. A. Kay, *Annu. Rev. Genet.* **44**, 419 (2010).
- X. Zheng, A. Sehgal, *Trends Neurosci.* **35**, 574 (2012).
- S. Kojima, D. L. Shingle, C. B. Green, *J. Cell Sci.* **124**, 311 (2011).
- D. Staiger, R. Green, *Trends Plant Sci.* **16**, 517 (2011).
- S. Bradley, S. Narayanan, M. Rosbash, *Genetics* **192**, 943 (2012).
- C. Lim *et al.*, *Nature* **470**, 399 (2011).
- G. Imbert *et al.*, *Nat. Genet.* **14**, 285 (1996).
- S. M. Pulst *et al.*, *Nat. Genet.* **14**, 269 (1996).
- K. Sanpei *et al.*, *Nat. Genet.* **14**, 277 (1996).
- A. C. Elden *et al.*, *Nature* **466**, 1069 (2010).
- O. A. Ross *et al.*, *Hum. Mol. Genet.* **20**, 3207 (2011).
- D. A. Mangus, N. Amrani, A. Jacobson, *Mol. Cell. Biol.* **18**, 7383 (1998).
- T. F. Satterfield, L. J. Pallanck, *Hum. Mol. Genet.* **15**, 2523 (2006).
- R. Ciosk, M. DePalma, J. R. Priess, *Development* **131**, 4831 (2004).
- M. Kaneko, J. C. Hall, *J. Comp. Neurol.* **422**, 66 (2000).
- B. Grima, E. Chélot, R. Xia, F. Rouyer, *Nature* **431**, 869 (2004).
- S. C. Renn, J. H. Park, M. Rosbash, J. C. Hall, P. H. Taghert, *Cell* **99**, 791 (1999).
- D. Stoleru, Y. Peng, J. Agosto, M. Rosbash, *Nature* **431**, 862 (2004).
- T. F. Satterfield, S. M. Jackson, L. J. Pallanck, *Genetics* **162**, 1687 (2002).
- I. Lastres-Becker *et al.*, *Hum. Mol. Genet.* **17**, 1465 (2008).
- C. McCann *et al.*, *Proc. Natl. Acad. Sci. U.S.A.* **108**, E655 (2011).
- C. Y. Chu, T. M. Rana, *PLoS Biol.* **4**, e210 (2006).
- U. Nonhoff *et al.*, *Mol. Biol. Cell* **18**, 1385 (2007).
- A. Eualio, E. Huntzinger, E. Izaurralde, *Nat. Struct. Mol. Biol.* **15**, 346 (2008).
- M. R. Fabian *et al.*, *Mol. Cell* **35**, 868 (2009).
- I. Tuin *et al.*, *Neurology* **67**, 1966 (2006).
- L. Velázquez-Pérez *et al.*, *Neurodegener. Dis.* **8**, 447 (2011).
- D. J. Dijk, C. A. Czeisler, *Neurosci. Lett.* **166**, 63 (1994).

Acknowledgments: We thank J. Choe, P. Hardin, E. Izaurralde, G. P. McNeil, A. Nakamura, L. Pallanck, M. Ramaswami, M. Rosbash, H. Saunweber, M. C. Siomi, N. Sonenberg, Bloomington *Drosophila* stock center, and Vienna *Drosophila* RNAi center for reagents; D. Nanavati (Northwestern

Proteomics Core) for assistance and helpful comments on proteomics data; G. Auburger for helpful comments; and P. Emery for communicating results before publication. This work was supported by National Institute of Neurological Disorders and Stroke (R01NS059042) and Defense Advanced Research Projects Agency (DARPA) (D12AP00023). This effort was in part sponsored by DARPA; the content of the information does not necessarily reflect the position or the policy of the government, and no official endorsement should be inferred.

Supplementary Materials

www.sciencemag.org/cgi/content/full/340/6134/875/DC1
Materials and Methods
Figs. S1 to S18
Table S1
References

4 January 2013; accepted 19 March 2013
10.1126/science.1234785

A Role for *Drosophila* ATX2 in Activation of PER Translation and Circadian Behavior

Yong Zhang,^{1*} Jinli Ling,^{1,2*} Chunyan Yuan,¹ Raphaëlle Dubruille,^{1†} Patrick Emery^{1,2‡}

A negative transcriptional feedback loop generates circadian rhythms in *Drosophila*. PERIOD (PER) is a critical state-variable in this mechanism, and its abundance is tightly regulated. We found that the *Drosophila* homolog of ATAXIN-2 (ATX2)—an RNA-binding protein implicated in human neurodegenerative diseases—was required for circadian locomotor behavior. ATX2 was necessary for PER accumulation in circadian pacemaker neurons and thus determined period length of circadian behavior. ATX2 was required for the function of TWENTY-FOUR (TYF), a crucial activator of PER translation. ATX2 formed a complex with TYF and promoted its interaction with polyadenylate-binding protein (PABP). Our work uncovers a role for ATX2 in circadian timing and reveals that this protein functions as an activator of PER translation in circadian neurons.

In animals, circadian pacemakers synchronize a wide range of processes with the day-night cycle, from basic cellular metabolism to complex behaviors. These molecular clocks are composed of highly conserved transcriptional feedback loops (1). In *Drosophila*, PERIOD (PER) is a critical component of the circadian pacemaker and is under tight transcriptional and posttrans-

lational control (1). PER, with the help of TIMELESS (TIM), negatively regulates its own gene expression by displacing the dimeric transactivator CLOCK-CYCLE from its promoter (2). PER phosphorylation—regulated by several kinases (NEMO, DOUBLETIME, and Casein Kinase II) and by the phosphatase PP2A (3, 4)—controls PER stability, activity, and nuclear entry, *per* mRNA

stability and translation are also regulated (5–9). The protein TWENTY-FOUR (TYF) (9) promotes PER translation in the Pigment-Dispersing Factor (PDF)-containing small ventral lateral neurons (sLNvs), which play a particularly important role in the control of circadian behavior (10, 11). TYF binds both polyadenylate-binding protein (PABP) and eukaryotic translation initiation factor 4F (eIF4F), thus presumably promoting *per* mRNA circularization and translation. However, TYF does not appear to bind *per* mRNA directly (9).

ATAXIN-2 (ATX2) is an RNA-binding protein that is proposed to regulate translation. It in-

teracts with PABP, is found in stress granules, and in *Drosophila* has an important role in miRNA silencing (12–14). In an RNA interference (RNAi) screen aimed at identifying previously unknown regulators of circadian behavior, *Atx2* was among the genes linked to miRNA silencing that were down-regulated with long or short double-stranded RNAs (dsRNAs). The expression of these dsRNAs is controlled by Upstream Activating Sequence (UAS)-binding sites (15, 16) and can thus be activated with tissue-specific *GAL4* transgenes. When *Atx2* dsRNAs (*Atx2^{RNAi-1}*) (fig. S1A) were expressed in all circadian neurons with *tim-GAL4* (17), the period of circadian locomotor behavior under constant darkness (DD) was lengthened to ~26.7 hours (Fig. 1A and table S1). We also noticed increased arrhythmicity and lower amplitude of rhythms (table S1, “power”). These data indicate a crucial role for ATX2 in the circadian molecular pacemaker. Depletion of GW182, a protein essential for miRNA silencing (18), resulted in a distinct circadian phenotype (19), indicating that ATX2 may regulate circadian behavior independently of miRNA silencing.

Because the PDF-containing sLNvs control circadian behavior in DD (10, 11), we restricted expression of *Atx2* dsRNAs with the *pdf-GAL4* driver. The phenotype in DD was as severe as that observed with *tim-GAL4* (Fig. 1A and table S1). Furthermore, no phenotype was observed when we restricted expression of *Atx2* dsRNAs by combining *tim-GAL4* with *pdf-GAL80*, which blocks *GAL4*-mediated transcription in PDF cells (Fig. 1A and table S1) (10). To exclude off-target effects, we expressed a second dsRNA in PDF-containing circadian neurons, which targets a different region of the *Atx2* mRNA (*Atx2^{RNAi-2}*) (fig. S1A). A similar long-period phenotype was observed (Fig. 1A and table S1). Moreover, when dsRNAs were expressed with *tim-GAL4*, ATX2 was depleted in all circadian neurons examined [sLNvs, large LNvs (lLNvs), dorsal Lateral Neurons (LNDs) and Dorsal Neurons 1 (DN1s)] (Fig. 1B). The long-period phenotype was prevented by expression of a chimeric *UAS-Atx2* (*UAS-Dm/pAtx2*), in which the region targeted by one of the dsRNAs was from *D. pseudoobscura* and thus sufficiently divergent to be resistant to RNAi (Fig. 1A, fig.

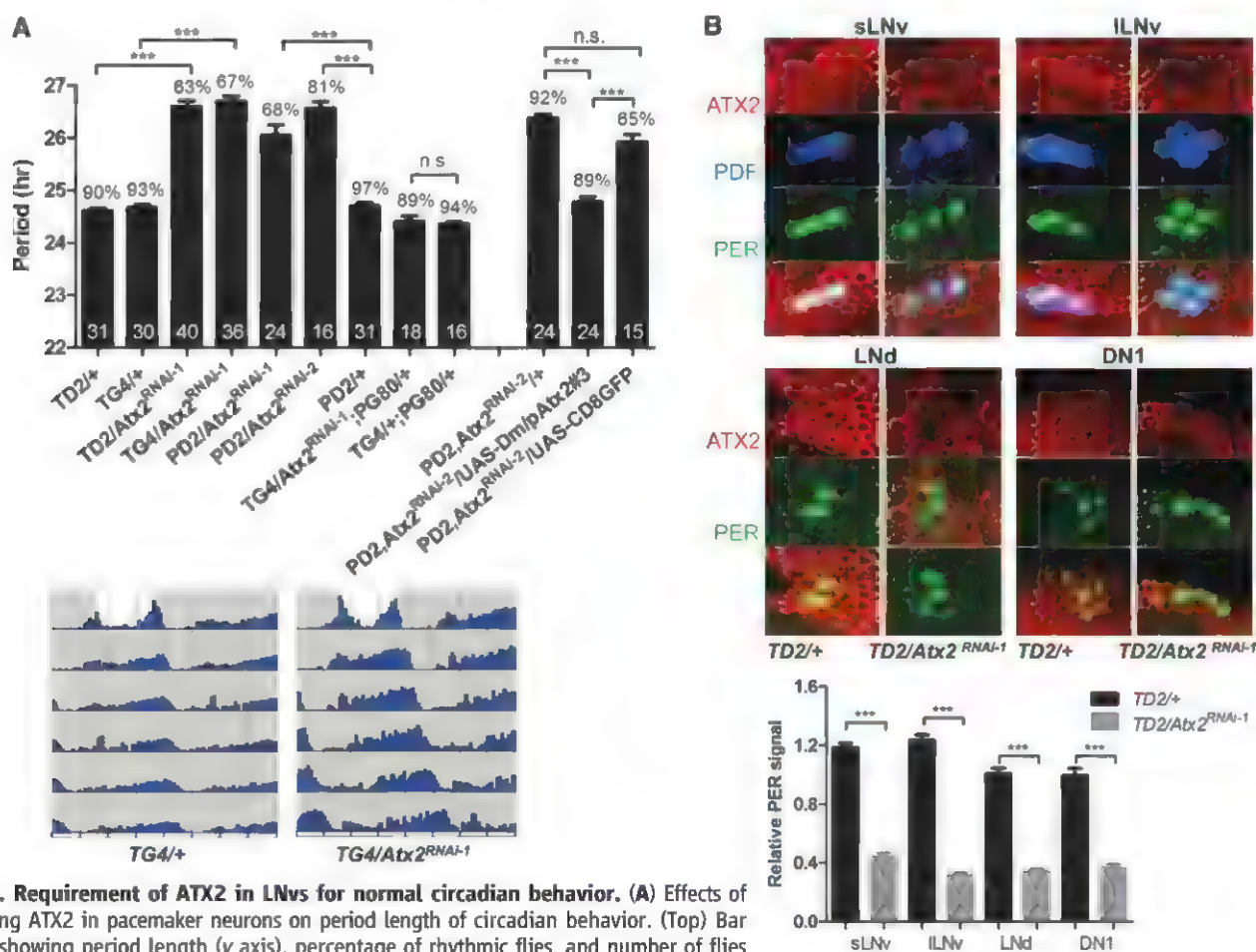


Fig. 1. Requirement of ATX2 in LNvs for normal circadian behavior. (A) Effects of depleting ATX2 in pacemaker neurons on period length of circadian behavior. (Top) Bar graph showing period length (y axis), percentage of rhythmic flies, and number of flies tested (in the bars). Error bars indicate SEM. TG4, *tim-GAL4*; TD2, *tim-GAL4,UAS-dicer2*; PD2, *pdf-GAL4,UAS-dicer2*; and PG80, *pdf-GAL80*. Dicer2 increases RNAi effects (15). (Bottom) Double-plotted actograms of control and *TG4/Atx2^{RNAi-1}* flies showing the last day of the light-dark (LD) cycle and 5 days of DD. (B) (Top) ATX2 is severely down-regulated in circadian neurons expressing *Atx2* dsRNA. Fly brains were dissected at Zeitgeber Time (ZT) 0 (ZT0 corresponds to the beginning of the light phase of the LD cycle) and immunostained with antibodies to ATX2, PER, and PDF. (Bottom) Quantification of ATX2 levels in sLNvs, lLNvs, LNDs, and DN1s. Between 11 to 20 neurons were quantified per data point. ****P* < 0.001 as determined with Tukey's multiple comparison test after one-way analysis of variance; n.s., not significant at the 0.05 level, in both (A) and (B).

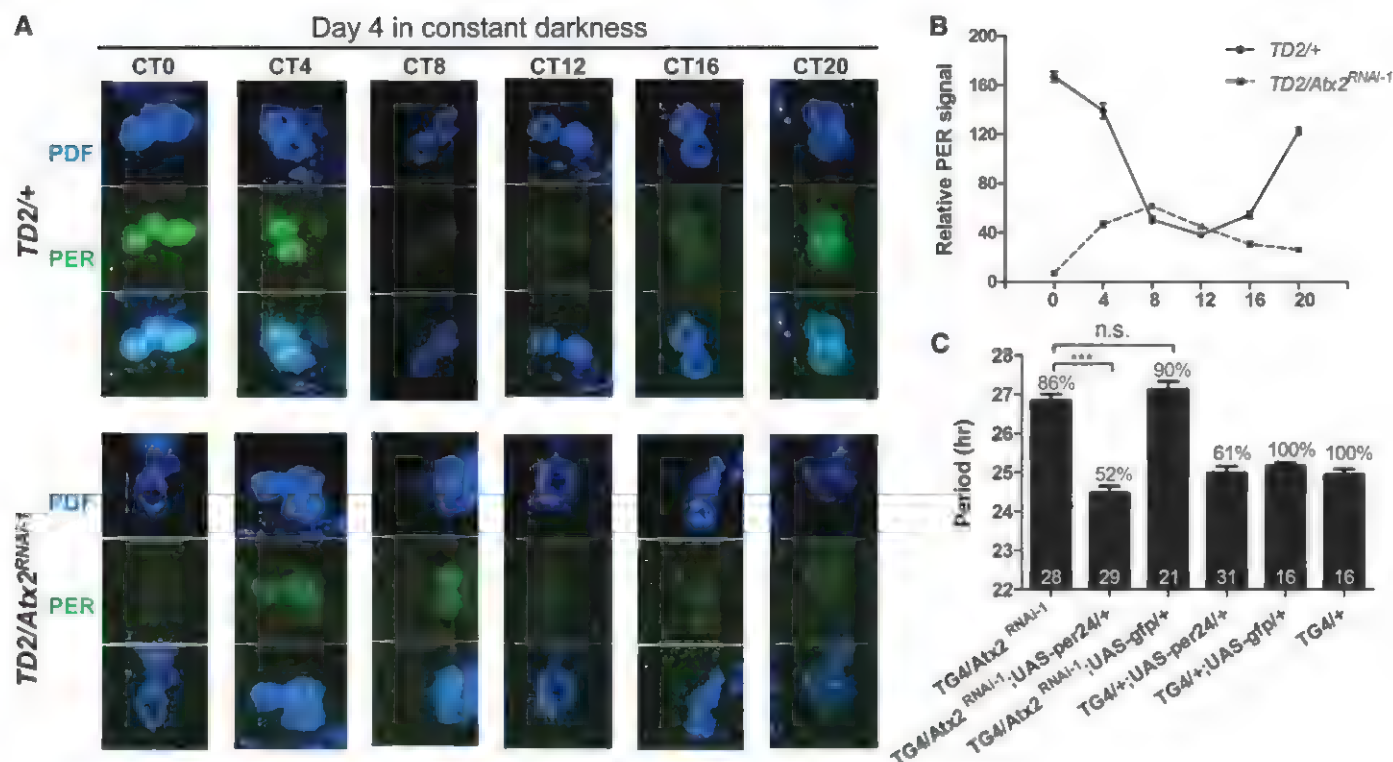
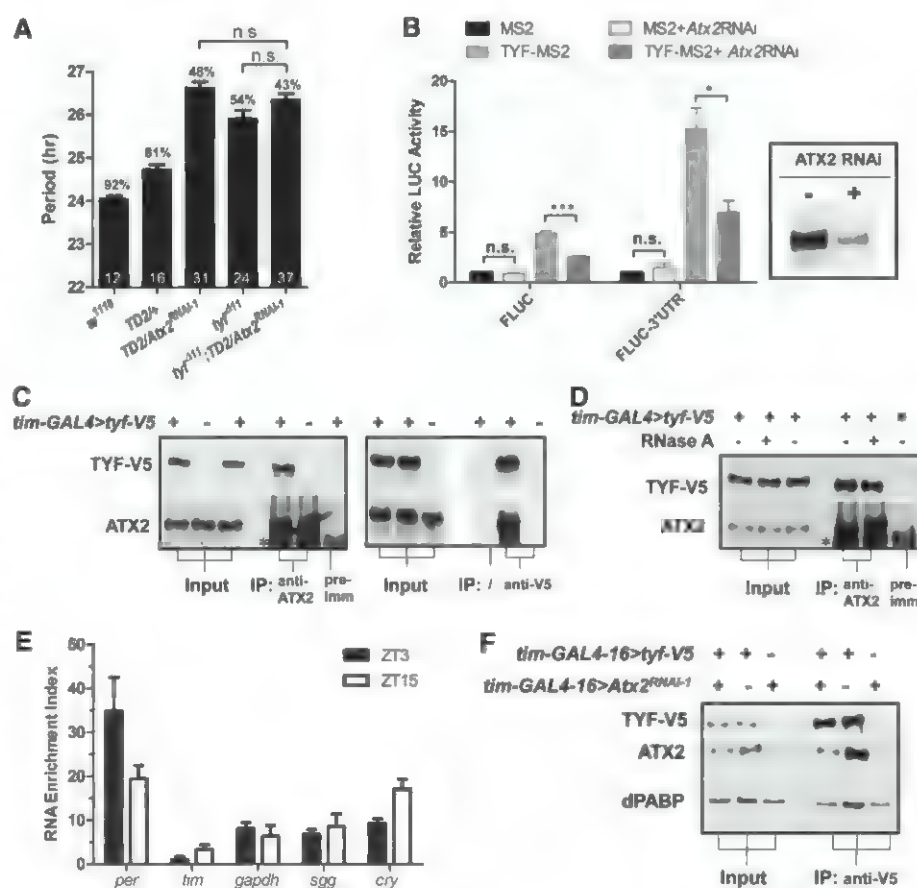


Fig. 2. Regulation of PER accumulation in sLNvs by ATX2. (A) sLNvs of brains from wild-type and *Atx2* RNAi flies, dissected at different time points (Circadian Time, CT) during the 4th day of DD and stained with antibodies to

PDF and PER. (B) Quantification of PER staining in 12 to 16 sLNvs per data point. (C) PER overexpression corrects the period-lengthening induced by means of *Atx2* knockdown. Statistics and abbreviations as in Fig. 1.

Fig. 3. Functional interaction between *Atx2* and *tyf*. (A) Effects of *Atx2* RNAi and *tyf* mutations on circadian period. Statistics and abbreviations are as in Fig. 1. (B) Requirement of ATX2 for TYF to promote *per* translation. MS2- and TYF-MS2-expression plasmids were cotransfected in *Drosophila* S₂R⁺ cells with firefly luciferase reporter plasmids (FLUC) controlled by MS2-binding sites, in the presence or absence of the *per* 3'UTR. Luciferase activity with MS2 was set to 1. dsRNAs targeting *Atx2* were added 2 days before transfection and strongly reduced ATX2 levels (see insertion). *n* = 3 biological repeats. Error bars indicate SEM. **P* < 0.05, ****P* < 0.001; n.s., not significant (*P* > 0.05) as determined with Student's *t* test with Bonferroni correction. (C) Physical association of ATX2 with TYF. Protein from head extracts of flies expressing (+) or not (–) TYF-V5 were immunoprecipitated (IP) with an antibody to ATX2 (left) or V5 (right). A serum obtained before immunization with ATX2 antigens was used as the negative control (pre-imm). Asterisk indicates cross-reacting band. (D) The association between ATX2 and TYF is resistant to ribonuclease (RNase) A treatment and thus independent of RNA. (E) Association of ATX2 with *per* and other transcripts. The RNA enrichment index (y axis) was calculated by subtracting the relative amount of RNA found “immunoprecipitated” with the preimmunization control from the relative amount found in the immunoprecipitation with the antibody to ATX2; *n* = 4 biological repeats. (F) ATX2 promotes TYF-PABP interactions. Much less PABP is coimmunoprecipitated with TYF-V5 when ATX2 is down-regulated by means of RNAi.



of RNAi.

S1A, and table S1) (20). We therefore conclude that ATX2 is required in PDF-containing sLNvs for normal circadian behavior in DD.

No obvious anatomical defects were observed in sLNvs when ATX2 was depleted (fig. S2A), but subtle developmental defects cannot be excluded. We therefore restricted expression of the dsRNAs either to development or to adulthood with GAL80^{ts}, a temperature-sensitive repressor of GAL4 (21). Flies that developed at 29°C and were transferred after eclosion to 18°C to prevent further production of *Atx2* dsRNAs behaved like control flies in DD. (fig. S2B and table S1). Thus, developmental expression of *Atx2* dsRNAs does not appear to affect circadian behavior in adult flies. On the contrary, flies that developed at 18°C and were transferred to 29°C after eclosion showed a ~1-hour increase in period (fig. S2B and table S1). The depletion of ATX2 in adults thus appears to be sufficient to lengthen circadian behavioral rhythms. The weaker effect on period as compared with that of life-long ATX2 down-regulation (Fig. 1A and table S1) may reflect less effective depletion of ATX2 in the presence of GAL80^{ts}, either because this protein still weakly represses GAL4 even at high temperature or because less time has elapsed for the sLNvs to accumulate dsRNAs. We conclude that ATX2 is required acutely in adult sLNvs.

To understand the consequences of ATX2 depletion on the circadian pacemaker, we measured abundance of PER in circadian neurons on the 4th day of DD. PER rhythms were delayed by ~8 hours in the sLNvs (Fig. 2) and in the LNds (fig. S3A) of flies with low ATX2 amounts, which is consistent with the long-period behavioral phenotype. Unexpectedly, in the DN1s peak PER concentrations were not delayed, although its minimum concentrations were (fig. S3A). The reason for this partial delay in DN1s is not clear. Amounts of PER in the sLNvs were low (Fig. 2) but close to normal in the DN1s and the LNds (fig. S3A). Amounts of TIM were not affected in any of these neurons (fig. S3B). Low abundance of PER appeared to be sufficient to explain the long-period phenotype because overexpression of PER restored normal period length in flies with depleted ATX2 (Fig. 2C).

The long-period phenotype, increased behavioral arrhythmicity, and low abundance of PER in the sLNvs are reminiscent of the phenotypes observed in *tyf* mutant flies (9). To determine whether ATX2 and TYF might work together in the circadian cycle, we tested double loss-of-function mutants. The double-mutants showed no additive effects compared with the single mutants (Fig. 3A), which indicates that ATX2 and TYF regulate the same step of the circadian cycle: PER translation.

TYF does not bind RNA on its own. Thus, to assay TYF's translational activity in cell culture, TYF was fused to the MS2 RNA-binding protein, and MS2-binding sites were placed in the 3' untranslated region (3'UTR) of a luciferase reporter gene (9). MS2-TYF promoted luciferase expression, and this transactivation was increased

in the presence of *per* 3'UTR sequences (Fig. 3B), as previously reported (9). If ATX2 was depleted with dsRNAs, TYF transactivation was decreased (Fig. 3B). However, basal luciferase expression was unaffected. We therefore conclude that TYF requires ATX2 to promote PER translation.

To further test cooperative action of ATX2 and TYF to regulate PER translation, we determined whether they form a complex in vivo. We overexpressed a V5-tagged TYF and either isolated TYF complexes with an antibody to V5 or immunoprecipitated endogenous ATX2 with a polyclonal antibody to this protein. In both cases, ATX2 and TYF coimmunoprecipitated (Fig. 3C). Moreover, the ATX2-TYF complexes were resistant to RNase A treatment (Fig. 3D). Because TYF is associated with *per* mRNA, we tested whether ATX2 is also associated with *per* mRNA. We immunoprecipitated ATX2 and found *per* mRNA to be enriched in ATX2 immunoprecipitates compared with that of the control (Fig. 3E and fig. S4A). Although TYF appears to bind *per* mRNAs preferentially (9), ATX2 also associated with other mRNAs. Thus, how TYF is specifically recruited to *per* mRNAs remains unclear. A rhythm in ATX2-*per* mRNA complex formation was observed. It appears to be largely driven by mRNA abundance rhythms (fig. S4, B and C).

TYF interacts with PABP and eIF4F (9). Because ATX2 also binds to PABP (12), we tested whether ATX2 contributes to the formation of a stable TYF complex that bridges eIF4F and PABP and thus stimulates PER translation through mRNA circularization (22). We immunoprecipitated TYF-V5 with an antibody to V5 from whole-head extracts of control flies, or from heads of flies expressing *Atx2* dsRNAs (Fig. 3F). Depletion of ATX2 reduced the amount of both ATX2 and PABP in the V5-TYF immunoprecipitate. Thus, ATX2 is necessary for the formation of a stable complex between TYF and PABP (fig. S5).

Our results implicate ATX2 in the control of circadian rhythms as a critical activator of PER translation. They support the emerging notion that translational control is critical for the function of circadian pacemaker neurons (8, 9). Our results also emphasize that ATX2 can function as a translational activator as well as a translational repressor (12–14). Whether ATX2 functions as an activator or repressor may depend on the combination of proteins associated with a specific mRNA. In the case of *per*, ATX2's association with TYF might explain its positive effect on PER translation.

In humans, extension of ATAXIN-2's Poly-Q stretch to pathological lengths is responsible for spinocerebellar ataxia and is associated with increased risk of amyotrophic lateral sclerosis (23, 24). Patients affected with spinocerebellar ataxia, and even asymptomatic carriers of a pathological *Atx2* allele, suffer from sleep disruption, particularly disruption of rapid eye movement (REM) sleep (25–28), which is under circadian regulation (29, 30). Decreased ATX2 activity in

the circadian clock perhaps contributes to these sleep disorders.

References and Notes

- W. Yu, P. E. Hardin, *J. Cell Sci.* **119**, 4793 (2006).
- J. S. Menet, K. C. Abruzzi, J. Desrochers, J. Rodriguez, M. Rosbash, *Genes Dev.* **24**, 358 (2010).
- H. W. Ko et al., *J. Neurosci.* **30**, 12664 (2010).
- S. Sathyanarayanan, X. Zheng, R. Xiao, A. Sehgal, *Cell* **116**, 603 (2004).
- W. V. So, M. Rosbash, *EMBO J.* **16**, 7146 (1997).
- V. Suri, A. Lanjuin, M. Rosbash, *EMBO J.* **18**, 675 (1999).
- R. Stanewsky, K. S. Lynch, C. Brandes, J. C. Hall, *J. Biol. Rhythms* **17**, 293 (2002).
- S. Bradley, S. Narayanan, M. Rosbash, *Genetics* **192**, 943 (2012).
- C. Lim et al., *Nature* **470**, 399 (2011).
- D. Stoleru, Y. Peng, P. Nawatthan, M. Rosbash, *Nature* **438**, 238 (2005).
- S. C. P. Renn, J. H. Park, M. Rosbash, J. C. Hall, P. H. Taghert, *Cell* **99**, 791 (1999).
- T. F. Satterfield, L. J. Pallanck, *Hum. Mol. Genet.* **15**, 2523 (2006).
- C. McCann et al., *Proc. Natl. Acad. Sci. U.S.A.* **108**, E655 (2011).
- U. Nonhoff et al., *Mol. Biol. Cell* **18**, 1385 (2007).
- G. Dietzl et al., *Nature* **448**, 151 (2007).
- J. Q. Ni et al., *Nat. Methods* **8**, 405 (2011).
- M. Kaneko, J. H. Park, Y. Cheng, P. E. Hardin, J. C. Hall, *J. Neurobiol.* **43**, 207 (2000).
- A. Eulalio, F. Tritschler, E. Izaurralde, *RNA* **15**, 1433 (2009).
- Y. Zhang, P. Emery, *Neuron* **78**, 152 (2013).
- C. C. Langer, R. K. Ejsmont, C. Schönbauer, F. Schnorrer, P. Tomancak, *PLoS ONE* **5**, e8928 (2010).
- S. E. McGuire, Z. Mao, R. L. Davis, *Sci. STKE* **2004**, 6pl (2004).
- N. Sonenberg, A. G. Hinnebusch, *Cell* **136**, 731 (2009).
- I. Lastres-Becker, U. Rüb, G. Auburger, *Cerebellum* **7**, 115 (2008).
- A. C. Elden et al., *Nature* **466**, 1069 (2010).
- L. Velázquez-Pérez et al., *Neurodegener. Dis.* **8**, 447 (2011).
- R. Rodríguez-Labrada et al., *Mov. Disord.* **26**, 347 (2011).
- I. Tuin et al., *Neurology* **67**, 1966 (2006).
- S. M. Boesch et al., *Mov. Disord.* **21**, 1751 (2006).
- D.-J. Dijk, C. A. Zeisler, *J. Neurosci.* **15**, 3526 (1995).
- M. L. Lee, B. E. Swanson, H. O. de la Iglesia, *Curr. Biol.* **19**, 848 (2009).

Acknowledgments: We thank D. Wentworth and D. Szydak for technical assistance; the Allada lab for communicating results before publication and for fly stocks and plasmids; M. Moore and her lab, as well as M. Ramaswami for helpful discussions and reagents; D. Weaver for critical reading of our manuscript; M. Rosbash for PER and PDF antibodies; N. Sonenberg for PABP antibody; the Vienna *Drosophila* RNAi Center (VDRC) for *Atx2* RNAi lines; R. Stanewsky for fly stocks; the *Drosophila* Genomics Research Center for the *Atx2* cDNA; and the Developmental Studies Hybridoma Bank for PDF antibodies. This work was supported by R01 grants GM66777, GM79182, and GM100091 to P.E.

Supplementary Materials

www.sciencemag.org/cgi/content/full/340/6134/879/DC1
Materials and Methods
Figs. S1 to S5
Table S1
References (31–40)

3 January 2013; accepted 19 March 2013
10.1126/science.1234746

3-D CELL CULTURE

Bio-Assembler Kits utilize magnetic levitation to culture cells in 3-D. Available in single-, six-, and 24-well configurations, the kits supply magnetic drivers, low-binding dishes/plates, and Nanoshuttle-PL solution in quantities and volumes appropriate for the kit's size. Nanoshuttle-PL solution delivers magnetic nanoparticles to cells. The magnetic driver that nests on top of the dish/plate then levitates the cells to create a 3-D environment. Using the Bio-Assembler Kits is as easy as performing standard 2-D cell culture plating and propagation. Culturing cells in 3-D facilitates rapid formation of floating yet connected scaffold-like structures with cell-cell interactions, thus providing a more accurate representation of tissue functionality *in vivo*. The process is compatible with virtually any cell type, including primary and stem cells, with any media type, with standard culturing protocols and diagnostic techniques, and is applicable to invasion studies and tissue engineering.

MIDSCI

For info: 800-227-9997 | www.midsci.com



BIOLOGICAL SAMPLE CARD PUNCHING

The easyPunch STARlet workstation is the first fully automated system integrating sample card punching and liquid handling into one easy workflow. The easyPunch STARlet system seamlessly integrates punching of GE Healthcare Whatman FTATM and DMPK sample collection cards with automated sample extraction, eliminating common bottlenecks in laboratory processes. The system minimizes human error and enables high throughput sample preparation for a variety of applications, such as forensic reference databasing, preclinical and clinical drug metabolism and pharmacokinetics (DMPK) studies, and toxicology studies. The easyPunch workstation is based on the Hamilton Robotics Microlab STARlet platform and features two special modules and robotic arms for transporting and punching paper cards. The samples are monitored by powerful tracking software to eliminate any chance of sample identification errors. The entire process is tracked using imaging recognition. Hamilton's proprietary software, based on industrial machine vision technology, provides complete control and monitoring of the punching process.

Hamilton Robotics

For info: 800-648-5950 | www.hamiltonrobotics.com

PROTEIN A ANTIBODY PURIFICATION BEADS

Magne Protein A Beads are designed for the purification of monoclonal and polyclonal antibodies from a range of diverse sources. These paramagnetic affinity beads offer a convenient method for achieving high purity and high recovery of immunoglobulins (Igs) from cell culture, ascites, and serum samples. They may also be used for high throughput antibody purification; antibody purification and concentration from small-volume or dilute source material; and for immunoglobulin depletion. Magne Protein A Beads are composed of iron encapsulated by macroporous cellulose, which results in low nonspecific binding and high-quality purification. Novel attachment chemistry is used to immobilize recombinant Protein A protein molecules all in the same orientation on the bead's surface. This orientation of attachment improves the functionality of the immobilized proteins. The beads' highly magnetic properties allow ease of handling as well as rapid and efficient protein capture, and can be used with a variety of magnetic stands.

Promega

For info: 608-274-4330 | www.promega.com/magne

CRYOPRESERVATION REAGENTS

HyClone HyCryo and HyCryo-STEM cryopreservation media enable researchers to maximize the preservation, recovery, and growth of post-thaw cells for general cell culture and stem cell applications. The new HyCryo media is a serum-free, animal component-free product intended for cryogenic preservation and storage of standard cell lines. Animal component-free assures the media is free of any human or animal nonhuman components to deliver better sample integrity and adaptability. Designed specifically for stem cell applications, HyCryo-STEM enhances cell recovery and post-thaw growth of pluripotent stem cells and neural progenitor cells. The serum-free formulation maintains differentiation potential and minimizes spontaneous differentiation of stem cells. HyCryo and HyCryo-STEM are designed to easily integrate into a researcher's existing cell culture workflow and processes. Researchers can simply add the HyCryo cryopreservation media directly to prepared cells and transfer to a Thermo Scientific Nunc Cryovial for sample integrity during freezing and long-term storage.

Thermo Fisher Scientific

For info: 800-766-7000 | www.thermofisher.com

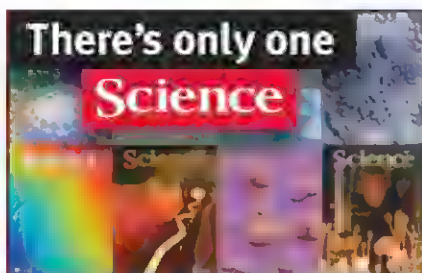
CORE-SHELL MEDIA

With the smallest diameter in the Kinetex family, the 1.3 μm UHPLC column delivers measurably better performance than conventional fully porous media on UHPLC equipment. The Kinetex core-shell family now includes four particle sizes, from 1.3 to 5 μm , providing separation solutions for virtually every chromatographic application and easy method transferability from UHPLC to HPLC to preparative-scale LC. With efficiency levels over 400,000 plates per meter, the Kinetex 1.3 μm represents a dramatic advancement in LC media technology. UHPLC users can now reach previously unavailable levels of sensitivity and performance, with the added benefit of easy method transferability and scalability to any of the three other Kinetex particle sizes. While fully porous sub-2 μm columns exhibit significant band broadening due to frictional heating as flow rate increases, the Kinetex particle morphology and packing technology help to reduce these and other effects to ensure high resolution and sensitivity over an extended linear velocity.

Phenomenex

For info: 310-212-0555 | www.phenomenex.com

Electronically submit your new product description or product literature information! Go to www.sciencemag.org/products/newproducts.dtl for more information. Newly offered instrumentation, apparatus, and laboratory materials of interest to researchers in all disciplines in academic, industrial, and governmental organizations are featured in this space. Emphasis is given to purpose, chief characteristics, and availability of products and materials. Endorsement by *Science* or AAAS of any products or materials mentioned is not implied. Additional information may be obtained from the manufacturer or supplier.



Science Careers Advertising

For full advertising details, go to ScienceCareers.org and click For Employers, or call one of our representatives.

Tracy Holmes

Worldwide Associate Director
Science Careers
Phone: +44 (0) 1223 326525

THE AMERICAS

E-mail: advertise@sciencecareers.org
Fax: 202-289-6742

Tina Burks

East Coast/West Coast/South America
Phone: 202-326-6577

Marci Gallun

Midwest/Canada
Phone: 202-326-6582

Candice Nulsen

Corporate
Phone: 202-256-1528

Online Job Posting Questions

Phone: 202-312-6375

EUROPE / INDIA / AUSTRALIA / NEW ZEALAND / REST OF WORLD

E-mail: ads@science-int.co.uk
Fax: +44 (0) 1223 326532

Axel Gesatzki

Phone: +44 (0)1223 326529

Lucy Nelson

Phone: +44 (0)1223 326527

Kelly Grace

Phone: +44 (0) 1223 326528

JAPAN

Yuri Kobayashi

Phone: +81-(0)90-9110-1719
E-mail: ykobayas@aaas.org

CHINA / KOREA / SINGAPORE / TAIWAN / THAILAND

Ruolei Wu

Phone: +86-1367-1015-294
E-mail: rwu@aaas.org

All ads submitted for publication must comply with applicable U.S. and non-U.S. laws. Science reserves the right to refuse any advertisement at its sole discretion for any reason, including without limitation for offensive language or inappropriate content, and all advertising is subject to publisher approval. Science encourages our readers to alert us to any ads that they feel may be discriminatory or offensive.



ScienceCareers.org



TEXAS TECH UNIVERSITY
Health Sciences Center
Paul L. Foster School of Medicine

Assistant or Associate Professors Center of Excellence in Diabetes and Obesity Research

The Department of Biomedical Sciences and the Center of Excellence in Diabetes and Obesity at the Paul L. Foster School of Medicine, Texas Tech University Health Sciences Center, El Paso, Texas are seeking candidates for tenure track faculty positions at the Assistant or Associate Professor level. This is part of a state-funded initiative to enhance research in diabetes and obesity in the US/Mexico border region. The Center is primarily interested in investigators with research interests in diabetes and obesity. Successful candidates are expected to maintain independently funded research programs in obesity and diabetes or a related field. The positions will report to the Chair of the Department of Biomedical Sciences until such time as a Director of the Center of Excellence is identified.

Minimum qualifications: M.D./D.O./Ph.D. in a field related to diabetes/obesity research from an accredited institution of higher education. Minimum 3 years of postdoctoral experience, and a strong publication record.

Preferred qualifications: Candidates with experience in diabetes/obesity research and experience in using the latest technology preferred. Funded grant support in an area of basic, clinical, or translational research is preferred. Regional or emerging reputation in the area of diabetes and obesity research for consideration at the rank of Associate Professor. Interest in assisting with the development of a new Graduate School of Biomedical Sciences strongly preferred. Access to graduate students will depend on development of a successful training program, and we look to the candidates to participate in the development of the program. A willingness to start something new, and to help a new institution to grow and develop, is also a strongly desired characteristic. Good communication skills and demonstrated ability to work in a collegial environment are essential.

The Center will provide start-up funds. Interested candidates must apply online at <http://jobs.texas-tech.edu>, requisition #84742. A curriculum vitae, short write up of research interests and three references may be attached and sent to: **Rajkumar Lakshmanaswamy, Ph.D., rajkumar.lakshmanaswamy@ttuhsc.edu, Interim Chair, Department of Biomedical Sciences.** The position is open until filled. Application review will begin immediately.

*Texas Tech University Health Sciences Center is an
Equal Opportunity/Affirmative Action Employer.*

Boston University School of Medicine

Boston University School of Medicine welcomes applications for its departments below at ranks of Instructor, Assistant & Associate Professor, or Professor.

- Anatomy & Neurobiology
- Biochemistry
- Microbiology
- Physiology & Biophysics
- Pharmacology & Experimental Therapeutics
- Pathology

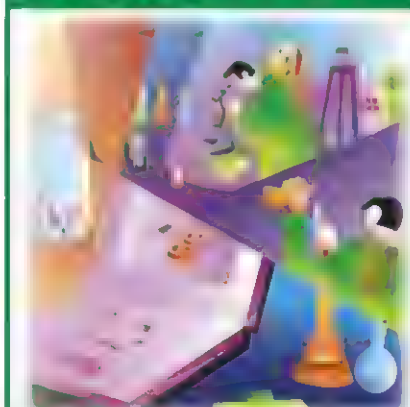
Email a cover letter specifying your department of interest with your CV to busrmdean@bu.edu.

Boston University is an equal opportunity and affirmative action employer



www.bumc.bu.edu

CAREER Running TRENDS Your Lab



Download your free copy today at
ScienceCareers.org/running



Brought to you by the
AAAS/Science Business Office

Institut national de la recherche scientifique (INRS) is a research-intensive university offering graduate-level training. One of Canada's leading research universities in terms of grants per professor, INRS brings together some 150 professors and close to 700 students and post-doctoral fellows in its centers in Montreal, Quebec City, Laval, and Varennes. Conducting fundamental research essential to the advancement of science in Quebec as well as internationally, INRS research teams also play a critical role in developing concrete solutions to problems facing our society.

The Centre Énergie Matériaux Télécommunications of INRS is currently seeking a

PROFESSOR-RESEARCHER

ULTRAFAST MATERIALS CHARACTERIZATION

(Tenure-track position – Research Chair – Tier II)

The areas of expertise aimed at, but not limited to, are: time-resolved electron microscopy, electron microscopy, ultrafast electron diffraction, ultrafast characterization of materials, ultra-fast lasers and photonics and their applications in materials science for various areas such as, for example, biomedical and energy.

The candidate should be able to establish collaborations with research teams already in place, while developing or maintaining partnerships with groups outside the Centre. The ability to develop partnerships with companies is particularly valuable.

This position is incorporated within an environment where about forty professors-researchers undertake leading-edge research and training in diverse fields of sustainable energy, advanced materials, ultrafast photonics, telecommunication systems and nanobiotechnology.

The Centre hosts unique major research infrastructure including the Advanced Laser Light Source and the Laboratory of Micro and Nanofabrication, comprising the Infrastructure of Nanostructures and Femtoscience (<http://lmn.emt.inrs.ca/EN/inf.htm>).

This new position is intended to lead a recent major **\$15M** addition, the Infrastructure for Advanced Imaging (IAI), which consists of a time-resolved electron microscope awarded by the Canada Foundation for Innovation (CFI) in the 2012 competition. **This microscope will be unique worldwide.**

REQUIREMENTS:

- Doctorate in a relevant discipline (physics, materials science, engineering, chemistry).
- An outstanding record of research accomplishments that will enable her/him to successfully develop a strong independent research program.
- The aptitude for teaching and supervising graduate students and other trainees.
- The ability to work in a multidisciplinary team and within research networks.
- The ability to collaborate with industrial partners.

We actively seek an outstanding candidate who is eligible to be nominated for a Tier II Canada Research Chair.

Potential sources of funding include the Natural Sciences and Engineering Research Council of Canada (NSERC) and the Fonds de recherche du Québec – Nature et technologies (FQRNT).

The Centre is located in Varennes, on the South Shore of Montreal.

The working language of INRS is French. Candidates whose native language is not French are encouraged to apply. The Centre will provide them with all the resources necessary to facilitate their learning of the French language.

Salary and benefits are in accordance with the current collective agreement at INRS.

Interested candidates should submit a full curriculum vitae by e-mail and registered mail, a statement of research interests (max. 3 pages), a statement of teaching philosophy, a copy of their three most representative publications, and the name and coordinates of three references, before **July 15th, 2013**, indicating competition number **DS 13-05** to:

Dr. Federico Rosei, Director, Centre Énergie Matériaux Télécommunications
1650, boul. Lionel-Boulet, Varennes (Québec) J3X 1S2
rosei@emt.inrs.ca

INRS is committed to equity in employment and diversity.

INRS welcomes applications from indigenous people, visible minorities, ethnic minorities, persons with disabilities, women, persons of minority sexual orientations. Priority is given to Canadian citizens and residents.

Currently, we plan to hold interviews at the end of August and/or beginning of September 2013.

There's only one DR. SHIRLEY MALCOM



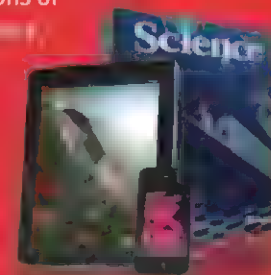
The launch of the Soviet satellite Sputnik in 1957, which seemed even less likely than the launch of the Soviet's Sputnik. But with Sputnik's success, the Space Race officially started and, in an instant, brought a laser-like focus to science education and ways to deliver a proper response. Not long after, Dr. Malcom entered the picture.

Although black schools at the time received fewer dollars per student and did not have sufficient resources to maintain their labs at a level equivalent to the white schools, Dr. Malcom found her way to the University of Washington where she succeeded in obtaining a B.S. in spite of the difficulties of being an African American woman in the field of science. From there she went on to earn a Ph.D. in ecology from Penn State and held a faculty position at the University of North Carolina, Wilmington.

Dr. Malcom has served at the AAAS in multiple capacities, and is presently Head of the Directorate for Education and Human Resources Programs. Nominated by President Clinton to the National Science Board, she also held a position on his Committee of Advisors on Science and Technology. She is currently a member of the Caltech Board of Trustees, a Regent of Morgan State University, and co-chair of the Gender Advisory Board of the UN Commission on Science and Technology for Development. She has held numerous other positions of

Of her active career in science, Dr. Malcom says, "I guess I have become a poster child for taking one's science background and using that in many other ways: we ask questions; we try to understand what we find; we consider what evidence we would need to confirm or refute hypotheses. And that happens in whatever setting one finds oneself."

For more information on the many opportunities available in science, visit ScienceCareers.org for forums, job postings, and more — all for free. Visit *Science* today at ScienceCareers.org.



For your career in science, there's only one **Science**



ScienceCareers.org

Faculty Positions in Emerging Infectious Diseases
– Principal Investigators (2 positions) –

Duke-NUS Graduate Medical School Singapore (Duke-NUS) is a strategic collaboration between Duke University (US) and the National University of Singapore. Duke-NUS is unique in bringing post-baccalaureate, research-intensive medical education to Asia. The Program in Emerging Infectious Diseases (EID) led by Professor Linfa Wang has the mission to conduct cutting-edge infectious diseases research that will enhance healthcare in Singapore and the region. The program has a strong core of researchers working on virus structure by cryo-EM, virus protein structure, virus-host interactions, pathogenesis mechanisms, innate immune response to viral infection, experimental therapeutics, antiviral clinical trials, epidemiology and pathogen discovery.

The EID Program is recruiting **TWO** principal scientists in any area of emerging infectious diseases. Scientists are encouraged to apply to fill tenure track faculty positions at the Assistant or Associate Professor level. The packages will include full salary and generous start-up for five years. Areas of current focus for the program include dengue, influenza, hepatitis and zoonotic diseases (www.duke-nus.edu.sg).

For further information, please contact the search committee co-chairs:

- **Professor Subhash Vasudevan** (subhash.vasudevan@duke-nus.edu.sg)
- **Professor Mariano Garcia-Blanco** (m.garciablanca@duke.edu)

Interested candidates should send a full application with CV and the names of three referees via email to: eid.search@duke-nus.edu.sg by 30th Jun 2013.

Transforming Medicine, Improving Lives

Partner in
Academic Medicine:  SingHealth

EMBL EBI and Wellcome Trust Sanger Institute share the Wellcome Trust Genome Campus near Cambridge. This proximity fosters close collaborations and contributes to an international and vibrant campus environment.

ESPOD fellowships

Call for applications 2013

The EMBL-EBI – Sanger Postdoctoral (ESPOD) Programme builds on the strong collaborative relationship between the two institutes, offering projects which combine experimental (wet lab) and computational approaches.

Select from pre-defined projects:

- Creating phenotype variation through epigenetics: DNA methylation variability in populations and individual cells
- Comparative genomic insights into parasite genome function
- Functional characterisation of Plasmodium kinase regulatory networks
- Genes, pathways, modules and organs that regulate bone mass

For further information on the ESPOD fellowships and how to apply please visit www.embl.ac.uk/research/postdocs/espods

Closing date: 26 July 2013

www.embl.org/jobs



Director Position

Institute of Biological Chemistry
Academia Sinica, Taiwan

Academia Sinica, Taiwan, invites applications and nominations for the position of Director of the Institute of Biological Chemistry (IBC). The initial appointment is for a period of three years (renewable for a second term) starting 15th August 2014. The director will also carry the title of Distinguished Research Fellow.

As the pre-eminent academic research institute in Taiwan, Academia Sinica is devoted to basic and applied research in mathematics and physical sciences, life sciences, and humanities and social sciences. IBC consists of 26 laboratories, focusing on two integrated research themes: structural basis of protein functions and drug design, and biochemical basis of post-translational regulation and cell signaling network. The institute is well funded and equipped with modern research facilities managed by experienced research specialists. It also maintains a high research standard with a high-quality publication record. For details about IBC, please see <http://www.bc.sinica.edu.tw/>

Interested candidates should have a PhD or equivalent degree, with outstanding research accomplishments and demonstrated leadership ability. Besides pursuing an internationally recognized research program at IBC, the successful candidate is also expected to provide intellectual leadership to the institute.

Applications and nominations, including a cover letter listing 3 to 5 names of references, and a complete curriculum vitae (prepared in English) with ten representative publications highlighted, should be sent to **Ms. Cathy Wang, Institute of Biological Chemistry, Academia Sinica, 128 Academia Road, Section 2, Nankang, Taipei 115, Taiwan** or by Email to cathyw@gate.sinica.edu.tw before 1st September 2013. Screening of application/ nominations will begin immediately, and will continue until the position is filled.



MISSOURI BOTANICAL GARDEN

Career opportunity with one of the top botanical gardens in the world

Senior Vice President, Science and Conservation

Summary of the position: The Senior Vice President of Science and Conservation is responsible for providing Science leadership in support of the Garden across multiple domestic and international locations. Responsible for leading the definition, development, and implementation of the Garden's scientific and conservation strategy and business plans to support the Garden's strategic plan. This role ensures that science and conservation initiatives function proactively to support the organization to achieve its objectives. Leads, develops and motivates an effective and professional research team. The Senior Vice President promotes the Garden's role in science and conservation to internal and external global audiences.

Qualifications and/or Experience:

- PhD Botany, Biology or related field required.
- Documented scientific record with a minimum of ten (10+) years scientific leadership experience and publication record.
- Demonstrated abilities in successful grant writing, fundraising, negotiating and managing budgets, and advanced understanding of financial operations.
- Minimum ten (10+) years relevant and increasingly responsible management responsibilities at an executive level, and with a proven track record in strategic business planning.
- Prior experience working in a non-profit or research and learning environment desired.

Supervisory Responsibilities: Directly and indirectly manages a team of 115 staff and scientific managers.

For more information, and to apply on-line please visit our website.

Link to comprehensive posting: http://www.mobot.org/jobs/mbgjobs_mrl.asp#M011

Missouri Botanical Garden Website: <http://www.mobot.org>

E-mail: recruiting@mobot.org

The Missouri Botanical Garden is an Equal Opportunity/Affirmative Action Employer



AAAS is here – helping scientists achieve career success.

Every month, over 400,000 students and scientists visit ScienceCareers.org in search of the information, advice, and opportunities they need to take the next step in their careers.

A complete career resource, free to the public, *Science Careers* offers a suite of tools and services developed specifically for scientists. With hundreds of career development articles, webinars and downloadable booklets filled with practical advice, a community forum providing answers to career questions, and thousands of job listings in academia, government, and industry, *Science Careers* has helped countless individuals prepare themselves for successful careers.

As a AAAS member, your dues help AAAS make this service freely available to the scientific community. If you're not a member, join us. Together we can make a difference.

To learn more, visit aaas.org/plusyou/sciencecareers



Science Careers is the forum that answers questions.



Science Careers is dedicated to opening new doors and answering questions on career topics that matter to you. With timely feedback and a community atmosphere, our careers forum allows you to connect with colleagues and experts to get the advice and guidance you seek as you pursue your career goals.

Science Careers Forum:

- » Relevant Career Topics
- » Timely Advice and Answers
- » Community, Connections, and More!

Visit the forum and join the conversation today!



Your Future Awaits.



ScienceCareers.org



The City
University
of
New York

PROFESSOR & DIRECTOR OF STRUCTURAL BIOLOGY Advanced Science Research Center

The Advanced Science Research Center (ASRC) at the City University of New York seeks a dynamic and innovative scientist with demonstrated leadership and research accomplishments in structural biology to serve as Professor and Director of Structural Biology. The position will be a tenured or tenure-track faculty member and program administrator. The successful candidate will be expected to teach, oversee the structural biology program and lead researchers in collaborative projects and activities; attract external funding; and ensure compliance with federal research guidelines and University policies. Applicants must be accomplished and respected researchers in structural biology with a solid record of scholarly activities, and possess appropriate credentials for a senior faculty appointment at one of the CUNY colleges. Preference will be given to those whose research utilizes NMR spectroscopy and with experience in building and/or overseeing an NMR facility. There is also an opportunity to recruit new faculty into related areas in structural biology. Exceptional candidates may be appointed as a Distinguished and/or Einstein Professor.

The ASRC is a 200,000 sq. ft. science facility located at 85 St. Nicholas Terrace (close to 133rd Street) on the south campus of CUNY's City College and adjacent to the New York Structural Biology Center. Construction of the ASRC is well underway and due for completion in 2014. The innovatively designed center is a University-wide science enterprise that builds on the strengths CUNY has developed in five distinct but interconnected disciplines, Nanoscience, Photonics, Structural Biology, Neuroscience and Environmental Sciences. The center will be the nucleus of an integrated research network and will provide core facilities for CUNY scientists with the goal of fostering interdisciplinary research. To learn more about the ASRC visit www.asrc.cuny.edu

Minimum Qualifications: Ph.D. degree in area(s) of experience or equivalent required. Other Qualifications: - Ph.D. in structural biology or closely related biomedical or life science area required; Experience using NMR spectrometers and managing an NMR facility

To Apply: Go to the CUNY website at <http://www.cuny.edu/employment.html> to see the complete job posting and qualification requirements. Click on Search Job Listings under the Career Positions Available section of the page; then click Faculty under the Employment Opportunities section; then look for the Job Posting Title and Job ID #8026. Submit a letter of interest, current curriculum vitae, summary of research interests/expertise area, a teaching statement, and the contact information for at least three professional references as One Document in the Resume Field Application reviews begin May 13, 2013. Compensation is commensurate with qualifications and experience.

The City University of New York (CUNY) is an EO/AA Employer.



UNIVERSITY OF
CAMBRIDGE

A world of opportunities

www.cam.ac.uk/jobs/

Professorships in the Sainsbury Laboratory

The Board of Electors invite applications for a Professorship in the Sainsbury Laboratory. In addition, the University hopes soon to be in a position to elect to a further Professorship, also to be based in the Sainsbury Laboratory.

Candidates for both posts will have an outstanding research record of international stature of relevance to plant developmental biology and the vision, leadership, experience and enthusiasm to build on current strengths in maintaining and developing a leading research presence. They will hold a PhD or equivalent postgraduate qualification.

Standard professorial duties include teaching and research, examining, supervision and administration. The Professor will be based in Cambridge. A competitive salary will be offered.

Further information is available at:

www.admin.cam.ac.uk/offices/academic/secretary/professorships/ or contact the Academic Secretary, University Offices, The Old Schools, Cambridge, CB2 1TT, (email: ibise@admin.cam.ac.uk), to whom a letter of application should be sent, together with details of current and future research plans, a curriculum vitae, a publications list and form CHRIS/6 (parts 1 and 3 only) with details of two referees, so as to reach him no later than 20 June 2013.

Informal enquiries may be made to Professor Ottoline Leyser, Director of the Sainsbury Laboratory.

The University is committed to Equality of Opportunity.

POSITIONS OPEN

POSTDOCTORAL POSITIONS—IMMUNOLOGISTS and a staff scientist or research associate in transgenic mice. Recent Ph.D. graduates in immunology (<three years postdoctoral experience) with a publication record to join a dynamic group of researchers in the laboratories of **Drs. Yang Liu** and **Pan Zheng** at Children's National Medical Center, Washington, DC to study the metabolic and/or tumor immunology. A Research Associate or Staff Scientist will set up CRISPR/Cas-Mediated Genome Engineering and thus require independent skills in transgenic mice. *Children's National is an Equal Opportunity Employer and offers a competitive compensation and benefits package.* To apply, please go to **website:** <http://www.childrensnational.org> and search for **requisition positions 12123 or 12124** (postdoctoral fellows), **11086** (staff scientist) or **11961** (research associate).

Your career is our cause.

Get help from the experts.

www.sciencecareers.org

- Job Postings
- Job Alerts
- Resume/CV Database
- Career Advice
- Career Forum

Science Careers

From the journal *Science* AAAS

We deliver customized job alerts.

Science Careers

From the journal *Science* AAAS

www.ScienceCareers.org

Download your free copy today.

ScienceCareers.org/booklets



From technology specialists to patent attorneys to policy advisers, learn more about the types of careers that scientists can pursue and the skills needed in order to succeed in nonresearch careers.

Science Careers

From the journal *Science* AAAS

Support the sciences. **Get rewarded.**

Show your AAAS pride and reward yourself with the new AAAS Platinum Advantage Rewards Card from NASA Federal Credit Union.

Apply now and get
10,000 bonus points!

Go to nasafcu.com/AAASpromo



Get **10,000 bonus points** if you sign up for a card and spend \$3,000 within 90 days of account opening.

Learn more at
nasafcu.com/AAASpromo.

Subject to credit approval.
Membership in AAAS and NASA FCU is required.
NASA FCU is federally insured by NCUA.



BE ASTONISHED BY THE RESULTS OF OUR REAL-TIME PCR. (YOU'LL NEVER NEED TO COMPROMISE AGAIN.)



CFX96 TOUCH™ REAL-TIME
PCR DETECTION SYSTEM



It's time to rethink what you know about real-time PCR. At the heart of our real-time PCR detection systems is a commitment to giving you the best results possible—quickly and easily. Our real-time PCR supermixes and new PrimePCR assays work together with our systems to deliver superior results every time. Enjoy a new degree of usability, quality and peace of mind that will launch your research forward.

Find out more at bio-rad.com/ad/rtPCR3

BIO-RAD